Synthetic Micro-Doppler Signatures of Non-Stationary Channels for the Design of Human Activity Recognition Systems

Ahmed Abdelmonem Abdelgawwad

UiA University of Agder

Doctoral Dissertations at the University of Agder 333

Ahmed Abdelmonem Abdelgawwad

Synthetic Micro-Doppler Signatures of Non-Stationary Channels for the Design of Human Activity Recognition Systems

Doctoral Dissertation for the Degree *Philosophiae Doctor (PhD)* at
the Faculty of Engineering and Science, Specialisation in
Information and Communication Technology

University of Agder
Faculty of Engineering and Science
2021

Doctoral Dissertations at the University of Agder 333
ISSN: 1504-9272
ISBN: 978-82-8427-039-5

Printed by 07 Media
Kristiansand

Abstract

The research interest in human activity recognition (HAR) to provide ambient assisted living (AAL) for elders living alone has increased. As a result, several HAR systems have been proposed. The categories of HAR systems fall into two types: wearable and non-wearable systems. Radio-frequency (RF)-based HAR systems are considered among the non-wearable types. They do not violate the users' privacy. Moreover, they do not require to be worn by the user. Furthermore, they are capable of sensing human activities through walls of buildings. That is why they catch more interest nowadays.

RF-based HAR systems capture the complex non-stationary behaviors of indoor channels influenced by human activities. Micro-Doppler signatures and time variant mean Doppler shifts (TV-MDSs) are considered among the extracted features used to train the human activity classifiers (HACs). The current approach is to train HACs by using measured RF-sensing data. The collection of such measured data is expensive and time-consuming. Furthermore, the collected data is not reproducible. An alternative approach is to generate the micro-Doppler signatures and the TV-MDSs of non-stationary channel simulation models for training the HACs.

The main aim of this dissertation is to generate synthetic micro-Doppler signatures and TV-MDSs to train the HACs. This is achieved by developing non-stationary fixed-to-fixed (F2F) indoor channel models. Such models provide an in-depth understanding of the channel parameters that influence the micro-Doppler signatures and TV-MDSs. Hence, the proposed non-stationary channel models help to generate the micro-Doppler signatures and the TV-MDSs, which fit those of the collected measurement data.

First, we start with a simple two-dimensional (2D) non-stationary F2F channel model with fixed and moving scatterers. Such a model assumes that the moving scatterers are moving in 2D geometry with simple time variant (TV) trajectories and they have the same height as the transmitter and the receiver antennas. The model of the Doppler shifts caused by the moving scatterers in 2D space is provided. The micro-Doppler signature of this model is explored by employing the spectrogram of which a closed-form expression is derived. Moreover, we demonstrate how the TV-MDSs can be computed from the spectrograms.

The aforementioned model is extended to provide two three-dimensional (3D) non-stationary F2F channel models. Such models allow simulating the micro-Doppler signatures

influenced by the 3D trajectories of human activities, such as walking and falling. Moreover, expressions of the trajectories of these human activities are also given. Approximate solutions of the spectrograms of these channels are provided by approximating the Doppler shifts caused by the human activities into linear piecewise functions of time. The impact of these activities on the micro-Doppler signatures and the TV-MDSs of the simulated channel models is explored.

The work done in this dissertation is not limited to analyzing micro-Doppler signatures and the TV-MDSs of the simulated channel models, but also includes those of the measured channels. The channel-state-information (CSI) software tool installed on commercial-off-the-shelf (COTS) devices is utilized to capture complex channel transfer function (CTF) data under the influence of human activities. To mitigate the TV phase distortions caused by the clock asynchronization between the transmitter and receiver stations, a back-to-back (B2B) connection is employed. Models of the measured CTF and its true phases are also shown. The true micro-Doppler signatures and TV-MDSs of the measured CTF are analyzed. The results showed that the CSI tool is reliable to validate the proposed channel models. This allows the micro-Doppler signatures and the TV-MDSs extracted from the data collected with this tool to be used to train the HACs.

Inertial measurement units (IMUs) can be used to capture the trajectories of moving objects or human activities. In this dissertation, two IMU-driven non-stationary CSI models are presented. Such models can be fed with trajectories collected by the IMUs to simulate realistic micro-Doppler signatures and the TV-MDSs. The aim of the first (second) model is to capture the influence of the trajectory of a rigid body (moving human) on the micro-Doppler signatures and the TV-MDSs of CSI channels. Frameworks are proposed for processing the IMU data to compute the trajectories and feed them to the CSI model to simulate the micro-Doppler signatures and the TV-MDSs. Both of IMU data and CSI data are recorded simultaneously to validate the proposed channel models. Then, the micro-Doppler signatures and the TV-MDSs of the IMU-driven models and CSI data are evaluated. The results show that there are strong agreements between the micro-Doppler signatures and the TV-MDSs of the IMU-driven model and the measured CSI. The outcomes of this dissertation pave the way towards simulation-based HAR systems.

List of Publications

The articles below are the results of the research work the author has done in the context of this dissertation. There are six articles. Five of them are published and one has been submitted.

Paper A [1]**A. Abdelgawwad** and M. Pätzold, "On the influence of walking people on the Doppler spectral characteristics of indoor channels," 2017 *IEEE 28th Annual International Symposium on Personal, Indoor, and Mobile Radio Communications (PIMRC2017)*, Montreal, QC, 2017, pp. 1-7, DOI: 10.1109/PIMRC.2017.8292482.

Paper B **A. Abdelgawwad** and M. Pätzold, "A framework for activity monitoring and fall detection based on the characteristics of indoor channels," *2018 IEEE 87th Vehicular Technology Conference (VTC2018-Spring)*, Porto, 2018, pp. 1-7, DOI: 10.1109/VTCSpring.2018.8417468.

Paper C **A. Abdelgawwad** and M. Pätzold, "A 3D non-stationary cluster channel model for human activity recognition," *2019 IEEE 89th Vehicular Technology Conference (VTC2019-Spring)*, Kuala Lumpur, Malaysia, 2019, pp. 1-7, DOI: 10.1109/VTC-Spring.2019.8746345.

Paper D **A. Abdelgawwad**, A. Català, and M. Pätzold, "Doppler power characteristics obtained from calibrated channel state information for human activity recognition," *2020 IEEE 91st Vehicular Technology Conference (VTC2020-Spring)*, Antwerp, Belgium, 2020, pp. 1-7, DOI: 10.1109/VTC2020-Spring48590.2020.9129187.

Paper E **A. Abdelgawwad**, A. Borhani, and M. Pätzold, "Modelling, analysis, and simulation of the micro-Doppler effect in wideband indoor channels with confirmation through pendulum experiments," *Sensors* 2020, vol. 20, no. 4, p. 1049, Feb. 2020, DOI: 10.3390/s20041049.

Paper F **A. Abdelgawwad**, A. Català, and M. Pätzold, "An IMU-driven 3D non-stationary channel model for human activity recognition," *IEEE Access, 2020, Submitted for publication.*

[1]This paper received the "Best Student Paper Award" from the PIMRC'17.

The following papers are relevant but not included in the dissertation.

Paper G A. Chelli, M. Muaaz, **A. Abdelgawwad**, and M. Pätzold, "Human activity recognition using Wi-Fi and machine learning," *2020 2nd International Conference on Telecommunications and Computing Technologies (ICTCT'20), Accepted for publication.*

Paper H M. Muaaz, A. Chelli, **A. Abdelgawwad**, A. C. Mallofré, and M. Pätzold, "WiWeHAR: multimodal human activity recognition using Wi-Fi and wearable sensing modalities," *IEEE Access*, vol. 8, pp. 164453-164470, 2020, DOI: 10.1109/ACCESS.2020.3022287.

Paper I M. Muaaz, **A. Abdelgawwad**, and M. Pätzold, "The influence of human walking activities on the Doppler characteristics of non-stationary indoor channel models," *Advances in Computational Intelligence.* pages 297–309, Cham, 2019. Springer International Publishing. DOI: 10.1007/978-3-030-20521-8_25.

Paper J R. Hicheri, **A. Abdelgawwad**, and M. Pätzold, "A new non-stationary 3D channel model with time-variant path gains for indoor human activity recognition," *2020 2nd International Conference on Telecommunications and Computing Technologies (ICTCT'20), Accepted for publication.*

Paper K R. Hicheri, **A. Abdelgawwad**, and M. Pätzold, "A non-stationary relay-based 3D MIMO channel model with time-variant path gains for human activity recognition in indoor environments," *Annals of Telecommunications, 2021, Submitted for publication.*

Contents

List of Figures

List of Tables

List of Abbreviations and Acronyms

2D	two-dimensional
3D	three-dimensional
AAL	ambient assisted living
AAOA	azimuth angle of arrival
AAOD	azimuth angle of departure
AOA	angle of arrival
AOD	angle of departure
AOM	angle of motion
B2B	back-to-back
CCG	complex channel gain
CoM	center of mass
COTS	commercial-off-the-shelf
CSI	channel-state-information
CTF	channel transfer function
CW	continuous-wave
DS	Doppler spread
EAOA	elevation angle of arrival
EAOD	elevation angle of departure
EMG	electromyography
F2F	fixed-to-fixed
F2M	fixed-to-mobile
FMCW	frequency-modulated-continuous-wave
HAC	human activity classifier
HAOM	horizontal angle of motion
HAR	human activity recognition
IF	image formation
IMU	inertial measurement unit
LOS	line-of-sight

LPC	linear predictive coding
MDS	mean Doppler shift
MFCC	mel frequency cepstral coefficient
MIMO	multiple-input multiple-output
MOCAP	motion capture
MP	matching pursuit
NLOS	non-line-of-sight
NMSE	normalized-mean-square error
OFDM	orthogonal-frequency-division-multiplexing
PCA	principal component analysis
RF	radio-frequency
RQ	research question
SIMO	single-input multiple-output
SISO	single-input single-output
SL	sign language
STFT	short-time Fourier transform
TiV	time invariant
TV	time variant
TV-CTF	TV channel transfer function
TV-PD	time variant propagation delay
TV-AAOA	time variant azimuth angle of arrival
TV-EAOA	time variant elevation angle of arrival
TV-AAOD	time variant azimuth angle of departure
TV-EAOD	time variant elevation angle of departure
TV-VAOM	time variant vertical angle of motion
TV-HAOM	time variant horizontal angle of motion
TV-DS	time variant Doppler spread
TV-MDS	time variant mean Doppler shift
USRP	universal software radio peripheral
V2V	vehicle-to-vehicle
VAOM	vertical angle of motion
ZUPT	zero-update

Part I

Main Chapters

Chapter 1

Introduction

The research interest in ambient assisted living (AAL) became higher in the last decade. This is due to the increase in the mortality rate among adults above 65 years [1]. The World Ageing Report by the United Nations expected in [2] that the number of adults over 80 will rise to 425 million by 2050. The aim of AAL is to provide assistance to the older people living alone. As a result, many contributions to the research and development of human activity recognition (HAR) systems have been proposed. HAR systems help to monitor the elders' activities and automatically detect their fall activities. HAR systems can be divided into two categories: wearable and non-wearable, as illustrated in Fig. 1.1.

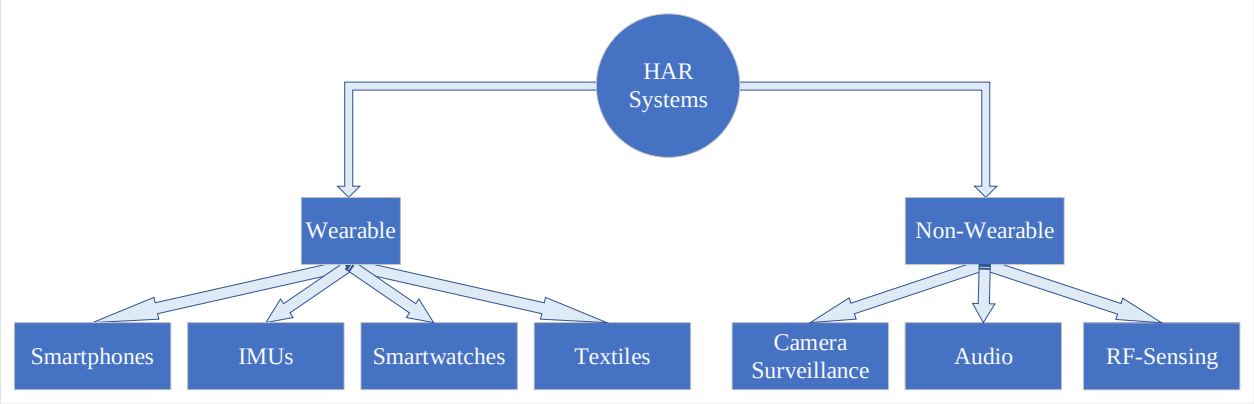

Figure 1.1: Categories of HAR systems.

1.1 Wearable HAR Systems

With reference to Fig. 1.1, there are four types of wearable technologies included in this section that can be used for HAR. These technologies are smartphones [3–9], inertial measurement

units (IMUs) [10–15], smartwatches [16, 17], and textiles [18–20]. The smartphones, smartwatches, and IMUs are equipped with sensors, such as accelerometer, linear accelerometer, gyroscope, and magnetometer, which can measure signs of human activities. According to Table 1.1, the accelerometer and linear accelerometer are able to capture the accelerations along the axes of the sensor including and excluding the impact of gravity, respectively. The gyroscopes can collect the rotational speed around the axes of the sensor. The magnetometer captures the geomagnetic field intensity the axes of the sensor.

Some other sensors can be embedded in clothes, trousers, shirts, shoes as in [19, 20]. Such kinds of wearable HAR systems belong to the textile-based category. These systems can be equipped with electromyography (EMG) electrodes [18] to monitor vital signs of humans or IMUs [21] to monitor human activities. Although the wearable systems have good accuracy, they have the following practical limitations. The sensors should be placed or worn by the user in particular body locations with specific orientations. They are obtrusive and require to be worn all day so that the system can recognize activities and vital signs continuously. The user might reject or forget to hold or wear the device. This might happen in real life between elders due to the discomfort or memory-related issues.

Table 1.1: Examples of inertial sensors in wearable HAR systems and their capabilities.

Sensor	**Measurement capabilities**
Accelerometer	Acceleration including gravitational forces in x, y, and z axes
Linear Accelerometer	Acceleration excluding gravitational forces in x, y, and z axes
Gyroscope	Rotational velocities around x, y, and z axes
Magnetometer	Geomagnetic field intensity in x, y, and z axes

1.2 Non-Wearable HAR Systems

Video surveillance-based HAR systems [22–29] are popular and widely used. They are able to continuously record images of body movements. Therefore, they are in great demand for monitoring the daily lives of the older people. Despite these advantages of camera-based HAR systems, they require very sophisticated image and video processing techniques to monitor daily human activities. Moreover, they consume a lot of storage and memory capacity. Furthermore, they can only be used in fixed locations and have a limited coverage area, which makes installing multiple camera systems inevitable. Hence, such a system requires calibration which is very complex. Thus, the system becomes more complicated and impractical. It is worth mentioning that lighting conditions can affect camera-based HAR systems, and they

are privacy-intrusive.

The main idea behind acoustic or audio HAR systems is that they rely on microphone sensors deployed in the area around the user to capture audio signals [30–32] caused by human activities. Such signals carry the fingerprints caused by the human activities. Then, various features are extracted from the audio signals, such as the spectrograms, linear predictive coding (LPC) [33], matching pursuit (MP) [34], and mel frequency cepstral coefficients (MFCCs) [35] to train the human activity classifier (HAC). These systems are accurate and unlike the wearable systems, they do not require user interaction. However, they have a limited coverage range, are highly dependent on the indoor layout, can be easily affected by background noise, and compromise privacy as they can record conversations.

1.3 RF-Based HAR Systems

Radio-frequency (RF)-sensing techniques have the following advantages in comparison to the aforementioned systems. They do not invade privacy like camera surveillance and audio-based systems. In addition, unlike wearable systems, they do not require the user's involvement. They are also not dependent on lighting conditions and their sensors are not blocked by walls. For wearable systems, the user might forget or refuse to wear the systems for memory-related or discomfort reasons. Therefore, RF-based HAR systems can be a reasonable choice to use.

RF-sensing relies on the rapid change of the channel characteristics triggered by the body movements. Such characteristics include the phases and amplitudes of the complex received signal. These variations of the characteristics hold the fingerprints of the body movements. The rapid changes in these characteristics make the channels non-stationary. Many RF-sensing technologies have been commonly used to collect channel measurements, such as radar, Wi-Fi, universal software radio peripherals (USRPs), and channel sounders. Radar employs the continuous-wave (CW) and frequency-modulated-continuous-wave (FMCW) transmission techniques to capture the characteristics of narrowband and wideband channels, respectively.

Table 1.2 shows four different RF sensing technologies, and the progress made in collecting data from extracted features that can be used to train HACs. In the literature, radars, USRPs, and channel sounders have been incorporated to extract micro-Doppler signatures[1] [36–39] to train the HACs. The term micro-Doppler refers to the Doppler effect that an electromagnetic signal experiences due to the motion of a target [40]. This term was introduced in [41–43]. Fig. 1.2 shows an example of using the micro-Doppler signatures and time variant mean Doppler shifts (TV-MDSs) to classify human activities. There are many attempts to simulate micro-Doppler signatures of radar signals under the influence of human walking activities in [44–46]. Another feature depicted in Fig. 1.2 is the TV-MDS, which can be further computed

[1]Throughout this dissertation, the terms micro-Doppler signatures and the time variant (TV) Doppler power characteristics are interchangeably used.

from the micro-Doppler signatures. This feature can be used to train the HACs and will be addressed in the next chapters of this dissertation.

Another alternative to radars is collecting channel-state-information (CSI) data by using commercial-off-the-shelf (COTS) devices [47–49]. A CSI tool has been developed by the authors of [50] as an open source software. Such a tool can be installed on COTS devices equipped with Intel NIC 5300 network interface cards that operate on Wi-Fi 802.11n protocol. COTS devices with such an installed tool and NIC cards are able to record CSI data via 30 subcarriers according to the orthogonal-frequency-division-multiplexing (OFDM) access scheme. Although this tool allows for capturing complex RF data with inexpensive devices, it has the disadvantage of containing highly distorted phases. This happens due to the clock asynchronization of the transmitter and the receiver stations. Many approaches have been introduced in the literature to clean the collected CSI data. One of the approaches was denoising the amplitudes by applying filters or the principal component analysis (PCA) on the amplitudes for the purpose of smoothing before training the HAC [47,48]. Another alternative approach was to compute one-sided spectrograms of the amplitudes as in [51, 52], which are used as features to train the classifiers. The last approach was to use linear transformations to sanitize the highly distorted phases as in [49, 52–54] to train the HAC.

Table 1.2: State of the art contributions in RF-sensing for HAR

Articles	**Technology**	**Features**	**Measurements**	**Simulations**
[36, 55] [37, 56–58]	Radar	Micro-Doppler signatures	✓	–
[44–46, 59]	Radar	Micro-Doppler signatures	–	✓
[39, 60]	Channel sounder	Micro-Doppler signatures	✓	–
[38, 61]	USRP	Fourier transform	✓	–
[47, 48]	Wi-Fi	Amplitudes	✓	–
[51, 52]	Wi-Fi	One-sided spectrograms of the amplitudes	✓	–
[52, 62] [49, 53, 54]	Wi-Fi	Sanitized phases	✓	–

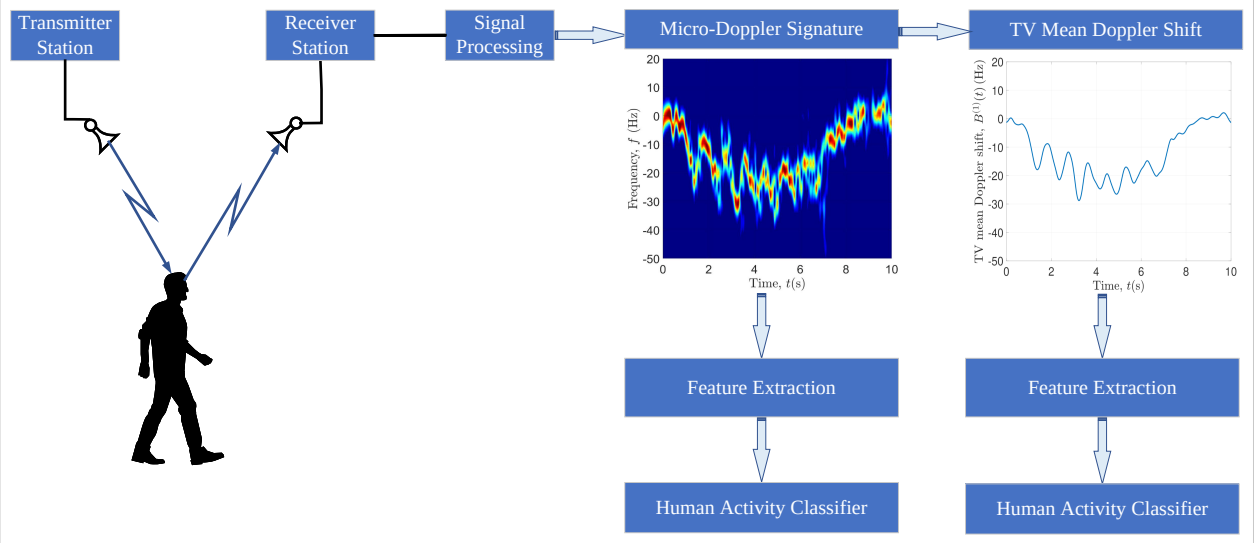

Figure 1.2: Obtaining and using the micro-Doppler signature or, alternatively, the TV-MDS of the complex measured RF data to classify human activities.

1.4 Motivation

By looking at Table 1.2, most of the RF-sensing related works have been done with measured channels. Fig. 1.3(a) shows the current approach used for training and testing the HACs. This approach requires collecting RF-sensing data by conducting measurement campaigns. Such campaigns are time-consuming and expensive. They require having many candidates, expensive tools and time-consuming setups. Moreover, the micro-Doppler signatures and the TV-MDSs of the collected measurement data are non-reproducible. For a specific human activity, the micro-Doppler signatures and the TV-MDSs might be different for each scenario as they depend on the direction of motion, speed, and locations of the transmitter and receiver. Hence, different scenarios and activities require conducting further campaigns.

This dissertation paves the way from the current approach for training HACs depicted in Fig. 1.3(a) to a new paradigm, as shown in Fig. 1.3(b). This paradigm relies on training HACs with synthetic micro-Doppler signatures or TV-MDSs instead of those extracted from measured RF data. This paradigm enables the HAC trained by using synthetic data to detect human activities when it is tested on measured RF data as illustrated in Fig. 1.4. The new paradigm requires in-depth studies of non-stationary fixed-to-fixed (F2F) channels in the presence of moving persons and their influence on the micro-Doppler signatures and the TV-MDSs. Understanding the underlying propagation phenomena is indispensable for the development of a new class of channel simulation models. Such models enable the generation of reproducible synthetic micro-Doppler signatures and TV-MDSs mimicking the effects of human activities. Note that this dissertation focuses on channel modelling, not machine

learning.

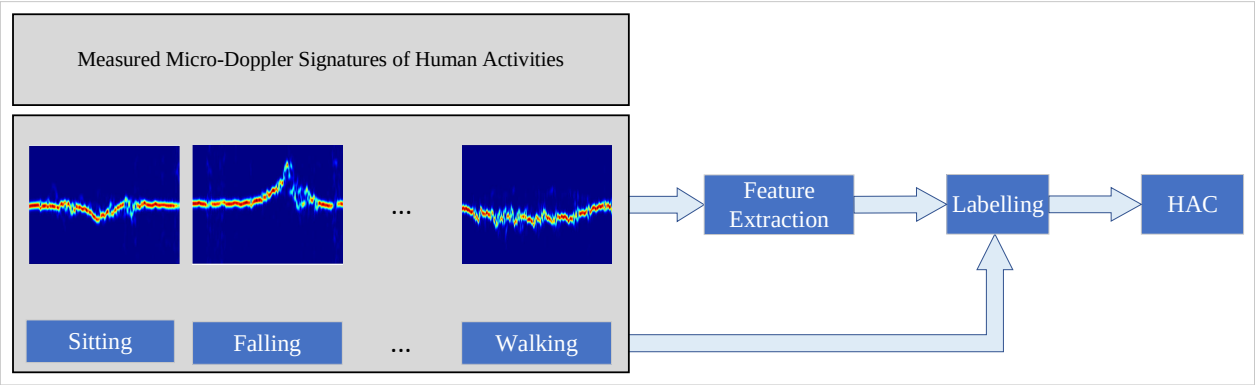

(a) Training the HAC with measurement data.

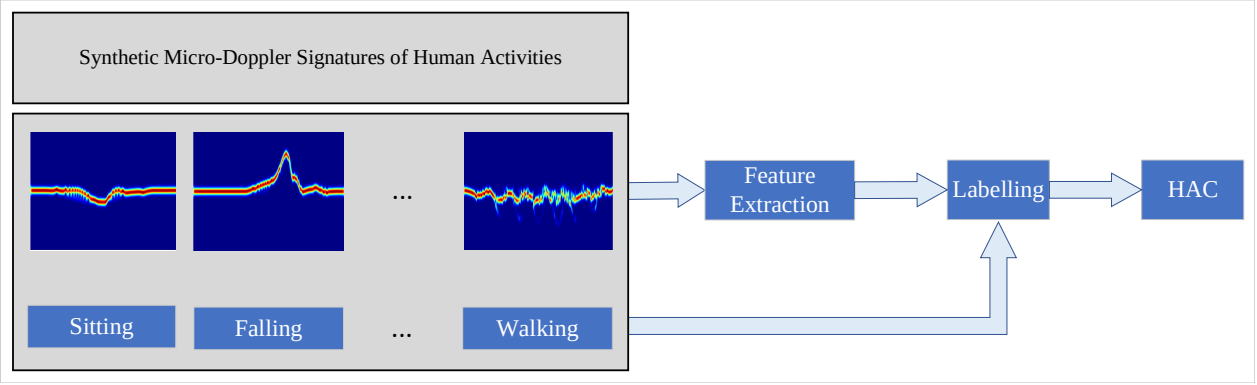

(b) Training the HAC with synthetic data.

Figure 1.3: (a) The current measurement-based approach and (b) the new simulation-based approach to train HACs.

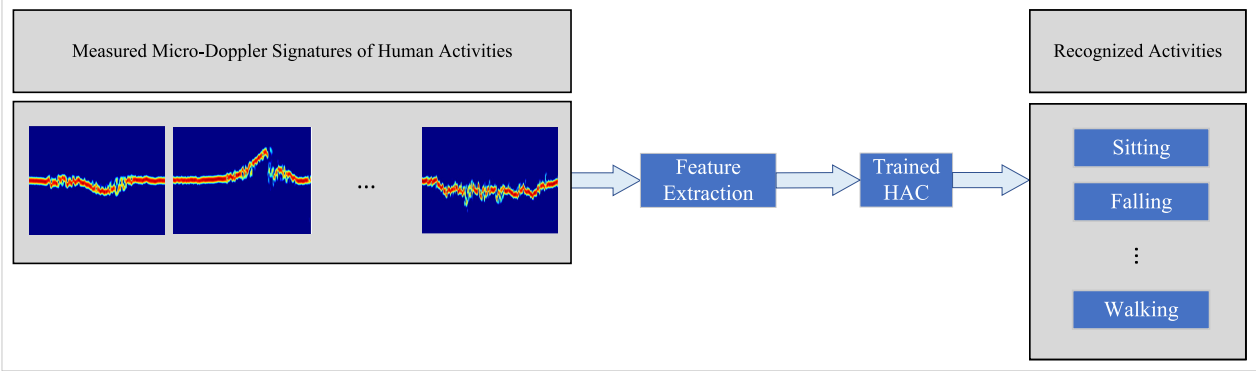

Figure 1.4: Employing the HAC trained with synthetic data to recognize human activities when measurement data is given.

1.5 Contributions

Table 1.3 exhibits the contributions of developing non-stationary channel simulation models HAR in the literature. The marks (×), (✓), and (–) in the table denote that the parameters are modelled as time invariants (TiVs), modelled as TVs, and not modelled, respectively. As depicted in the table, there are limitations in channel modelling in the previous studies when considering the channel parameters, such as the TV path gains, TV Doppler frequencies, TV phases, phase-Doppler relationship, and propagation delay-Doppler relationship. The focus of this dissertation is to model the aforementioned TV parameters and put more emphasis on the phase and the Doppler frequencies in order to generate reproducible micro-Doppler signatures and TV-MDSs for different human activities and indoor scenarios. The contributions of **Papers A–F** are not limited to the simulations of micro-Doppler signatures of non-stationary channel models, but also include the micro-Doppler signatures of the measured indoor channels for validity. A summary of the channel modelling contributions in this dissertation is depicted in Fig. 1.5.

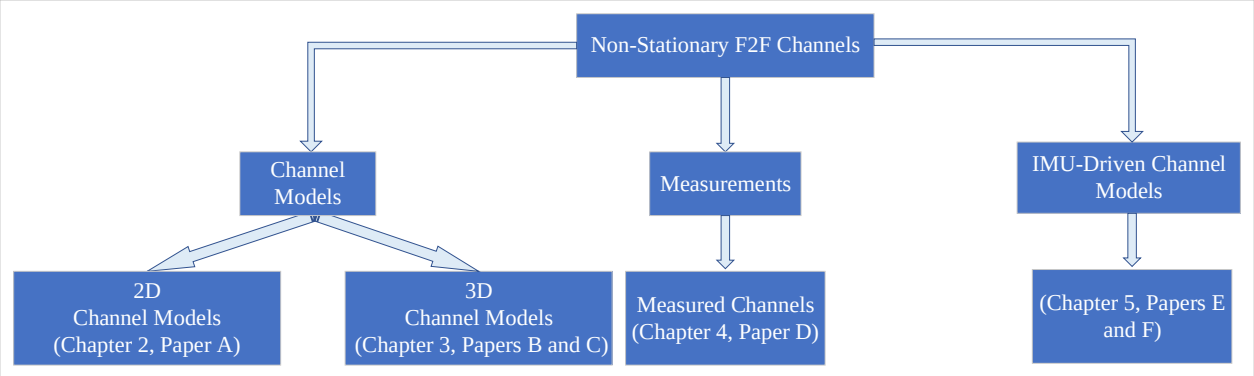

Figure 1.5: Non-stationary F2F channel models described in this dissertation.

1.6 Research Questions

Here is the list of research questions (RQs) based on the aforementioned overview and motivation, which will be addressed in the next chapters:

RQ 1: How to model two-dimensional (2D) non-stationary F2F channels under the influence of moving scatterers?

RQ 2: How to analyze the effect of moving scatterers on the TV Doppler power characteristics of indoor channels?

RQ 3: How to model the influence of three-dimensional (3D) human body trajectories on the micro-Doppler signatures of indoor F2F channels?

Table 1.3: Contributions to channel modelling for HAR using RF-sensing.

Papers	**Path gains**	**Doppler frequencies**	**Phases**	**Phase-Doppler relationship**	**Delay-Doppler relationship**	**Fixed scatterers**
[36, 44, 45, 48, 49, 52]	–	–	–	no	no	no
[37, 46]	×	–	–	no	no	no
[38, 61]	–	×	–	no	no	no
[47]	×	–	–	no	no	no
[51]	–	–	✓	no	no	no
[62]	–	–	×	no	no	no
A–C	×	✓	✓	yes	no	yes
E	×	✓	✓	yes	yes	yes
D,F	✓	✓	✓	yes	yes	yes

RQ 4: How to model the true phases of the measured CSI?

RQ 5: Is it possible to extract the true micro-Doppler signatures from the CSI measured with COTS devices?

RQ 6: How to develop channel models driven by measured trajectories to generate realistic and reproducible micro-Doppler signatures?

RQ 7: How to validate the micro-Doppler signatures and the TV-MDSs of the trajectory-driven models?

1.7 Structure of the Dissertation

The dissertation is divided into two parts. The first part (**Part I**) presents an overview of the contributions of this dissertation. The second part (**Part II**) is structured as a list of the technical papers, which exploit the detailed contributions and their results. Table 1.4 exhibits the specific chapters and papers that answer each of the aforementioned RQs. The rest of **Part I** is organized as follows:

Table 1.4: The relationships between the chapters, RQs, and papers are indicated by check marks (✓).

	Papers						**RQs**						
Chapters	**A**	**B**	**C**	**D**	**E**	**F**	RQ 1	RQ 2	RQ 3	RQ 4	RQ 5	RQ 6	RQ 7
2	✓	–	–	–	–	–	✓	✓	–	–	–	–	–
3	–	✓	✓	–	–	–	–	✓	✓	–	–	–	–
4	–	–	–	✓	–	–	–	✓	–	✓	✓	–	–
5	–	–	–	–	✓	✓	–	✓	–	–	–	✓	✓

- Chapter 2 answers RQ 1 by covering the work presented in **Paper A**. The paper proposes a 2D non-stationary F2F model with moving and fixed point scatterers. Doppler shifts caused by the 2D trajectories of the moving point scatterers are modelled.

- Chapter 3 addresses RQ 3 by providing an overview of the contributions of **Papers B** and **C** as follows:

    1. A 3D non-stationary channel model, which considers the moving person as a single moving point scatterer representing the head (**Paper B**). Such a model allows to simulate the micro-Doppler signatures of the head motion in activities, such as walking and falling.

2. A 3D cluster channel model, which considers the moving person as a cluster of synchronized moving point scatterers (**Paper C**). This model allows the simulation of micro-Doppler signatures of different body segments, such as head, torso, ankles, and wrists for different walking and running scenarios. Such a model is also useful for gait analysis.

- Chapter 4 answers RQs 4 and 5 by covering the contents of **Paper D**. This paper model the true phases of the measured CSI. Furthermore, the paper solves the problem of the TV phase distortions, which appears when measuring the CSI with COTS devices. This problem is addressed by employing a back-to-back (B2B) connection between the transmitter and receiver stations. The paper reports the true micro-Doppler signatures and the TV-MDSs of the measured CSI after eliminating the phase distortions. The contribution of the paper enables to use CSI data collected by using COTS devices to validate the synthetic micro-Doppler signatures and the TV-MDSs of the channel simulation models.

- Chapter 5 answers RQ 6 by summarizing the contributions of **Papers E** and **F**. They present the following contributions:

  1. **Paper E** presents a non-stationary IMU-driven CSI model to simulate the micro-Doppler signature of a moving rigid body, where the center of mass (CoM) of the rigid body is modelled as a single moving point scatterer.
  2. **Paper F** develops an extended non-stationary IMU-driven CSI model, in which the moving person is modelled as a cluster of moving point scatterers.

  To answer RQ 7, both of IMU and CSI data are collected, simultaneously. The trajectories computed from the measured IMU data were fed to the channel models. Then, the micro-Doppler signatures and the TV-MDSs of IMU-driven models and the measured CSI data were evaluated.

- RQ 2 is answered by employing the spectrogram to reveal the micro-Doppler signatures of simulated and measured channels in **Papers A**–**F** and Chapters 2–5.

- Chapter 6 summarizes the major contributions of this dissertation and provides an outlook for future research directions.

Chapter 2

2D Non-Stationary Channel Model

2.1 Introduction

The wireless communication channel is considered stationary when its statistical properties do not vary with time, i.e., they are time invariant (TiV). This is generally assumed when the angle of arrival (AOA), angle of departure (AOD), and the speed of the transmitter station, receiver station, or the moving point scatterers are TiV. When monitoring indoor scenarios for long periods, the AOAs and AODs become time variant (TV). Moreover, the speed of the transmitter station, receiver station, or the moving point scatterers might change with time due to acceleration or deceleration. Thus, the Doppler effect is TV and the channel becomes non-stationary. Thus, the Doppler power characteristics, mean Doppler shift (MDS), and Doppler spread (DS) are TV.

For wireless-based human activity recognition (HAR), considering the TV angles of motion (AOMs), AODs, AOAs, and speed is inevitable. This is since the moving point scatterers might change their speed or their direction of motion. In the literature, the compound Doppler effect caused by moving point scatterers has been modelled in stationary fixed-to-mobile (F2M) [63], vehicle-to-vehicle (V2V) [64, 65], and fixed-to-fixed (F2F) [66] channel models.

In the literature, the non-stationary F2F channel model under the time variations of the AOAs, AODs, and the speed of the moving point scatterers has not been investigated. To close this gap, this chapter gives an overview of the contribution of **Paper A**, which contains a non-stationary F2F channel model associated with two-dimensional (2D) geometry. The TV AODs and AOAs are presented corresponding to the 2D trajectories and the 2D positions of the transmitter (T_x) and the receiver (R_x), and the TV displacements of the moving point scatterers. Furthermore, the TV Doppler frequencies caused by the trajectories of the moving point scatterers are derived. In addition, the expressions of the TV channel phases and the complex channel gain (CCG) are provided. **Paper A** explores the micro-Doppler signature of the proposed model by using the spectrogram. The spectrogram can be used to visualize the temporal change of the frequency content of a non-stationary signal. It has many applications

in radar detection [67], music [68], remote sensing [69], and earthquake records [70]. The main disadvantage of the spectrogram is spectral interference due to its quadratic nature. The work in **Paper A** provides the approximate solution of the spectrogram and proposes a way to remove the spectral interference in computer simulations.

2.2 A Geometrical 2D Model

The Doppler shifts caused by moving point scatterers in the 2D space depend not only on the speed of the scatterers, but also on the AODs, AOAs, and AOMs. The AODs are TV functions of the displacements of the moving point scatterer and the location of the T_x, whereas the AOAs are TV functions of the displacements of the moving point scatterers and the location of the R_x. The AOMs are functions of the TV velocities of the moving point scatterers. To understand how these functions are modelled, a 2D geometrical model is needed. Such a model provides insights into the aforementioned TV functions, the TV Doppler frequencies, the TV phases, and the non-stationary CCG. Then, the micro-Doppler signatures are computed from the CCG. In indoor F2F channels, both T_x and R_x are fixed. Studying the 2D geometrical model helps to understand how to model the AODs and AOAs that affect the Doppler shifts caused by the moving point scatterers.

In the following, we will outline briefly how we can derive the angular functions AODs, AOAs, and AOMs. Our starting point is a geometrical model that helps to derive these functions. Then, we compute the Doppler frequencies caused by the moving scatterers in terms of the aforementioned functions. Subsequently, we derive the stochastic channel phases caused by the moving scatterers. Next, we provide an expression of the CCG $\mu(t)$ from which the time variant mean Doppler shift (TV-MDS), time variant Doppler spread (TV-DS), and micro-Doppler signatures are extracted.

The scenario in Fig. 2.1 exhibits a 2D multipath propagation scenario with a fixed T_x and R_x. There exist $\mathcal{M}$ fixed objects. For simplicity, each object is described as a fixed single point scatterer S_m^{F} for $m = 1, 2, \ldots, \mathcal{M}$. Moreover, there are $\mathcal{N}$ moving persons. Each person is modelled as a single moving point scatterer S_n^{M} for $n = 1, 2, \ldots, \mathcal{N}$ and has an initial position at $\left(x_n^{\mathrm{M}}, y_n^{\mathrm{M}}\right)$. The trajectory of each moving point scatterer is described by its TV speed $\mathrm{v}_n(t)$ and its AOM α_{v_n}, and has a constant acceleration/deceleration a_n. The line-of-sight (LOS) is assumed to be obstructed.

Paper A describes the relationship between the TV speed $\mathrm{v}_n(t)$, AOD α_{v_n}, the TV displacement in x-direction $x_n^{\mathrm{M}}(t)$, and the TV displacement in y-direction $y_n^{\mathrm{M}}(t)$ as

$$x_n^{\mathrm{M}}(t) = x_n^{\mathrm{M}} + \left[\mathrm{v}_n t + \frac{1}{2} a_n t^2\right] \cos\left(\alpha_{v_n}\right) \tag{2.1}$$

$$y_n^{\mathrm{M}}(t) = y_n^{\mathrm{M}} + \left[\mathrm{v}_n t + \frac{1}{2} a_n t^2\right] \sin\left(\alpha_{v_n}\right), \tag{2.2}$$

respectively. From (2.1)-(2.2), the TV AOA and AOD are given by

$$\alpha_n^R(t) = \text{atan2}\left(\frac{y_n^{\text{M}}(t) - y^R}{x_n^{\text{M}}(t) - x^R}\right), \tag{2.3}$$

$$\alpha_n^T(t) = \text{atan2}\left(\frac{y_n^{\text{M}}(t) - y^T}{x_n^{\text{M}}(t) - x^T}\right), \tag{2.4}$$

where $\alpha_n^T(t)$, $\alpha_n^R(t) \in [-\pi, \pi)$, respectively. The TV expression in (2.3) represents the angle between the direction of the wave arriving at the R_x from the S_n^{M}, and the positive x-axis. The TV formula in (2.4) describes the angle between the positive x-axis and the wave travelling from the T_x and impinging on the S_n^{M}. By using the AOA and AOD expressions in (2.3)–(2.4), the TV Doppler frequency caused by the nth moving point scatterer S_n^{M} is expressed by

$$f_n(t) = -f_{n,\max}(t)\left[\cos\left(\alpha_n^T(t) - \alpha_{v_n}\right) + \cos\left(\alpha_{v_n} - \alpha_n^R(t)\right)\right], \tag{2.5}$$

where the TV function $f_{n,\max}(t)$ denotes the maximum TV Doppler shift caused by the speed $\text{v}_n(t)$ of the S_n^{M} and is given by

$$f_{n,\max}(t) = \frac{f_0 \text{v}_n(t)}{c_0}. \tag{2.6}$$

The parameters f_0 and c_0 in (2.6) designate the carrier frequency and the speed of light, respectively. By utilizing the Doppler frequency $f_n(t)$ expressed in (2.5), the TV channel phase associated with the nth moving point scatterer S_n^{M} is given by

$$\theta_n(t) = 2\pi \int_{-\infty}^{t} f_n(t')dt' \approx \theta_n + 2\pi \int_{0}^{t} f_n(t')dt'. \tag{2.7}$$

The parameter θ_n is unknown and modelled as a random variable with a uniform distribution between 0 and 2π, i.e., $\mathcal{U} \sim (0,\, 2\pi]$. In **Paper A**, the Doppler frequency associated with the nth moving point scatterer has been approximated by using the Taylor series. The CCG $\mu(t)$, which consists of $\mathcal{N} + \mathcal{M}$ components has been given by

$$\mu(t) = \sum_{n=1}^{\mathcal{N}} c_n e^{j\theta_n(t)} + \sum_{m=1}^{\mathcal{M}} c_m e^{j\theta_m}. \tag{2.8}$$

The first term in (2.8) denotes the sum of $\mathcal{N}$ multipath components corresponding to the moving point scatterers S_n^{M}. Each component of the first term is characterized by the constant path gain c_n and a stochastic phase process $\theta_n(t)$. The second term in (2.8) is the sum of $\mathcal{M}$ multipath components corresponding to the fixed point scatterers S_m^{F}. Each component of the second term in (2.8) is characterized by a constant path gain c_m and a random phase variable θ_m. Note that θ_m and θ_n are independently and identically distributed (i.i.d.). The

fixed point scatterers S_m^{F} do not cause any Doppler shifts in F2F channels. The model in (2.8) is non-stationary. Its TV-MDS and the TV-DS have been given by [71]

$$B_f^{(1)}(t) = \frac{\sum_{n=1}^{N} c_n^2 f_n(t)}{\sum_{n=1}^{N} c_n^2 + \sum_{m=1}^{M} c_m^2}, \tag{2.9}$$

$$B_f^{(2)}(t) = \sqrt{\frac{\sum_{n=1}^{N} c_n^2 f_n^2(t)}{\sum_{n=1}^{N} c_n^2 + \sum_{m=1}^{M} c_m^2} - \left(B_f^{(1)}(t)\right)^2}, \tag{2.10}$$

respectively.

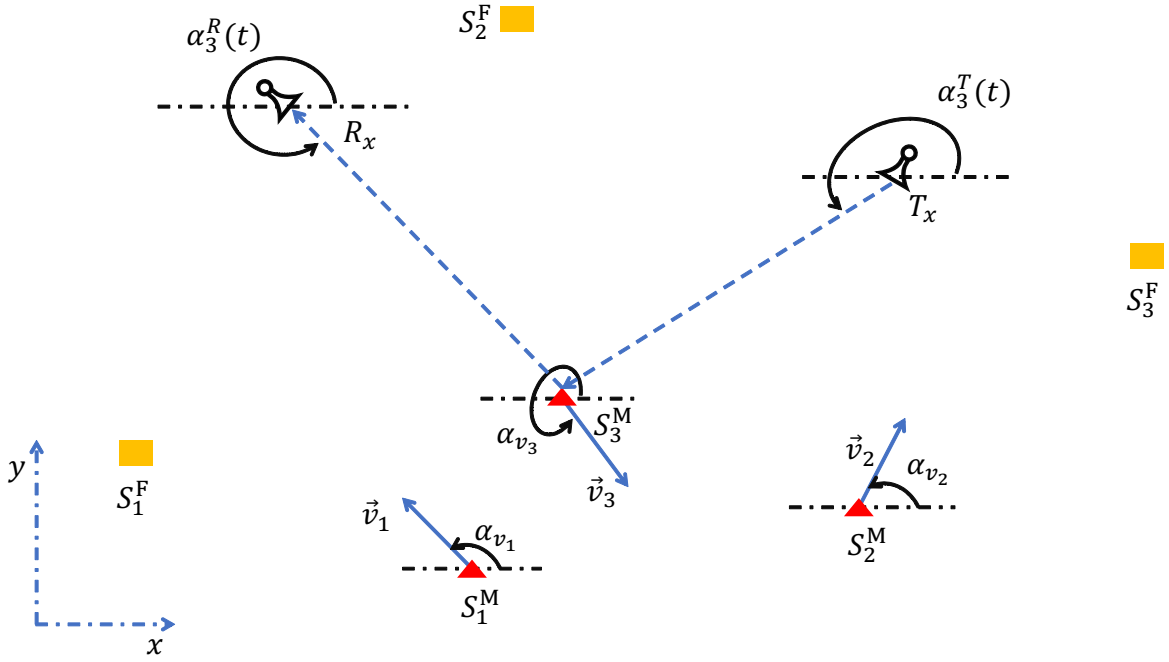

Figure 2.1: Geometrical channel model of a 2D propagation scenario with moving point scatterers S_n^{M} (▲), fixed point scatterers S_m^{F} (■), fixed T_x, and fixed R_x.

2.3 Micro-Doppler Effect of Non-Stationary 2D F2F Channels

To explore the micro-Doppler signatures of the non-stationary CCG presented in (2.8), a time-

frequency distribution, such as the spectrogram is employed. The spectrogram is one of the quadratic time-frequency distributions, often used to analyze the power spectral characteristics of stationary or non-stationary signals [72], such as the CCG. It provides insights into the TV power spectral density of the signal. It has many applications in the area of TV signals [73], speech analysis and identification [74], acoustics [75], and seismology [76]. The spectrogram consists of two terms, the auto-term and the cross-term. The auto-term provides insights into the true TV power spectral density of the signal. The cross-term is considered as the undesired spectral interference component that reduces the resolution of the spectrogram. This term results from the quadratic nature of the spectrogram. Many attempts have been made to address this issue in the field of mobile fading channels in [77, 78].

In **Paper A**, the spectrogram has been used to explore the micro-Doppler signature of the model presented in (2.8). The spectrogram helps to show TV Doppler frequencies caused by the moving point scatterers S_n^{M}. To compute the spectrogram, an even and positive window function $w(t)$ with normalized energy is needed. In a first step, this window is slid over $\mu(t)$ to compute the short-time CCG $x(t', t)$ as

$$x(t', t) = \mu(t')w(t' - t). \tag{2.11}$$

The parameters t and t' denote the local time, at which the micro-Doppler signature is explored and the run time, respectively. The second step is to compute the short-time Fourier transform (STFT) by transforming the run time t' into the frequency domain as follows

$$X(f, t) = \int_{-\infty}^{\infty} x(t', t)e^{-j2\pi ft'}dt'. \tag{2.12}$$

The third step is to compute the spectrogram $S_\mu(f, t)$ by taking the squared magnitude of $X(f, t)$ as

$$S_\mu(f, t) = |X(f, t)|^2 = S_\mu^{(a)}(f, t) + S_\mu^{(c)}(f, t). \tag{2.13}$$

The TV functions $S_\mu^{(a)}(f, t)$ and $S_\mu^{(c)}(f, t)$ in (2.12) designate the *auto-term* and *cross-term*, respectively. The auto-term has the desired micro-Doppler characteristics of the CCG $\mu(t)$ in (2.8). The cross-term contains the undesired interference components that reduce the resolution of the spectrogram. In **Paper A**, the full expressions of $X(f, t)$, $S_\mu^{(a)}(f, t)$, and $S_\mu^{(c)}(f, t)$ are provided in terms of the path gains and the Doppler frequencies. These expressions have been derived by taking advantage of the Taylor series approximation of the Doppler frequencies mentioned in Section 2.2. Moreover, a method for the elimination of the cross-term $S_\mu^{(c)}(f, t)$ has been applied in the paper by exploiting the random channel phases θ_n and θ_m. Furthermore, the paper shows how to compute the TV-MDS and the TV-DS from the spectrogram $S_\mu(f, t)$. Computing the TV-MDS and the TV-DS from the spectrogram is useful when analyzing measurement data, because the Doppler frequencies and the path gains of the measured channels are not accessible.

2.4 Principle Results

In the results section of **Paper A**, a realistic scenario with fixed point scatterers and moving point scatterers with speed variations has been considered. The CCG $\mu(t)$ was computed. A method for computing the optimal spectrogram window size was presented. The spectrogram $S_\mu(f,t)$ and the auto-term $S_\mu^{(a)}(f,t)$ have been evaluated according to the expressions in the paper and have been computed numerically. Furthermore, the TV-MDSs $B_f^{(1)}(t)$ and $B_\mu^{(1)}(t)$ and the TV-DSs $B_f^{(2)}(t)$ and $B_\mu^{(2)}(t)$ have been computed.

In this section, some of the results in the paper will be exploited. In the simulated scenario in the paper, the number of moving scatterers $\mathcal{N}$ was chosen to be 3, and the number of fixed scatterers $\mathcal{M}$ was equal to 7. One of the moving scatterers was moving at a constant speed towards the T_x and R_x during the whole simulation time. The other two moving scatterers were moving towards a terminating point away from the T_x and R_x with a constant speed. Then, they decelerated before reaching the point. The other parameters related to the simulation setup, such as the carrier frequency and the locations of T_x and R_x can be found in the paper. Fig. 2.2(a) depicts the analytical solution of the spectrogram $S_\mu(f,t)$. The spectrogram in Fig. 2.2(a) provides insight into the Doppler shifts caused by all the point scatterers. The Doppler patterns at the zero frequency values during the whole observation time correspond to the fixed point scatterers. The other three Doppler shifts, which are TVs are associated with the moving point scatterers. The scatterer moving with a constant speed during the whole observation time has an initial Doppler frequency value of 40 Hz approximately. Then, its Doppler frequency slightly decreases. This is due to the time variations of the AOD and AOA.

In Fig. 2.2(a), the Doppler effect caused by the second moving point scatterer has an initial value of -20 Hz approximately. The moving point scatterer kept moving at a constant speed until time $t \approx 1.5$ s. The Doppler frequency is TV due to the time variations of the AOD and AOA. After time $t \approx 1.5$ s, the moving point scatterer started to decelerate until it stopped at time $t \approx 3.5$ s. That is why the Doppler frequency increases from $t \approx 1.5$ s to $t \approx 3.5$ s. After time $t \approx 3.5$ s the scatterer, was no longer moving. The Doppler frequency should have a zero value; however, it does not due to the error from the Taylor series approximation. For the last moving point scatterer, the same aforementioned discussion applies, but for the time instants $t \approx 2.5$ s to $t \approx 4$ s. The cross-term of the spectrogram has an impact on the frequency values of the fixed point scatterers. Moreover, it has an impact on the frequency values of the moving point scatterers in the time interval from $t \approx 4.5$ s to $t \approx 5$ s. Fig 2.2(b) depicts the analytical solution of the auto-term $S_\mu^{(a)}(f,t)$. All the spectral interference components are eliminated, and their previously mentioned impacts on the spectrogram $S_\mu(f,t)$ depicted in Fig. 2.2(a) are removed. The Doppler frequency patterns of the fixed point scatterers are clearer. Furthermore, the spectral interference between the Doppler frequency patterns of the moving point scatterer is eliminated in the time interval

from $t \approx 4.5$ s to $t \approx 5$ s. The results of the analytical solution depicted in Figs. 2.2(a) and 2.2(b) have been validated by the numerical computation of the spectrogram $\hat{S}_\mu(f,t)$ and the auto-term $\hat{S}_\mu^{(a)}(f,t)$. We demonstrated that the numerical computation of the spectrogram $\hat{S}_\mu(f,t)$ and the auto-term $\hat{S}_\mu^{(a)}(f,t)$ are identical to the analytical solutions $S_\mu(f,t)$ and the auto-term $S_\mu^{(a)}(f,t)$, respectively.

Fig. 2.3(a) depicts the TV-MDSs $B_f^{(1)}(t)$, $B_\mu^{(1)}(t)$, and $\hat{B}_\mu^{(1)}(t)$. The TV-MDS $B_f^{(1)}(t)$ has been computed by (2.9). The TV-MDSs $B_\mu^{(1)}(t)$, and $\hat{B}_\mu^{(1)}(t)$ have been computed from the analytical solution of the auto-term $S_\mu^{(a)}(f,t)$ and the numerical computation of the auto-term $\hat{S}_\mu^{(a)}(f,t)$, respectively. The figure shows that there is a good match between $B_f^{(1)}(t)$, $B_\mu^{(1)}(t)$, and $\hat{B}_\mu^{(1)}(t)$. Futhermore, the figure illustrates the influence of the speed variations, AOAs and AODs on the TV-MDSs. The visible changes in the slopes of the TV-MDSs are due to the decelerations of the moving scatterers. Fig. 2.3(b) illustrates the TV-DSs $B_f^{(2)}(t)$, $B_\mu^{(2)}(t)$, and $\hat{B}_\mu^{(2)}(t)$. The TV-DS $B_f^{(2)}(t)$ has been evaluated by (2.10). The aforementioned comments on Fig. 2.3(a) applies to the TV-DSs depicted in Fig. 2.3(b).

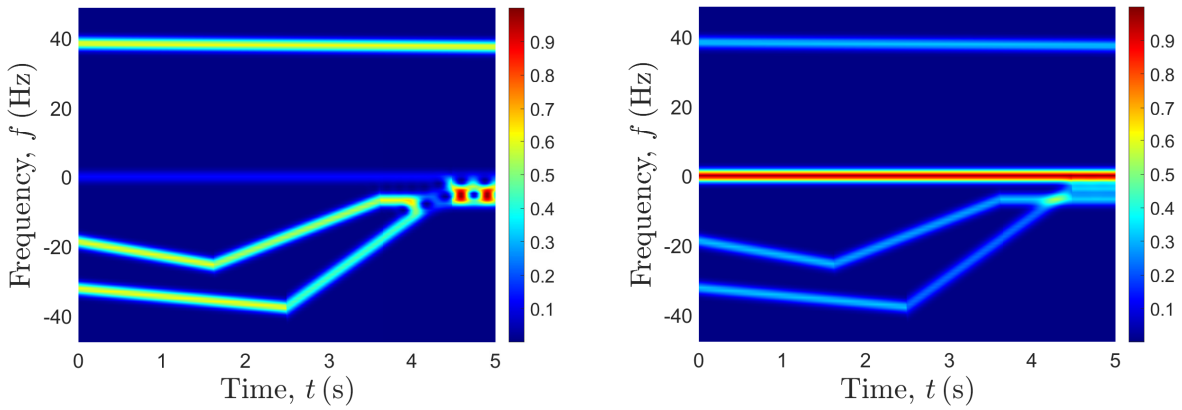

Figure 2.2: The analytical solution of (a) the spectrogram $S_\mu(f,t)$ and (b) the auto-term $S_\mu^{(a)}(f,t)$ of the provided scenario in **Paper A**.

2.5 Chapter Conclusion

In this chapter, a non-stationary F2F channel model has been developed that allows for the variations of the speed of moving point scatterers in 2D geometry. The derivations of the TV channel parameters, such as the AOAs, the AODs, and the TV Doppler frequencies are derived (see **Paper A**). Furthermore, the TV channel phases, CCG, TV-MDS, and TV-DS are presented. The micro-Doppler signature of the proposed model is investigated by utilizing

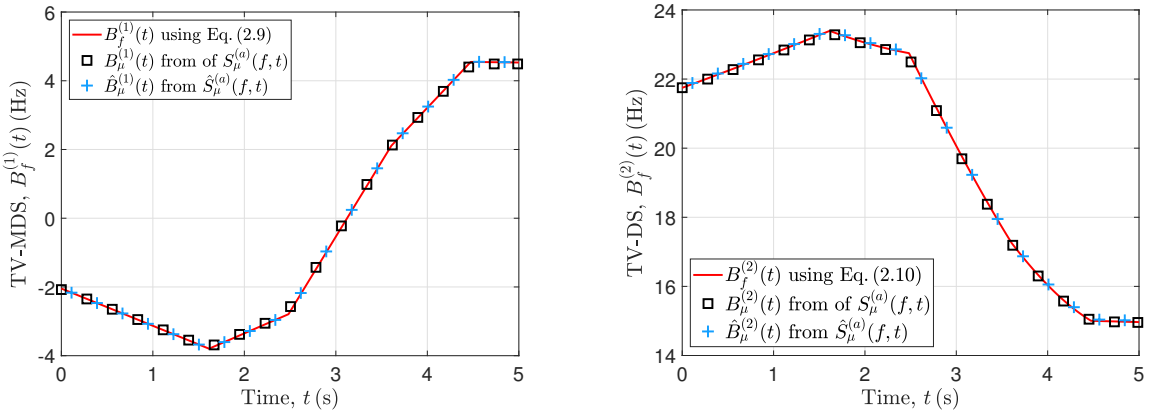

(a) The TV-MDSs $B_f^{(1)}(t)$, $B_\mu^{(1)}(t)$, and $\hat{B}_\mu^{(1)}(t)$.

(b) The TV-DSs $B_f^{(2)}(t)$, $B_\mu^{(2)}(t)$, and $\hat{B}_\mu^{(2)}(t)$.

Figure 2.3: The TV-MDSs and TV-DSs in **Paper A**.

the spectrogram. An approximate solution of the spectrogram is derived by making use of the Taylor series approximation. The results show how the moving point scatterers influence the micro-Doppler signature, TV-MDS, and TV-DS. Although this model is a good start for non-stationary F2F channels, it does not allow for three-dimensional (3D) trajectories. The 3D non-stationary channel models are addressed in the next chapter.

Chapter 3

3D Non-Stationary F2F Channels

3.1 Introduction

The model discussed in Chapter 2 is not feasible when considering human trajectories in three-dimensional (3D) environments, such as walking, falling, standing, sitting, etc. 3D trajectories are required for real-life applications, such as fall detection [79–81], human gait assessment [82, 83], drone detection [84], distinction between armed and unarmed persons [85], and gesture recognition [86]. This chapter presents an overview of the contributions of **Paper B** and **Paper C**. These papers presented two non-stationary F2F channel models that allow for 3D trajectories of the moving point scatterers. In **Paper B** the moving person is modelled as a single moving point scatterer, whereas in **Paper C** considers the person is modelled as a cluster of synchronized moving point scatterers. The contribution of **Paper C** can be helpful in different human gait and running scenarios, such as those in [82, 83, 85].

3.2 Geometrical 3D Channels

When the scatterer moves in 3D space in indoor fixed-to-fixed (F2F) channels, the angular functions that affect the Doppler shifts caused by the moving point scatterers must be defined. To understand how to model these functions, a study of the 3D geometrical model should be developed. In this section, the new angular functions, such as time variant horizontal angle of motion (TV-HAOM), time variant vertical angle of motion (TV-VAOM), time variant elevation angle of departure (TV-EAOD), time variant azimuth angle of departure (TV-AAOD), time variant elevation angle of arrival (TV-EAOA), and time variant azimuth angle of arrival (TV-AAOA) are introduced based on the 3D geometrical model. Such functions help to model the Doppler shifts caused by the scatterers moving in 3D space.

We have a multipath propagation scenario as depicted in Fig. 3.1. There exists a moving

person[1], a fixed receiver (R_x), and a fixed transmitter (T_x). In Fig. 3.2 a geometrical model is presented in detail. We have in Fig. 3.2 $\mathcal{N}$-moving point scatterers S_n^{M} for $n = 1, 2, \ldots, \mathcal{N}$ and $\mathcal{M}$-fixed point scatterers S_m^{F} for $m = 1, 2, \ldots, \mathcal{M}$. Each moving point scatterer S_n^{M} has a fixed initial 3D position $\left(x_n^{\mathrm{M}}, y_n^{\mathrm{M}}, z_n^{\mathrm{M}}\right)$. The trajectory of S_n^{M} is defined by its time variant (TV) velocity vector $\vec{v}_n(t)$, which is presented in terms of its TV speed $\mathrm{v}_n(t)$, TV-HAOM $\alpha_{v_n}(t)$, and TV-VAOM $\beta_{v_n}(t)$. The fixed positions of T_x and R_x are $\left(x^T, y^T, z^T\right)$ and $\left(x^R, y^R, z^R\right)$, respectively. The 3D TV Euclidean distance between T_x (R_x) and S_n^{M} is denoted by $d_n^T(t)$ ($d_n^R(t)$). Single bounce scattering and line-of-sight (LOS) are assumed. The depicted TV functions $\beta_n^T(t)$, $\alpha_n^T(t)$, $\beta_n^R(t)$, and $\alpha_n^R(t)$ denote the TV-EAOD, TV-AAOD, TV-EAOA, and TV-AAOA, respectively. The non-line-of-sight (NLOS) conditions are assumed.

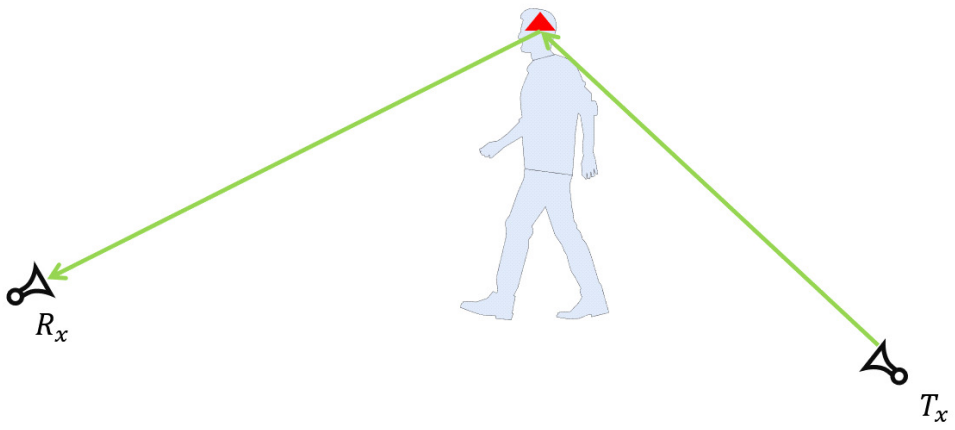

Figure 3.1: 3D multipath propagation scenario with a moving person.

3.2.1 The TV Velocity and Angular Functions

In Paper B, the expression of the TV velocity vector $\vec{v}_n(t)$ of each moving point scatterer (see Fig. 3.2) has been provided in terms of the velocities in x, y, z directions. Each of these velocity components has been presented in terms of the speed $\mathrm{v}_n(t)$, the TV-VAOM $\beta_{v_n}(t)$, and the TV-HAOM $\alpha_{v_n}(t)$. The displacements of each moving point scatterer have been computed in terms of the velocities in x, y, and z directions. The expressions of the TV-EAOAs $\beta_n^R(t)$, TV-AAOAs $\alpha_n^R(t)$, TV-EAODs $\beta_n^T(t)$, and TV-EAODs $\alpha_n^T(t)$ have been calculated by using inverse trigonometric functions in terms of the TV displacements and the fixed locations of the T_x and R_x.

[1]In Fig. 3.1, we have a single moving person for simplicity; however, for the rest of the chapter, we consider multiple moving persons.

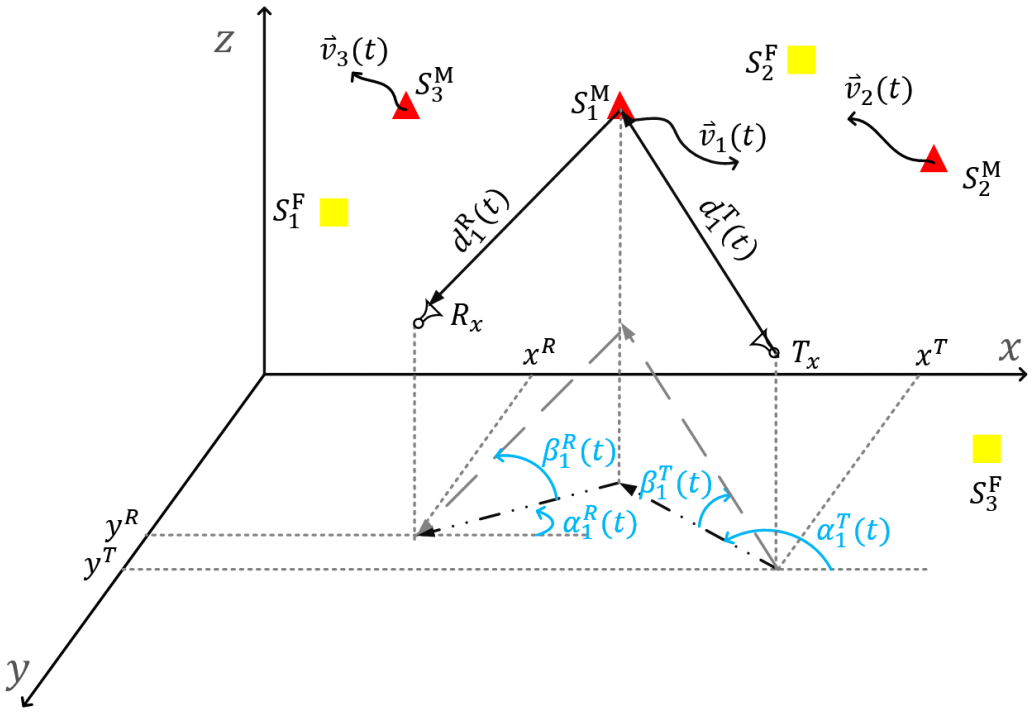

Figure 3.2: Geometrical model of 3D non-stationary F2F channel with $\mathcal{N}$-moving ($\mathcal{M}$-fixed) scatterers S_n^{M} (S_m^{F}).

3.2.2 Modelling the TV Doppler Frequency

The Doppler frequency $f_n(t)$ caused by the nth moving point scatterer S_n^{M} has been described in the paper by taking into account the TV speed, carrier frequency, speed of light, TV-EAOA $\beta_n^R(t)$, TV-AAOA $\alpha_n^R(t)$, TV-EAOD $\beta_n^T(t)$, TV-EAOD $\alpha_n^T(t)$, TV-VAOM $\beta_{v_n}(t)$, and TV-HAOM $\alpha_{v_n}(t)$ by the following expression

$$f_n(t) = -\, f_{n,\max}(t) \Big\{ \cos\left(\beta_{v_n}(t)\right) \left[\cos\left(\beta_n^T(t)\right) \cos\left(\alpha_n^T(t) - \alpha_{v_n}(t)\right) + \cos\left(\beta_n^R(t)\right) \cos\left(\alpha_{v_n}(t) - \alpha_n^R(t)\right) \right] + \sin\left(\beta_{v_n}(t)\right) \left[\sin\left(\beta_n^T(t)\right) + \sin\left(\beta_n^R(t)\right) \right] \Big\}, \tag{3.1}$$

where

$$f_{n,\max}(t) = \frac{\mathrm{v}_n(t)\, f_0}{c_0} \tag{3.2}$$

denotes the maximum Doppler frequency caused by S_n^{M}. The Doppler frequency expression (3.1) allows for 3D trajectories of the moving point scatterers S_n^{M}. In **Paper B**, it has been shown that the expression of the Doppler frequency in (2.5) is a special case of the expression in (3.1). Such a case happens when the TV-EAOA, TV-EAOD, and TV-HAOM

have zero values, i.e., $\beta_n^R(t) = 0$, $\beta_n^T(t) = 0$, and $\beta_{v_n}(t) = 0$. There are other special cases that can be found in **Paper B**. The Doppler frequency provided in (3.1) has been approximated by linear piecewise functions.

3.2.3 The TV Channel Phases and Complex Channel Gain

The instantaneous channel phase model of the nth moving point scatterer S_n^{M} in **Paper B** is the same as the one presented in **Paper A** (see (2.7)). Both are stochastic and modelled in terms of the Doppler frequencies $f_n(t)$. However, the main difference between the phases is the Doppler frequency expressions used (see (2.5) and (3.1)). Moreover, the expressions of the complex channel gain (CCG), time variant mean Doppler shift (TV-MDS), and time variant Doppler spread (TV-DS) are the same in both papers.

The CCG has been defined in the paper as a sum of two terms. The first term of the CCG has been represented as a single sum of $\mathcal{N}$ weighted complex exponentials associated with the moving point scatterers. Each component of this term has been characterized by the path gain and the stochastic phase variable corresponding to a moving point scatterer. The path gains of the moving point scatterers have been assumed to be constant, i.e., time invariant (TiV). The second term has been described as a sum of $\mathcal{M}$ weighted complex exponentials. Each component of the second term of the CCG has been represented in terms of the path gains and the random channel phases of the fixed point scatterers. The TV-MDS and TV-DS have taken into account the path gains and the Doppler frequencies of the moving point scatterers, and the path gains of the fixed point scatterers.

3.2.4 Principle Results

The micro-Doppler signatures of the CCG have been analyzed by using the spectrogram. The expressions of the short-time Fourier transform (STFT), spectrogram, auto-term, and cross-term have been derived in **Paper B** by taking advantage of the piecewise linear approximation of the TV Doppler frequencies.

In this section, the results of **Paper B** will be exploited. In the simulation scenario of the paper, the head trajectory of walking followed by falling was considered. The head has been modelled as a single moving point scatterer. The head trajectory model and its parameters described in [87–89] have been employed. The simulation scenario comprises the following three phases:

- *Phase 1*: The person walks a distance of 2 m at constant speed in a time interval of 2.5 s.

- *Phase 2*: The fall takes about 1 s, from the phase when the person's head starts to fall forward until the head touches the floor.

- *Phase 3*: After the person's body has reached the floor, the moving scatterer becomes a fixed scatterer.

The other simulation parameters, such as the locations of T_x and R_x and the carrier frequency can be found in the results section of the paper. Fig. 3.3(a) depicts the analytical solution of the spectrogram $S_\mu(f,t)$. The figure visualizes the TV frequency patterns corresponding to the moving point scatterer (the head) and the fixed point scatterers. The fixed scatterers have frequencies with zero values as they do not cause Doppler shifts in F2F channels. The fluctuations of the Doppler frequency that appear in Fig. 3.3(a) correspond to *Phase 1* (walking) from $t = 0$ s until $t \approx 2.5$ s. These fluctuations are due to the head oscillations when walking. The Doppler frequency patterns during *Phase 1* are slightly decreasing. This is due to the angular functions discussed in Section 3.2.1. In *Phase 2* (falling), which lasts from time $t \approx 2.5$ s to $t \approx 3.5$ s, the Doppler frequency caused by the head motion is decreasing rapidly. This is due to the high fluctuations in the speed. In *Phase 3* (non-moving), which lasts from time $t \approx 3.5$ s to $t \approx 4$ s, the Doppler frequency has a zero value as the scatterer does not move after the fall. In Fig. 3.3(a), the cross-term causes spectral interference during the walking interval. Fig. 3.3(b) visualizes the analytical solution of the auto-term $S_\mu^{(a)}(f,t)$. The Doppler frequency patterns are clearer as the cross-term is eliminated.

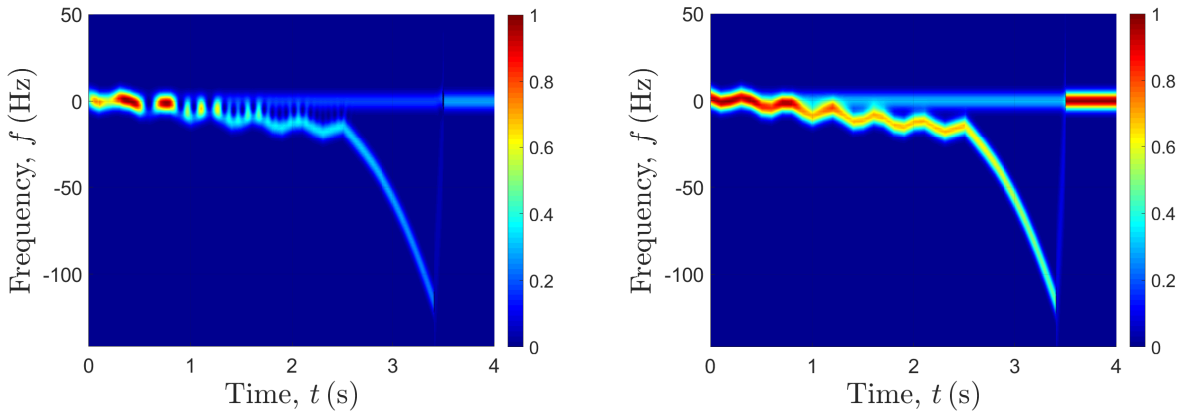

Figure 3.3: The analytical solution of (a) the spectrogram $S_\mu(f,t)$ and (b) the auto-term $S_\mu^{(a)}(f,t)$ provided in **Paper B**.

Fig. 3.4(a) depicts the TV-MDSs $B_f^{(1)}(t)$, $B_\mu^{(1)}(t)$, and $\hat{B}_\mu^{(1)}(t)$. The TV-MDS $B_f^{(1)}(t)$ has been computed by (2.9). The TV-MDSs $B_\mu^{(1)}(t)$, and $\hat{B}_\mu^{(1)}(t)$ have been computed from the analytical solution of the spectrogram $S_\mu(f,t)$ and the numerical computation of the spectrogram $\hat{S}_\mu(f,t)$, respectively. There is a good match between the $B_f^{(1)}(t)$, $B_\mu^{(1)}(t)$, and $\hat{B}_\mu^{(1)}(t)$. We can still distinguish between the patterns corresponding to all three phases in

the scenario, despite of the existing cross-term in $B_{\mu}^{(1)}(t)$, and $\hat{B}_{\mu}^{(1)}(t)$. Fig. 3.4(b) depicts the TV-DSs $B_{f}^{(2)}(t)$, $B_{\mu}^{(2)}(t)$, and $\hat{B}_{\mu}^{(2)}(t)$. The TV-MDS $B_{f}^{(2)}(t)$ has been computed by (2.10). The TV-DSs $B_{\mu}^{(2)}(t)$ and $\hat{B}_{\mu}^{(2)}(t)$ have been computed from the analytical solution of the spectrogram $S_{\mu}(f,t)$ and the numerical computation of the spectrogram $\hat{S}_{\mu}(f,t)$, respectively. The values of $B_{f}^{(2)}(t)$ and $\hat{B}_{\mu}^{(2)}(t)$ are different during *Phase 2* due to the impact of the cross-term. However, the patterns corresponding to all phases are distinguishable.

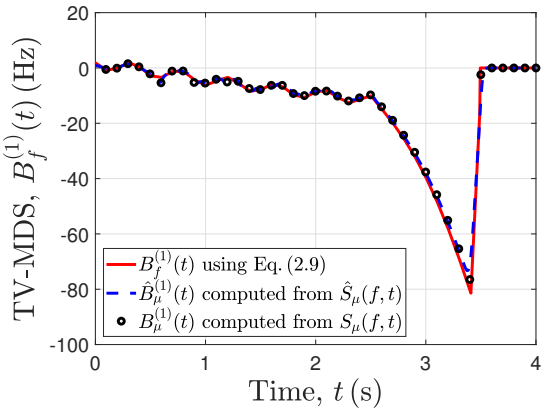

(a) The TV-MDSs $B_{f}^{(1)}(t)$, $B_{\mu}^{(1)}(t)$, and $\hat{B}_{\mu}^{(1)}(t)$.

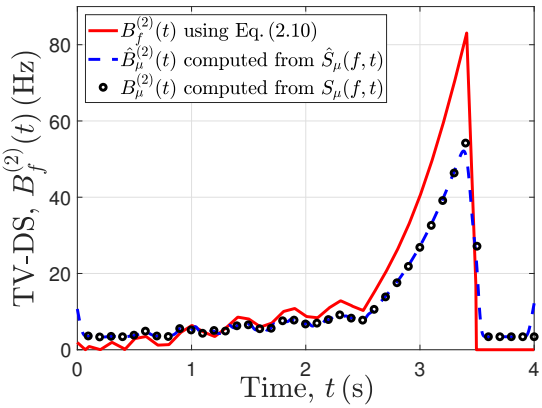

(b) The TV-DSs $B_{f}^{(2)}(t)$, $B_{\mu}^{(2)}(t)$, and $\hat{B}_{\mu}^{(2)}(t)$.

Figure 3.4: The TV-MDSs and TV-DSs in **Paper B**.

3.3 Cluster Channel Models

To make the model in **Paper B** more realistic especially for walking and running scenarios, such as those in [82, 83, 85], a non-stationary cluster channel model is proposed in **Paper C**. The moving person has been modelled as a cluster $\mathcal{N}_m$ of moving point scatterers representing his major body segments for $m = 1, 2, \ldots, \mathcal{N}_{\mathrm{C}}$ (see Fig. 3.5). The parameter $\mathcal{N}_{\mathrm{C}}$ denotes the number of the clusters (persons) in the case of having multiple persons. The TV-HAOM, TV-VAOM, TV-AAOD, TV-EAOD, TV-AAOA, and TV-EAOA are rewritten as $\alpha_{v_{n,m}}(t)$, $\beta_{v_{n,m}}(t)$, $\alpha_{n,m}^{T}(t)$, $\beta_{n,m}^{T}(t)$, $\alpha_{n,m}^{R}(t)$, and $\beta_{n,m}^{R}(t)$, respectively. These functions are associated with the nth moving point scatterer $S_{n,m}^{\mathrm{M}}$ of the mth cluster. Hence, the TV Doppler frequency $f_{n,m}(t)$ corresponding to $S_{n,m}^{\mathrm{M}}$ is written as follows

$$
\begin{aligned}
f_{n,m}(t) \;=\; & -f_{n,m,\max}(t) \Big\{ \cos\left(\beta_{v_{n,m}}(t)\right) \left[\cos\left(\beta_{n,m}^{T}(t)\right) \cos\left(\alpha_{n,m}^{T}(t) - \alpha_{v_{n,m}}(t)\right) \right. \\
& \left. + \cos\left(\beta_{n,m}^{R}(t)\right) \cos\left(\alpha_{v_{n,m}}(t) - \alpha_{n,m}^{R}(t)\right) \right] \\
& + \sin\left(\beta_{v_{n,m}}(t)\right) \left[\sin\left(\beta_{n,m}^{T}(t)\right) + \sin\left(\beta_{n,m}^{R}(t)\right) \right] \Big\}. \qquad (3.3)
\end{aligned}
$$

Hence, the stochastic phase process $\theta_{n,m,\mathrm{M}}(t)$ associated with the nth moving point scatterer $S^{\mathrm{M}}_{n,m}$ of the mth cluster has been expressed by

$$\theta_{n,m,\mathrm{M}}(t) \;=\; \theta_{n,m,\mathrm{M}} + 2\pi \int_0^t f_{n,m}(t')dt', \tag{3.4}$$

where the parameter $\theta_{n,m,\mathrm{M}}$ is $\mathcal{U} \sim (0,\, 2\pi]$.

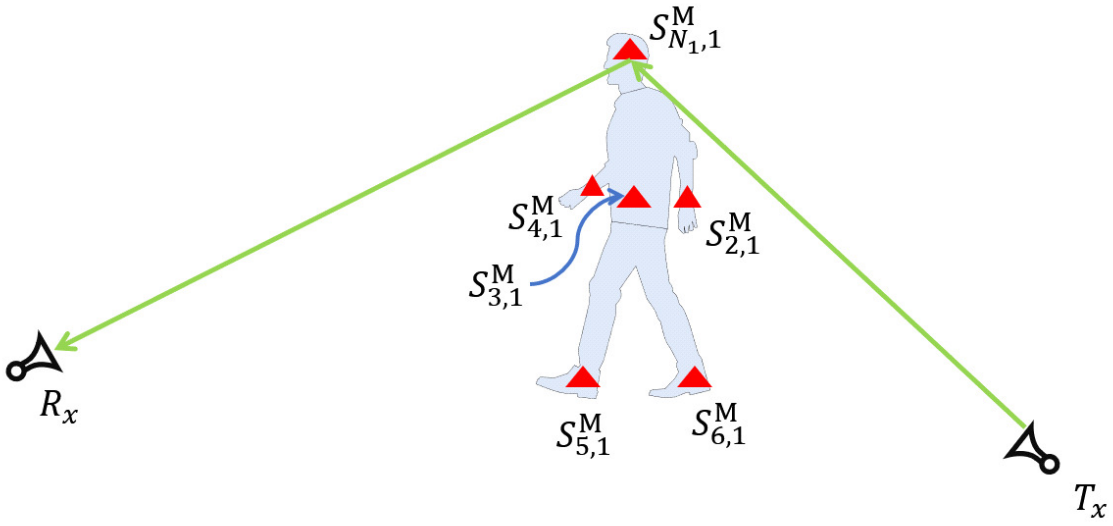

Figure 3.5: An example of a person modelled as a cluster of six moving point scatterers $S^{\mathrm{M}}_{n,m}$ for $n = 1, 2, \ldots, N_m$ and $m = 1, 2, \ldots, N_c$.

3.3.1 The Complex Channel Gain

To account for all the received multipath components from all moving point scatterers in all $\mathcal{N}_c$ clusters, the CCG $\mu(t)$ of the cluster channel model presented in **Paper C** has been written by

$$\mu(t) = \sum_{m=1}^{\mathcal{N}_{\mathrm{C}}} \sum_{n=1}^{\mathcal{N}_m} c_{n,m,\mathrm{M}}\, e^{j\theta_{n,m,\mathrm{M}}(t)} + \sum_{m=1}^{\mathcal{M}} c_{m,\mathrm{F}}\, e^{j\theta_{m,\mathrm{F}}}. \tag{3.5}$$

The expression in (3.5) consists of $\sum_{m=1}^{N_{\mathrm{C}}} \mathcal{N}_m + \mathcal{M}$ components. The first term in (3.5) represents the superposition of multipath components corresponding to $\mathcal{N}_{\mathrm{C}}$ clusters and the $\mathcal{N}_m$ scatterers in each cluster. Each component of the first term has a stochastic phase process $\theta_{n,m,\mathrm{M}}(t)$ and constant path gain $c_{n,m,\mathrm{M}}$. The second term in (3.5) is the sum of $\mathcal{M}$ multipath

components associated with the fixed point scatterers. Each component of the second term is characterized by a random phase variable $\theta_{m,\mathrm{F}}$ and a constant path gain $c_{m,\mathrm{F}}$. The TV-MDS and TV-DS of the model in (3.5) are given by

$$B_f^{(1)}(t) = \frac{\sum_{m=1}^{\mathcal{N}_\mathrm{C}} \sum_{n=1}^{\mathcal{N}_m} c_{n,m,\mathrm{M}}^2 \, f_{n,m}(t)}{\sum_{m=1}^{\mathcal{N}_\mathrm{C}} \sum_{n=1}^{\mathcal{N}_m} c_{n,m,\mathrm{M}}^2 + \sum_{m=1}^{\mathcal{M}} c_{m,\mathrm{F}}^2}, \tag{3.6}$$

$$B_f^{(2)}(t) = \sqrt{\frac{\sum_{m=1}^{\mathcal{N}_\mathrm{C}} \sum_{n=1}^{\mathcal{N}_m} c_{n,m,\mathrm{M}}^2 \, f_{n,m}^2(t)}{\sum_{m=1}^{\mathcal{N}_\mathrm{C}} \sum_{n=1}^{\mathcal{N}_m} c_{n,m,\mathrm{M}}^2 + \sum_{m=1}^{\mathcal{M}} c_{m,\mathrm{F}}^2} - \left(B_f^{(1)}(t)\right)^2}, \tag{3.7}$$

respectively. The double sums in (3.6)-(3.7) take into account the moving point scatterers associated with the clusters.

3.3.2 Principle Results

In **Paper C** the STFT, spectrogram, auto-term, and the cross-term of the CCG presented in (3.5) have been derived. In the results of the paper, the ankles, wrists, head, and trunk have been considered as the major body segments (moving point scatterers) of a walking person, i.e., $\mathcal{N}_C = 1$ and $\mathcal{N}_m = 6$. The person walked ten steps. The derived trajectory models for the body segments are inspired by those mentioned in [87–91]. The TV-HAOMs, TV-VAOMs, TV-AAODs, TV-EAODs, TV-AAOAs, and TV-EAOAs have been computed from the presented trajectory models and the fixed locations of the T_x and R_x. The TV Doppler frequencies and the TV channel phases associated with the moving point scatterers have been computed according to (3.3) and (3.4), respectively. Then, CCG $\mu(t)$ has been computed using the expression in (3.5).

Now, we are going to explore some results of **Paper C**. Fig. 3.6(a) depicts the analytical solution of the spectrogram $S_\mu(f,t)$. The figure shows the Doppler shifts caused by the walking activity of the person. However, these Doppler patterns corresponding to the moving body segments are not clear enough. This is due to the spectral interference caused by the cross-term of the spectrogram. Fig. 3.6(b) visualizes the auto-term $S_\mu^{(a)}(f,t)$. The figure shows the clear Doppler patterns caused by the motion of the body segments. Note that the Doppler shifts caused by the ankles have the highest values. The other body segments cause almost the same Doppler shifts. The Doppler shifts of the body segments have positive values in the time between $t = 0$ s and $t \approx 5$ s when the person moves towards the T_x and R_x and negative values in the time between $t \approx 5$ s and $t \approx 10$ s when the person moves away from the T_x and

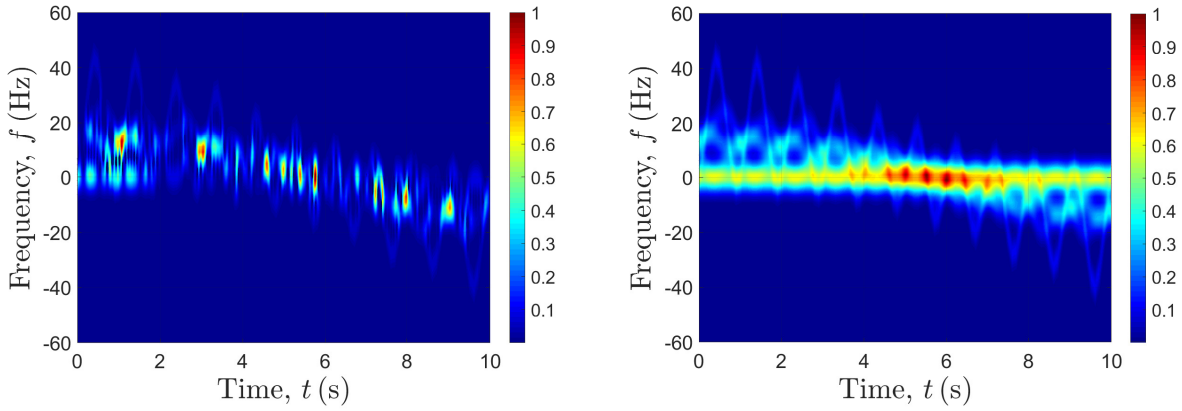

Figure 3.6: The analytical solution of (a) the spectrogram $S_\mu(f,t)$ and (b) the auto-term $S_\mu^{(a)}(f,t)$ provided in **Paper C**.

R_x. Fig. 3.7(a) exhibits the TV-MDSs. The TV-MDSs $B_f^{(1)}(t)$ have been computed from the expression in (3.6), whereas $\hat{B}_\mu^{(1)}(t)$ have been calculated from the spectrogram $S_\mu(f,t)$, and from the auto-term $S_\mu^{(a)}(f,t)$. There is a good match between the TV-MDSs $B_f^{(1)}(t)$ and $\hat{B}_\mu^{(1)}(t)$ computed from the auto-term $S_\mu^{(a)}(f,t)$. The TV-MDS has positive values in the time between $t = 0$ s and $t \approx 5$ s when the person moves towards the T_x and R_x and negative values in the time between $t \approx 5$ s and $t \approx 10$ s when the person moves away from the T_x and R_x. The number of the steps can be counted from the TV-MDSs $B_f^{(1)}(t)$. The TV-MDSs computed from the spectrogram $S_\mu(f,t)$ is distorted due to the cross-term. Nevertheless, the walking pattern can still be recognized.

Fig. 3.7(b) exhibits the TV-DSs. The TV-DSs $B_f^{(2)}(t)$ have been calculated from the expression in (3.7), whereas $B_\mu^{(2)}(t)$ have been evaluated from the spectrogram $S_\mu(f,t)$, and from the auto-term $S_\mu^{(a)}(f,t)$. The TV-DSs have only positive values. The TV-DSs decrease in the time between $t = 0$ s and $t \approx 5$ s when the person moves towards the T_x and R_x. Furthermore, the TV-DSs increase in the time between $t \approx 5$ s and $t = 10$ s when the person moves away the T_x and R_x. The TV-DSs computed from the spectrogram $S_\mu(f,t)$ is distorted due to the cross-term.

3.4 Chapter Conclusion

In this chapter, two 3D non-stationary F2F channel models have been introduced. These models allow for 3D trajectories of moving persons. The first model presented in **Paper B** considers the person as a single moving point scatterer. On the other hand, the model shown

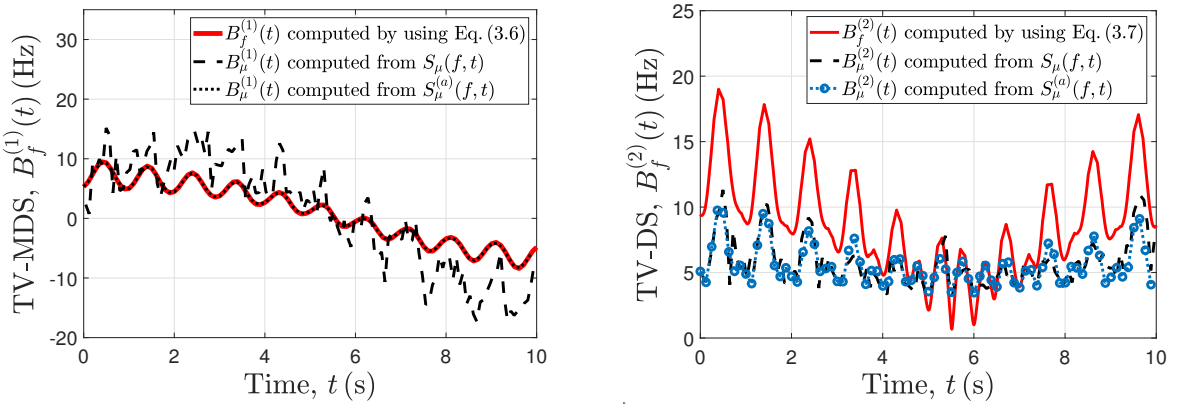

(a) The TV-MDSs $B_f^{(1)}(t)$, $B_\mu^{(1)}(t)$, and $\hat{B}_\mu^{(1)}(t)$.

(b) The TV-DSs $B_f^{(2)}(t)$, $B_\mu^{(2)}(t)$, and $\hat{B}_\mu^{(2)}(t)$.

Figure 3.7: The TV-MDSs and TV-DSs in **Paper C**.

in **Paper C** considers the major body parts of a person as a cluster of moving point scatterers. The influence of the human activity on the micro-Doppler signature, the TV-MDS, and the TV-DS of the proposed models have been demonstrated. The analytical solution of the spectrograms, the TV-MDS, and the TV-DS are confirmed by simulation. In the next chapters, exploration of the true micro-Doppler signatures of the measured channel-state-information (CSI) are demonstrated. Moreover, the simulation of the micro-Doppler signatures of the CSI models driven by inertial measurement unit (IMU) data is explored.

Chapter 4

Micro-Doppler Signature of Measured RF Data Using Commercial Off-the-Shelf-Devices

4.1 Introduction

This chapter demonstrates the possibility of capturing the true micro-Doppler signatures of measured radio-frequency (RF) signals using cheap commercial-off-the-shelf (COTS) devices. Open-source software has been developed by the authors of [50], that allows for recording the complex channel-state-information (CSI) of 30 subcarriers corresponding to orthogonal-frequency-division-multiplexing (OFDM). Such a tool can work on devices equipped with NIC5300 wireless and adhere to the IEEE 802.11n protocol standard [92]. The tool was used in various areas of activity, signal, and action recognition in [93–96] by utilizing only the amplitudes. The amplitudes are used in most of the work involving the CSI measurements because of the highly distorted phases found in the measured data. These distortions occur due to the asynchronization between transmitter (T_x) and receiver (R_x) stations. Thus, the spectrogram of the complex CSI data is unable to provide insights into the micro-Doppler signatures. One of the proposed approaches to address the issue of the highly distorted phases of the measured CSI was to apply a linear transformation to the phases in [49,53,54]. Although this method helps to get a cleaner pattern of the phases, it can partially eliminate the desired important phases. Thus, such a method is not reliable to investigate the micro-Doppler signature of the collected CSI measurements. The other approach was to employ the principal component analysis (PCA) to the amplitude of the CSI data. Then, the one-sided spectrogram is applied on the first principle component [48, 49, 51, 52] to reveal the positive frequency components. This approach improves the quality of the spectrogram; however, it does not provide the true micro-Doppler signature of the measured CSI, as it only uses the amplitudes.

This chapter summarizes the contribution of **Paper D**, which provides a model of true phases of the received CSI. These true phases are corresponding to the moving scatterers. Also, this chapter demonstrates the relationship between the time variant propagation delays (TV-PDs) and the time variant (TV) Doppler shifts caused by the moving scatterers. After that, a method for eliminating the TV phase distortions using a back-to-back (B2B) connection is shown. Finally, a framework for processing the measured CSI is provided to reveal the true micro-Doppler signature.

4.2 Modelling the True CSI Channel Phases

In Chapters 2 and 3, the relationship between the TV channel phases and the TV Doppler frequencies caused by the moving scatterers was shown. The discussed relationship between the TV Doppler frequencies and the TV channel phases can be used in the case of narrowband transmission, i.e., the bandwidth B of the transmitted signal has a value of zero. This section will demonstrate the relationship between the TV channel phases and the TV-PDs. Also, the relationship between TV-PDs and the TV Doppler frequencies caused by the moving scatterers will be discussed. These relationships take consider wideband transmission over multiple subcarriers in OFDM systems.

When it comes to the collection of CSI measurement data, the TV phases of the collected data are highly distorted due to the clock synchronization between the T_x and R_x stations. The presented model of the TV phases in this section assumes that they are appropriately sanitized. The method of sanitizing the TV phases will be presented in Section 4.3. In **Paper D**, the TV channel phase caused by the nth moving scatterer S_n^{M} and associated with the qth subcarrier has been modelled by

$$\theta_{\mathrm{M},n,q}(t) = \theta_{\mathrm{M},n} - 2\pi \left(f_0 + f_q\right) \tau_{\mathrm{M},n}(t). \tag{4.1}$$

The function $\tau_{\mathrm{M},n}(t)$ denotes the TV-PD of the wave transmitted from T_x via S_n^{M} arriving at R_x. The TV propagation delay is given by

$$\tau_{\mathrm{M},n}(t) = \frac{d_{\mathrm{M},n}^{T}(t) + d_{\mathrm{M},n}^{R}(t)}{c_0}, \tag{4.2}$$

where the functions $d_{\mathrm{M},n}^{T}(t)$ and $d_{\mathrm{M},n}^{R}(t)$ are the TV Euclidean distances described in Section 3.2. In the case of measurement, the parameter $\theta_{\mathrm{M},n}$ is unknown; however, in the simulation, it can be modelled as a random variable with uniform distribution between 0 and 2π as mentioned in Chapter 2. The parameter f_q denotes the subcarrier frequency associated with the qth subcarrier index. This parameter is given by

$$f_q = q \cdot \Delta f, \tag{4.3}$$

for $q = -28, -26, \ldots, -2, -1, 1, 3, \ldots, 27, 28$ according to the IEEE 802.11n standard [92]. The parameter Δf denotes the subcarrier frequency separation, which has a value of 312.5 kHz. Note that $f_q \in [-B/2, B/2]$ for all values of q, where the parameter B designates the bandwidth. By using the TV phase expression in (4.1), the TV Doppler shift $f_{n,q}(t)$ caused by S_n^{M} and associated with the qth subcarrier is given by

$$f_{n,q}(t) = \frac{1}{2\pi}\dot{\theta}_{\mathrm{M},n}(t) = -(f_0 + f_q)\,\dot{\tau}_{\mathrm{M},n}(t) \tag{4.4}$$

$$= -f_{n,q,\max}(t)\gamma_n(t), \tag{4.5}$$

where

$$f_{n,q,\max}(t) = \frac{(f_0 + f_q)\,\mathrm{v}_n(t)}{c_0}, \tag{4.6}$$

$$\begin{aligned}\gamma_n(t) = &\cos\left(\beta_{v_n}(t)\right)\Big[\cos\left(\beta_n^T(t)\right)\cos\left(\alpha_n^T(t) - \alpha_{v_n}(t)\right)\\ &+ \cos\left(\beta_n^R(t)\right)\cos\left(\alpha_{v_n}(t) - \alpha_n^R(t)\right)\Big]\\ &+ \sin\left(\beta_{v_n}(t)\right)\Big[\sin\left(\beta_n^T(t)\right) + \sin\left(\beta_n^R(t)\right)\Big].\end{aligned} \tag{4.7}$$

The main difference between the expression in (4.6) and the one provided in (3.2) is that the subcarrier frequency f_q is included in (4.6). The proof of the relationship between $f_{n,q}(t)$ and $\tau_{\mathrm{M},n}(t)$ is analogous to the one found in [97]. The time variant elevation angle of departure (TV-EAOD) $\beta_n^T(t)$, time variant azimuth angle of departure (TV-AAOD) $\alpha_n^T(t)$, time variant elevation angle of arrival (TV-EAOA) $\beta_n^R(t)$, time variant azimuth angle of arrival (TV-AAOA) $\alpha_n^R(t)$, time variant horizontal angle of motion (TV-HAOM) $\alpha_{v_n}(t)$, and time variant vertical angle of motion (TV-VAOM) $\beta_{v_n}(t)$ are described in Chapter 3. The TV function $\gamma_n(t)$ in (4.7) can have positive or negative values, depending on whether the TV propagation delay is increasing or decreasing. If the TV propagation delay $\tau_{\mathrm{M},n}(t)$ is increasing, i.e., the moving scatterer S_n^{M} is moving away from the T_x and R_x, its rate of change $\dot{\tau}_{\mathrm{M},n}(t)$ and $\gamma_n(t)$ are positive. Thus, the Doppler frequency $f_{n,q}(t)$ has negative values according to the expression in (4.5). If the TV propagation delay $\tau_{\mathrm{M},n}(t)$ is decreasing, i.e., the moving scatterer S_n^{M} is towards the T_x and R_x, its rate of change $\dot{\tau}_{\mathrm{M},n}(t)$ is negative. Thus, the Doppler frequency $f_{n,q}(t)$ has positive values as $\gamma_n(t)$ is negative. Note that $\gamma_n(t)$ scales the TV maximum Doppler shift $f_{n,q,\max}(t)$.

4.3 Processing Measured CSI Data

In order to reveal the true micro-Doppler signature of the measured CSI, a B2B connection has been employed in **Paper D**. Fig. 4.1 demonstrates the B2B setup between T_x and R_x stations. The T_x and R_x stations are operating in single-input multiple-output (SIMO) mode,

i.e., one RF port is active at the T_x station and two RF ports are active at the R_x station. A splitter is connected to the active T_x port. The splitter has two output ports. One of them is connected to one of the R_x ports (B2B connection) and the other one is connected to the T_x antenna. The other active port at the R_x station is connected to the R_x antenna. Further details about hardware used in the setup can be found in **Paper D**. This setup allows us to capture two channel transfer functions (CTFs). One of them, denoted by $H_{\mathrm{B2B}}(t, f_q)$, captures distortions due to the asynchronization between T_x and R_x stations, which result in carrier frequency offset [98–100], packet boundary delay [101, 102], and sampling frequency offset [103–105]. The other CTF, which is denoted by $H_1(t, f_q)$ captures the indoor channel characteristics and the distortions due to the asynchronization. The CTFs are divided by each other in elementwise form as follows

$$H(t, f_q) = \frac{H_1(t, f_q)}{H_{\mathrm{B2B}}(t, f_q)}. \tag{4.8}$$

The CTF $H(t, f_q)$ resulting from the operation in (4.8) carries the true channel characteristics. The noise signals associated with each subcarrier of the CTF in (4.8) are uncorrelated. These signals result in some background noise in the spectrogram. To reduce the impact of this background noise of the spectrogram, the average of the CTF over the subcarriers is computed as follows

$$\mu(t) = \frac{1}{\mathcal{N}_q} \sum_{q} H(t, f_q), \tag{4.9}$$

where the parameter $\mathcal{N}_q$ denotes the number of subcarriers and is equal to 30, i.e., $\mathcal{N}_q = 30$. The operation described above has no impact on the Doppler frequencies associated with each subcarrier. This is because the bandwidth B is much smaller than the carrier frequency f_0, i.e., $B \ll f_0$. Hence, the Doppler shifts among all the subcarriers are the same. A notch filter is used to eliminate the strong zero-frequency components due to the fixed objects. Then, the spectrogram $S_\mu(f, t)$ is computed by applying the steps described in Section 2.13 to $\mu(t)$. After computing the spectrogram, the time variant mean Doppler shift (TV-MDS) of the measured CSI data is computed by the following expression

$$B_\mu^{(1)}(t) = \frac{\int_{-\infty}^{\infty} f S_\mu(f, t) df}{\int_{-\infty}^{\infty} S_\mu(f, t) df}. \tag{4.10}$$

4.4 Principle Results

For the experimental setup in the paper, the T_x and R_x antennas are collocated. A candidate was asked to perform four different activities. The activities are walking, falling, bending

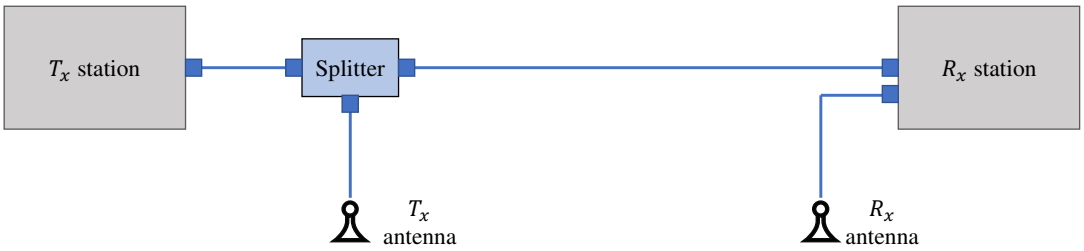

Figure 4.1: Illustration of the B2B connection to calibrate the measured CSI data.

and straightening, and sitting. The falling and walking activities were done in two different directions, i.e., there were *walking away*, *walking towards*, *falling away*, and *falling towards* activities. In the results of the paper, the spectrograms and TV-MDSs corresponding to the activities are demonstrated.

Now, we will discuss some results of the spectrograms and the TV-MDSs in **Paper D**. Figs. 4.2(a), 4.2(b), 4.2(c), and 4.2(d) show the spectrograms $S_\mu(f,t)$ corresponding to the activities: *walking away*, *falling away*, *walking towards*, and *falling towards*, respectively. The spectrograms depicted in Fig. 4.2 reveal the true micro-Doppler signatures of the captured CSI data under the influence of the human activities. The Doppler frequencies shown in Figs. 4.2(a) and 4.2(b) are negative when the candidate moves away from the T_x and R_x and the propagation delays are increasing. The opposite applies to the spectrograms in Figs. 4.2(c) and 4.2(d). The Doppler frequencies are positive when the candidate moves towards the T_x and R_x. Such illustrations go along with the demonstrated relationship in Section 4.2. The TV-MDSs associated with the activities: *walking away*, *falling away*, *walking towards*, and *falling towards* are exhibited in Figs. 4.2(a), 4.2(b), 4.2(c), and 4.2(d), respectively. The TV-MDSs depicted in Fig. 4.3 have been computed from (4.10). They reveal the true TV-MDSs of the collected CSI influenced by these activities. Note that the patterns provided in Figs. 4.2–4.3 are uniquely distinguishable and, thus can therefore be used to train human activity classifiers (HACs).

4.5 Chapter Conclusion

In this chapter, an overview of the contribution of **Paper D** was presented. The relationship between the propagation delays and the Doppler frequencies caused by the moving scatterers has been demonstrated. Moreover, a framework was presented for processing the captured CSI and elimination of the TV phase distortions caused by the clock asynchronization between T_x and R_x stations. The spectrograms and the TV-MDSs of the measured CSI have been explored in the paper. The results of the spectrograms have validated the relationship between the propagation delays and the Doppler frequencies demonstrated in Section 4.2. Furthermore,

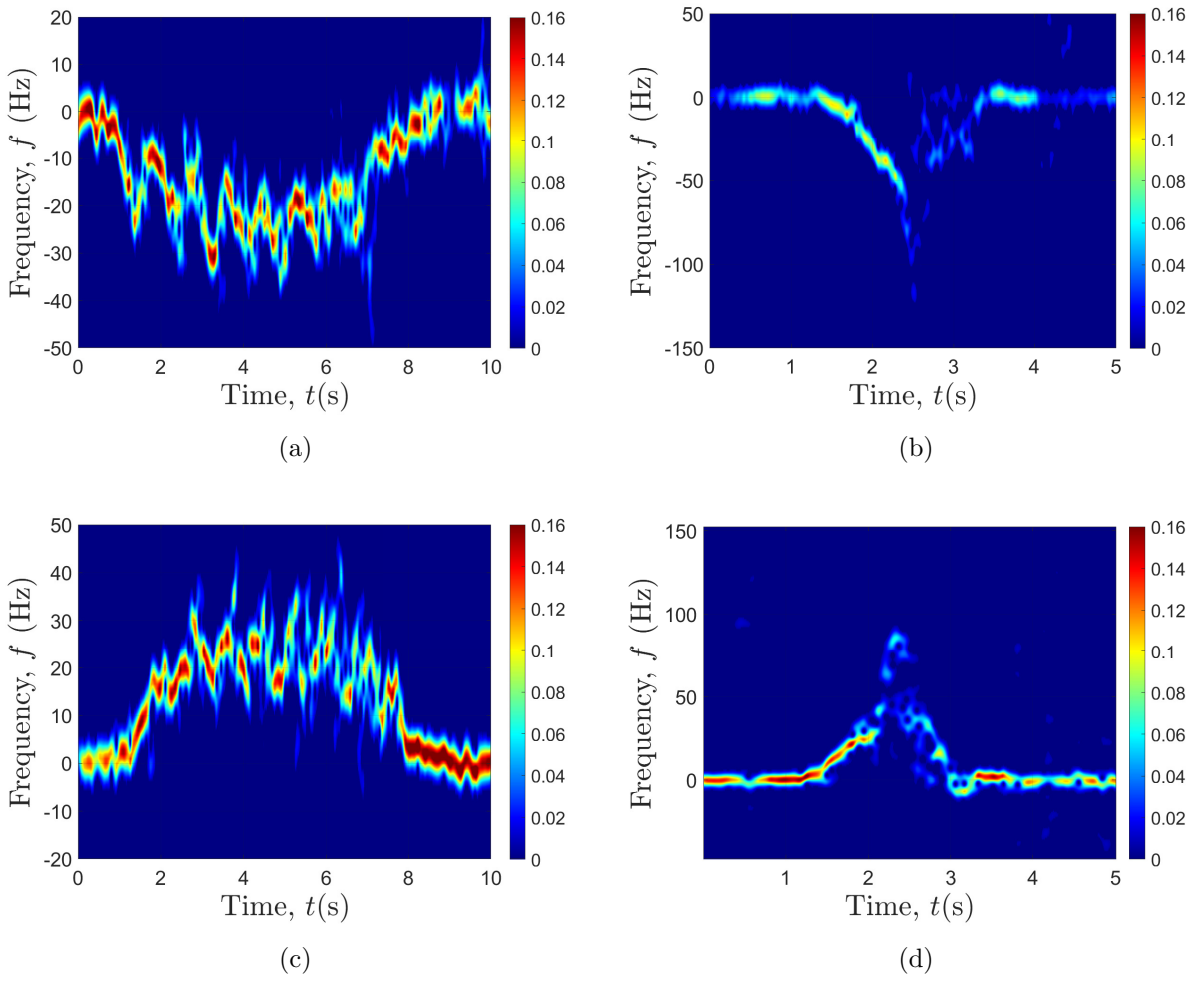

Figure 4.2: Spectrograms $S_\mu(f,t)$ of the (a) *walking away*, (b) *falling away* (c) *walking towards*, and (d) *falling towards* activities.

the results of spectrograms and the TV-MDSs have shown that they can be used for training the HACs using machine learning and deep learning techniques. Moreover, the results have shown the possibility of using the measured CSI to extract the micro-Doppler signatures of human activity. The paper has demonstrated the suitability of using the micro-Doppler signatures and the TV-MDSs of the measured CSI to validate those generated from channel simulation models. This will be shown in detail in the next chapter.

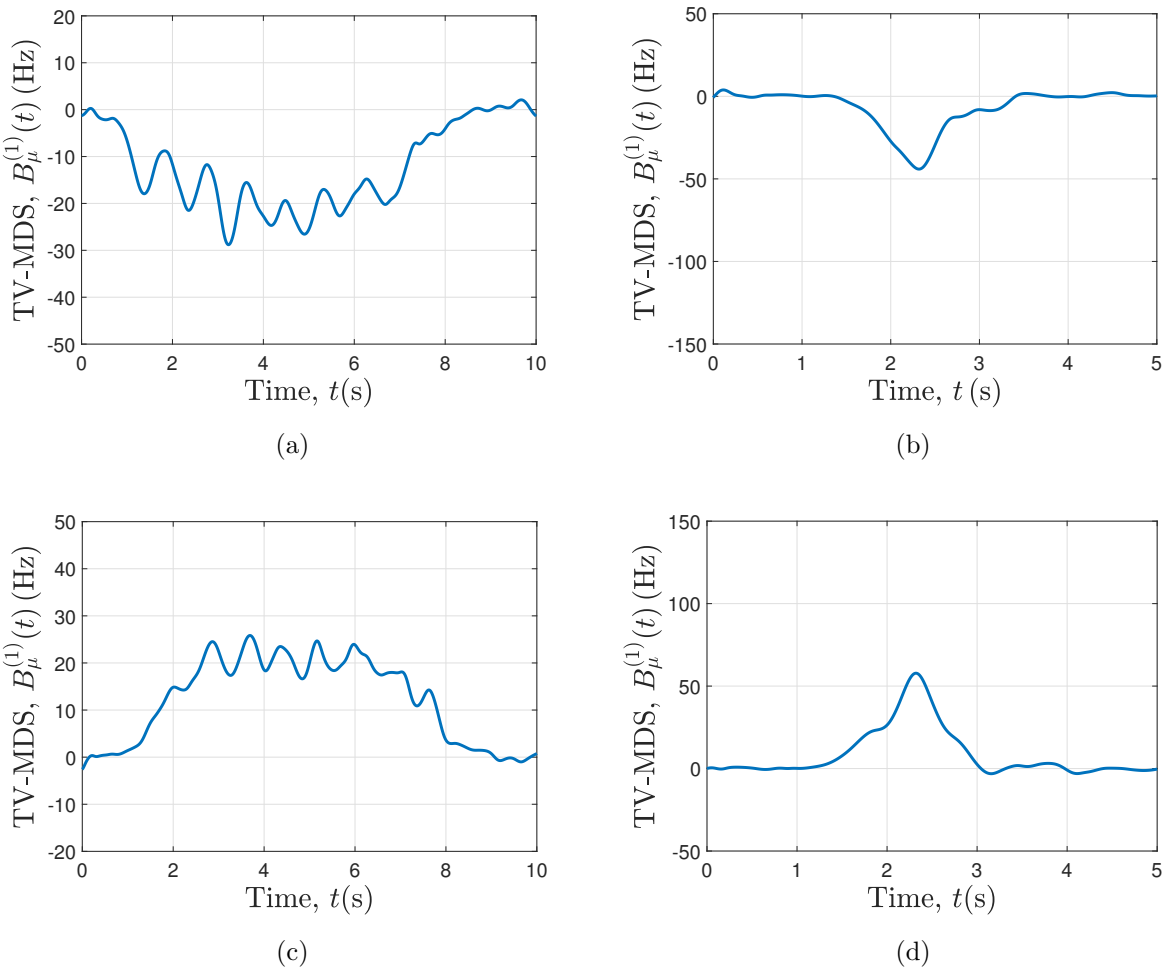

Figure 4.3: TV-MDSs $B_\mu^{(1)}(t)$ corresponding to the (a) *walking away*, (b) *falling away*, (a) *walking towards*, and (b) *falling towards* activities.

Chapter 5

IMU-Driven Channel Models

5.1 Introduction

In the previous chapters, the influence of the biomechanics of human activities and the locations of the transmitter (T_x) and receiver (R_x) on the micro-Doppler characteristics of indoor fixed-to-fixed (F2F) channels have been demonstrated. Moreover, Chapter 4 has shown the possibility of extracting the true micro-Doppler signatures from collected channel-state-information (CSI) measurement data using commercial-off-the-shelf (COTS) devices by using back-to-back (B2B) connections between the T_x and R_x stations.

In the literature, radar systems have been used to extract micro-Doppler signatures in [36, 37, 55–58] for many applications, such as arm recognition, human-computer interaction in smart environments [106], the detection of gait asymmetries [82, 83], differentiation of unarmed and armed people for security services [85], and gesture recognition [86, 107, 108]. For these mentioned applications, the spectrogram was employed to extract the micro-Doppler signatures.

When it comes to the design of human activity recognition (HAR) systems, collections of measured data from either CSI or radar equipment are required to train the human activity classifier (HAC). This consumes a huge amount of time to conduct experiments. Furthermore, the collected measurement data is not reproducible. To overcome this issue, many attempts have been made to simulate radar micro-Doppler signatures of human activities such as walking in [44, 45]. A framework for the estimation of the human gait parameters from simulated radar micro-Doppler signatures has been provided in [109]. Other attempts to simulate radar micro-Doppler signatures included the use of human trajectory data as crawling, creeping, and running from motion capture (MOCAP) databases in [46]. The Kinect sensor was another approach for collecting the human trajectories, such as running, walking, boxing, and leaping to simulate the radar micro-Doppler signatures in [110].

Inertial measurement units (IMUs) have not been incorporated to simulate the micro-Doppler signatures of CSI. As shown in Chapter 4, the true micro-Doppler signatures can

be extracted from measured CSI by employing the B2B connection between the T_x and R_x stations, making it possible to verify the simulated CSI micro-Doppler signatures. This chapter gives an overview of the contributions of **Paper E** and **Paper F**. **Paper E** provides an IMU-driven channel model that allows for extracting the micro-Doppler signature of a moving rigid body. Then, this work is extended in **Paper F** to simulate an IMU-driven channel model to extract micro-Doppler signatures of human activities. These contributions are the first step towards the design of simulation-based HAR systems.

5.2 Modelling the Received CSI from a Single Moving Object

This section presents an overview of the contribution of **Paper E**. The paper provides a wideband channel model to study the impact of a single moving object on the micro-Doppler signatures of the measured CSI. As mentioned in Chapter 4, the measured CSI contains the characteristics of wideband channels. Thus, a model of the channel transfer function (CTF) representing wideband channels with multiple subcarriers is provided in this section. The presented CTF considers the moving object as a single moving point scatterer, while the fixed objects are multiple fixed point scatterers.

5.2.1 The CTF Model

According to **Paper E**, the center of mass (CoM) of the moving rigid body is modelled as a single moving point scatterer S^{M}. There are $\mathcal{M}$ fixed scatterers representing the stationary objects in the room, such as walls, furniture, etc. Hence, the CTF representing the received CSI is modelled by

$$H\left(t, f_q\right) = H_{\mathrm{M}}\left(t, f_q\right) + \sum_{m=1}^{\mathcal{M}} H_{\mathrm{F},m}, \tag{5.1}$$

where

$$H_{\mathrm{M}}\left(t, f_q\right) = c_{\mathrm{M}}\, e^{j\theta_{\mathrm{M},q}(t)}, \tag{5.2}$$

$$H_{\mathrm{F},m} = c_{\mathrm{F},m}\, e^{j\theta_{\mathrm{F},m}}. \tag{5.3}$$

The first term in (5.1) denotes the CTF corresponding to the CoM of the moving object and associated with the qth subcarrier frequency f_q. The second term is the CTF corresponding to the fixed scatterers. The time variant (TV) function $\theta_{\mathrm{M},q}(t)$ in (5.2) denotes the phase shift caused by the CoM of the moving object, which is given by

$$\theta_{\mathrm{M},q}(t) = \theta_{\mathrm{M}} - 2\pi\left(f_0 + f_q\right)\tau_{\mathrm{M}}(t). \tag{5.4}$$

The expression for the TV channel phase in (5.4) is a special case of the one provided in (4.1), as there exists only one moving point scatterer. The same applies to the time variant propagation delay (TV-PD) $\tau_{\mathrm{M}}(t)$ and the expression in (4.2), as well. Note that in the simulation the phases θ_{M} and $\theta_{\mathrm{F},m}$ are independently and identically distributed (i.i.d.) with uniform distribution from 0 to 2π. Intuitively, the time variant mean Doppler shift (TV-MDS) of the CTF model provided in (5.1) is given by

$$B_{f_q}^{(1)}(t) = \frac{c_{\mathrm{M}}^2 \, f_{\mathrm{M},q}(t)}{c_{\mathrm{M}}^2 + \sum\limits_{m=1}^{\mathcal{M}} c_{\mathrm{F},m}^2}. \tag{5.5}$$

The function $f_{\mathrm{M},q}(t)$ denotes the Doppler frequency caused by the moving point scatterer S^{M} corresponding to the CoM of the rigid body and associated with the qth subcarrier frequency. The expression of $f_{\mathrm{M},q}(t)$ is similar to the one provided in (4.5).

5.2.2 Trajectory Model of a Moving Pendulum

In **Paper E**, a pendulum experiment has been conducted. Measured CSI and IMU data have been collected simultaneously. A 3 kg medicine ball was attached to the ceiling with a rope. The ball was covered with aluminium foil. There was an IMU device attached to the center of the ball. The IMU was configured to collect linear accelerations and Euler angles. The ball was swinging while the IMU and the CSI data has been collected. More information about the measurement scenario can be found in the paper. The rotation matrix of the collected IMU data has been computed to rotate the linear acceleration by using the Euler angles from the IMU's frame to the reference frame. Then, the rotated accelerations were integrated twice to obtain the displacements. To resolve the drift issues resulting from the integral computation, an extended version of the zero-update (ZUPT) algorithm provided in [111] has been implemented. After that, the displacements have been fed to the channel model proposed in the paper. The pendulum displacements in x, y, and z directions are modelled by

$$x_{\mathrm{M}}(t) = L \sin\left(\arcsin\left(\frac{x_{\max}}{L}\right)\cos\left(\sqrt{\frac{g}{L}}t\right)\right), \tag{5.6}$$

$$y_{\mathrm{M}}(t) = 0, \tag{5.7}$$

$$z_{\mathrm{M}}(t) = L\left\{1 - \cos\left[\arcsin\left(\frac{x_{\mathrm{M}}(t)}{L}\right)\right]\right\}, \tag{5.8}$$

respectively. The parameter L denotes the distance between the ceiling and the CoM of the ball. The parameters g and $x_{\max}$ designate the gravitational acceleration and the pendulum's maximum displacement, respectively. Further details about the values of these parameter can be found in **Paper E**.

The results have shown a good fit between the IMU data and the mechanical model. There were two models, one model was fed with the IMU data, while the other one was fed with the mechanical model presented in (5.6)–(5.8).

5.2.3 Principle Results

The spectrogram has been employed to extract the micro-Doppler signatures of the modelled and measured CSI. The micro-Doppler signatures and the TV-MDSs of the measured CSI, the channel model fed with IMU data, and channel model fed with the trajectory model provided in (5.6)–(5.8) have been evaluated in the paper. The results have shown good qualitative agreements.

Fig. 5.1 shows the spectrograms $\tilde{S}(f,t)$, $S(f,t)$, and $\hat{S}(f,t)$ of the channel model with IMU data as input (a), the channel model fed with the mechanical model as input (b), and the recorded CSI data (c), respectively. The sinusoid Doppler frequency patterns exhibited in Fig. 5.1 are due to the periodic trajectory of the pendulum. Figs. 5.1 shows a good agreement between the spectrograms $\tilde{S}(f,t)$, $S(f,t)$, and $\hat{S}(f,t)$. Figure 5.2 depicts the TV-MDSs $\tilde{B}^{(1)}(t)$, $B^{(1)}(t)$, and $\hat{B}^{(1)}(t)$ evaluated from the spectrograms $\tilde{S}(f,t)$, $S(f,t)$, and $\hat{S}(f,t)$ by using (4.10), respectively. There is a good match between the TV-MDSs in Fig. 5.2.

For further quantitative evaluation, more trials have been collected. Then, the normalized-mean-square error (NMSE) between the TV-MDS of the measured CSI $\hat{B}^{(1)}_{\mu,k}(t)$ and the TV-MDS of the IMU-driven channel model $B^{(1)}_{\mu,k}(t)$ has been computed for each trial. The NMSE γ_k of the kth is given by the following expression

$$\gamma_{\mu,k} = \frac{\int_0^{T_{\text{obs}}} \left(\tilde{B}^{(1)}_{\mu,k}(t) - \hat{B}^{(1)}_{\mu,k}(t)\right)^2 dt}{\int_0^{T_{\text{obs}}} \left(\hat{B}^{(1)}_{\mu,k}(t)\right)^2 dt}, \tag{5.9}$$

for $k = 1, 2, \ldots, K$. Note that the TV-MDSs $\hat{B}^{(1)}_{\mu,k}(t)$ and $\tilde{B}^{(1)}_{\mu,k}(t)$ have been computed from the micro-Doppler signatures of the measured CSI and the IMU-driven model, respectively. The parameters T_{obs} and K denote the observation time and the total number of trials, which were 15 s and 20 in the paper, respectively. In the results of the paper, the maximum, minimum, and average NMSE values are 0.1829, 0.0477, and 0.0932, respectively. From the results in the paper, it can be concluded that the model presented has a good accuracy.

5.3 Modelling the Received CSI from a Moving Person

This section provides an overview of the contribution of **Paper F**. The paper presents an IMU-driven non-stationary wideband channel model to study the impact of a single moving person on the micro-Doppler signatures of the measured CSI. In the paper the major body segments

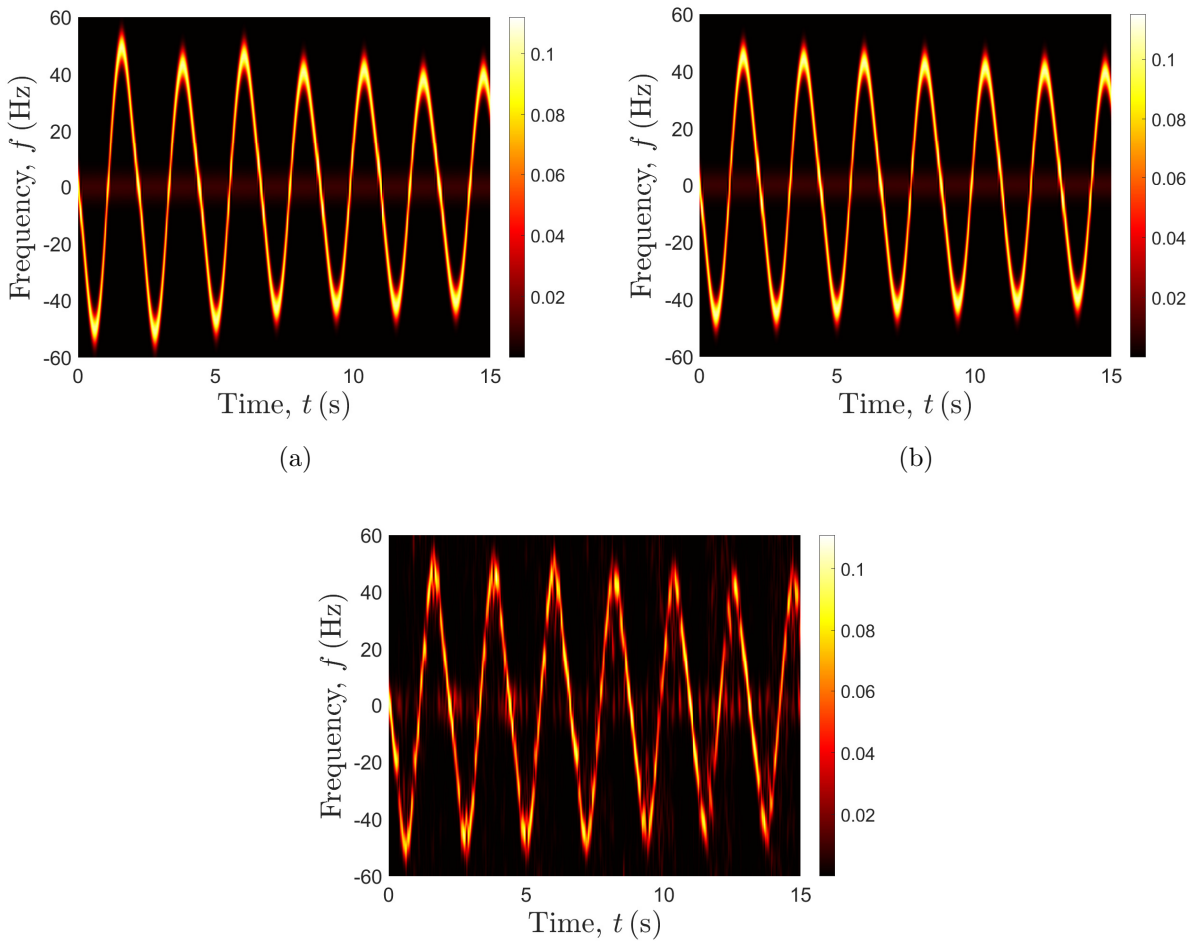

Figure 5.1: Spectrograms (a) $\tilde{S}_\mu(f,t)$ of the channel model fed with the IMU data as input, (b) $S_\mu(f,t)$ of the channel model with the mechanical trajectory model of the pendulum as input, and (c) $\hat{S}_\mu(f,t)$ of the measured CSI.

of the moving person have been modelled as a single cluster of moving point scatterers. A model of the CTF representing the wideband channels with multiple subcarriers is provided in this section. Furthermore, the model takes into account the TV path gains associated with the moving point scatterers.

5.3.1 The CTF Model

In the paper, the major body segments of a single moving person have been modelled as a cluster of $\mathcal{N}$ moving point scatterers. Hence, the CTF is modelled as

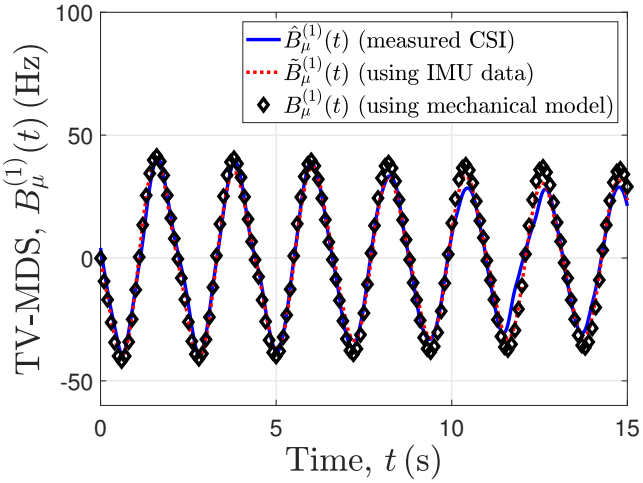

Figure 5.2: The TV-MDSs $\tilde{B}_\mu^{(1)}(t)$, $B_\mu^{(1)}(t)$, and $\hat{B}_\mu^{(1)}(t)$ computed from the spectrograms of the channel model with the IMU data as input, the mechanical model as input, and the measured CSI, respectively.

$$H\left(t, f_q\right) \;=\; \sum_{n=1}^{\mathcal{N}} H_{\mathrm{M},n}\left(t, f_q\right) + \sum_{m=1}^{\mathcal{M}} H_{\mathrm{F},m}, \tag{5.10}$$

where

$$H_{\mathrm{M},n}\left(t, f_q\right) \;=\; c_{\mathrm{M},n}(t)\, e^{j\theta_{\mathrm{M},n,q}(t)}. \tag{5.11}$$

The first term in (5.10) denotes the CTF of the received signals from the moving point scatterers corresponding to the active person. The second term in (5.10) designates the CTF associated with the fixed scatterers representing the fixed objects in indoor environments, such as walls, floor, ceiling, furniture, etc, and was discussed in Section 5.2. The TV function $\theta_{\mathrm{M},n,q}(t)$ in (5.11) is the phase shift caused by the nth moving point scatterer S_n^{M} and associated with the qth subcarrier frequency. The expressions of the TV phase $\theta_{\mathrm{M},n,q}(t)$ and the TV Doppler shift $f_{n,q}(t)$ caused by the nth moving point scatterer S_n^{M} have been discussed previously in (4.1) and (4.5), respectively. The TV path gain in (5.10) corresponding to the nth moving point scatterer S_n^{M} is given by

$$c_{\mathrm{M},n}(t) \;=\; \lambda\, a_{\mathrm{M},n}\, \left[d_{\mathrm{M},n}^{R}(t)\, d_{\mathrm{M},n}^{T}(t)\right]^{-\frac{\eta}{2}}, \tag{5.12}$$

where the parameters $\lambda = c_0/f_0$ and η denote the wavelength of the signal and the path loss exponent, respectively. The parameter $a_{\mathrm{M},n}$ depends on the cross-section, the transmission

power, and the transmitter and receiver antenna gains [40] associated with the nth moving point scatterer S_n^{M}. The functions $d_{\mathrm{M},n}^{T}(t)$ and $d_{\mathrm{M},n}^{R}(t)$ are the Euclidean distances mentioned in Section 3.2. From the model presented in (5.10), it is straight forward to express its TV-MDS by the following expression

$$B_{f_q}^{(1)}(t) = \frac{\sum_{n=1}^{\mathcal{N}} c_{\mathrm{M},n}^2(t) f_{n,q}(t)}{\sum_{n=1}^{\mathcal{N}} c_{\mathrm{M},n}^2(t) + \sum_{m=1}^{\mathcal{M}} c_{\mathrm{F},m}^2}. \tag{5.13}$$

5.3.2 Human Activity Micro-Doppler Signature of the IMU-driven Channel Model

In **Paper F**, the micro-Doppler signatures of the CTF model have been extracted by employing the spectrogram. An approximate solution of the spectrogram has been provided by approximating the Doppler frequencies of the moving point scatterers into linear functions of time during the spectrogram window interval. Moreover, the path gain in (5.12) has been assumed to be constant during the window interval of the spectrogram. Furthermore, it has been shown how to extract the TV-MDS from the micro-Doppler signatures of the CTF.

Measurement data has been collected from the CSI and IMU devices simultaneously for the following human activities *walking away*, *sitting*, and *falling towards*. For the walking activity, the candidate wore six IMUs, two on the candidate's ankles, two on his wrists, one on his torso, and one on his head. For the falling and sitting activities, two IMUs were used, one was on the candidate's torso, and the other one was on his head.

The data collected by using the IMUs, have been rotated by using the Euler angles to construct the rotation matrix, so that the measured linear accelerations are projected onto the reference frame. Then, the linear accelerations have been processed to compute the TV displacements. Finally, the TV displacements corresponding to each activity have been fed to the channel model to compute the spectrogram and the TV-MDSs. For the measured CSI, the procedures for computing the spectrogram are the same as in Section 4.3 and **Paper D**. **Paper F** provides a more detailed flow chart for processing the raw measured IMU and the measured CSI data. Moreover, it has been shown how to extract the radar cross-section $a_{\mathrm{M},n}$ of each moving point scatterer S_n^{M} from the TV-MDS computed from the micro-Doppler signature of the measured CSI.

In the paper, the spectrograms and the TV-MDSs of the IMU-driven channel model and the measured CSI are depicted. The spectrograms of the IMU-driven channel model have been evaluated by numerical computation and the approximated solution provided in the paper. The results have shown good agreement between the spectrograms of the simulated IMU-driven model and the measured CSI. Furthermore, the TV-MDSs computed from the spectrograms of the IMU-driven channel model and the measured CSI have been provided.

The results in the paper have shown good fit between the TV-MDSs of the IMU-driven model and the measured CSI.

5.3.3 Principle Results

In this section, we will explore some results of **Paper F**. Figs. 5.3(a) and 5.3(b) exhibit the walking activity spectrograms $\hat{S}_\mu(f,t)$ and $\tilde{S}_\mu(f,t)$ of the measured CSI and the IMU-driven channel model, respectively. There is a good match between the two spectrograms in Fig. 5.3. In Fig. 5.3(b) the Doppler patterns associated with the ankles are blurred due to the cross-term; however, they are clear in the auto-term demonstrated in the paper. The spectrograms $\hat{S}_\mu(f,t)$ and $\tilde{S}_\mu(f,t)$ of the measured CSI and the IMU-driven channel model are depicted in Figs. 5.4(a) and 5.4(b), respectively. These spectrograms correspond to the falling activity. There is also a good match between $\hat{S}_\mu(f,t)$ and $\tilde{S}_\mu(f,t)$. Although the candidate only wore two IMUs in this scenario, there is also a good agreement between $\hat{S}_\mu(f,t)$ and $\tilde{S}_\mu(f,t)$ as shown in Fig. 5.4. Figs. 5.5(a) and 5.5(b) illustrate the falling activity spectrograms $\hat{S}_\mu(f,t)$ and $\tilde{S}_\mu(f,t)$ of the measured CSI data and the IMU-driven channel model, respectively. Again, there is a good match between the spectrograms in Fig. 5.5. The auto-terms of the IMU-driven model corresponding to the aforementioned activity are presented in the paper. The TV-MDSs of the walking, falling, and sitting activities are demonstrated in Figs. 5.6(b), 5.6(a), and 5.6(c), respectively. The TV-MDSs have been computed by using the expression provided by (4.10). The results in Fig. 5.2 show good agreement between the TV-MDSs of the measured CSI and the IMU-driven model.

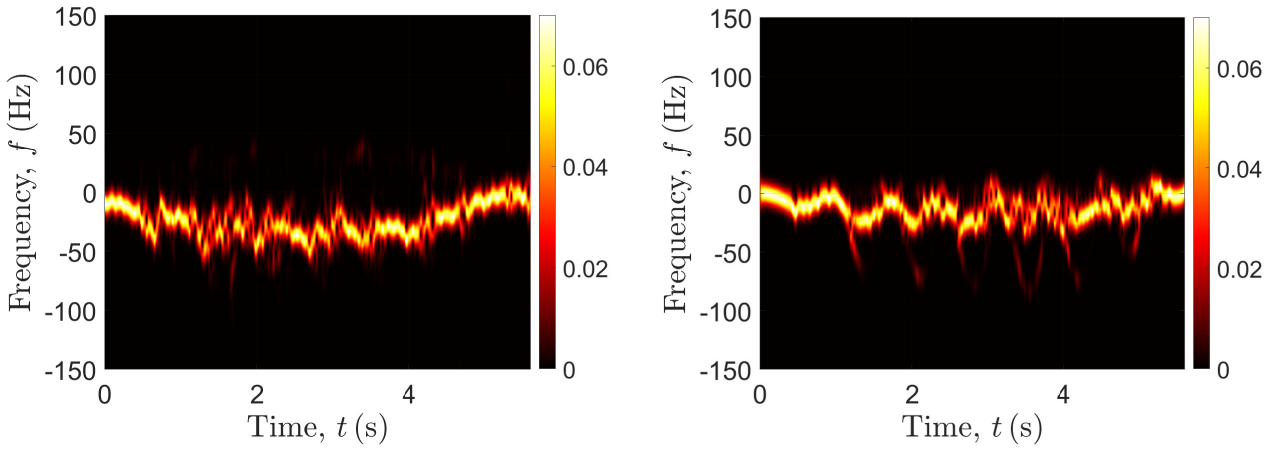

(a) $\hat{S}_\mu(f,t)$ (b) $S_\mu(f,t)$

Figure 5.3: Walking activity spectrograms of the (a) measured CSI data and (b) IMU-driven channel model.

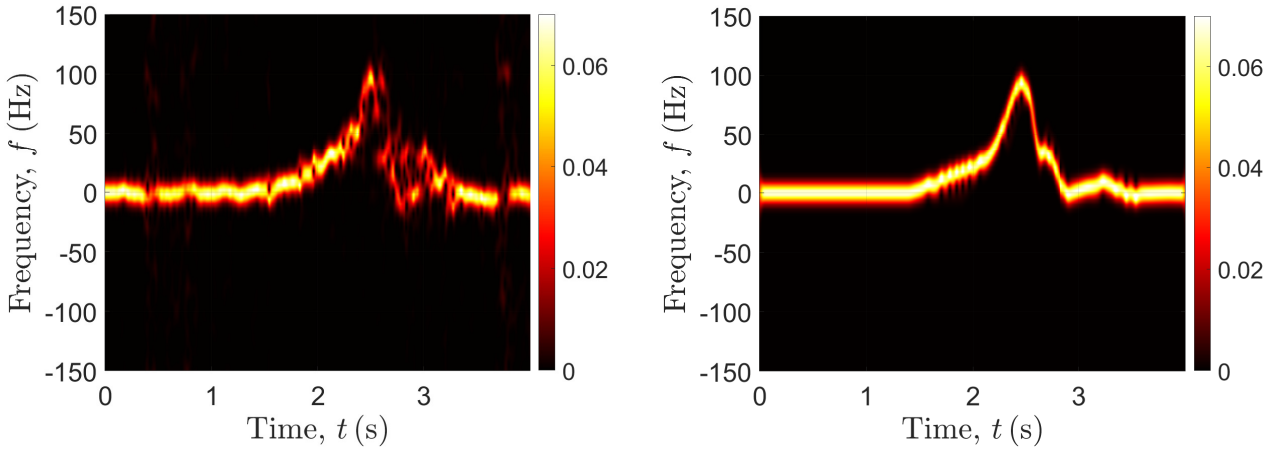

(a) $\hat{S}_\mu(f,t)$ (b) $S_\mu(f,t)$

Figure 5.4: Falling activity spectrograms of the (a) measured CSI data and (b) IMU-driven channel model.

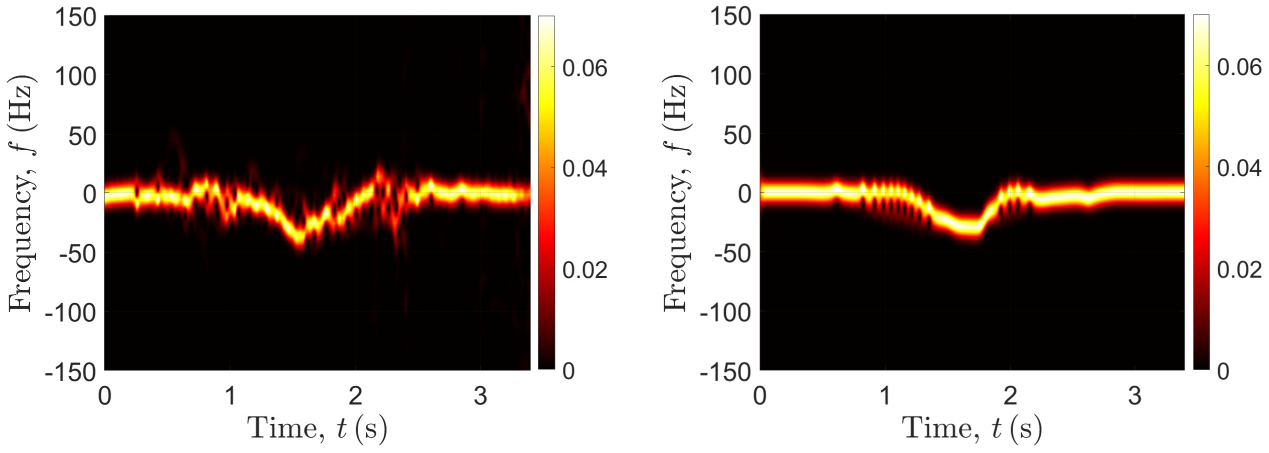

(a) $\hat{S}_\mu(f,t)$ (b) $S_\mu(f,t)$

Figure 5.5: Sitting activity spectrograms of the (a) measured CSI data and (b) IMU-driven channel model.

5.4 Chapter Conclusion

In this chapter an overview of the contributions of **Papers E** and **F** has been provided. The papers have developed IMU-driven channel models that allow for the extraction of the micro-Doppler signatures corresponding to a moving object and a moving human. The expressions of the CTF of both models have been provided. Moreover, a framework for

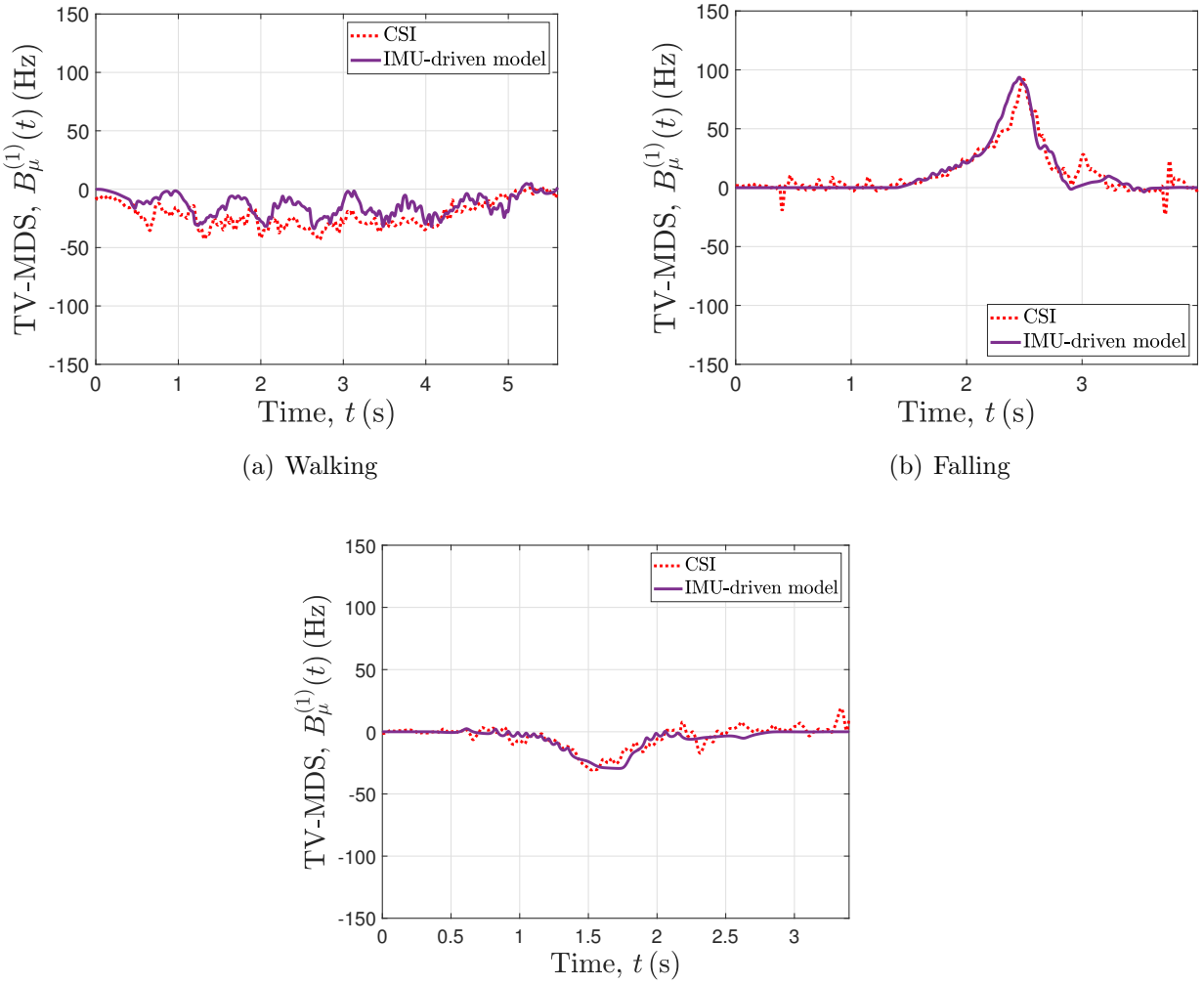

(a) Walking

(b) Falling

(c) Sitting

Figure 5.6: The TV-MDSs of the measured CSI and the IMU-driven channel model corresponding to (a) walking, (b) falling, and (c) sitting activities.

processing the raw data collected from the CSI and the IMUs has been demonstrated. The results of the contribution allow for the design of simulation-based HAR systems. The next chapter summarizes the major contributions of the dissertation and discusses possible future research ideas.

Chapter 6

Summary and Outlook

This dissertation establishes a relationship between the field of the non-stationary channel modelling and non-wearable human activity recognition (HAR) systems based on radio-frequency (RF) sensing technologies. In this chapter, the major contributions of this dissertation are summarized in Section 6.1. Furthermore, future research directions are discussed in Section 6.2.

6.1 Major Contributions

In this dissertation, several new channel models were presented to simulate the micro-Doppler signatures of human activities. These channel models put more emphasis on the time variant (TV) phases caused by the moving scatterers. The models take into account the TV speed, horizontal angle of motion (HAOM), vertical angle of motion (VAOM), azimuth angle of departure (AAOD), elevation angle of departure (EAOD), azimuth angle of arrival (AAOA), and elevation angle of arrival (EAOA) associated with the moving scatterers. The work in this dissertation shifts the paradigm towards the design of simulation-based HAR systems. This can be done by using synthetic data to train the classifiers instead of using real data, which is not reproducible and time-consuming. The contribution of this dissertation is summarized as follows:

- A two-dimensional (2D) non-stationary fixed-to-fixed (F2F) channel model was proposed. This channel model allows extracting the micro-Doppler features associated with the moving scatterers in 2D geometry.

- A three-dimensional (3D) non-stationary channel model was developed. Such a model considers a moving person as a moving single point scatterer representing the head and takes into account the 3D trajectory of a moving scatterer. Thus, it enables the generation of realistic micro-Doppler signatures associated with human activities and can therefore be used in simulating the falling activities of a moving person.

- Another 3D cluster channel model was developed. This model considers the moving person as a cluster of moving scatterers. Such a model allows simulating the micro-Doppler signatures of human gait scenarios. The trajectories of wrists, head, torso, and ankles associated with human walking activity were developed, as well (see **Paper C**).

- The possibility of extracting the true micro-Doppler signatures from measured channel-state-information (CSI) signals has been demonstrated. This was achieved by employing back-to-back (B2B) connection between the transmitter (T_x) and receiver (R_x) stations. This connection helps to eliminate the TV phase distortions caused by the clock asynchronization between the stations while keeping the true phases associated with human activities. Also, this helps to use commercial-off-the-shelf (COTS) devices to benchmark the proposed channel models.

- An inertial measurement unit (IMU)-driven channel model was presented. This model allows simulating the micro-Doppler signature associated with a moving rigid body. This is done by modelling the center of mass (CoM) of the rigid body as a single moving point scatterer. The model was validated by taking the measurements of CSI and IMU, simultaneously. The extracted trajectories from the measured IMU was fed to the channel model. The micro-Doppler signatures and the time variant mean Doppler shifts (TV-MDSs) of the IMU-driven and the measured CSI showed good agreement.

- Another IMU-driven channel model was developed. This model can be used to simulate the micro-Doppler signatures of human activities. The model takes into account the TV path gain associated with the moving scatterers, as well. The micro-Doppler signatures and the TV-MDSs of the IMU-driven model were confirmed with those computed from measured CSI. Both of the IMU and the CSI measurements were collected simultaneously. The micro-Doppler signatures and the TV-MDSs of the measured CSI and the IMU-driven showed good matches.

6.2 Future Work

This dissertation focuses on modelling, analysis, and simulation of non-stationary F2F channels. Such a work paves the way towards shifting the paradigm of HAR systems from measurement-based to simulation-based approaches. This section lights up some future ideas such as:

- The proposed work in this dissertation was for single-input single-output (SISO) channels. The work can be extended to massive multiple-input multiple-output (MIMO) channels. Massive MIMO systems theoretically have shown their eligibility of reducing the cross-terms of the micro-Doppler signatures in fixed-to-mobile (F2M) channels [78]. It

worth investigating the eligibility of such systems in reducing the cross-term of the micro-Doppler signatures of measured indoor F2F channels.

- In **Papers G** and **H** (not included in the dissertation), the human activity classifiers (HACs) have been trained using the TV-MDSs of the measured and calibrated CSI data. It worth training the classifiers by the micro-Doppler signatures or the TV-MDSs of the IMU-driven channel models and investigating their eligibility recognizing the human activities of the measured CSI or any other RF data.

- An alternative way to extract the trajectories of the moving human is to employ distributed MIMO systems. These systems can be used to estimate the trajectories of the moving human from the micro-Doppler signatures of each channel. This has been proven in simulated channels in [112, 113]. If the methods mentioned in [112, 113] are applicable for measured channels, then the extracted trajectories can be used to reproduce the micro-Doppler signatures and TV-MDSs.

- Moreover, RF-sensing can be used for the understanding of sign language (SL). For example, the micro-Doppler signatures of the measured RF signals influenced by the hand gestures can be used to train machines to generate to translate text messages. Hence, it can help to understand people with hearing disabilities by translating SL to text.

- Time-frequency distributions used to compute the micro-Doppler signatures can be employed for further computation, such as image formation (IF). IF is helpful to understand the facial expressions of humans as a further application in the field of RF-sensing.

Bibliography

[1] K. A. Hartholt *et al.*, "Mortality from falls among US adults aged 75 years or older, 2000-2016," *JAMA*, vol. 321, pp. 2131–2133, 06 2019.

[2] United Nations, Department of Economic and Social Affairs, Population Division , "World population ageing," 2017. Highlights (ST/ESA/SER.A/408).

[3] K. Nurhanim, I. Elamvazuthi, L. I. Izhar, and T. Ganesan, "Classification of human activity based on smartphone inertial sensor using support vector machine," in *2017 IEEE 3rd International Symposium in Robotics and Manufacturing Automation (ROMA)*, pp. 1–5, 2017.

[4] S. Ntalampiras and M. Roveri, "An incremental learning mechanism for human activity recognition," in *2016 IEEE Symposium Series on Computational Intelligence (SSCI)*, pp. 1–6, 2016.

[5] L. Sun *et al.*, "Activity recognition on an accelerometer embedded mobile phone with varying positions and orientations," in *7th International Conference on Ubiquitous Intelligence and Computing*, pp. 548–562, 2010.

[6] M. M. Hassan *et al.*, "A robust human activity recognition system using smartphone sensors and deep learning," *Future Generation Computer Systems*, vol. 81, pp. 307–313, 2018.

[7] J. Guo *et al.*, "Smartphone-based patients' activity recognition by using a self-learning scheme for medical monitoring," *Journal of Medical Systems*, vol. 40: 140, no. 6, 2016.

[8] S. L. Lau and K. David, "Movement recognition using the accelerometer in smartphones," in *2010 Future Network Mobile Summit*, pp. 1–9, 2010.

[9] I. Suarez *et al.*, "Improved activity recognition by using enriched acceleration data," in *Proceedings of the 2015 ACM International Joint Conference on Pervasive and Ubiquitous Computing*, UbiComp '15, (New York, NY, USA), p. 1011–1015, Association for Computing Machinery, 2015.

[10] M. Georgi, C. Amma, and T. Schultz, "Recognizing hand and finger gestures with IMU based motion and EMG based muscle activity sensing," in *International Conference on Bio-Inspired Systems and Signal Processing (BIOSIGNALS-2015)*, pp. 99–108, 2015.

[11] S. Jiang *et al.*, "Developing a wearable wrist glove for fieldwork support: A user activity-driven approach," in *2014 IEEE/SICE International Symposium on System Integration*, pp. 22–27, 2014.

[12] Y. Chen *et al.*, "Monitoring elder's living activity using ambient and body sensor network in smart home," in *2015 IEEE International Conference on Systems, Man, and Cybernetics*, pp. 2962–2967, 2015.

[13] W. Sansrimahachai and M. Toahchoodee, "Mobile-phone based immobility tracking system for elderly care," in *2016 IEEE Region 10 Conference (TENCON)*, pp. 3550–3553, 2016.

[14] R. B. Lakshmi and S. Parthasarathy, "An efficient human action recognition approach using fcm and random forest," in *2016 International Conference on Control, Instrumentation, Communication and Computational Technologies (ICCICCT)*, pp. 167–172, 2016.

[15] M. Muaaz *et al.*, "Wiwehar: Multimodal human activity recognition using Wi-Fi and wearable sensing modalities," *IEEE Access*, vol. 8, pp. 164453–164470, 2020.

[16] P. Vepakomma *et al.*, "A-wristocracy: Deep learning on wrist-worn sensing for recognition of user complex activities," in *12th International Conference on Wearable and Implantable Body Sensor Networks (BSN)*, pp. 1–6, 2015.

[17] G. Uslu *et al.*, "Human activity monitoring with wearable sensors and hybrid classifiers," *International Journal of Computer Information Systems and Industrial Management Applications*, vol. 5, pp. 345–353, 2013.

[18] F. Lorussi *et al.*, "Wearable textile platform for assessing stroke patient treatment in daily life conditions," *Frontiers in Bioengineering and Biotechnology*, vol. 4, p. 28, 2016.

[19] S. Kim, S. Lee, and W. Jeong, "EMG measurement with textile-based electrodes in different electrode sizes and clothing pressures for smart clothing design optimization," *Polymers*, vol. 12, no. 10, 2020.

[20] G. Cho, S. Lee, and J. Cho, "Review and reappraisal of smart clothing," *International Journal of Human–Computer Interaction*, vol. 25, no. 6, pp. 582–617, 2009.

[21] L. A. Rocha and J. H. Correia, "Wearable sensor network for body kinematics monitoring," in *2006 10th IEEE International Symposium on Wearable Computers*, pp. 137–138, 2006.

[22] J. Zou and Q. Zhao, "Video object segmentation using background model based on pixel time series clustering," in *2017 23rd International Conference on Automation and Computing (ICAC)*, pp. 1–6, 2017.

[23] C. R. Wren, A. Azarbayejani, T. Darrell, and A. P. Pentland, "Pfinder: real-time tracking of the human body," *IEEE Transactions on Pattern Analysis and Machine Intelligence*, vol. 19, no. 7, pp. 780–785, 1997.

[24] X. Peng, L. Wang, X. Wang, and Y. Qiao, "Bag of visual words and fusion methods for action recognition: Comprehensive study and good practice," *Computer Vision and Image Understanding*, vol. 150, pp. 109 – 125, 2016.

[25] Y. Shi, Y. Tian, Y. Wang, and T. Huang, "Sequential deep trajectory descriptor for action recognition with three-stream CNN," *IEEE Transactions on Multimedia*, vol. 19, no. 7, pp. 1510–1520, 2017.

[26] A. Coates, A. Ng, and H. Lee, "An analysis of single-layer networks in unsupervised feature learning," in *Proceedings of the Fourteenth International Conference on Artificial Intelligence and Statistics*, vol. 15, (Fort Lauderdale, FL, USA), pp. 215–223, JMLR Workshop and Conference Proceedings, 11–13 Apr 2011.

[27] J. Shotton *et al.*, "Real-time human pose recognition in parts from single depth images," in *Conference on Computer Vision and Pattern Recognition (CVPR) 2011*, pp. 1297–1304, 2011.

[28] H. Chen, G. Wang, J. Xue, and L. He, "A novel hierarchical framework for human action recognition," *Pattern Recognition*, vol. 55, pp. 148 – 159, 2016.

[29] J. Wang *et al.*, "Learning actionlet ensemble for 3D human action recognition," *IEEE Transactions on Pattern Analysis and Machine Intelligence*, vol. 36, no. 5, pp. 914–927, 2014.

[30] M. Cheffena, "Fall detection using smartphone audio features," *IEEE Journal of Biomedical and Health Informatics*, vol. 20, no. 4, pp. 1073–1080, 2016.

[31] Y. Li *et al.*, "Acoustic fall detection using a circular microphone array," in *2010 Annual International Conference of the IEEE Engineering in Medicine and Biology*, pp. 2242–2245, 2010.

[32] M. S. Khan *et al.*, "An unsupervised acoustic fall detection system using source separation for sound interference suppression," *Signal Processing*, vol. 110, pp. 199 – 210, 2015.

[33] M. Hariharan *et al.*, "Classification of speech dysfluencies using LPC based parameterization techniques," *J. Med. Syst.*, vol. 36, p. 1821–1830, June 2012.

[34] S. G. Mallat and Z. Zhang, "Matching pursuits with time-frequency dictionaries," *IEEE Transactions on Signal Processing*, vol. 41, no. 12, pp. 3397–3415, 1993.

[35] S. Davis and P. Mermelstein, "Comparison of parametric representations for monosyllabic word recognition in continuously spoken sentences," *IEEE Transactions on Acoustics, Speech, and Signal Processing*, vol. 28, no. 4, pp. 357–366, 1980.

[36] B. Jokanović and M. Amin, "Fall detection using deep learning in range-Doppler radars," *IEEE Transactions on Aerospace and Electronic Systems*, vol. 54, pp. 180–189, Feb 2018.

[37] B. Erol and M. G. Amin, "Radar data cube processing for human activity recognition using multisubspace learning," *IEEE Transactions on Aerospace and Electronic Systems*, vol. 55, no. 6, pp. 3617–3628, 2019.

[38] M. Raja *et al.*, "Wireless multifrequency feature set to simplify human 3-D pose estimation," *IEEE Antennas and Wireless Propagation Letters*, vol. 18, no. 5, pp. 876–880, 2019.

[39] A. Borhani and M. Pätzold, "The impact of human walking on the time-frequency distribution of in-home radio channels," in *2018 Asia-Pacific Microwave Conference (APMC)*, pp. 920–922, 2018.

[40] V. C. Chen, *The Micro-Doppler Effect in Radar, Second Edition.* Artech House radar library, Artech House, 2019.

[41] V. C. Chen *et al.*, "Micro-Doppler effect in radar: phenomenon, model, and simulation study," *IEEE Transactions on Aerospace and Electronic Systems*, vol. 42, no. 1, pp. 2–21, 2006.

[42] V. Chen and H. Ling, *Time-Frequency Transforms for Radar Imaging and Signal Analysis.* Artech House, 2001.

[43] V. C. Chen, "Analysis of radar micro-Doppler with time-frequency transform," in *Proceedings of the Tenth IEEE Workshop on Statistical Signal and Array Processing (Cat. No.00TH8496)*, pp. 463–466, 2000.

[44] S. S. Ram, R. Bhalla, and H. Ling, "Simulation of human radar signatures in the presence of ground," in *2009 IEEE International Symposium on Antennas and Propagation*, pp. 1–4, 2009.

[45] J. Park and J. T. Johnson, "Measurements and simulations of multi-frequency human radar signatures," in *Proceedings of the 2012 IEEE International Symposium on Antennas and Propagation*, pp. 1–2, 2012.

[46] C. Karabacak *et al.*, "Knowledge exploitation for human micro-Doppler classification," *IEEE Geoscience and Remote Sensing Letters*, vol. 12, no. 10, pp. 2125–2129, 2015.

[47] S. Kim, T. G. Kim, and S. H. Kim, "Human activity recognition and prediction based on Wi-Fi channel state information and machine learning," in *2019 International Conference on Artificial Intelligence in Information and Communication (ICAIIC)*, pp. 418–422, 2019.

[48] X. Wu *et al.*, "TW-See: human activity recognition through the wall with commodity Wi-Fi devices," *IEEE Transactions on Vehicular Technology*, vol. 68, pp. 306–319, Jan 2019.

[49] J. Chen *et al.*, "Dynamic gesture recognition using wireless signals with less disturbance," *Personal and Ubiquitous Computing*, vol. 23, pp. 17–27, Feb 2019.

[50] D. Halperin, W. Hu, A. Sheth, and D. Wetherall, "Tool release: gathering 802.11n traces with channel state information," *ACM SIGCOMM CCR*, vol. 41, p. 53, Jan. 2011.

[51] C. Du, X. Yuan, W. Lou, and Y. T. Hou, "Context-free fine-grained motion sensing using WiFi," in *2018 15th Annual IEEE International Conference on Sensing, Communication, and Networking (SECON)*, pp. 1–9, June 2018.

[52] W. Wang, A. X. Liu, and M. Shahzad, "Gait recognition using WiFi signals," in *Proceedings of the 2016 ACM International Joint Conference on Pervasive and Ubiquitous Computing*, UbiComp '16, (New York, NY, USA), pp. 363–373, ACM, 2016.

[53] S. Sen *et al.*, "You are facing the Mona Lisa: spot localization using PHY layer information," in *Proceedings of the 10th International Conference on Mobile Systems, Applications, and Services*, MobiSys '12, (New York, NY, USA), pp. 183–196, ACM, 2012.

[54] K. Qian *et al.*, "PADS: Passive detection of moving targets with dynamic speed using PHY layer information," in *2014 20th IEEE International Conference on Parallel and Distributed Systems (ICPADS)*, pp. 1–8, Dec 2014.

[55] J. Kwon, S. Lee, and N. Kwak, "Human detection by deep neural networks recognizing micro-Doppler signals of radar," in *2018 15th European Radar Conference (EuRAD)*, pp. 198–201, 2018.

[56] F. Fioranelli, J. Le Kernec, and S. A. Shah, "Radar for health care: Recognizing human activities and monitoring vital signs," *IEEE Potentials*, vol. 38, no. 4, pp. 16–23, 2019.

[57] Y. Kim, S. Ha, and J. Kwon, "Human detection using Doppler radar based on physical characteristics of targets," *IEEE Geoscience and Remote Sensing Letters*, vol. 12, no. 2, pp. 289–293, 2015.

[58] Y. He, F. Le Chevalier, and A. G. Yarovoy, "Range-Doppler processing for indoor human tracking by multistatic ultra-wideband radar," in *2012 13th International Radar Symposium*, pp. 250–253, 2012.

[59] A. Liland, "A radar simulator for generating micro- Doppler datasets to be used for automatic target recognition," Master's thesis, Norwegian University of Science and Technology, 2018.

[60] A. Borhani, M. Pätzold, and K. Yang, "Time-frequency characteristics of in-home radio channels influenced by activities of the home occupant," *Sensors*, vol. 19, no. 16, p. 3557, 2019.

[61] M. Raja *et al.*, "3D head motion detection using millimeter-wave Doppler radar," *IEEE Access*, vol. 8, pp. 32321–32331, 2020.

[62] M. Raja, V. Ghaderi, and S. Sigg, "WiBot! in-vehicle behaviour and gesture recognition using wireless network edge," in *2018 IEEE 38th International Conference on Distributed Computing Systems (ICDCS)*, pp. 376–387, July 2018.

[63] V.-H. Pham, M.-H. Taieb, J.-Y. Chouinard, S. Roy, and H.-T. Huynh, "On the double Doppler effect generated by scatterer motion," *REV Journal on Electronics and Communications*, vol. 1, pp. 30–37, Mar. 2011.

[64] A. Borhani and M. Pätzold, "Modeling of vehicle-to-vehicle channels in the presence of moving scatterers," in *Proc. IEEE 76th Vehicular Technology Conference, VTC2012-Fall*, Quebec City, Canada, Sept. 2012.

[65] A. Zajić, "Modeling impact of moving scatterers on Doppler spectrum in wideband vehicle-to-vehicle channels," in *9th European Conference on Antennas and Propagation, EuCAP 2015*, pp. 1–5, May 2015.

[66] X. Zhao *et al.*, "Doppler spectra for F2F radio channels with moving scatterers," *IEEE Trans. on Antennas and Propag.*, vol. 64, pp. 4107–4112, Sep. 2016.

[67] R. I. A. Harmanny, J. J. M. de Wit, and G. P. Cabic, "Radar micro-Doppler feature extraction using the spectrogram and the cepstrogram," in *Proc. 11th European Radar Conference, EuRAD 2014*, pp. 165–168, Oct. 2014.

[68] J. F. Alm and J. S. Walker, "Time-frequency analysis of musical instruments," *SIAM Review*, vol. 44, no. 3, pp. 457–476, 2002.

[69] T. A. Lampert and S. E. M. O'Keefe, "A survey of spectrogram track detection algorithms," *Applied Acoustics*, vol. 71, no. 2, pp. 87–100, 2010.

[70] C. I. Huerta-Lopez, Y. J. Shin, E. J. Powers, and J. M. Roesset, "Time-frequency analysis of earthquake records," in *Proc. 12th World Conf. on Earthquake Engineering, 12WCEE2000*, vol. 33, pp. 1–9, Auckland, New Zealand, Feb. 2000.

[71] M. Pätzold, C. A. Gutiérrez, and N. Youssef, "On the consistency of non-stationary multipath fading channels with respect to the average Doppler shift and the Doppler spread," in *Proc. IEEE Wireless Communications and Networking Conference, WCNC 2017*, San Francisco, CA, USA, 2017.

[72] F. Hlawatsch and G. F. Boudreaux-Bartels, "Linear and quadratic time-frequency signal representations," *IEEE Signal Processing Magazine*, vol. 9, pp. 21–67, Apr. 1992.

[73] B. A. J and R. R. L, "A unified approach to short-time Fourier analysis and synthesis," *Proceedings of the IEEE*, vol. 65, pp. 1558–1564, Nov. 1977.

[74] J. Allen, "Applications of the short-time Fourier transform to speech processing and spectral analysis," in *ICASSP '82. IEEE International Conference on Acoustics, Speech, and Signal Processing*, vol. 7, pp. 1012–1015, May 1982.

[75] L. G. Durand, J. Genest, and R. Guardo, "Modeling of the transfer function of the heart-thorax acoustic system in dogs," *IEEE Transactions on Biomedical Engineering*, vol. BME-32, pp. 592–601, Aug. 1985.

[76] J. Tribolet, "Applications of short-time homomorphic signal analysis to seismic wavelet estimation," *IEEE Transactions on Acoustics, Speech, and Signal Processing*, vol. 26, pp. 343–353, Aug. 1978.

[77] M. Pätzold and C. A. Gutiérrez, "Spectrogram analysis of multipath fading channels under variations of the mobile speed," in *Proc. 84rd IEEE Vehicular Technology Conference, IEEE VTC2016-Fall*, Montreal, Canada, Sept. 2016.

[78] M. Pätzold and C. A. Gutiérrez, "Enhancing the resolution of the spectrogram of non-stationary channels by using massive MIMO techniques," in *Proc. IEEE 86th Vehicular Technology Conference, VTC2017-Fall*, pp. 1–7, Toronto, Canada, Sep. 2017.

[79] G. A. M, Y. D. Zhang, F. Ahmad, and K. C. D. Ho, "Radar signal processing for elderly fall detection: the future for in-home monitoring," *IEEE Signal Processing Magazine*, vol. 33, pp. 71–80, Mar. 2016.

[80] M. Wu, X. Dai, Y. D. Zhang, B. Davidson, M. G. Amin, and J. Zhang, "Fall detection based on sequential modeling of radar signal time-frequency features," in *IEEE International Conference on Healthcare Informatics*, pp. 169–174, Sep. 2013.

[81] F. Adib, Z. Kabelac, D. Katabi, and R. Miller, "3D tracking via body radio reflections," in *Proc. of the 11th USENIX Conference on Networked Systems Design and Implementation NSDI'14*, (Berkeley, CA, USA), pp. 317–329, USENIX Association, 2014.

[82] A. Seifert, A. M. Zoubir, and M. G. Amin, "Detection of gait asymmetry using indoor Doppler radar," in *2019 IEEE Radar Conference (RadarConf)*, pp. 1–6, April 2019.

[83] A. Seifert, M. G. Amin, and A. M. Zoubir, "Toward unobtrusive in-home gait analysis based on radar micro-Doppler signatures," *IEEE Transactions on Biomedical Engineering*, vol. 66, pp. 2629–2640, Sep. 2019.

[84] M. Jian, Z. Lu, and V. C. Chen, "Drone detection and tracking based on phase-interferometric Doppler radar," in *2018 IEEE Radar Conference (RadarConf18)*, pp. 1146–1149, April 2018.

[85] F. Fioranelli, M. Ritchie, S.-Z. Gürbüz, and H. Griffiths, "Feature diversity for optimized human micro-Doppler classification using multistatic radar," *IEEE Transactions on Aerospace and Electronic Systems*, vol. 53, pp. 640–654, Apr. 2017.

[86] M. Ritchie and A. M. Jones, "Micro-Doppler gesture recognition using Doppler, time and range based features," in *2019 IEEE Radar Conference (RadarConf)*, pp. 1–6, April 2019.

[87] S.-U. Jung and M.-S. Nixon, "Estimation of 3D head region using gait motion for surveillance video," in *4th International Conference on Imaging for Crime Detection and Prevention 2011, ICDP 2011*, pp. 1–6, London, UK, Nov. 2011. DOI: 10.1049/ic.2011.0105.

[88] T. Oberg, A. Karsznia, and K. Oberg, "Basic gait parameters: reference data for normal subjects, 10-–79 years of age," *Journal of Rehabilitation Research and Development*, vol. 33, no. 2, pp. 210–223, 1993.

[89] G. Wu, "Distinguishing fall activities from normal activities by velocity characteristics," *Journal of Biomechanics*, vol. 33, no. 11, pp. 1497 – 1500, 2000.

[90] J. Carpentier, M. Benallegue, and J. P. Laumond, "On the centre of mass motion in human walking," *International Journal of Automation and Computing*, vol. 14, pp. 542–551, Oct. 2017.

[91] J. Liu and O. Urbann, "Walking pattern generation involving 3D waist motion for a biped humanoid robot," in *13th International Conference on Control Automation Robotics Vision (ICARCV)*, pp. 462–467, Singapore, Dec. 2014.

[92] "IEEE standard for information technology– local and metropolitan area networks– Specific requirements– Part 11: Wireless LAN medium access control (MAC) and physical layer (PHY) specifications amendment 5: Enhancements for higher throughput," *IEEE Std 802.11n-2009 (Amendment to IEEE Std 802.11-2007 as amended by IEEE Std 802.11k-2008, IEEE Std 802.11r-2008, IEEE Std 802.11y-2008, and IEEE Std 802.11w-2009)*, pp. 1–565, Oct 2009.

[93] Z. Wang, B. Guo, Z. Yu, and X. Zhou, "Wi-Fi CSI-based behavior recognition: from signals and actions to activities," *IEEE Communications Magazine*, vol. 56, pp. 109–115, May 2018.

[94] F. Zhang *et al.*, "Towards a diffraction-based sensing approach on human activity recognition," *Proc. ACM Interact. Mob. Wearable Ubiquitous Technol.*, vol. 3, Mar. 2019.

[95] F. Zhang *et al.*, "From Fresnel diffraction model to fine-grained human respiration sensing with commodity Wi-Fi devices," *Proceedings of the ACM on Interactive, Mobile, Wearable and Ubiquitous Technologies*, vol. 2, no. 1, pp. 1–23, 2018.

[96] T. Xin *et al.*, "FreeSense: a robust approach for indoor human detection using Wi-Fi signals," *IMWUT*, vol. 2, pp. 143:1–143:23, 2018.

[97] M. Pätzold and C. A. Gutierrez, "Modelling of non-WSSUS channels with time-variant Doppler and delay characteristics," in *2018 IEEE Seventh International Conference on Communications and Electronics (ICCE)*, pp. 1–6, Hue, Vietnam, July 2018.

[98] X. Wang, C. Yang, and S. Mao, "PhaseBeat: exploiting CSI phase data for vital sign monitoring with commodity WiFi devices," in *2017 IEEE 37th International Conference on Distributed Computing Systems (ICDCS)*, pp. 1230–1239, June 2017.

[99] Y. Xie, Z. Li, and M. Li, "Precise power delay profiling with commodity WiFi," in *21st Annual International Conference on Mobile Computing and Networking*, MobiCom '15, (New York, NY, USA), pp. 53–64, ACM, 2015.

[100] D. Vasisht, S. Kumar, and D. Katabi, "Decimeter-level localization with a single WiFi access point," in *Proceedings of the 13th Usenix Conference on Networked Systems Design and Implementation*, NSDI'16, (Berkeley, CA, USA), pp. 165–178, USENIX Association, 2016.

[101] K. Qian *et al.*, "Tuning by turning: Enabling phased array signal processing for WiFi with inertial sensors," in *IEEE INFOCOM 2016 - The 35th Annual IEEE International Conference on Computer Communications*, pp. 1–9, April 2016.

[102] Y. Zhuo, H. Zhu, and H. Xue, "Identifying a new non-linear CSI phase measurement error with commodity WiFi devices," in *2016 IEEE 22nd International Conference on Parallel and Distributed Systems (ICPADS)*, pp. 72–79, Dec 2016.

[103] L. Gong *et al.*, "WiFi-based real-time calibration-free passive human motion detection," vol. 15, p. 32213–32229, MDPI AG, Dec 2015.

[104] M. N. Mahfoudi *et al.*, "Orion: orientation estimation using commodity Wi-Fi," in *2017 IEEE International Conference on Communications Workshops (ICC Workshops)*, pp. 1233–1238, May 2017.

[105] M. Kotaru *et al.*, "SpotFi: decimeter level localization using WiFi," *SIGCOMM Comput. Commun. Rev.*, vol. 45, pp. 269–282, August 2015.

[106] Z. Zeng, M. Amin, and T. Shan, "Automatic arm motion recognition based on radar micro-Doppler signature envelopes," *IEEE Sensors Journal*, vol. 20, no. 22, pp. 13523–13532, 2020.

[107] S. Skaria *et al.*, "Hand-gesture recognition using two-antenna Doppler radar with deep convolutional neural networks," *IEEE Sensors Journal*, vol. 19, no. 8, pp. 3041–3048, 2019.

[108] J. Lien *et al.*, "Soli: Ubiquitous gesture sensing with millimeter wave radar," *ACM Trans. Graph.*, vol. 35, July 2016.

[109] P. van Dorp and F. C. A. Groen, "Human walking estimation with radar," *IEE Proceedings - Radar, Sonar and Navigation*, vol. 150, no. 5, pp. 356–365, 2003.

[110] B. Erol *et al.*, "Simulation of human micro-Doppler signatures with Kinect sensor," in *2014 IEEE Radar Conference*, pp. 0863–0868, 2014.

[111] "MATLAB code for 3D tracking with IMU," Available online: `https://github.com/xioTechnologies/Gait-Tracking-With-x-IMU`.

[112] R. Hicheri and M. Pätzold, "Estimation of the velocity of multiple moving persons in non-stationary indoor environments from received RF signals," in *2019 IEEE 89th Vehicular Technology Conference (VTC2019-Spring)*, pp. 1–7, 2019.

[113] R. Hicheri, M. Pätzold, and N. Youssef, "Estimation of the time-variant velocity of a single walking person in two-dimensional non-stationary indoor environments using radio-frequency techniques," *IEEE Access*, vol. 8, pp. 169759–169774, 2020.

Part II

Appended Papers

Appendix A

Paper A

Title:	On the Influence of Walking People on the Doppler Spectral Characteristics of Indoor Channels
Authors:	Ahmed Abdelgawwad and Matthias Pätzold
Affiliation:	University of Agder, Faculty of Engineering and Science, P. O. Box 509, NO-4898 Grimstad, Norway
Conference:	*2017 IEEE 28th Annual International Symposium on Personal, Indoor, and Mobile Radio Communications (PIMRC)*, Montreal, Canada, Oct. 2017.
DOI:	10.1109/PIMRC.2017.8292482.

A

On the Influence of Walking People on the Doppler Spectral Characteristics of Indoor Channels

Ahmed Abdelgawwad and Matthias Pätzold
Department of Information and Communication Technology
Faculty of Engineering and Science, University of Agder
P.O. Box 509, NO-4898 Grimstad, Norway
E-mails: {ahmed.abdel-gawwad, matthias.paetzold}@uia.no

Abstract **— When modelling mobile radio channels with moving scatterers, it is generally assumed that the angles of departure (AODs), angles of arrival (AOAs), and the speed of the scatterers are time-invariant. However, this assumption is violated as the AODs and AOAs vary with the positions of the moving scatterers. Also, the speed of the moving scatterers might vary with time due to acceleration/deceleration. In this paper, we model the time-variant Doppler frequencies by taking into account the time-variant AODs, AOAs, and the variations of the speed of the moving scatterers. Furthermore, the complex channel gain of non-stationary single-input-single-output (SISO) fixed-to-fixed (F2F) indoor channels with moving and fixed scatterers is presented. The spectrogram of the complex channel gain using a Gaussian window is provided. The correctness of the analytical solutions is confirmed by simulations. The contribution of this paper paves the way towards the development of a passive in-home activity tracking system.**

A.1 Introduction

By 2060, around one third of the Europeans will be over 65 years old according to the report [1] released by the European Commission in 2015. At this point in time, the ratio between the working people and the retired seniors will become 2 to 1 instead of 4 to 1. The demand for in-home activity tracking of older people will increase to distinguish critical instances such as falls due to health problems from normal instances like walking, standing, and sitting down. This motivates us to analyze the Doppler spectral characteristics which is influenced by the in-home activity of older people.

In the literature, the Doppler effect caused by moving scatterers has been incorporated in wide-sense stationary vehicle-to-vehicle (V2V) [2, 3], fixed-to-fixed (F2F) [4], and fixed-to-mobile (F2M) [5] channel models. However, to the best of our knowledge, there is no study on the Doppler characteristics of non-stationary F2F indoor channels with moving people. In this paper, we apply the concept of the spectrogram to reveal the time-variant spectral information of non-stationary F2F indoor channels. The spectrogram is one of the time-frequency distributions that has many applications in music [6, 7], radar detection [8], earthquake records [9], and remote data sensing in underwater environments [10]. The concept of the spectrogram in the field of mobile radio channels has been first introduced in [11], where it has been applied to the estimation of the Doppler power spectral density of multipath fading channels. Later, it has been extended in [12] to reveal the time-variant spectral information of multipath fading channels by taking into account the speed variations of the mobile station. Moreover, the authors showed that the quality of the spectrogram can be improved by removing the spectral interference by averaging over the random channel phases of the multipath components. Other contributions to the reduction of the spectral interference can be found in, e.g., [13–15].

Our work starts with introducing a new indoor non-stationary SISO F2F channel model in which the locations of the scatterers are restricted to be inside a rectangular propagation area such as a room or an office. From this model, the time-variant AOAs, AODs, and their approximations using a first-order Taylor series are derived. Then, the time-variant Doppler frequencies based on the time-variant AOAs, AODs, and speeds are derived with their approximations using a first-order Taylor series. Based on these approximations, the instantaneous channel phases are presented. Using the instantaneous channel phases, the complex channel gain that consists of the sum of the plane wave components arriving from fixed and moving scatterers at the receiver is presented. The closed-form solution of the spectrogram of the complex channel gain is provided in this paper and represented as a sum of an auto-term and a cross-term. The auto-term of the spectrogram shows the desired time-variant spectral characteristics of each component of the complex channel gain. However, the cross-term, which represents the undesired spectral interference between the multipath components, affects the resolution of the spectrogram. In this paper, we use the method

proposed in [12, 16] to reduce the effect of the cross-term. In addition, the time-variant mean Doppler shift and the time-variant Doppler spread will be derived using the spectrogram.

The rest of the paper is organized as follows. Section A.2 presents the indoor F2F multipath propagation scenario. Section A.3 derives the complex channel gain of the F2F indoor non-stationary channel with time-variant AODs, AOAs, and speed of moving scatterers. Section A.4 shows the analytical solution of the spectrogram of the complex channel gain using a Gaussian window. Section A.5 presents the numerical results and simulations. Section A.6 summarizes our contribution and discusses directions of future work.

A.2 The Indoor Multipath Propagation Scenario

The indoor multipath propagation scenario under consideration (see Fig. A.1) consists of a room with length A and width B centralized at the origin O, a fixed transmitter (T_x) at position (x^T, y^T), and fixed receiver (R_x) at position (x^R, y^R). Also, the scenario includes N moving persons, which are modelled for simplicity by N moving point scatterers S_n^{M} ($n = 1, 2, \ldots, N$) located at initial positions $(x_n^{\mathrm{M}}, y_n^{\mathrm{M}})$, where the trajectory of each scatterer is described by a time-variant speed $v_n(t)$ and a constant angle of motion (AOM) α_{v_n}. In addition, the scenario includes walls and fixed objects which are considered as sources for M fixed point scatterers S_m^{F} ($m = 1, 2, \ldots, M$) located at positions $(x_m^{\mathrm{F}}, y_m^{\mathrm{F}})$. For simplicity, we model each moving (fixed) object as a single moving (fixed) scatterer. Single bounce scattering is assumed, i.e., each transmitted plane wave arrives at the receiver after a single bounce either on a fixed scatterer S_m^{F} or a moving scatterer S_n^{M}. Moreover, it is assumed that the T_x and R_x are equipped with single omnidirectional antennas. Furthermore, the line-of-sight (LOS) component is assumed to be obstructed. The initial Euclidean distance at time $t = 0$ between the moving scatterer S_n^{M} and T_x and between S_n^{M} and R_x are determined by

$$d_n^T = \sqrt{(x_n^{\mathrm{M}} - x^T)^2 + (y_n^{\mathrm{M}} - y^T)^2} \tag{A.1}$$

$$d_n^R = \sqrt{(x_n^{\mathrm{M}} - x^R)^2 + (y_n^{\mathrm{M}} - y^R)^2}, \tag{A.2}$$

respectively.

A.3 Derivation of The Complex Channel Gain

A.3.1 Modelling the Time-Variant Speed

The moving scatterers S_n^{M} in the considered multipath propagation scenario in the previous section have velocities $\vec{v}_n(t)$ for $n = 1, 2, \ldots, N$, which are expressed as vectors in Cartesian

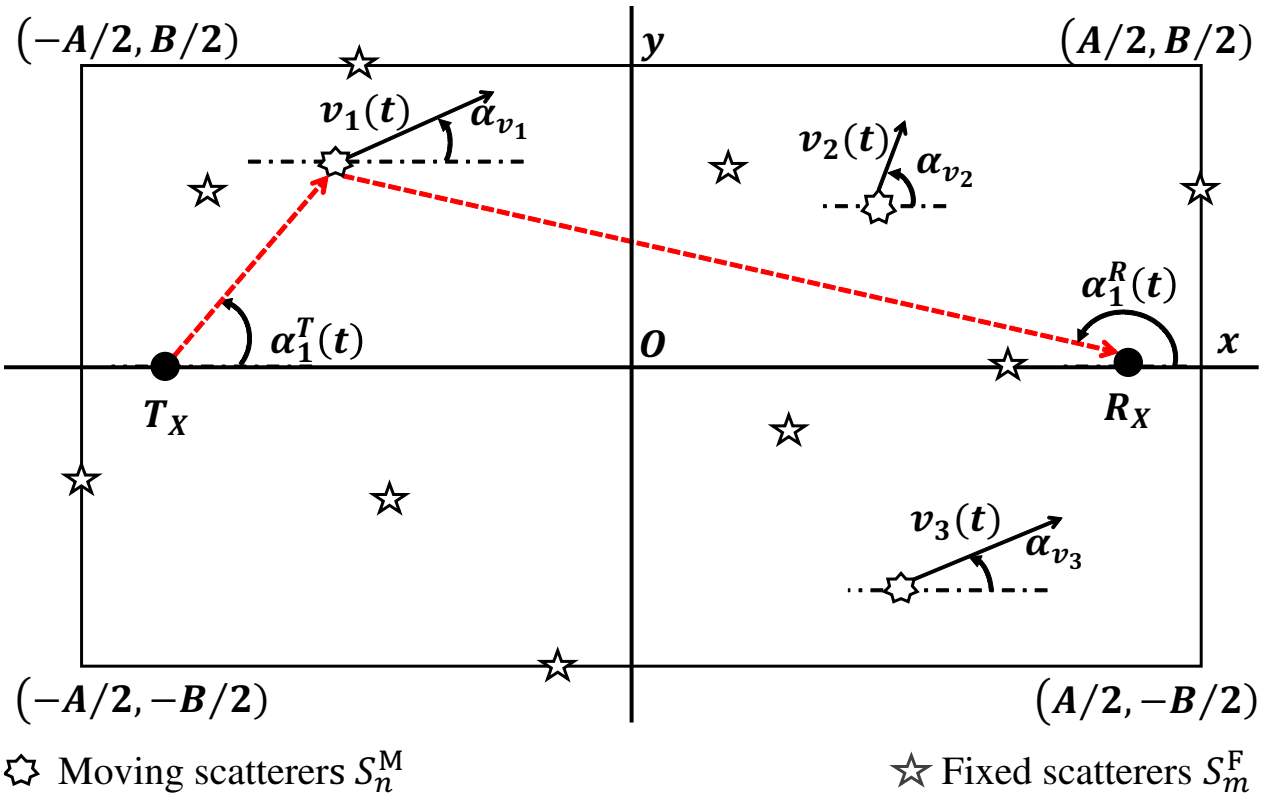

Figure A.1: An indoor propagation scenario with fixed scatterers S_m^{F} and moving scatterers S_n^{M}.

coordinates by $\vec{v}_n(t) = v_n(t)\cos(\alpha_{v_n})\,\hat{x} + v_n(t)\sin(\alpha_{v_n})\,\hat{y}$, where $\hat{x}$ ($\hat{y}$) denotes the x (y) direction. The time-variant speed of the nth moving scatterer S_n^{M} is given by

$$v_n(t) \;=\; v_n + a_n t \tag{A.3}$$

where v_n and a_n denote the initial speed of the nth moving scatterer and its acceleration/deceleration, respectively. From the speed of the moving scatterer, the time-variant positions $x_n(t)$ and $y_n(t)$ of the nth moving scatterer S_n^{M} can be calculated as follows

$$x_n^{\mathrm{M}}(t) = x_n^{\mathrm{M}} + \left[v_n t + \frac{1}{2}a_n t^2\right]\cos(\alpha_{v_n}) \tag{A.4}$$

$$y_n^{\mathrm{M}}(t) = y_n^{\mathrm{M}} + \left[v_n t + \frac{1}{2}a_n t^2\right]\sin(\alpha_{v_n})\,, \tag{A.5}$$

respectively. The parameters x_n^{M} and y_n^{M} are the initial x and y coordinates of the nth moving scatterer S_n^{M}, respectively.

A.3.2 Modelling the Time-Variant AODs and AOAs

The time-variant AOD $\alpha_n^T(t)$ is defined as the angle between the direction of the transmitted wave travelling towards the nth moving scatterer S_n^{M} and the positive x-axis. According to Fig.A.1, $\alpha_n^T(t)$ can be expressed as

$$\alpha_n^T(t) = \arctan\left(\frac{y_n^{\mathrm{M}}(t) - y^T}{x_n^{\mathrm{M}}(t) - x^T}\right). \tag{A.6}$$

Similarly, the time-variant AOA $\alpha_n^R(t)$ is determined by the angle between the direction of the wave travelling from the nth moving scatterer S_n^{M} to R_x and the positive x-axis. The AOA $\alpha_n^R(t)$ can be expressed as

$$\alpha_n^R(t) = \arctan\left(\frac{y_n^{\mathrm{M}}(t) - y^R}{x_n^{\mathrm{M}}(t) - x^R}\right). \tag{A.7}$$

From (A.6) and (A.7), the AODs $\alpha_n^T(t)$ and AOAs $\alpha_n^R(t)$ are non-linear functions of time t. However, using the first-order Taylor series, they can be approximated by the following expressions

$$\alpha_n^T(t) \approx \alpha_n^T + \gamma_n^T t \tag{A.8}$$
$$\alpha_n^R(t) \approx \alpha_n^R + \gamma_n^R t \tag{A.9}$$

where

$$\alpha_n^T = \alpha_n^T(t)|_{t=0} = \arctan\left(\frac{y_n^{\mathrm{M}} - y^T}{x_n^{\mathrm{M}} - x^T}\right) \tag{A.10}$$
$$\alpha_n^R = \alpha_n^R(t)|_{t=0} = \arctan\left(\frac{y_n^{\mathrm{M}} - y^R}{x_n^{\mathrm{M}} - x^R}\right) \tag{A.11}$$
$$\gamma_n^T = \frac{d}{dt}\alpha_n^T(t)|_{t=0} = \frac{v_n \sin\left(\alpha_{v_n} - \alpha_n^T\right)}{d_n^T} \tag{A.12}$$
$$\gamma_n^R = \frac{d}{dt}\alpha_n^R(t)|_{t=0} = \frac{v_n \sin\left(\alpha_{v_n} - \alpha_n^R\right)}{d_n^R}. \tag{A.13}$$

A.3.3 Modelling the Time-Variant Doppler Frequencies

Due to the Doppler effect, the instantaneous time-variant Doppler frequency introduced by the nth moving scatterer with time-variant speed $v_n(t)$, AOA $\alpha_n^R(t)$, and AOD $\alpha_n^T(t)$ is given by [2, 5]

$$f_n(t) = -f_{n,\max}(t)\left[\cos\left(\alpha_n^T(t) - \alpha_{v_n}\right) + \cos\left(\alpha_{v_n} - \alpha_n^R(t)\right)\right] \tag{A.14}$$

where

$$f_{n,\max}(t) = \frac{f_0 v_n(t)}{c_0} \tag{A.15}$$

denotes the maximum time-variant Doppler frequency due to the speed of the nth moving scatterer.

The parameters f_0 and c_0 in (A.15) represent the carrier frequency and the speed of light, respectively. The expression of the Doppler frequency introduced by the nth moving scatterer S_n^{M} in (A.14) can be simplified using the first-order Taylor series. This simplified expression is given by

$$f_n(t) \approx f_n + k_n t \tag{A.16}$$

where

$$\begin{aligned} f_n &= f_n(0) \\ &= -f_{n,\max}\left[\cos\left(\alpha_n^T - \alpha_{v_n}\right) + \cos\left(\alpha_{v_n} - \alpha_n^R\right)\right] \qquad \text{(A.17)} \\ k_n &= \frac{d}{dt} f_n(t)|_{t=0} \\ &= f_{n,\max}\Bigg\{\gamma_n^T \sin\left(\alpha_n^T - \alpha_{v_n}\right) - \gamma_n^R \sin\left(\alpha_{v_n} - \alpha_n^R\right) \\ &\quad - \frac{a_n}{v_n}\left[\cos\left(\alpha_n^T - \alpha_{v_n}\right) + \cos\left(\alpha_{v_n} - \alpha_n^R\right)\right]\Bigg\} \qquad \text{(A.18)} \end{aligned}$$

in which $f_{n,\max}$ is the initial maximum Doppler frequency at $t = 0$, i.e, $f_{n,\max} = f_{n,\max}(0) = f_0 v_n / c_0$. The term k_n in (A.18) can be expressed as the sum of four terms. The first and second terms are due to the rate of change of the AOD and AOA respectively, and the third and fourth terms correspond to the acceleration (deceleration) of the nth moving scatterer. For the given indoor propagation scenario, if the parameters given by (A.10)–(A.13) and α_{v_n} are constant, the time-variant Doppler frequency $f_n(t)$ is a deterministic process. Otherwise, $f_n(t)$ becomes a stochastic process if at least one of these parameters or more are random variables. It should be mentioned that, if we set the parameters γ_n^R, γ_n^T, and a_n to zero, the expressions in (A.14) and (A.16) reduce to $f_n = -f_{n,\max}\left[\cos\left(\alpha_n^T - \alpha_{v_n}\right) + \cos\left(\alpha_{v_n} - \alpha_n^R\right)\right]$, which represents the Doppler shift caused by a moving scatterer S_n^{M} in stationary channels without velocity variations [2–5].

A.3.4 Time-Variant Channel Phases and Complex Channel Gain

The time-variant channel phases using the instantaneous Doppler frequency in (A.16) are calculated according to [17] as

$$\theta_n(t) = 2\pi \int_{-\infty}^{t} f_n(x)dx \approx \theta_n + 2\pi\left(f_n t + \frac{k_n}{2}t^2\right) \tag{A.19}$$

where the first term θ_n is the initial channel phase, which can be modelled as a random variable with uniform distribution over the interval between 0 and 2π (i.e., $\mathcal{U} \sim (0, 2\pi)$) [17].

After the instantaneous channel phase is obtained, we can express the complex channel gain consisting of $N + M$ paths in non-line-of-sight environments as

$$\mu(t) = \sum_{n=1}^{N} c_n e^{j\left[2\pi\left(f_n t + \frac{k_n}{2}t^2\right) + \theta_n\right]} + \sum_{m=1}^{M} c_m e^{j\theta_m}. \tag{A.20}$$

The first term in (A.20) represents the sum of multipath components coming from N moving scatterers. It has to be mentioned that, this term is analogous to the complex channel gain of the models presented in [12, 16, 17]. The second term denotes the sum of multipath components coming from M fixed scatterers. The parameter c_n (c_m) represents the attenuation that happens due to the interaction between the signal and the nth moving (mth fixed) scatterer. The phase shift θ_n (θ_m) is caused by the signal interaction with the na moving scatterer S_n^{M} for $n = 1, 2, \ldots, N$ (mth fixed scatterer S_n^{F} for $m = 1, 2, \ldots, M$) scatterer. These quantities are supposed to be identically and independently distributed (i.i.d.) random variables each with uniform distribution between 0 and 2π. The model expressed by (A.20) is a non-stationary indoor channel model. From this model, the time-variant mean Doppler shift and Doppler spread can be expressed according to [17] as

$$B_f^{(1)}(t) = \frac{\sum_{n=1}^{N} c_n^2 f_n(t)}{\sum_{n=1}^{N} c_n^2 + \sum_{m=1}^{M} c_m^2} \tag{A.21}$$

and

$$B_f^{(2)}(t) = \sqrt{\frac{\sum_{n=1}^{N} c_n^2 f_n^2(t)}{\sum_{n=1}^{N} c_n^2 + \sum_{m=1}^{M} c_m^2} - \left(B_f^{(1)}(t)\right)^2}, \tag{A.22}$$

respectively. In the next section, the spectrogram analysis will be presented in order to identify the spectral behaviour of the proposed model.

A.4 Spectrogram Analysis Using a Gaussian Window

The main idea behind the spectrogram is to divide the time-variant signal into short-time overlapping signals. This is done by multiplying this signal with a short-time signal (sliding window) $h(t)$. Then, the Fourier-transform of each overlapping signal is calculated to get the so-called short-time Fourier transform (STFT). Finally, the STFT is multiplied by its complex conjugate to obtain the spectrogram. This concept is used to identify the spectral

behavior of time-variant deterministic or stochastic signals. The Gaussian window function is defined as

$$h(t) = \frac{1}{\sqrt{\sigma_w}\pi^{1/4}} \; e^{-\frac{t^2}{2\sigma_w^2}} \tag{A.23}$$

where σ_w is called the window spread. A high value of the window spread σ_w results in a high frequency resolution and a low time localization and vice versa. Hence, choosing the window size is always a trade-off between the time and frequency resolutions. The window used to calculate the spectrogram is real, positive, and even. It has also a unit energy (i.e., $\int_{-\infty}^{\infty} h^2(t)dt = 1$). After multiplying the complex channel gain presented in (A.20) by the window function in (A.23), we can express the short-time complex channel gain as follows

$$x(t', t) = \mu(t')h(t' - t) \tag{A.24}$$

where t denotes the local time in which we want to analyze the spectral properties of the complex channel gain, and t' is the running time. The window is centralized around the local time t in (A.24). The STFT of the complex channel gain $\mu(t)$ is obtained by computing the Fourier transform of (A.24) w.r.t. the running time t', i.e.,

$$X(f, t) = \int_{-\infty}^{\infty} x(t', t)e^{-j2\pi ft'}dt'. \tag{A.25}$$

Finally, the spectrogram of the complex channel gain $\mu(t)$ in (A.20) is obtained by multiplying (A.25) by its complex conjugate. It can be represented as

$$S_\mu(f, t) = |X(f, t)|^2. \tag{A.26}$$

After substituting the complex channel gain presented in (A.20) and the Gaussian window function according to (A.23) in (A.24) and applying the Fourier transformation with respect to t' [see (A.25)], we obtain the following closed-form solution of the STFT of the complex channel gain

$$\begin{aligned} X(f, t) =& \frac{e^{-j2\pi ft}}{\sqrt{\sigma_w}\pi^{1/4}} \Bigg[\sum_{n=1}^{N} \mu_n(t)\, G(f, f_n(t), \sigma_{x,n}^2) \\ &+ \sum_{m=1}^{M} \mu_m(t) G(f, 0, \sigma_{x,m}^2) \Bigg] \end{aligned} \tag{A.27}$$

where

$$G(f, f_n(t), \sigma_x^2) = \frac{e^{-\frac{(f - f_n(t))^2}{2\sigma_x^2}}}{\sqrt{2\pi}\sigma_x} \tag{A.28}$$

$$\sigma_{x,n}^2 = \frac{1 - j2\pi\sigma_w^2 k_n}{(2\pi\sigma_w)^2} \tag{A.29}$$

$$\sigma_{x,m}^2 = \frac{1}{(2\pi\sigma_w)^2}. \tag{A.30}$$

In the equations above, the function $f_n(t)$ and the parameter k_n are given by (A.16) and (A.18), respectively. After substituting (A.27) in (A.26), we get the spectrogram of the complex channel gain $\mu(t)$. By using the results in [16], the spectrogram $S_\mu(f,t)$ in (A.26) can be expressed in closed form as

$$S_\mu(f,t) = S_\mu^{(a)}(f,t) + S_\mu^{(c)}(f,t) \tag{A.31}$$

where $S_\mu^{(a)}(f,t)$ is called the *auto-term*, and the second term $S_\mu^{(c)}(f,t)$ denotes the *cross-term*. The auto-term is given by

$$S_\mu^{(a)}(f,t) = \sum_{n=1}^{N} c_n^2 G(f, f_n(t), \sigma_n^2) + \sum_{m=1}^{M} c_m^2 G(f, 0, \sigma_m^2) \tag{A.32}$$

where

$$\sigma_n^2 = \frac{1 + (2\pi\sigma_w^2 k_n)^2}{2(2\pi\sigma_w)^2} \tag{A.34}$$

$$\sigma_m^2 = \frac{1}{2(2\pi\sigma_w)^2}. \tag{A.35}$$

The auto-term $S_\mu^{(a)}(f,t)$ in (A.32) is a real and positive function that represents the desired spectral characteristics of the channel due to the time-variant Doppler frequencies. The result in (A.32) states that $S_\mu^{(a)}(f,t)$ can be expressed as a sum of Gaussian functions weighted by the squared path gains c_n^2 and c_m^2 for moving and fixed scatterers, respectively, and centralized at their corresponding instantaneous Doppler frequencies. The weighted Gaussian functions of the first term of the auto-term $S_\mu^{(a)}(f,t)$ in (A.32) are centralized at the instantaneous Doppler frequencies introduced by the moving scatterers. In the second term of (A.32), the weighted Gaussian functions are centralized at zero frequency, as stationary scatterers do not cause Doppler shifts in F2F channels. An interesting observation is that the variance σ_n^2 in (A.35) of the Gaussian function $G(f, f_n(t), \sigma_n^2)$ of the first term of the auto-term $S_\mu^{(a)}(f,t)$ depends on the parameter k_n, which determines the rate of change of the Doppler frequency in (A.16).

The cross-term $S_\mu^{(c)}(f,t)$ of the spectrogram is presented in (A.33), where $\mu_n(t)$ and $\mu_m(t)$ are the complex gains corresponding to the moving scatterer S_n^{M} and the fixed scatterer S_n^{F}, respectively is considered as the undesired spectral interference component. This term consists of a sum of $(N+M)(N+M-1)/2$ components. From (A.33), it is obvious that the cross-term is real valued, but not necessarily positive. In order to remove the cross-term, the statistical average over the random channel phases θ_n of the spectrogram has to be taken [12], i.e,

$$E\left\{S_\mu(f,t)\right\}\Big|_{\theta_n} = E\left\{S_\mu^{(a)}(f,t)\right\}\Big|_{\theta_n} + E\left\{S_\mu^{(c)}(f,t)\right\}\Big|_{\theta_n} = S_\mu^{(a)}(f,t) \tag{A.36}$$

$$S_{\mu}^{(c)}(f,t) = \frac{2}{\sigma_w\sqrt{\pi}}\Bigg[\sum_{n=1}^{N-1}\sum_{m=n+1}^{N}\Re\Big\{G(f,f_n(t),\sigma_{x,n}^2)\,G^*(f,f_m(t),\sigma_{x,m}^2)\,\mu_n(t)\,\mu_m^*(t)\Big\} + \sum_{m=1}^{M-1}\sum_{n=m+1}^{M}\Re\Big\{G(f,0,\sigma_{x,m}^2)G^*(f,0,\sigma_{x,n}^2)\,\mu_m(t)\,\mu_n^*(t)\Big\} + \sum_{n=1}^{N}\sum_{m=1}^{M}\Re\Big\{G(f,f_n(t),\sigma_{x,n}^2)\,G^*(f,0,\sigma_{x,m}^2)\,\mu_n(t)\,\mu_m^*(t)\Big\}\Bigg] \tag{A.33}$$

where $E\{\cdot\}$ is the expectation operator. The reason behind canceling the cross-term $S_{\mu}^{(c)}(f,t)$ by taking the average over θ_n is that $E\{e^{j(\theta_n-\theta_m)}\}$ equals zero in the case of $n \neq m$. Note that the auto-term $S_{\mu}^{(a)}(f,t)$ is not affected by taking the average over θ_n, as $E\{e^{j(\theta_n-\theta_m)}\} = 1$ for $n = m$. This method requires many sample functions of $S_{\mu}(f,t)$, which can be generated for different realizations of θ_n and θ_m. Then, the spectrograms of each trial will be summed up and divided by the total number of trials, and hence, the cross-term approaches zero. The results of this method will be presented in Section A.5.

Since the auto-term $S_{\mu}^{(a)}(f,t)$ in (A.32) contains the desired spectral information of the channel, one can calculate the time-variant mean Doppler shift $B_{\mu}^{(1)}(t)$ as follows

$$B_{\mu}^{(1)}(t) = \frac{\int_{-\infty}^{\infty} f S_{\mu}^{(a)}(f,t)}{\int_{-\infty}^{\infty} S_{\mu}^{(a)}(f,t)}\,. \tag{A.37}$$

Analogously, the time-variant Doppler spread $B_{\mu}^{(2)}(t)$ can be obtained from the auto-term $S_{\mu}^{(a)}(f,t)$ and is given by means of

$$B_{\mu}^{(2)}(t) = \sqrt{\frac{\int_{-\infty}^{\infty} f^2 S_{\mu}^{(a)}(f,t)}{\int_{-\infty}^{\infty} S_{\mu}^{(a)}(f,t)} - \Big(B_{\mu}^{(1)}(t)\Big)^2}\,. \tag{A.38}$$

A.5 Numerical Results and Simulations

In this section, simulations and numerical results are presented for an indoor scenario with certain parameters. The value for the carrier frequency f_0 has been set to 5.9 GHz. The spectral behavior of the channel was studied over the interval from $t = 0$ to 5 s. With reference to Fig. A.2, the chosen values for the length A and the width B of the room were 10 m and 5 m, respectively. The locations of T_x and R_x were $(-3.5,\, 2.4)$ and $(-4.9,\, 0)$, respectively. The number of the moving scatterers (persons) N was chosen to be 3, and the number of fixed scatterers (walls and other objects) M was equal to 7. In the considered scenario, the first two moving scatterers S_1^{M} and S_2^{M}, which start from different locations, and move towards

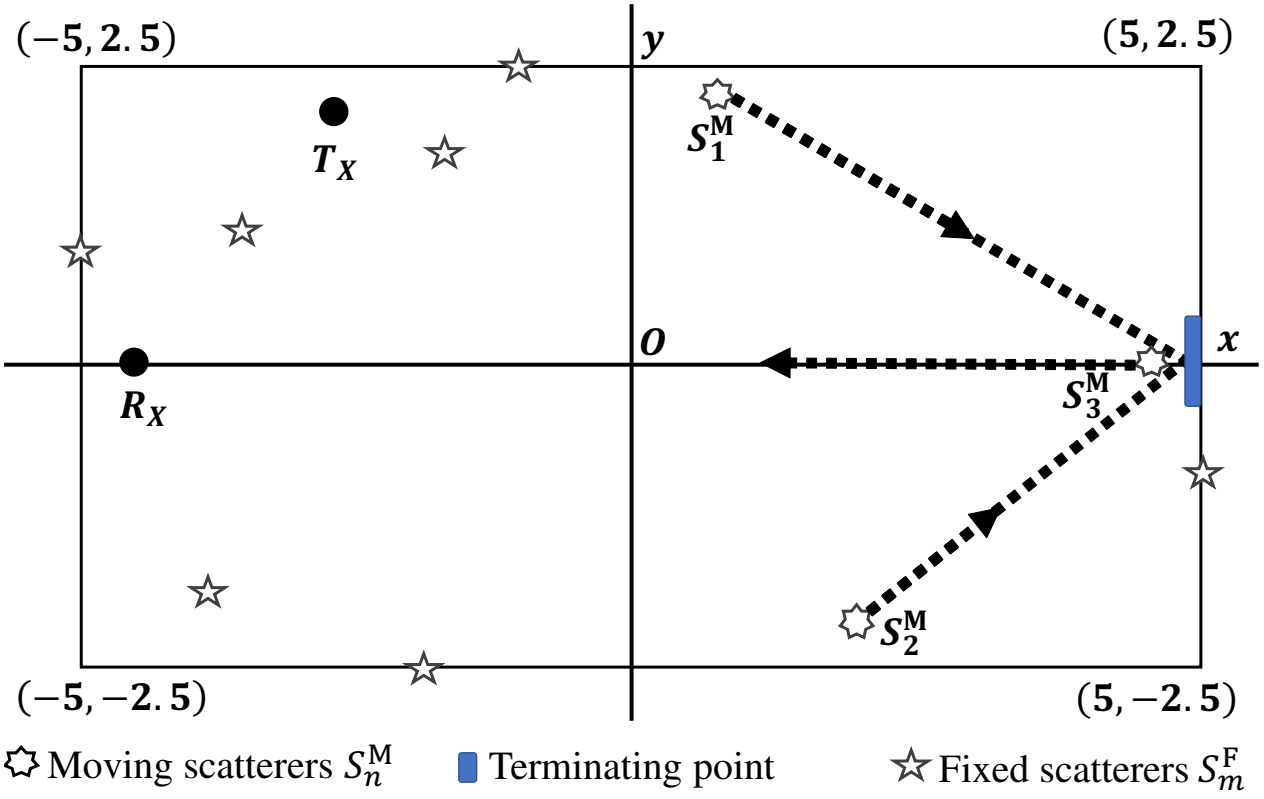

Figure A.2: The chosen scenario illustrates the locations of T_x, R_x, and the moving scatterers as well as their directions of motion.

the same destination (termination) point at constant initial speeds. Then, they start to decelerate until they reach the termination point with zero speed value and stop moving. The third scatterer S_3^{M} moves away from the termination point along a horizontal line at a constant speed and during the whole observation interval. The motion directions of the moving scatterers are indicated in Fig. A.2 by dashed lines. In order to simulate this scenario, the initial locations of the moving scatterers S_1^{M}, S_2^{M}, and S_3^{M} according to Fig. A.2 are (1, 2), (−2, 2), and (4.5, 0), respectively, and the termination point of S_1^{M} and S_2^{M} is located at (5, 0). The AOMs of S_1^{M} and S_2^{M} are computed based on their initial locations and the termination point. The AOM of the moving scatterer S_3^{M} is π rad. The initial speed of each of the moving scatterers is 1 m/s and the deceleration parameters of S_1^{M} and S_2^{M} are $-0.5\,\mathrm{m/s}^2$. The path gains of the moving and fixed scatterers were calculated from the following equations

$$c_n = \sigma_0 \sqrt{\frac{2\eta_N}{N}} \qquad \text{and} \qquad c_m = \sigma_0 \sqrt{\frac{2\eta_M}{M}} \tag{A.39}$$

respectively. The parameters η_N and η_M were used to determine the contribution of the moving and fixed scatterers, such that $\eta_N + \eta_M = 1$. The chosen values of σ_0, η_N and η_M are 1, 0.5, and 0.5, respectively. The time-variant Doppler frequencies introduced by the moving scatterers are shown in Fig. A.3. This figure depicts the Doppler frequencies of the

moving scatterers after substituting the exact expression of the AODs and AOAs given by (A.6) and (A.7), respectively in (A.14). Also, Fig. A.3 depicts the approximate solution of the time-variant Doppler frequencies according to (A.16). Since, the moving scatterers S_1^{M} and S_2^{M} have three speed states, their approximated time-variant Doppler frequencies using Taylor series have three states, which can be expressed as follows

$$f_n(t) = \begin{cases} f_{n,1} + k_{n,1}t, & \text{if } 0 \leq t < t_{n,1}, \\ f_{n,2} + k_{n,2}(t - t_{n,1}), & \text{if } t_{n,1} \leq t < t_{n,2}, \\ f_{n,3}, & \text{if } t_{n,2} \leq t \end{cases} \tag{A.40}$$

for $n = 1, 2$. The time instants $t_{n,1}$ and $t_{n,2}$ are those in which the moving scatterers start to decelerate and stop moving, respectively. The parameter $k_{n,2}$ is evaluated at the time instance $t_{n,2}$, which means that γ_n^T, γ_n^R, α_n^T, and α_n^R were evaluated at the same time instant. It is shown in Fig. A.3 that the approximations represented in (A.16) deviate from the exact solution according to (A.14). These deviations happen due to the approximation of the AODs and AOAs given by (A.8) and (A.9), respectively.

The analysis and simulations of the spectrogram are shown in Figs. A.4 and A.5, respectively. We have chosen $\sigma_w = 1/\sqrt{2\pi|k_{1,2}|}$ [16]. The figures show that the results of the analytical solution in (A.31) are similar to those of the simulations. They also show how the cross-term of the spectrogram interferes with the auto-term. This happens especially with the spectrum of the fixed scatterers at $f = 0\,\mathrm{Hz}$, as they are about to vanish. The effect of the cross-term is also obvious starting from time $t \approx 4\,\mathrm{s}$. It should be mentioned that the parameters θ_n and θ_m are the same for the analysis and the simulation. Figure A.4 shows the auto-term of the spectrogram according to (A.32). In Fig. A.6, the simulations of the spectrogram are depicted, after taking the average over multiple trials as mentioned in Section A.4. The simulations in Fig. A.6 show a perfect removal of the cross-term such that the spectrogram approaches the auto-term depicted in Fig. A.7. After removing the cross-term, the spectral lines become clearer, especially those of the fixed scatterers at $f = 0\,\mathrm{Hz}$ and after $t \approx 4\,\mathrm{s}$. Fig. A.8 depicts the time-variant mean Doppler shift $B_f^{(1)}(t)$ after substituting (A.14) and (A.16) in (A.21). This figure shows the deviations between the time-variant mean Doppler shift after substituting the exact expression given by (A.14) and the approximation expressed by (A.16) in (A.21). These deviations occur due to the approximation using the Taylor series of the AODs and AOAs given by (A.8) and (A.9), respectively. Also, Fig. A.8 depicts the time-variant mean Doppler shift $B_\mu^{(1)}(t)$ after applying (A.37) to the auto-term given by (A.32) and to the simulation of the spectrogram after taking the average over the random phases. This figure shows a perfect match between $B_f^{(1)}(t)$ and $B_\mu^{(1)}(t)$, meaning that the proposed channel model is consistent w.r.t the time-variant mean Doppler shift [17].

Fig. A.9 depicts the time-variant Doppler spread $B_f^{(2)}(t)$. This figure shows the deviations between the time-variant Doppler spread after substituting the exact expression given by (A.14) and the approximation expressed by (A.16) in (A.22). Also, Fig. A.9 depicts the

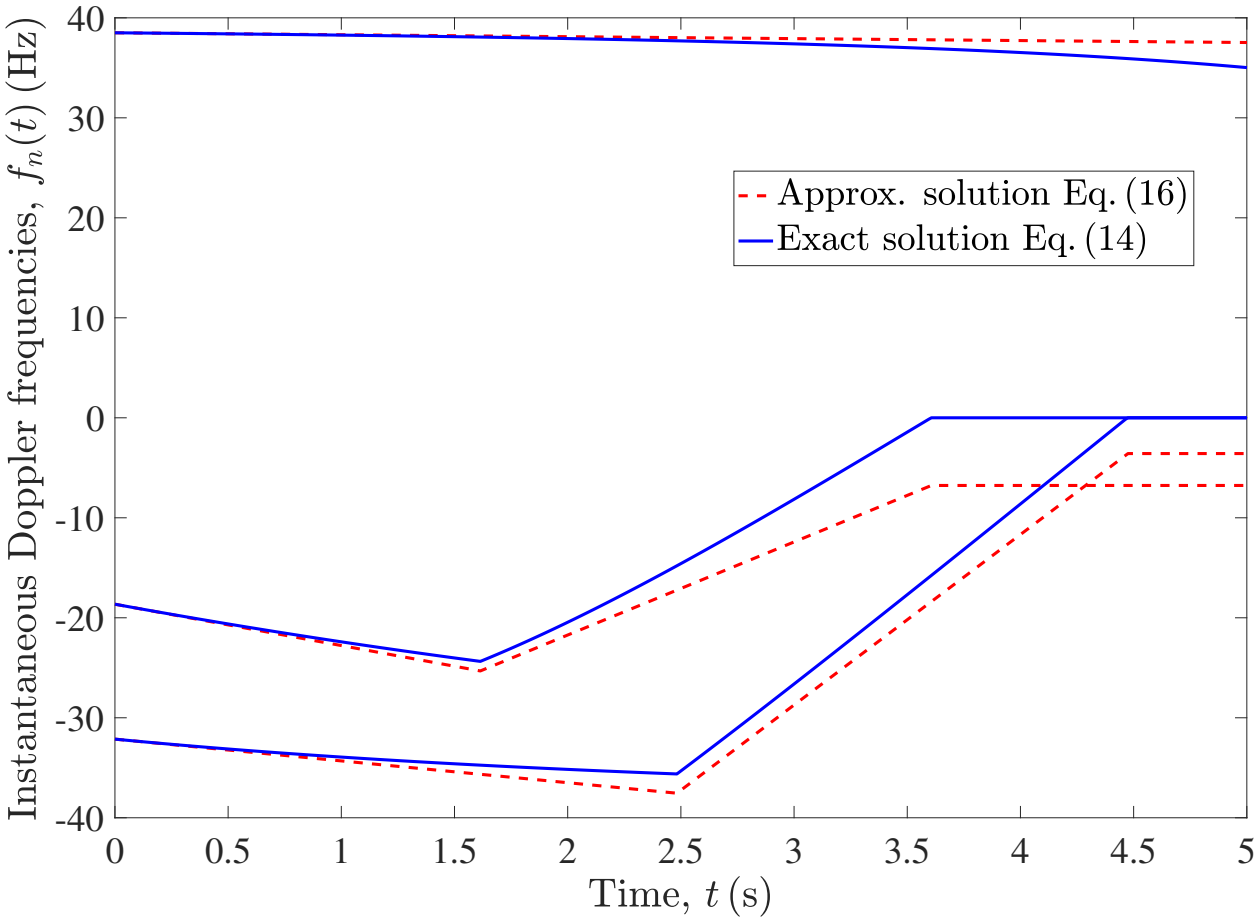

Figure A.3: Instantaneous Doppler frequencies caused by the moving scatterers using the exact expression in (A.14) and the approximation in (A.16).

time-variant Doppler spread $B_{\mu}^{(2)}(t)$ after applying (A.38) to the auto-term given by (A.32) and to the simulation of the spectrogram after taking the average over the random phases. This figure shows a perfect match between $B_{f}^{(2)}(t)$ and $B_{\mu}^{(2)}(t)$, i.e, the model is also consistent w.r.t the time-variant Doppler spread [17].

A.6 Conclusion

In this paper, we presented the spectrogram of indoor non-stationary F2F channels with fixed and moving scatterers. We derived the time-variant channel parameters, their approximations, and the complex channel gain from the geometrical model. Then, a closed-form solution of the spectrogram using a Gaussian window was presented. Moreover, we introduced how the cross-term of the spectrogram can be eliminated by taking the average over the random channel phases. Furthermore, we showed how to calculate the time-variant mean Doppler shift and Doppler spread from the spectrogram. Finally, a good match between the results

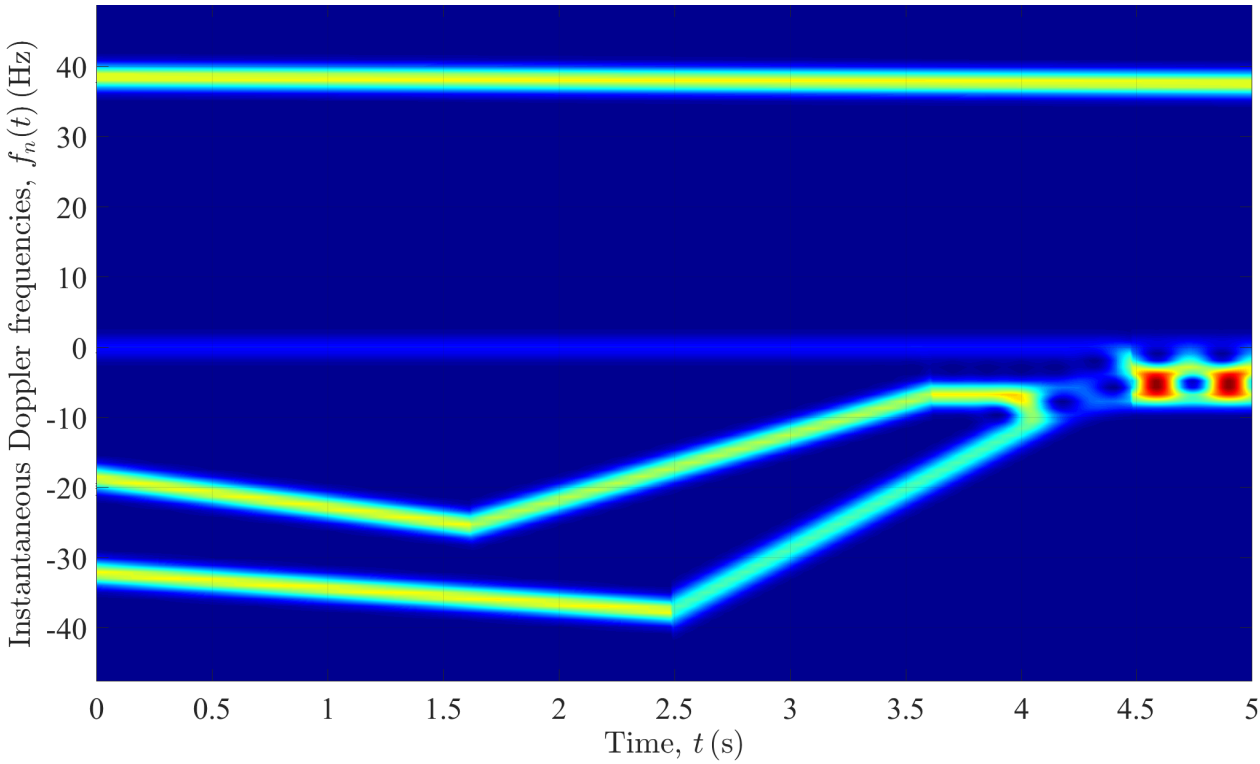

Figure A.4: Spectrogram $S_\mu(f,t)$ of the complex channel gain $\mu(t)$ according to (A.31).

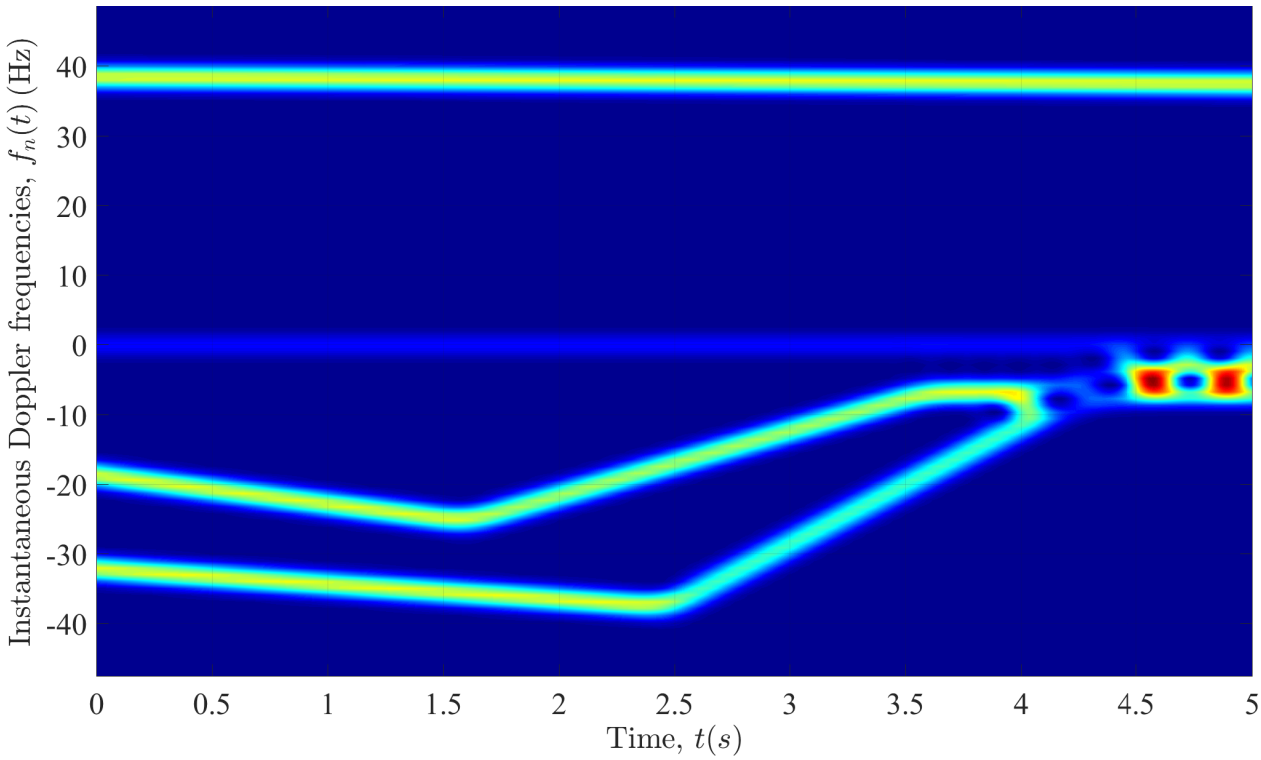

Figure A.5: Spectrogram $S_\mu(f,t)$ (simulation) of the complex channel gain $\mu(t)$.

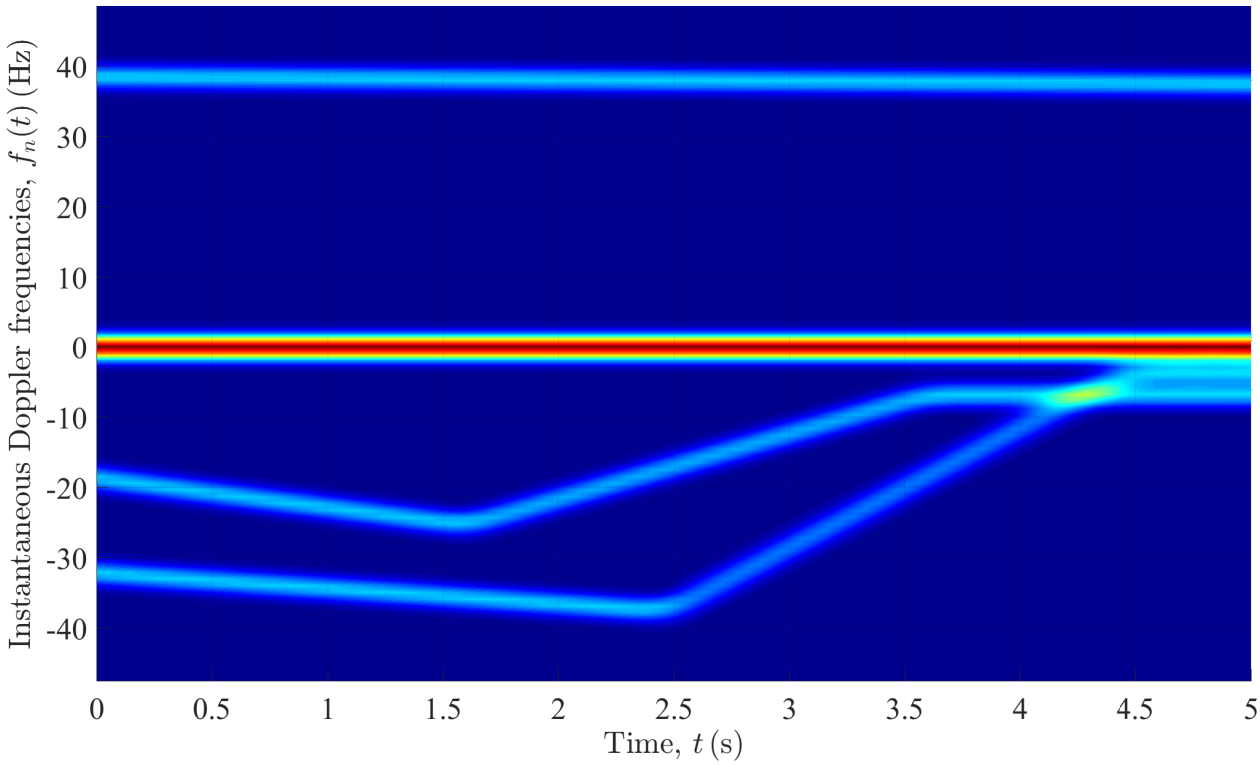

Figure A.6: Spectrogram $S_\mu(f,t)$ (simulation) of the complex channel gain $\mu(t)$ after taking the average over the channel phases θ_n.

of the analysis and the simulations was shown. This model is beneficial for passive fall detection systems because it reveals the time-variant spectral information in the case of walking scenarios.

For future work, we propose to extend this model to three-dimensional (3D) MIMO channels as the MIMO techniques allow to reduce the cross-term of the spectrogram by taking the average in the spatial domain rather than taking the average over the random phases. Also, we propose to extend this model to 3D geometry so that the spectral information can be analyzed in the case of 3D motions such as, standing, sitting, falling or jumping.

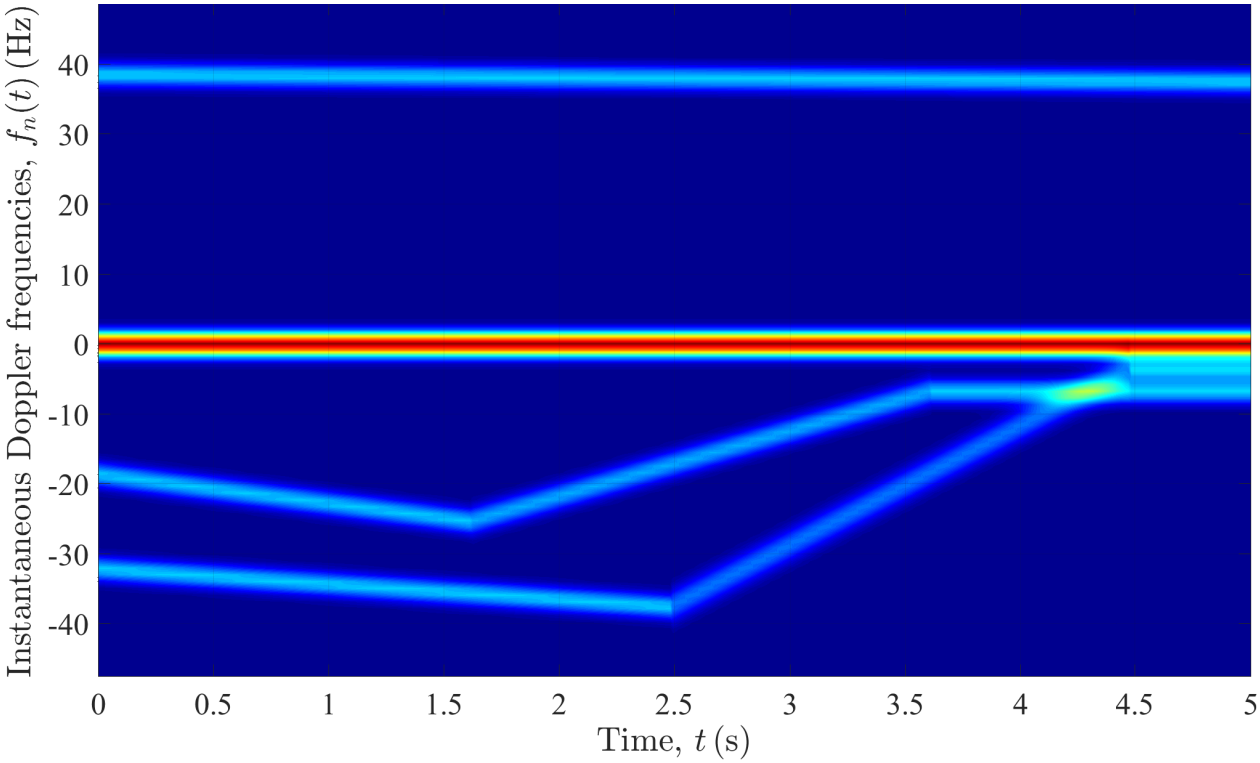

Figure A.7: Auto-term of the spectrogram $S_{\mu}^{(a)}(f,t)$ of the complex channel gain $\mu(t)$ according to (A.32).

A

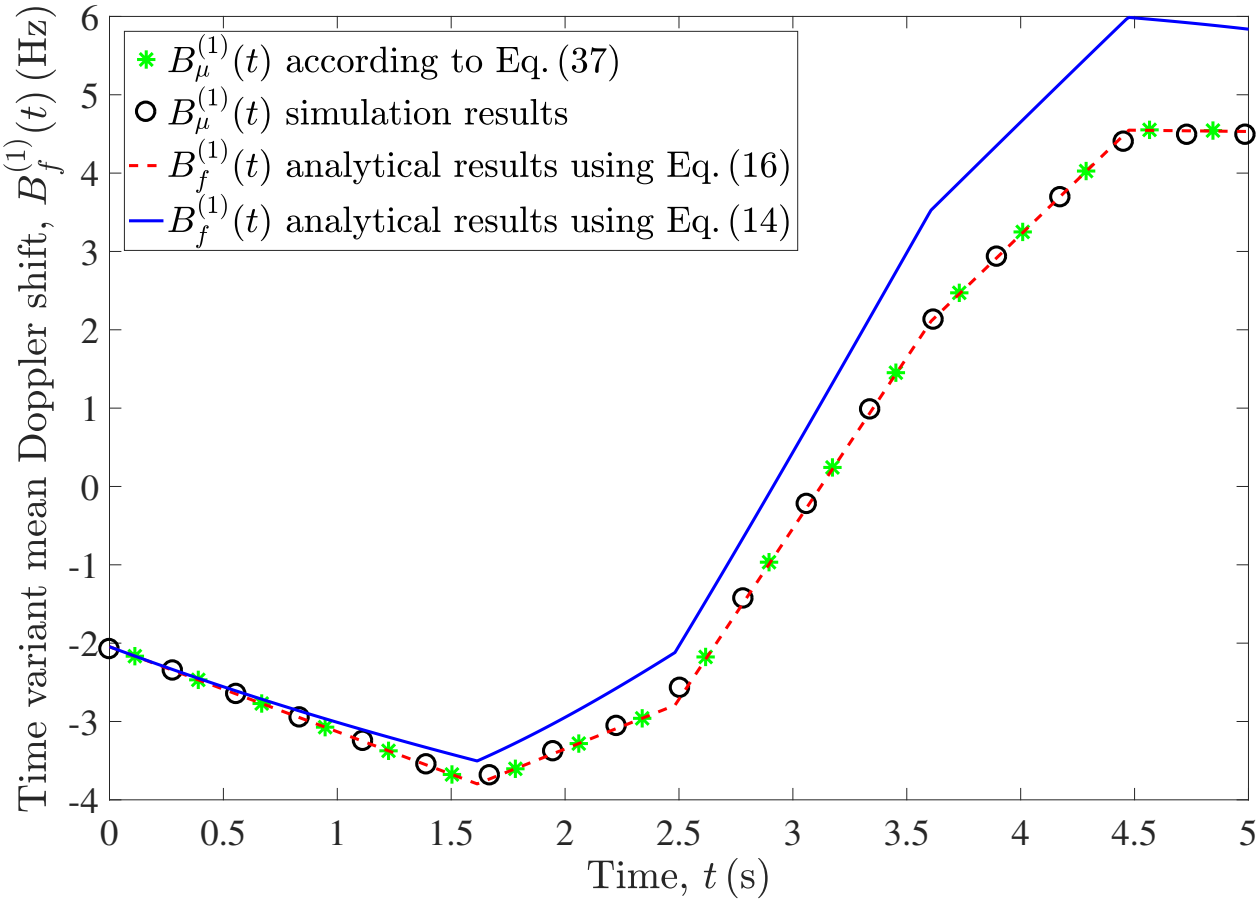

Figure A.8: Time-variant mean Doppler shifts $B_f^{(1)}(t)$ and $B_\mu^{(1)}(t)$ obtained from (A.21) and (A.37), respectively.

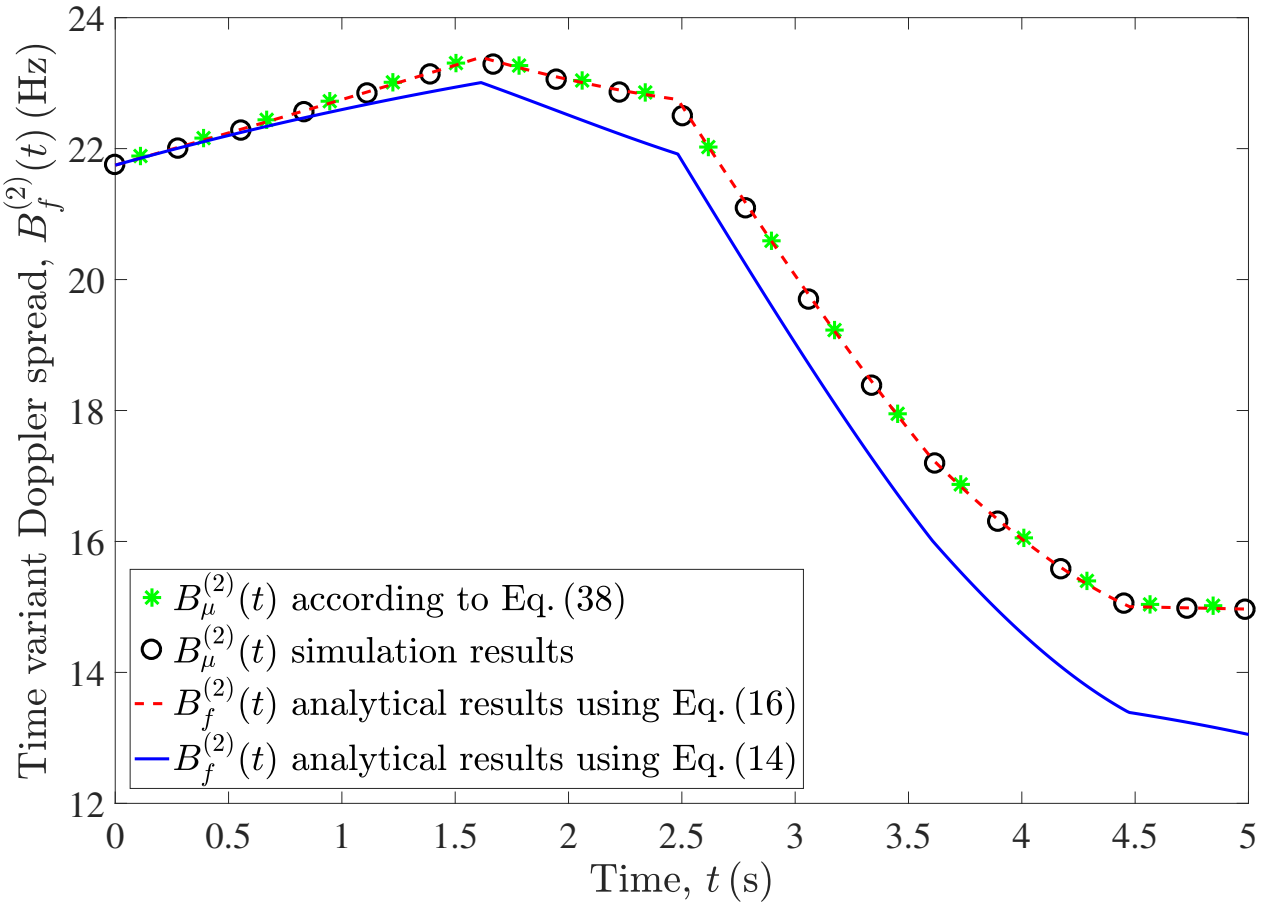

Figure A.9: Time-variant Doppler spreads $B_f^{(2)}(t)$ and $B_\mu^{(2)}(t)$ computed according to (A.22) and (A.38), respectively.

A

Bibliography

[1] The European Commission, "The 2015 ageing report: underlying assumptions and projection methodologies," *European Economy*, August 2014. DOI: 10.2765/76255.

[2] A. Borhani and M. Pätzold, "Modeling of vehicle-to-vehicle channels in the presence of moving scatterers," in *Proc. IEEE 76th Vehicular Technology Conference, VTC2012-Fall*, Quebec City, Canada, Sept. 2012.

[3] A. Zajić, "Modeling impact of moving scatterers on Doppler spectrum in wideband vehicle-to-vehicle channels," in *2015 9th European Conference on Antennas and Propagation (EuCAP)*, pp. 1–5, May 2015.

[4] X. Zhao, Q. Han, X. Liang, B. Li, J. Dou, and W. Hong, "Doppler spectra for F2F radio channels with moving scatterers," *IEEE Transactions on Antennas and Propagation*, vol. 64, pp. 4107–4112, Sept 2016.

[5] V. H. Pham, M. H. Taieb, J. Y. Chouinard, S. Roy, and H. T. Huynh, "On the double Doppler effect generated by scatterer motion," *REV Journal on Electronics and Communications*, vol. 1, pp. 30–37, Mar. 2011.

[6] J. F. Alm and J. S. Walker, "Time-frequency analysis of musical instruments," *SIAM Review*, vol. 44, no. 3, pp. 457–476, 2002.

[7] S. K. Banchhor and A. Khan, "Musical instrument recognition using spectrogram and autocorrelation," *Int. J. Soft Computing and Engineering*, vol. 2, pp. 1–4, Mar. 2012.

[8] R. I. A. Harmanny, J. J. M. de Wit, and G. Prémel Cabic, "Radar micro-Doppler feature extraction using the spectrogram and the cepstrogram," in *Proc. 11th European Radar Conference, EuRAD 2014*, pp. 165–168, Oct. 2014.

[9] C. I. Huerta-Lopez, Y. J. Shin, E. J. Powers, and J. M. Roesset, "Time-frequency analysis of earthquake records," in *Proc. 12th World Conf. on Earthquake Engineering, 12WCEE2000*, vol. 33, pp. 1–9, Auckland, New Zealand, Feb. 2000.

[10] T. A. Lampert and S. E. M. O'Keefe, "A survey of spectrogram track detection algorithms," *Applied Acoustics*, vol. 71, pp. 87–100, Feb. 2010.

[11] M. Pätzold and N. Youssef, "Spectrogram analysis of multipath fading channels," in *Proc. 26th IEEE Personal, Indoor and Mobile Radio Communications, PIMRC 2015*, Hong Kong, China, Aug./Sept. 2015.

[12] M. Pätzold and C. A. Gutiérrez, "Spectrogram analysis of multipath fading channels under variations of the mobile speed," in *Proc. 84rd IEEE Veh. Technol. Conf., IEEE VTC2016-Fall*, Montreal, Canada, Sept. 2016.

[13] D. Gabor, "Theory of communication," *J. IEE*, vol. 93[III], pp. 429–457, Nov. 1946.

[14] A. W. Rihaczek, "Signal energy distribution in time and frequency," *IEEE Trans. Inform. Theory*, vol. 14, pp. 369–374, May 1968.

[15] L. Cohen, "Time-frequency distributions–A review," *Proceedings of the IEEE*, vol. 77, pp. 941–981, July 1989.

[16] M. Pätzold, C. A. Gutiérrez, and N. Youssef, "Enhancing the resolution of the spectrogram of non-stationary channels by using massive MIMO techniques," in *Proc. IEEE 86th Vehicular Technology Conference, VTC2017-Fall*, Toronto, Canada, Sept. 2017.

[17] M. Pätzold, C. A. Gutiérrez, and N. Youssef, "On the consistency of non-stationary multipath fading channels with respect to the average Doppler shift and the Doppler spread," in *Proc. IEEE Wireless Communications and Networking Conference, WCNC 2017*, San Francisco, CA, USA, Mar. 2017.

Appendix B

Paper B

Title:	A Framework for Activity Monitoring and Fall Detection Based on the Characteristics of Indoor Channels
Authors:	Ahmed Abdelgawwad and Matthias Pätzold
Affiliation:	University of Agder, Faculty of Engineering and Science, P. O. Box 509, NO-4898 Grimstad, Norway
Conference:	*2018 IEEE 87th Vehicular Technology Conference (VTC Spring)*, Porto, Portugal, 2018.
DOI:	10.1109/VTCSpring.2018.8417468.

A Framework for Activity Monitoring and Fall Detection Based on the Characteristics of Indoor Channels

Ahmed Abdelgawwad and Matthias Pätzold
Department of Information and Communication Technology
Faculty of Engineering and Science, University of Agder
P.O. Box 509, NO-4898 Grimstad, Norway
E-mails: {ahmed.abdel-gawwad, matthias.paetzold}@uia.no

Abstract **— This paper concerns the Doppler power spectrum of three- dimensional non-stationary indoor fixed-to-fixed channels with moving people. Each moving person is modelled as a moving point scatterer with time-variant (TV) speed, TV vertical angles of motion, and TV horizontal angles of motion of the moving scatterers. Furthermore, we derive the TV angular parameters of each moving scatterer, such as the elevation angle of departure, the azimuth angle of departure, the elevation angle of arrival, and the azimuth angle of arrival. In addition, the TV unit vectors of departure and the TV unit vectors of arrival are derived. Furthermore, to present the approximated Doppler power spectrum characteristics of such channels, we provide an approximate solution of the spectrogram of the complex channel gain. The correctness of the analysis is approved by simulations. The contribution of this paper is an initiative for the development of device-free indoor activity monitoring and fall detection systems.**

B.1 Introduction

By 2060, over one third of the Europeans will be above 65 years old according to the study reported by the European Commission in 2015 [1]. According to this study, the ratio between the retired seniors and the working people will be doubled. This will result in an increased demand for in-home activity recognition systems for elder people to distinguish falls from other normal activities such as, walking, sitting, standing, and jumping. These activities follow three-dimensional (3D) trajectories. This motivates us to analyze the influence of human activities on the Doppler power spectrum of 3D fixed-to-fixed (F2F) indoor channels.

The aim of this paper is to design a channel simulator that helps to analyze the influence of fall activities of the people on the approximated Doppler power spectrum characteristics of 3D indoor channels. In the literature, many fall detection systems have been developed using video-surveillance [2, 3] or wearable sensors [4]. The main disadvantage of video surveillance-based or portable sensor-based fall detection systems is that the person might be outside the surveillance area or forget to wear the sensor. The authors of [5, 6] tracked the motion of people by analyzing the measured received signal power. In this paper, we analyze the approximation of the true Doppler power spectrum of indoor channels, which is influenced by the movement of people, by means of the spectrogram.

In the literature, the Doppler frequency caused by the motion of the scatterers has been incorporated in wide-sense stationary vehicle-to-vehicle [7], F2F [8], and fixed-to-mobile channels [9]. The time-variant (TV) Doppler effect caused by moving scatterers has been modelled in two-dimensional (2D) indoor F2F channels in [10]. In this paper, we use the spectrogram to study the influence of human activities, such as walking and falling, on the characteristics of 3D indoor multipath propagation channels. The spectrogram is one of the time-frequency representations used to represent the TV power spectrum of multi-component signals [11]. It has many applications in the area of TV signals [12], speech analysis and identification [13], acoustics [14], and seismology [15]. Furthermore, it has first been introduced in non-stationary multipath fading channels with variations of the mobile speed in [16]. One of the main disadvantages of the spectrogram, is the cross-term that reduces its resolution. Due to this problem, contributions to enhance the resolution of the spectrogram in mobile fading channels can be found in [10, 16, 17].

This paper begins with the introduction of a new 3D non-stationary single-input single-output (SISO) F2F channel model with TV parameters, such as the elevation angles of departure (EAODs), azimuth angles of departure (AAODs), elevation angles of arrival (EAOAs), azimuth angles of arrival (AAOAs), vertical angles of motion (VAOMs), and horizontal angles of motion (HAOMs) of the moving scatterers. The model also accounts for the TV speed of the moving scatterers. From these TV parameters, the expressions of the TV Doppler frequencies, instantaneous channel phases, and complex channel gain of the multipath non-stationary F2F channels are provided. Furthermore, an approximation of the

spectrogram of the complex channel gain is presented in closed-form as a sum of two terms, an auto-term and a cross-term. The auto-term provides an insight into the approximation of the desired Doppler power spectrum of the proposed model. On the other hand, the cross-term, which is considered as an undesired spectral interference term, reduces the resolution of the spectrogram. The closed-form approximation of the spectrogram is confirmed by simulations.

The rest of the paper is organized as follows. Section B.2 illustrates the 3D multipath propagation F2F propagation scenario with moving and fixed scatterers. Section B.3 discusses the TV channel parameters, TV Doppler frequencies, and the complex channel gain of our proposed model. Section B.4 provides the closed-form approximation of the spectrogram including the auto-term and the cross-term of the complex channel gain. Section B.5 discusses the numerical results of the spectrogram and illustrates the influence of human activities on 3D indoor multipath channels. Section B.6 summarizes our contribution and proposes possible extensions of our work.

B.2 The 3D Multipath Propagation Scenario

We consider the 3D indoor multipath propagation scenario presented in Fig. B.1, which consists of a fixed transmitter (T_x), a fixed receiver (R_x), fixed objects, and moving persons. A more abstract representation of such a 3D indoor propagation scenario leads to the geometrical channel model shown in Fig. B.2. This geometrical model describes a propagation scenario with a fixed transmitter (T_x) at position $\left(x^T, y^T, z^T\right)$ and a fixed receiver (R_x) located at $\left(x^R, y^R, z^R\right)$. The scenario includes N moving persons, modelled for simplicity by N moving point scatterers S_n^{M} (▲) for $n = 1, 2, \ldots, N$, where each one starts from an initial position at $\left(x_n^{\mathrm{M}}, y_n^{\mathrm{M}}, z_n^{\mathrm{M}}\right)$ and moves with a TV velocity vector $\vec{v}_n(t)$. The 3D trajectory of each moving scatterer S_n^{M} is described by its TV speed $v_n(t) = |\vec{v}_n(t)|$, the TV VAOM $\beta_{v_n}(t)$, and the TV HAOM $\alpha_{v_n}(t)$. In addition, the scenario includes walls and other objects which are modelled for simplicity as M fixed point scatterers S_m^{F} (★) for $m = 1, 2, \ldots, M$. Furthermore, single bounce scattering is assumed, i.e., each plane wave that the transmitter emits bounces on either a fixed or moving scatterer before arriving at the receiver. Both T_x and R_x are equipped with omnidirectional antennas. It is also assumed that the line-of-sight (LOS) is obstructed. The parameters $\beta_n^T(t)$, $\alpha_n^T(t)$, $\beta_n^R(t)$, and $\alpha_n^R(t)$ shown in Fig. B.2 are TV functions that denote EAOD, AAOD, EAOA, and AAOA, respectively.

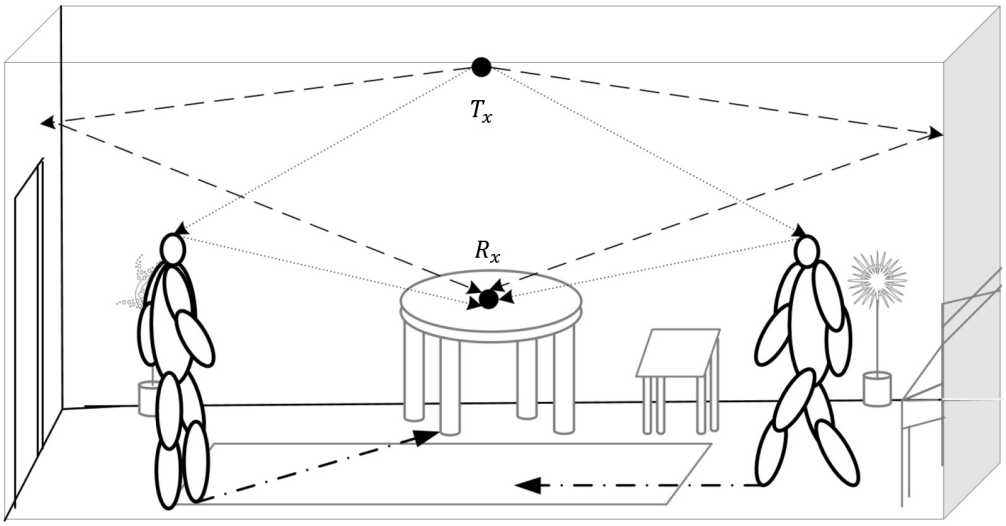

Figure B.1: A 3D non-stationary indoor multipath propagation scenario with moving persons.

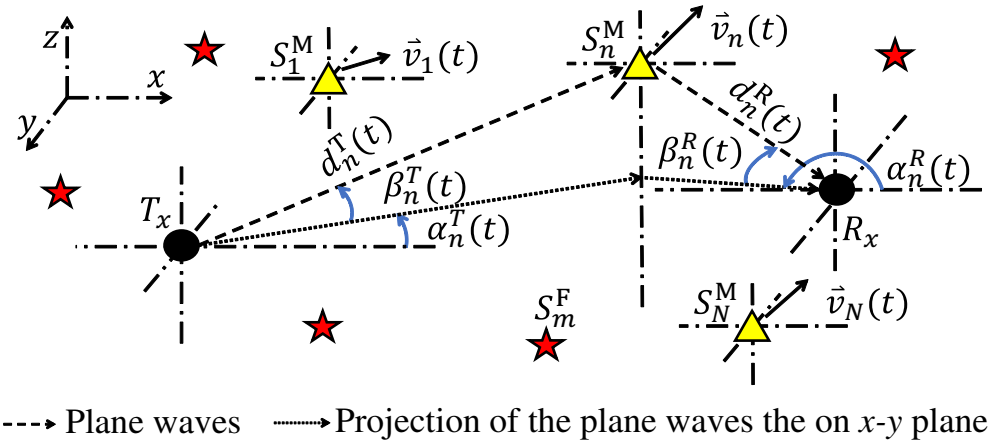

Figure B.2: A 3D non-stationary indoor multipath propagation scenario with N moving scatterers S_n^{M} $(n = 1, 2, \ldots, N)$ and M fixed scatterers S_m^{F} $(m = 1, 2, \ldots, M)$.

B.3 Derivation of the Complex Channel Gain

B.3.1 TV Velocity and TV Angular Functions

According to Fig. B.2, each moving scatterer S_n^{M} is described by a TV velocity vector $\vec{v}_n(t)$ which is given by

$$\vec{v}_n(t) = \left[v_{n,x}(t) \;,\; v_{n,y}(t) \;,\; v_{n,z}(t)\right] \tag{B.1}$$

where the velocities $v_{n,x}(t)$, $v_{n,y}(t)$, and $v_{n,z}(t)$ can be expressed in terms of the TV speed $v_n(t)$, TV VAOM $\beta_{v_n}(t)$, and TV HAOM $\alpha_{v_n}(t)$ as

$$v_{n,x}(t) = v_n(t)\cos(\beta_{v_n}(t))\cos(\alpha_{v_n}(t)) \quad \text{(B.2)}$$

$$v_{n,y}(t) = v_n(t)\cos(\beta_{v_n}(t))\sin(\alpha_{v_n}(t)) \quad \text{(B.3)}$$

$$v_{n,z}(t) = v_n(t)\sin(\beta_{v_n}(t)). \quad \text{(B.4)}$$

The TV locations $x_n(t)$, $y_n(t)$, and $z_n(t)$ of the nth moving scatterer S_n^{M} can be obtained from each component of the TV velocity vector $\vec{v}_n(t)$ by

$$x_n(t) = x_n^{\mathrm{M}} + \int_0^t v_{n,x}(t')dt' \quad \text{(B.5)}$$

$$y_n(t) = y_n^{\mathrm{M}} + \int_0^t v_{n,y}(t')dt' \quad \text{(B.6)}$$

$$z_n(t) = z_n^{\mathrm{M}} + \int_0^t v_{n,z}(t')dt'. \quad \text{(B.7)}$$

From the TV locations in (B.5)–(B.7), the TV Euclidean distance $d_n^T(t)$ between T_x and the nth moving scatterer S_n^{M} can be obtained as

$$d_n^T(t) = \sqrt{(x_n(t)-x^T)^2 + (y_n(t)-y^T)^2 + (z_n(t)-z^T)^2}. \quad \text{(B.8)}$$

Similarly, the TV Euclidean distance $d_n^R(t)$ between R_x and the nth moving scatterer S_n^{M} is given by

$$d_n^R(t) = \sqrt{(x_n(t)-x^R)^2 + (y_n(t)-y^R)^2 + (z_n(t)-z^R)^2}. \quad \text{(B.9)}$$

From the TV locations in (B.5)–(B.7) and the TV distances in (B.8) and (B.9), one can obtain the TV EAOD $\beta_n^T(t)$, TV AAOD $\alpha_n^T(t)$, TV EAOA $\beta_n^R(t)$, and TV AAOA $\alpha_n^R(t)$ as follows:

$$\beta_n^T(t) = \arcsin\left(\frac{z_n(t)-z^T}{d_n^T(t)}\right) \quad \text{(B.10)}$$

$$\alpha_n^T(t) = \operatorname{atan2}\left(y_n(t)-y^T,\, x_n(t)-x^T\right) \quad \text{(B.11)}$$

$$\beta_n^R(t) = \arcsin\left(\frac{z_n(t)-z^R}{d_n^R(t)}\right) \quad \text{(B.12)}$$

$$\alpha_n^R(t) = \operatorname{atan2}\left(y_n(t)-y^R,\, x_n(t)-x^R\right). \quad \text{(B.13)}$$

The atan2 function in (B.11) stands for the inverse trigonometric function that returns the angle between $-\pi$ and π, unlike the arctan function which returns the angle between $-\pi/2$

and $\pi/2$. It should be mentioned that the elevation angles $\beta_n^T(t)$ and $\beta_n^R(t)$ range from $-\pi/2$ to $\pi/2$ and the azimuth angles $\alpha_n^T(t)$ and $\alpha_n^R(t)$ from $-\pi$ and π. The TV HAOM $\alpha_{v_n}(t)$ and TV VAOM $\beta_{v_n}(t)$ can be expressed by the instantaneous velocities $v_{n,x}(t)$, $v_{n,y}(t)$, and $v_{n,z}(t)$ of the nth moving scatterer by

$$\alpha_{v_n}(t) = \operatorname{atan2}\left(v_{n,y}(t), v_{n,x}(t)\right) \tag{B.14}$$

$$\beta_{v_n}(t) = \arcsin\left(\frac{v_{n,z}(t)}{\sqrt{v_{n,x}^2(t) + v_{n,y}^2(t) + v_{n,z}^2(t)}}\right) \tag{B.15}$$

respectively, where $\alpha_{v_n}(t) \in (-\pi, \pi]$ and $\beta_{v_n}(t) \in \left[-\frac{\pi}{2}, \frac{\pi}{2}\right]$.

The unit vector of departure $\vec{\phi}_n^T(t)$ of the wave transmitted from T_x towards the nth moving scatterer S_n^{M} can be expressed by the TV EAOD $\beta_n^T(t)$ and AAOD $\alpha_n^T(t)$ as follows

$$\vec{\phi}_n^T(t) = \begin{bmatrix} \cos\left(\alpha_n^T(t)\right)\cos\left(\beta_n^T(t)\right) \\ \sin\left(\alpha_n^T(t)\right)\cos\left(\beta_n^T(t)\right) \\ \sin\left(\beta_n^T(t)\right) \end{bmatrix}. \tag{B.16}$$

Analogously, the unit vector of arrival $\vec{\phi}_n^R(t)$ of the wave travelling from the nth moving scatterer S_n^{M} to R_x can be expressed by the TV EAOA $\beta_n^R(t)$ and AAOA $\alpha_n^R(t)$ as follows

$$\vec{\phi}_n^R(t) = \begin{bmatrix} \cos\left(\alpha_n^R(t)\right)\cos\left(\beta_n^R(t)\right) \\ \sin\left(\alpha_n^R(t)\right)\cos\left(\beta_n^R(t)\right) \\ \sin\left(\beta_n^R(t)\right) \end{bmatrix}. \tag{B.17}$$

B.3.2 Modelling the TV Doppler Frequency

The Doppler frequency $f_n(t)$ caused by the motion of the nth moving scatterer S_n^{M} can be calculated by

$$\begin{aligned} f_n(t) &= -\frac{\vec{v}_n(t)\,\vec{\phi}_n^T(t) + \vec{v}_n(t)\,\vec{\phi}_n^R(t)}{\lambda} \\ &= -f_{n,\max}(t) \\ &\times \Bigg\{ \cos\left(\beta_{v_n}(t)\right)\left[\cos\left(\beta_n^T(t)\right)\cos\left(\alpha_n^T(t) - \alpha_{v_n}(t)\right)\right. \\ &+ \left.\cos\left(\beta_n^R(t)\right)\cos\left(\alpha_{v_n}(t) - \alpha_n^R(t)\right)\right] + \sin\left(\beta_{v_n}(t)\right) \\ &\times \left[\sin\left(\beta_n^T(t)\right) + \sin\left(\beta_n^R(t)\right)\right] \Bigg\} \end{aligned} \tag{B.18}$$

where

$$f_{n,\max}(t) = \frac{v_n(t)}{\lambda} \tag{B.19}$$

denotes the maximum Doppler frequency. The symbol λ in (B.19) represents the wavelength of the carrier signal. The Doppler frequency $f_n(t)$ in (B.18) is a TV deterministic process if the initial position $\left(x_n^{\mathrm{M}},\, y_n^{\mathrm{M}},\, z_n^{\mathrm{M}}\right)$ and the velocity $\vec{v}_n(t)$ of the scatterer S_n^{M} are known and the locations of T_x and R_x are fixed.
The model for the Doppler frequencies $f_n(t)$ in (B.18) includes several special cases. For example, if the function $\beta_{v_n}(t)$ equals zero, then (B.18) reduces to

$$\begin{aligned} f_n(t) = &- f_{n,\max}(t)\Big\{ \cos\left(\beta_n^T(t)\right)\, \cos\left(\alpha_n^T(t) - \alpha_{v_n}(t)\right) \\ &+ \cos\left(\beta_n^R(t)\right)\, \cos\left(\alpha_{v_n}(t) - \alpha_n^R(t)\right)\Big\} \end{aligned} \tag{B.20}$$

which is analogous to the Doppler frequencies of moving scatterers in 3D non-stationary vehicle-to-vehicle (V2V) channels. If we set the functions $\beta_{v_n}(t)$, $\beta_n^T(t)$, and $\beta_n^R(t)$ to zero, and $\alpha_{v_n}(t)$ is supposed to be a constant, i.e., $\alpha_{v_n}(t) = \alpha_{v_n}$, then (B.18) reduces further to

$$\begin{aligned} f_n(t) = &- f_{n,\max}(t)\Big\{ \cos\left(\alpha_n^T(t) - \alpha_{v_n}\right) \\ &+ \cos\left(\alpha_{v_n} - \alpha_n^R(t)\right)\Big\} \end{aligned} \tag{B.21}$$

which equals the Doppler frequency caused by a moving scatterer in 2D non-stationary F2F channels as modelled in [10]. Moreover, if all the parameters in (B.18) are constants, then the Doppler frequency becomes independent of time, i.e.,

$$\begin{aligned} f_n = &- f_{n,\max}\Big\{ \cos\left(\beta_{v_n}\right)\left[\cos\left(\beta_n^T\right)\cos\left(\alpha_n^T - \alpha_{v_n}\right)\right. \\ &\left. + \cos\left(\beta_n^R\right)\cos\left(\alpha_{v_n} - \alpha_n^R\right)\right] + \sin\left(\beta_{v_n}\right) \\ &\times \left[\sin\left(\beta_n^T\right) + \sin\left(\beta_n^R\right)\right]\Big\} \end{aligned} \tag{B.22}$$

which equals the Doppler frequency of 3D stationary F2F channels with scatterers moving with constant velocities and time-invariant angular parameters. Finally, if we set β_{v_n} to zero, then the expression in (B.22) reduces to

$$\begin{aligned} f_n \;\; = \;\; -f_{n,\max}\Big\{ &\cos\left(\beta_{v_n}\right)\left[\cos\left(\beta_n^T\right)\cos\left(\alpha_n^T - \alpha_{v_n}\right)\right. \\ &\left. + \cos\left(\beta_n^R\right)\cos\left(\alpha_{v_n} - \alpha_n^R\right)\right]\Big\} \end{aligned} \tag{B.23}$$

which equals the expression of the Doppler frequencies of scatterers moving in the x-y plane of 2D wide-sense stationary channels.

For the purpose of this paper, we approximate the Doppler frequencies $f_n(t)$ in (B.18) by L piecewise linear functions according to

$$f_n(t) \approx f_{n,l}(t) = f_n(t_l) + k_{n,l}(t - t_l) \tag{B.24}$$

for $t_l < t \leq t_{l+1}$ and $l = 0, 1, \ldots, L$, where

$$k_{n,l} = \frac{f_n(t_{l+1}) - f_n(t_l)}{t_{l+1} - t_l}. \tag{B.25}$$

It should be noted that the difference between two adjacent time instances t_{l+1} and t_l, i.e., $\Delta = t_{l+1} - t_l$, is the same for all values of $l = 0, 1, \ldots, L$.

B.3.3 Modelling the TV Channel Phases and Complex Channel Gains

As shown in [18], the instantaneous channel phases $\theta_{n,\mathrm{M}}(t)$ of the multipath component associated with the nth moving scatterer S_n^{M} can be computed from the Doppler frequency $f_n(t)$ by

$$\theta_{n,\mathrm{M}}(t) = 2\pi \int_{-\infty}^{t} f_n(t')dt' = \theta_{n,\mathrm{M}} + 2\pi \int_{0}^{t} f_n(t')dt' \tag{B.26}$$

where the first term $\theta_{n,\mathrm{M}}$ denotes the initial channel phase at $t = 0$ which is generally unknown and will thus be modelled by a random variable with a uniform distribution between 0 and 2π, i.e., $\theta_{n,\mathrm{M}} \sim \mathcal{U}(0, 2\pi]$. After the instantaneous channel phases $\theta_{n,\mathrm{M}}(t)$ are obtained, the complex channel gain $\mu(t)$ of the $N + M$ received multipath components can be modelled by

$$\mu(t) = \sum_{n=1}^{N} c_{n,\mathrm{M}}\, e^{j\theta_{n,\mathrm{M}}(t)} + \sum_{m=1}^{M} c_{m,\mathrm{F}}\, e^{j\theta_{m,\mathrm{F}}}. \tag{B.27}$$

The first term in (B.27) represents the sum of the multipath components associated with the N moving scatterers. Each component is determined by a stochastic phase process $\theta_{n,\mathrm{M}}(t)$ and a constant path gain $c_{n,\mathrm{M}}$. The second term in (B.27) represents the sum of the multipath components associated with the M fixed scatterers. The parameters $c_{n,\mathrm{M}}$ and $\theta_{n,\mathrm{M}}$ ($c_{m,\mathrm{F}}$ and $\theta_{m,\mathrm{F}}$) are the path gain and the phase shift caused by the interaction of the signal with the nth moving (mth fixed) scatterer S_n^{M} (S_m^{F}), respectively. It has to be mentioned that $\theta_{n,\mathrm{M}}$ and $\theta_{m,\mathrm{F}}$ are uniformally, independent, and identically distributed in the interval $(0, 2\pi]$. The expression in (B.27) represents a stochastic model for the complex channel gain of a 3D non-stationary indoor F2F channel with moving and fixed scatterers.

From this model, the TV mean Doppler shift $B_f^{(1)}(t)$ and the TV Doppler spread $B_f^{(2)}(t)$ can be calculated by [18]

$$B_f^{(1)}(t) = \frac{\sum_{n=1}^{N} c_{n,\mathrm{M}}^2 \, f_n(t)}{\sum_{n=1}^{N} c_{n,\mathrm{M}}^2 + \sum_{m=1}^{M} c_{m,\mathrm{F}}^2} \tag{B.28}$$

and

$$B_f^{(2)}(t) = \sqrt{\frac{\sum_{n=1}^{N} c_{n,\mathrm{M}}^2 \, f_n^2(t)}{\sum_{n=1}^{N} c_{n,\mathrm{M}}^2 + \sum_{m=1}^{M} c_{m,\mathrm{F}}^2} - \left(B_f^{(1)}(t)\right)^2} \tag{B.29}$$

respectively.

B.4 Spectrogram Analysis

The spectrogram $S_\mu(f,t)$ of $\mu\,(t)$ is obtained in 3 steps. In the first step, the TV complex channel gain $\mu(t)$ is multiplied by a window function $h(t)$. Here, the chosen window function is a Gaussian function

$$h(t) = \frac{1}{\sqrt{\sigma_w \sqrt{\pi}}} e^{-\frac{t^2}{2\sigma_w^2}} \tag{B.30}$$

where σ_w is the Gaussian window spread parameter. In general, the window function is real and even with unit energy, i.e., $\int_\infty^\infty h^2(t)dt = 1$. The short-time complex channel gain $x(\tau,t)$ is defined in [19, Eq. (2.3.1)] by

$$x(\tau,t) = \mu(\tau)h(\tau - t) \tag{B.31}$$

where τ denotes the running time, and t is the local time. The second step is to compute the Fourier transform of the short-time signal w.r.t. the running time τ to obtain the short-time Fourier transform (STFT). The STFT $X(f,t)$ of the complex channel gain $\mu(t)$ in (B.27) can be obtained as

$$\begin{aligned} X(f,t) &= \int_{-\infty}^{\infty} x(\tau,t) e^{-j2\pi f\tau} d\tau \\ &= \frac{e^{-j2\pi ft}}{\sqrt{\sigma_w}\pi^{1/4}} \Bigg\{ \sum_{n=1}^{N} \mu_{n,\mathrm{M}}(t) \, G\left(f, f_{n,l}(t), \sigma_{x,n,l,\mathrm{M}}^2\right) \\ &\quad + \sum_{m=1}^{M} \mu_{m,\mathrm{F}} \, G\left(f, 0, \sigma_{x,m,\mathrm{F}}^2\right) \Bigg\} \end{aligned} \tag{B.32}$$

for $t_l < t \leq t_{l+1}$ $(l = 0, 1, \cdots, L)$, where

$$G\left(f, f_{n,l}(t), \sigma^2_{x,n,l,\mathrm{M}}\right) = \frac{e^{-\frac{(f-f_{n,l}(t))^2}{2\sigma^2_{x,n,l,\mathrm{M}}}}}{\sqrt{2\pi}\sigma_{x,n,l,\mathrm{M}}} \tag{B.33}$$

$$\sigma^2_{x,n,l,\mathrm{M}} = \frac{1 - j2\pi\sigma_w^2 k_{n,l}}{(2\pi\sigma_w)^2} \tag{B.34}$$

$$\sigma^2_{x,m,\mathrm{F}} = \frac{1}{(2\pi\sigma_w)^2}. \tag{B.35}$$

The function $\mu_{n,\mathrm{M}}(t)$ (parameter $\mu_{m,\mathrm{F}}$) denotes the complex gain corresponding to the nth moving (mth fixed) scatterer S_n^{M} (S_m^{F}). The expression in (B.33) represents a complex Gaussian function with a time-variant mean $f_{n,l}(t)$ and variance $\sigma^2_{x,n,l,\mathrm{M}}$. The parameter $k_{n,l}$ in (B.34), which is defined in (B.25), denotes the rate of change of the Doppler frequency $f_{n,l}(t)$. By multiplying the STFT $X(f,t)$ presented in (B.32) by its complex conjugate, one obtains the spectrogram $S_\mu(f,t)$ as follows

$$S_\mu(f,t) = |X(f,t)|^2 = S_\mu^{(a)}(f,t) + S_\mu^{(c)}(f,t) \tag{B.36}$$

where $S_\mu^{(a)}(f,t)$ and $S_\mu^{(c)}(f,t)$ denote the *auto-term* and the *cross-term*, respectively. The auto-term is given by

$$\begin{aligned} S_\mu^{(a)}(f,t) = &\sum_{n=1}^{N} c^2_{n,\mathrm{M}}\, G\left(f, f_{n,l}(t), \sigma^2_{n,l,\mathrm{M}}\right) \\ &+ \sum_{m=1}^{M} c^2_{m,\mathrm{F}}\, G\left(f, 0, \sigma^2_{m,\mathrm{F}}\right) \end{aligned} \tag{B.37}$$

for $t_l < t \leq t_{l+1}$, where

$$\sigma^2_{n,l,\mathrm{M}} = \frac{1 + \left(2\pi\sigma_w^2 k_{n,l}\right)^2}{2(2\pi\sigma_w)^2} \tag{B.38}$$

$$\sigma^2_{m,\mathrm{F}} = \frac{1}{2(2\pi\sigma_w)^2}. \tag{B.39}$$

The auto-term $S_\mu^{(a)}(f,t)$ given by (B.37) is real and positive. This term consists of a sum of $N + M$ components and represents the approximation of the desired Doppler power characteristics of the 3D indoor non-stationary F2F channel with moving scatterers. It is a sum of weighted Gaussian functions, where the weighting factors are given by the squared path gains $c^2_{n,\mathrm{M}}$ and $c^2_{m,\mathrm{F}}$ of the moving scatterers and the fixed scatterers, respectively. The Gaussian functions of the first term in (B.37) are centered on $f_{n,l}(t)$ of the moving scatterers. The second term of $S_\mu^{(a)}(f,t)$ in (B.37) is centered on the origin as the fixed scatterers do

not cause Doppler shifts in F2F channels. The cross-term $S_\mu^{(c)}(f,t)$, which is given by (B.40) at the bottom of this page, represents the undesired spectral interference term consisting of $(N+M)\,(N+M-1)/2$ components. This term is a real, but not necessarily a positive function. The operator $\Re\{\cdot\}$ in (B.40) denotes the real part of a complex function. It is obvious that the auto-term $S_\mu^{(a)}(f,t)$ in (B.37) is independent of the phases $\theta_{n,\mathrm{M}}$ and $\theta_{m,\mathrm{F}}$, unlike the cross-term $S_\mu^{(c)}(f,t)$ in (B.40) which depends on them. Hence, the cross-term can be eliminated by applying the expectation operator to the spectrogram $S_\mu(f,t)$ and averaging over the random channel phases $\theta_{n,\mathrm{M}}$ and $\theta_{m,\mathrm{F}}$, i.e., $E\{S_\mu(f,t)\}\big|_{\theta_{n,\mathrm{M}},\theta_{m,\mathrm{F}}} = S_\mu^{(a)}(f,t)$.

The TV mean Doppler shift $B_\mu^{(1)}(t)$ and the TV Doppler spread $B_\mu^{(2)}(t)$ can be computed from the spectrogram $S_\mu(f,t)$ by [10]

$$B_\mu^{(1)}(t) = \frac{\int\limits_{-\infty}^{\infty} f S_\mu(f,t)df}{\int\limits_{-\infty}^{\infty} S_\mu(f,t)df} \tag{B.41}$$

and

$$B_\mu^{(2)}(t) = \sqrt{\frac{\int\limits_{-\infty}^{\infty} f^2 S_\mu(f,t)df}{\int\limits_{-\infty}^{\infty} S_\mu(f,t)df} - \left(B_\mu^{(1)}(t)\right)^2} \tag{B.42}$$

respectively.

B.5 Numerical Results

In this section, numerical results are presented for a 3D non-stationary indoor scenario, which is illustrated in Fig. B.3. The value of the carrier frequency f_0 was chosen to be 5.9 GHz. The

---

$$\begin{aligned} S_\mu^{(c)}(f,t) = \\ \frac{2}{\sigma_w\sqrt{\pi}}\Bigg[&\sum_{n=1}^{N-1}\sum_{m=n+1}^{N} \Re\Big\{ G\left(f, f_{n,l}(t), \sigma^2_{x,n,l,\mathrm{M}}\right)\, G^*\left(f, f_{m,l}(t), \sigma^2_{x,m,l,\mathrm{M}}\right)\, \mu_{n,\mathrm{M}}(t)\, \mu^*_{m,\mathrm{M}}(t) \Big\} \\ &+ \sum_{n=1}^{M-1}\sum_{m=n+1}^{M} \Re\Big\{ G\left(f, 0, \sigma^2_{x,n,\mathrm{F}}\right)\, G^*\left(f, 0, \sigma^2_{x,m,\mathrm{F}}\right)\, \mu_{n,\mathrm{F}}\, \mu^*_{m,\mathrm{F}} \Big\} \\ &+ \sum_{n=1}^{N}\sum_{m=1}^{M} \Re\Big\{ G\left(f, f_{n,l}(t), \sigma^2_{x,n,l,\mathrm{M}}\right)\, G^*\left(f, 0, \sigma^2_{x,m,\mathrm{F}}\right)\, \mu_{n,\mathrm{M}}(t)\, \mu^*_{m,\mathrm{F}} \Big\} \Bigg] \end{aligned} \tag{B.40}$$

channel has been analyzed over an observation interval T_{obs} of 4 s. The size of the room was 10 m long, 5 m wide, and 2.4 m high. The transmitter and the receiver had the same location at (5 m, 5 m, 2.25 m). The chosen number of fixed scatterers (walls and fixed objects) M was equal to 7. The number of moving scatterers N (moving persons) was chosen to be 1. In this scenario, we considered the head trajectory of the moving person. The path gains of the moving and fixed scatterers were computed using the following equations

$$c_{n,\text{M}} = \sigma_0 \sqrt{\frac{2\eta_N}{N}} \qquad \text{and} \qquad c_{m,\text{F}} = \sigma_0 \sqrt{\frac{2\eta_M}{M}} \tag{B.43}$$

respectively, where the parameters η_N and η_M allow for balancing the contribution of moving and fixed scatterers, respectively, which are subject to the following condition $\eta_N + \eta_M = 1$. The values of σ_0, η_N, and η_M were set to 1, 0.7, and 0.3, respectively. The chosen value for the window spread parameter σ_w is 0.033 s. The value of the parameter Δ introduced in Subsection B.3.2 was set to $2\sigma_w$. With reference to Fig. B.3, we consider a scenario that includes one moving scatterer representing the head of a moving person. There are three phases in the scenario:
Phase 1: The person walks 2 m at a constant speed in a time interval of 2.5 s.
Phase 2: When the person starts to fall forward, this phase lasts about 1 s until the head reaches the floor.
Phase 3: After the person's body reaches the floor, the moving scatterer becomes a fixed scatterer.
The head trajectory during the walking phase is modelled by

$$z(t) = h_{\text{step}} \cos\left(2\pi f_{\text{step}} t\right) + h_{\text{head}}. \tag{B.44}$$

The accuracy of this model has been confirmed in [20] by the trajectory extracted from a video surveillance-based human activity detection system. The azimuth angle of motion $\alpha_{v_n}(t)$ during the walking phase was 50°. The parameter h_{step} in (B.44) denotes the step height of the head during the walk. This parameter was equal to 2.7 cm. The parameter h_{head} stands for the height of the person, which was set to 1.7 m. The parameter f_{step} denotes the walking frequency, which is equivalent to the horizontal speed V_h over the step length L_s [21]. The value of the step length L_s was set to 30 cm. The horizontal speed value V_h during the walking phase was 0.8 m/s. The vertical speed V_v during the walking phase was computed by taking the derivative of (B.44) with respect to time. After the fall starts, V_h and V_v increase linearly with time until they reach the final speed values 2.5 m/s and 3.25 m/s at the end of fall, respectively [22].

Fig. B.4 depicts the results of the analysis of the spectrogram $S_\mu(f,t)$ by using (B.36). The simulation results were similar to the analytical results, but they were not included in this paper for brevity. In the simulation, the complex channel gain $\mu(t)$ was generated using the values provided earlier in this section. The values of $\theta_{n,\text{M}}$ and $\theta_{m,\text{F}}$ were obtained

from the outcomes of a random generator with uniform distribution between $(0, 2\pi]$. The simulation results have been obtained by simulating $\mu(t)$ in (B.27) by using MATLAB and then, computing the spectrogram from the simulated waveform $\mu(t)$. Fig. B.4 visualizes the influence of the head trajectory and walking speed on the spectrogram of the complex channel gain during the interval starting from $t = 0\,\mathrm{s}$ to $t = 2.5\,\mathrm{s}$. Also, this figure illustrates the impact of the variation of the head speed on the spectrogram during the fall starting from $t = 2.5\,\mathrm{s}$ to $t = 3.5\,\mathrm{s}$. During this interval, the speed increases rapidly with time due to the fall. From $t = 3.5\,\mathrm{s}$ until $t = 4\,\mathrm{s}$, the spectrogram has a strong spectral component at $f = 0\,\mathrm{Hz}$ because the head is no longer moving after the fall, i.e., its speed as well as the Doppler frequency are zero. It has to be mentioned that the characteristics of the approximated Doppler power spectrum of the fixed and moving scatterers is not obvious due to the impact of the cross-term reducing the resolution of the spectrogram. Fig. B.5 shows the auto-term of the spectrogram $S_{\mu}^{(a)}(f,t)$ according to (B.37). In this figure, it can be seen that the resolution of the spectrogram has been enhanced after removing the cross-term by taking the average of the spectrogram $S_{\mu}(f,t)$ over the random phases $\theta_{n,\mathrm{M}}$ and $\theta_{m,\mathrm{F}}$.

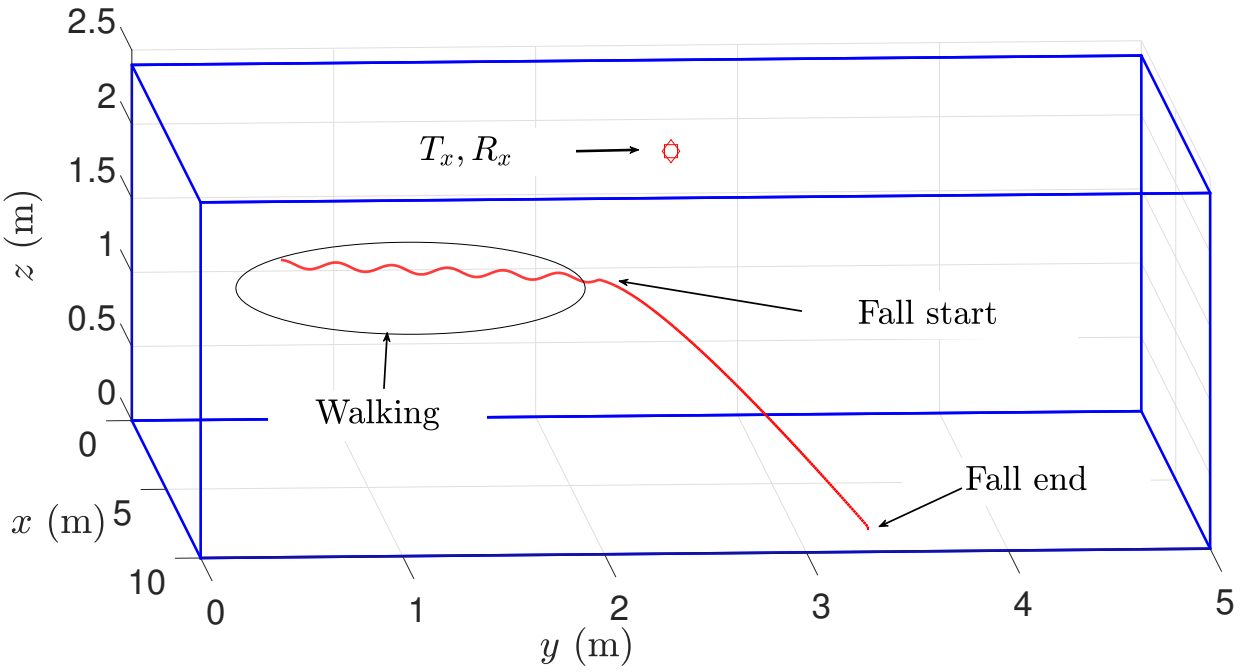

Figure B.3: Test scenario and the head trajectory.

Fig. B.6 depicts the TV mean Doppler shifts $B_f^{(1)}(t)$ and $B_{\mu}^{(1)}(t)$ obtained from (B.28) and (B.41), respectively. The TV mean Doppler shift $B_{\mu}^{(1)}(t)$ was computed numerically from the analytical expression in (B.41) and the simulation of the spectrogram using MATLAB. Although $B_{\mu}^{(1)}(t)$ is influenced by the cross-term of the spectrogram, one can recognize the impact of the fall during the interval between $t = 2.5\,\mathrm{s}$ and $t = 3.5\,\mathrm{s}$. There is a good

match between analytical and simulation results in Fig. B.6. Fig. B.7 depicts the TV Doppler spreads $B_f^{(2)}(t)$ and $B_\mu^{(2)}(t)$ obtained from (B.29) and (B.42), respectively. Again, the analytical solution of the spectrogram and the corresponding simulation results were used to obtain $B_\mu^{(2)}(t)$ by means of (B.42). Notice that, the impact of the fall on $B_\mu^{(2)}(t)$ is recognizable despite of the cross-term.

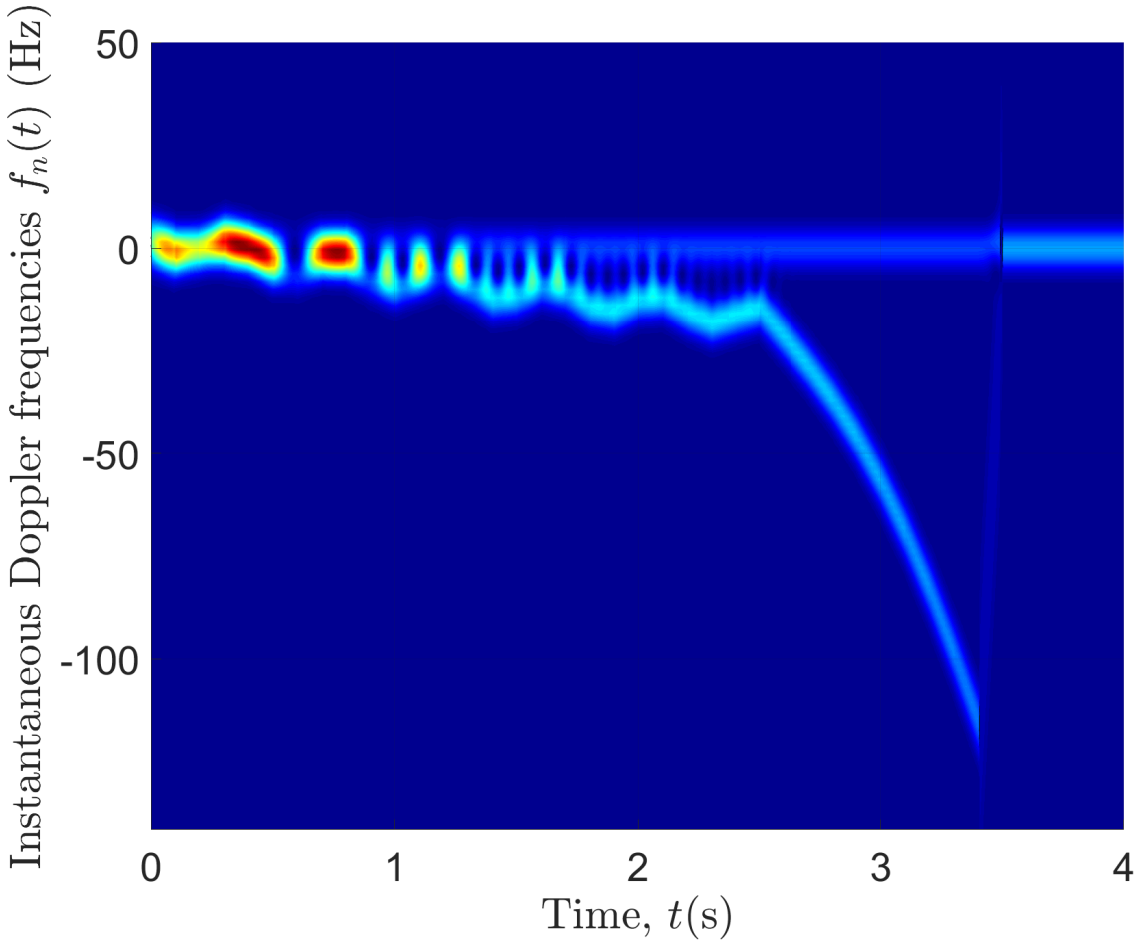

Figure B.4: Spectrogram (analysis) of the complex channel gain $\mu(t)$.

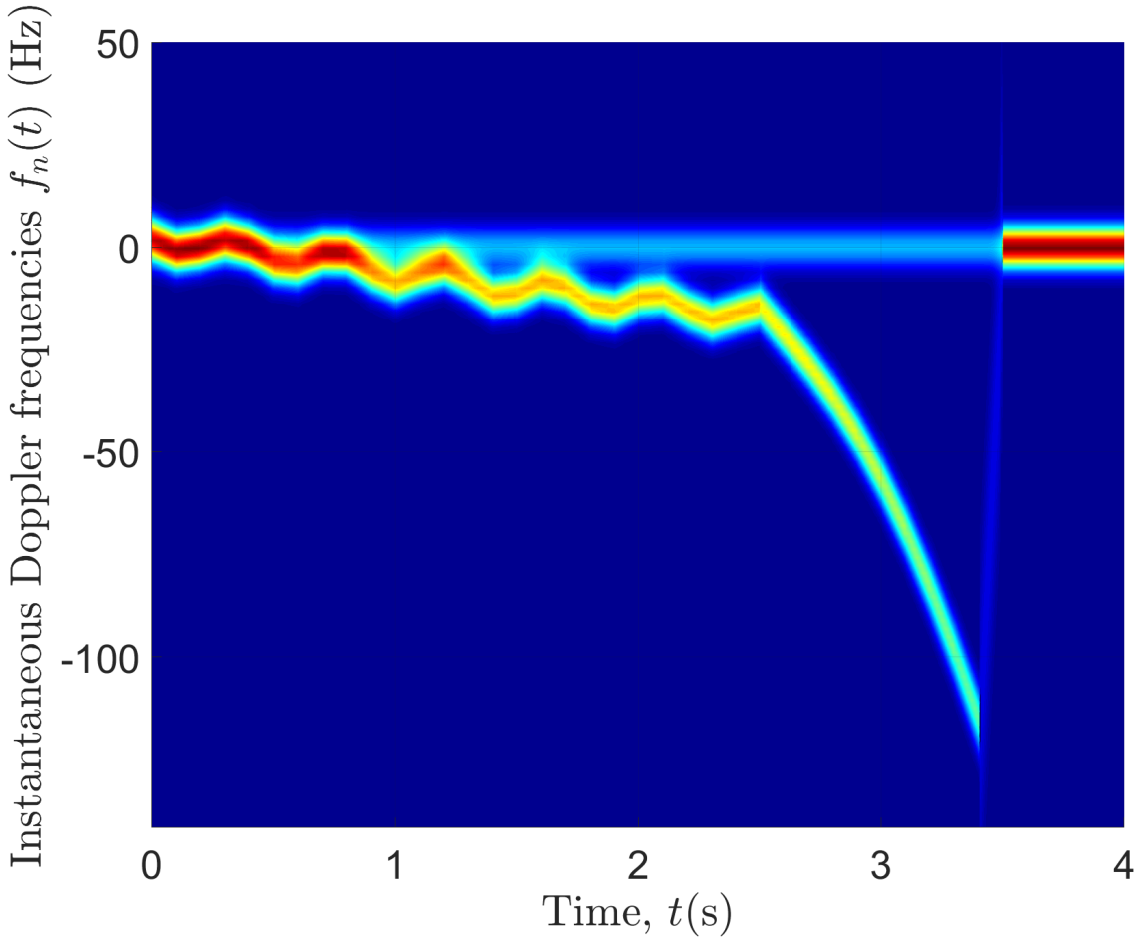

Figure B.5: The auto-term $S_{\mu}^{(a)}(f,t)$ (analysis) of the spectrogram of the complex channel gain $\mu(t)$.

B.6 Conclusion

In this paper, we presented a 3D multipath propagation model that reveals the influence of human activity on the characteristics of indoor multipath fading channels using the spectrogram. We started to model moving people as moving point scatterers. Then, we derived of the TV EAOAs, AAOAs, EAODs, AAODs, HAOMs, VAOMs, the Doppler frequencies caused by the moving point scatterers, and the complex channel gain of the indoor channels. After that, we showed the influence of moving people on such channels by providing an approximate solution of the spectrogram. Moreover, we showed the influence of the human activity on the TV mean Doppler shift and TV Doppler spread derived from the spectrogram. The spectrogram, TV mean Doppler shift, and TV Doppler spread enable us to distinguish between fall and walking activities. For future work, we plan to model people by a more

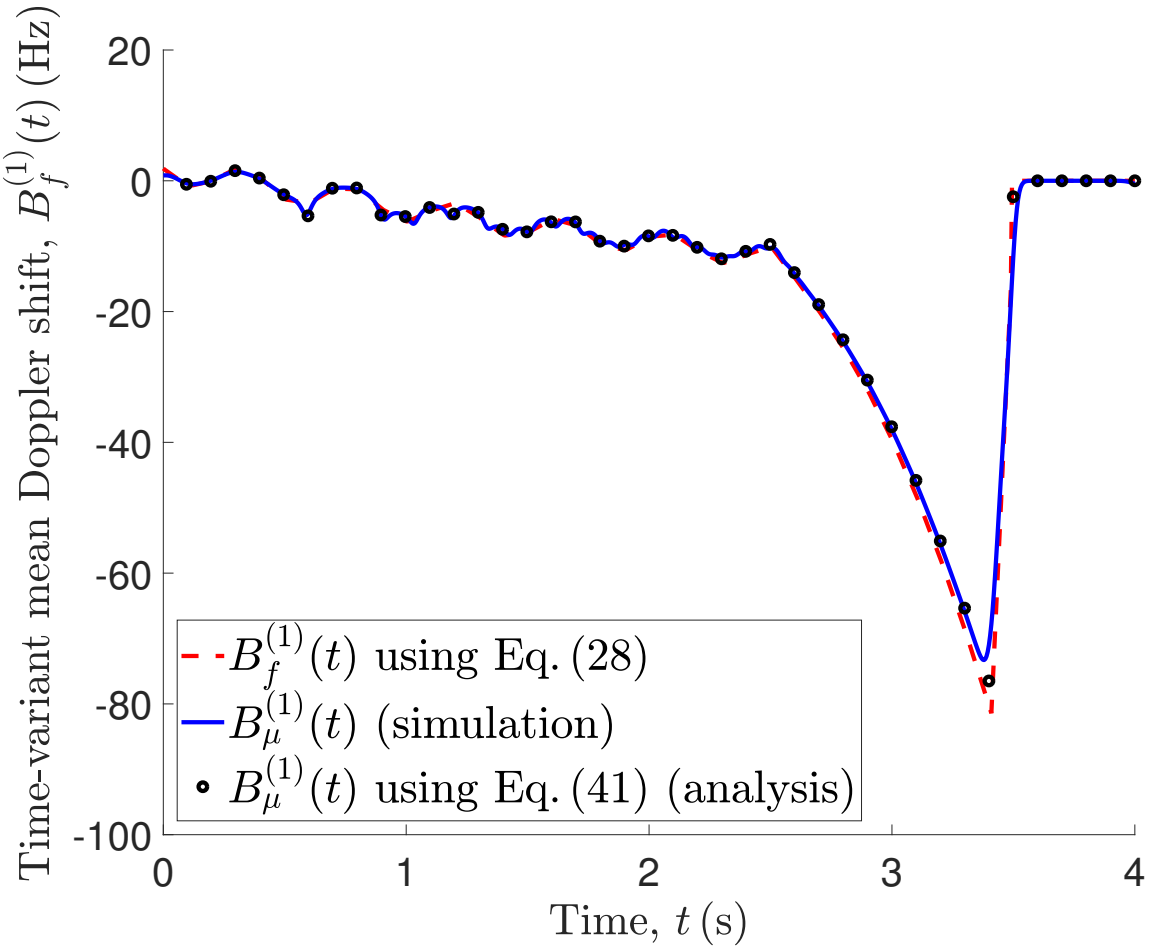

Figure B.6: TV mean Doppler shifts $B_f^{(1)}(t)$ and $B_\mu^{(1)}(t)$ obtained from (B.28) and (B.41), respectively.

realistic cluster of moving scatterers.

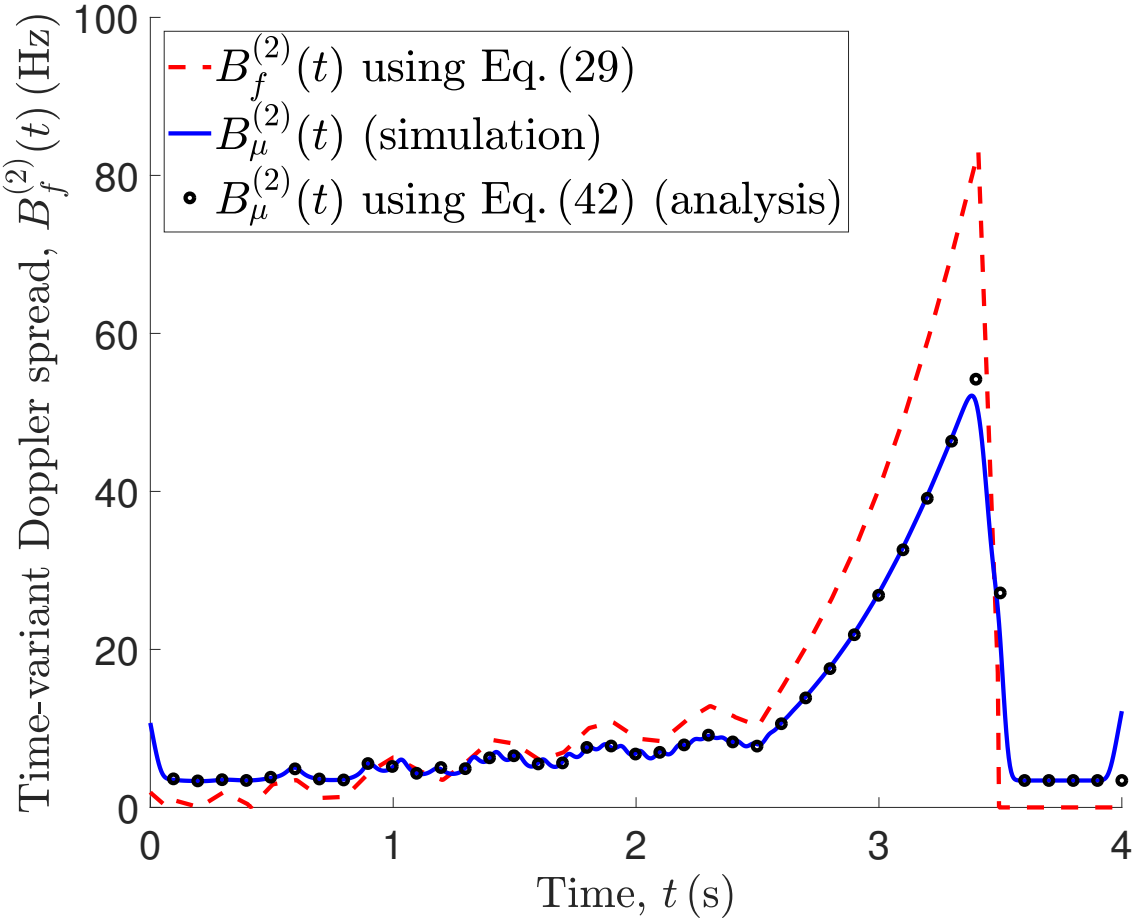

Figure B.7: TV Doppler spreads $B_f^{(2)}(t)$ and $B_\mu^{(2)}(t)$ computed according to (B.29) and (B.42), respectively.

Bibliography

[1] The European Commission, "The 2015 ageing report: underlying assumptions and projection methodologies," *European Economy*, Aug. 2014. DOI: 10.2765/76255.

[2] R. Cucchiara, A. Prati, and R. Vezzani, "A multi-camera vision system for fall detection and alarm generation," *Expert Systems*, vol. 24, no. 5, pp. 334–345, 2007. DOI:10.1111/j.1468-0394.2007.00438.x.

[3] C. Rougier, J. Meunier, A. St-Arnaud, and J. Rousseau, "3D head tracking for fall detection using a single calibrated camera," *Image Vision Computing.*, vol. 31, pp. 246–254, Mar. 2013.

[4] G. Anania *et al.*, "Development of a novel algorithm for human fall detection using wearable sensors," in *Proc. IEEE Sensors*, pp. 1336–1339, Oct. 2008.

[5] J. Wilson and N. Patwari, "See-through walls: Motion tracking using variance-based radio tomography networks," *IEEE Transactions on Mobile Computing*, vol. 10, pp. 612–621, May 2011.

[6] S. Sigg, M. Scholz, S. Shi, Y. Ji, and M. Beigl, "RF-sensing of activities from non-cooperative subjects in device-free recognition systems using ambient and local signals," *IEEE Transactions on Mobile Computing*, vol. 13, pp. 907–920, Apr. 2014.

[7] A. Zajić, "Modeling impact of moving scatterers on Doppler spectrum in wideband vehicle-to-vehicle channels," in *9th European Conference on Antennas and Propagation, EuCAP 2015*, pp. 1–5, May 2015.

[8] X. Zhao, Q. Han, X. Liang, B. Li, J. Dou, and W. Hong, "Doppler spectra for F2F radio channels with moving scatterers," *IEEE Trans. on Antennas and Propag.*, vol. 64, pp. 4107–4112, Sep. 2016.

[9] V. H. Pham, M. H. Taieb, J. Y. Chouinard, S. Roy, and H. T. Huynh, "On the double Doppler effect generated by scatterer motion," *REV Journal on Electronics and Communications*, vol. 1, pp. 30–37, Mar. 2011.

[10] A. Abdelgawwad and M. Pätzold, "On the influence of walking people on the Doppler spectral characteristics of indoor channels," in *Proc. 28th IEEE Int. Symp. on Personal, Indoor and Mobile Radio Communications, PIMRC 2017*, Montreal, Canada, Oct. 2017.

[11] F. Hlawatsch and G. F. Boudreaux-Bartels, "Linear and quadratic time-frequency signal representations," *IEEE Signal Processing Magazine*, vol. 9, pp. 21–67, Apr. 1992.

[12] J. B. Allen and L. R. Rabiner, "A unified approach to short-time Fourier analysis and synthesis," *Proceedings of the IEEE*, vol. 65, pp. 1558–1564, Nov. 1977.

[13] J. Allen, "Applications of the short-time Fourier transform to speech processing and spectral analysis," in *ICASSP '82. IEEE International Conference on Acoustics, Speech, and Signal Processing*, vol. 7, pp. 1012–1015, May 1982.

[14] L. G. Durand, J. Genest, and R. Guardo, "Modeling of the transfer function of the heart-thorax acoustic system in dogs," *IEEE Transactions on Biomedical Engineering*, vol. BME-32, pp. 592–601, Aug. 1985.

[15] J. Tribolet, "Applications of short-time homomorphic signal analysis to seismic wavelet estimation," *IEEE Transactions on Acoustics, Speech, and Signal Processing*, vol. 26, pp. 343–353, Aug. 1978.

[16] M. Pätzold and C. A. Gutiérrez, "Spectrogram analysis of multipath fading channels under variations of the mobile speed," in *Proc. 84rd IEEE Vehicular Technology Conference, IEEE VTC2016-Fall*, Montreal, Canada, Sept. 2016.

[17] M. Pätzold and C. A. Gutiérrez, "Enhancing the resolution of the spectrogram of non-stationary channels by using massive MIMO techniques," in *Proc. IEEE 86th Vehicular Technology Conference, VTC2017-Fall*, Toronto, Canada, Sep. 2017.

[18] M. Pätzold, C. A. Gutiérrez, and N. Youssef, "On the consistency of non-stationary multipath fading channels with respect to the average Doppler shift and the Doppler spread," in *Proc. IEEE Wireless Communications and Networking Conference, WCNC 2017*, San Francisco, CA, USA, Mar. 2017.

[19] B. Boashash, *Time-Frequency Signal Analysis and Processing – A Comprehensive Reference*. Elsevier, Academic Press, 2nd ed., 2015.

[20] S. U. Jung and M. S. Nixon, "Estimation of 3D head region using gait motion for surveillance video," in *4th International Conference on Imaging for Crime Detection and Prevention 2011, ICDP 2011*, pp. 1–6, London, UK, Nov. 2011. DOI: 10.1049/ic.2011.0105.

[21] T. Oberg, A. Karsznia, and K. Oberg, "Basic gait parameters: reference data for normal subjects, 10-–79 years of age," *Journal of Rehabilitation Research and Development*, vol. 33, no. 2, pp. 210–223, 1993.

[22] G. Wu, "Distinguishing fall activities from normal activities by velocity characteristics," *Journal of Biomechanics*, vol. 33, no. 11, pp. 1497 – 1500, 2000. DOI: https://doi.org/10.1016/S0021-9290(00)00117-2.

Appendix C

Paper C

Title:	A 3D Non-Stationary Cluster Channel Model for Human Activity Recognition
Authors:	Ahmed Abdelgawwad and Matthias Pätzold
Affiliation:	University of Agder, Faculty of Engineering and Science, P. O. Box 509, NO-4898 Grimstad, Norway
Conference:	*2019 IEEE 89th Vehicular Technology Conference (VTC Spring)*, Kuala Lumpur, Malaysia, 2019.
DOI:	10.1109/VTCSpring.2019.8746345.

A 3D Non-Stationary Cluster Channel Model for Human Activity Recognition

Ahmed Abdelgawwad and Matthias Pätzold
Department of Information and Communication Technology
Faculty of Engineering and Science, University of Agder
P.O. Box 509, NO-4898 Grimstad, Norway
E-mails: {ahmed.abdel-gawwad, matthias.paetzold}@uia.no

Abstract **— This paper proposes a three-dimensional (3D) non-stationary fixed-to-fixed indoor channel simulator model for human activity recognition. The channel model enables the formulation of temporal variations of the received signal caused by a moving human. The moving human is modelled by a cluster of synchronized moving scatterers. Each of the moving scatterers in a cluster is described by a 3D deterministic trajectory model representing the motion of specific body parts of a person, such as wrists, ankles, head, and waist. We derive the time-variant (TV) Doppler frequencies caused by the motion of each moving scatterer by using the TV angles of motion, angles of arrival, angles of departure. Moreover, we derive the complex channel gain of the received signal. Furthermore, we analyze the TV Doppler power spectral density of the complex channel gain by using the concept of the spectrogram and present its expression in approximated form. Also, we derive the TV mean Doppler shift and TV Doppler spread from the approximated spectrogram. The accuracy of the results is validated by simulations. The channel simulator is beneficial for the development of activity recognition systems with non-wearable devices as the demand for such systems has increased recently.**

C.1 Introduction

In 2017, according to the United Nations' World Aging Report the number of people age 60 and older was 962 million, which is more than double the 1980 figure [1]. By 2050, the number of over-60s is expected to double from 2017. Also, the number of people age 80 and older is expected to triple from 137 million to 425 million between 2017 and 2050. These figures indicate a high demand for eldercare systems, such as in-home activity recognition systems to classify normal activities such as walking and sitting as well as abnormal activities such as falls.

In the literature, fall detection systems have been developed using wearable inertial measurement units (IMUs) [2] and video surveillance systems [3]. The main drawback of such systems is that the user may forget to wear the sensor or might go outside the coverage area of the video surveillance system. Another disadvantage is that these systems break the privacy of the user. To overcome these drawbacks, radio-frequency-based (RF-based) non-wearable human tracking systems have been introduced by the authors of [4]. Such systems use RF-based sensors that operate by using frequency-modulated carrier waves. These systems track humans by using wave components scattered by their bodies.

The compound Doppler effect caused by moving scatterers has been studied in two-dimensional fixed-to-mobile channels in [3]. The time-variant (TV) Doppler effect caused by moving scatterers has been modelled in F2F non-stationary indoor channels [5, 6], and in 3D non-stationary MIMO channels in [7]. In order to analyze the TV Doppler power spectrum, we use the concept of the spectrogram, which is one of the time-frequency distributions that provides insight into the TV power spectral density of multicomponent signals [8]. It is also used in applications such as fall detection [9, 10], classification of human activities [11], and enables to distinguish between armed and unarmed persons for security and rescue services [12]. The main drawback of the spectrogram is the cross-term that has an impact on its resolution. Contributions have been introduced to overcome this problem in mobile fading channels in [13].

The goal of this paper is to model the influence of different body parts of a walking person on the Doppler power spectrum characteristics of three-dimensional (3D) fixed-to-fixed (F2F) indoor channels. We introduce a 3D non-stationary F2F channel model with fixed scatterers and clusters of synchronized moving scatterers as an extension to the model presented in [6]. An expression of the TV Doppler frequency of each moving scatterer in a cluster is provided in terms of the TV speed, the TV azimuth angles of departure (AAOD), the TV elevation angles of departure (EAOD), the TV azimuth angles of arrival (AAOA), the TV elevation angles of arrival (EAOA), the TV horizontal angles of motion (HAOM), and the TV vertical angles of motion (VAOM). Furthermore, the instantaneous channel phases and the complex channel gain of the 3D non-stationary F2F multipath fading channel are presented. Moreover, an approximation of the spectrogram of the complex channel gain is provided as a sum of

the auto-term and the cross-term. The auto-term gives us an approximation of the true TV Doppler power spectral density of the complex channel gain, while the cross-term is considered as an undesired spectral interference term that reduces the resolution of the spectrogram. The TV mean Doppler shift and the TV Doppler spread are also derived from the spectrogram. The novelty of this paper lies not only in presenting a non-stationary F2F model with fixed scatterers and clusters of moving scatterers, but also in presenting deterministic trajectory models of different body parts of a walking person.

The remaining sections of this paper are divided as follows. Section C.2 discusses a multipath propagation scenario with a fixed transmitter, a fixed receiver, fixed scatterers, and clusters of moving scatterers. Section C.3 derives an exact and approximate solution of the TV Doppler frequencies of the moving scatterers of the clusters, TV channel phases, complex channel gain, TV mean Doppler shift, and TV Doppler spread. Section C.4 presents an approximate solution of the spectrogram. By using the spectrogram, we compute the TV mean Doppler shift and the TV Doppler spread. Section C.5 discusses the numerical results, introduces realistic mathematical trajectory models of the motion of the major body parts of a walking human, and shows the influence of them on the spectrogram, the TV mean Doppler shift, and the TV Doppler spread. Section C.6 summarizes our work and suggests possible ideas for future work.

C

C.2 The 3D Indoor Propagation Scenario

Consider the multipath propagation scenario in Fig. C.1. This scenario consists of a fixed transmitter (T_x), a fixed receiver (R_x), moving persons, and fixed objects. The transmitter and the receiver are located at (x^T, y^T, z^T) and (x^R, y^R, z^R), respectively. Each moving person is modelled by a cluster of synchronized moving scatterers $S^{\mathrm{M}}_{n,m}$ for $n = 1, 2, \ldots, N_m$ and $m = 1, 2, \ldots, N_c$, where N_m is the number of moving scatterers of the mth cluster, and N_c is the number of clusters. Each moving scatterer $S^{\mathrm{M}}_{n,m}$ has a starting position at $\left(x^{\mathrm{M}}_{n,m}, y^{\mathrm{M}}_{n,m}, z^{\mathrm{M}}_{n,m}\right)$. The 3D trajectory of the nth moving scatterer of the mth cluster is described by its TV speed $\mathrm{v}_{n,m}(t)$, TV HAOM $\alpha_{v_{n,m}}(t)$, and TV VAOM $\beta_{v_{n,m}}(t)$. In Fig. C.1, we have stationary objects, such as walls and furniture which are simply modelled as M fixed scatterers S^{F}_m for $m = 1, 2, \ldots, M$. Single bounce scattering and non-line-of-sight (NLOS) conditions are assumed. Moreover, it is assumed that the T_x and R_x are deployed with omnidirectional antennas.

C.3 The Complex Channel Gain

The TV Doppler frequency $f_{n,m}(t)$ caused by the TV speed $\mathrm{v}_{n,m}(t)$, TV HAOM $\alpha_{v_{n,m}}(t)$, TV VAOM $\beta_{v_{n,m}}(t)$, TV AAOD $\alpha^T_{n,m}(t)$, TV EAOD $\beta^T_{n,m}(t)$, TV AAOA $\alpha^R_{n,m}(t)$, and TV EAOA

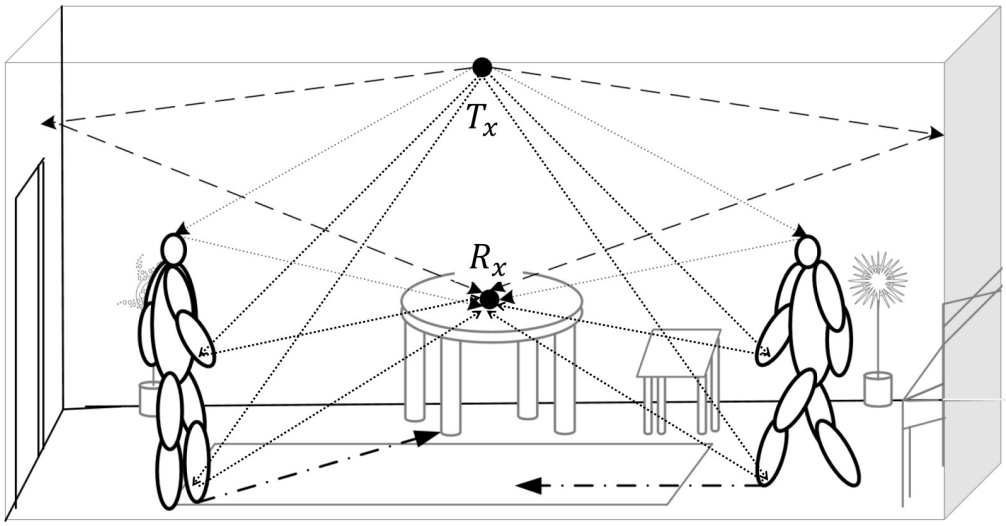

Figure C.1: A 3D non-stationary multipath propagation scenario with moving persons, a fixed transmitter, a fixed receiver, and fixed objects.

$\beta^R_{n,m}(t)$ of the nth moving scatterer $S^{\mathrm{M}}_{n,m}$ of the mth cluster is given by [6]

$$\begin{aligned} f_{n,m}(t) = -f_{n,m,\max}(t) \Big\{ & \cos\left(\beta_{v_{n,m}}(t)\right) \\ & \times \left[\cos\left(\beta^T_{n,m}(t)\right) \cos\left(\alpha^T_{n,m}(t) - \alpha_{v_{n,m}}(t)\right) \right. \\ & \left. + \cos\left(\beta^R_{n,m}(t)\right) \cos\left(\alpha_{v_{n,m}}(t) - \alpha^R_{n,m}(t)\right) \right] \\ & + \sin\left(\beta_{v_{n,m}}(t)\right) \left[\sin\left(\beta^T_{n,m}(t)\right) + \sin\left(\beta^R_{n,m}(t)\right) \right] \Big\} \end{aligned} \tag{C.1}$$

where

$$f_{n,m,\max}(t) = \frac{\mathrm{v}_{n,m}(t)\, f_0}{c}. \tag{C.2}$$

The parameters f_0 and c in (C.2) denote the carrier frequency of the transmitted signal and the speed of light, respectively. The expression in (C.2) represents the maximum Doppler shift caused by the motion speed of the nth moving scatterer $S^{\mathrm{M}}_{n,m}$ of the mth cluster. The expressions of the TV HAOM $\alpha_{v_{n,m}}(t)$, TV VAOM $\beta_{v_{n,m}}(t)$, TV AAOD $\alpha^T_{n,m}(t)$, TV EAOD $\beta^T_{n,m}(t)$, TV AAOA $\alpha^R_{n,m}(t)$, and TV EAOA $\beta^R_{n,m}(t)$ can be found in [6]. The expression of the Doppler frequency $f_{n,m}(t)$ in (C.1) can be approximated by using L piecewise linear functions of time as

$$f_{n,m}(t) \approx f_{n,m,l}(t) = f_{n,m}(t_l) + k_{n,m,l}(t - t_l) \tag{C.3}$$

for $t_l < t \leq t_{l+1}$ and $l = 0, 1, \ldots, L$, where

$$k_{n,m,l} = \frac{f_{n,m}(t_{l+1}) - f_{n,m}(t_l)}{t_{l+1} - t_l}. \tag{C.4}$$

Note that the interval length between two time instances in a row, i.e., $\Delta_l = t_{l+1} - t_l$, is the same for all values of $l = 0, 1, \ldots, L-1$, where L is the number of the time instances at which the Doppler frequencies were approximated. The parameter $k_{n,m,l}$ in (C.4) expresses the rate of change of the Doppler frequency $f_{n,m}(t)$ at time $t = t_l$.

The instantaneous channel phase $\theta_{n,m,\mathrm{M}}(t)$ caused by the motion of the nth moving scatterer of the mth cluster is given by [14]

$$\theta_{n,m,\mathrm{M}}(t) = 2\pi \int_{-\infty}^{t} f_{n,m}(t')dt' = \theta_{n,m,\mathrm{M}} + 2\pi \int_{0}^{t} f_{n,m}(t')dt'. \tag{C.5}$$

The first term in (C.5) is the initial phase shift, which is modelled as a zero-mean random variable with a uniform distribution between $-\pi$ and π. Hence, the instantaneous channel phase $\theta_{n,m,\mathrm{M}}(t)$ in (C.5) is a stochastic process. After obtaining the instantaneous channel phase $\theta_{n,m,\mathrm{M}}(t)$, the complex channel gain $\mu(t)$ consisting of $\sum_{m=1}^{N_\mathrm{C}} N_m + M$ received multipath components is modelled by

$$\mu(t) = \sum_{m=1}^{N_\mathrm{C}} \sum_{n=1}^{N_m} c_{n,m,\mathrm{M}}\, e^{j\theta_{n,m,\mathrm{M}}(t)} + \sum_{m=1}^{M} c_{m,\mathrm{F}}\, e^{j\theta_{m,\mathrm{F}}}. \tag{C.6}$$

The double sum in the first term in (C.6) represents the sum of the multipath components corresponding to N_C clusters and the N_m moving scatterers therein. Each moving scatterer in a cluster has a stochastic channel phase $\theta_{n,m,\mathrm{M}}(t)$, and a constant path gain $c_{n,m,\mathrm{M}}$. The second term in (C.6) designates the sum of the multipath components associated with the M fixed scatterers with constant path gains $c_{m,\mathrm{F}}$ and random phases $\theta_{m,\mathrm{F}}$. It should be noted that the phases $\theta_{n,m,\mathrm{M}}$ and $\theta_{m,\mathrm{F}}$ are modelled as zero-mean random variables with a uniform distribution that ranges from $-\pi$ to π. The complex channel gain $\mu(t)$ in (C.6) is a stochastic model for a 3D non-stationary indoor channel with clusters of moving scatterers, fixed scatterers, fixed transmitter, and fixed receiver. The TV mean Doppler shift and the TV Doppler spread of this model can be expressed as [14]

$$B_f^{(1)}(t) = \frac{\sum\limits_{m=1}^{N_\mathrm{C}} \sum\limits_{n=1}^{N_m} c_{n,m,\mathrm{M}}^2\, f_{n,m}(t)}{\sum\limits_{m=1}^{N_\mathrm{C}} \sum\limits_{n=1}^{N_m} c_{n,m,\mathrm{M}}^2 + \sum\limits_{m=1}^{M} c_{m,\mathrm{F}}^2} \tag{C.7}$$

and

$$B_f^{(2)}(t) = \sqrt{\frac{\sum\limits_{m=1}^{N_\mathrm{C}} \sum\limits_{n=1}^{N_m} c_{n,m,\mathrm{M}}^2\, f_{n,m}^2(t)}{\sum\limits_{m=1}^{N_\mathrm{C}} \sum\limits_{n=1}^{N_m} c_{n,m,\mathrm{M}}^2 + \sum\limits_{m=1}^{M} c_{m,\mathrm{F}}^2} - \left(B_f^{(1)}(t)\right)^2} \tag{C.8}$$

respectively.

C.4 Spectrogram Analysis

The spectrogram $S_\mu(f,t)$ of the complex channel gain $\mu(t)$ is computed in three steps. *Step* 1: we multiply the complex channel gain $\mu(t)$ by a sliding window to obtain the short-time signal. In this paper, we use the Gaussian window function

$$h(t) = \frac{1}{\sqrt{\sigma_w \sqrt{\pi}}} e^{-\frac{t^2}{2\sigma_w^2}} \tag{C.9}$$

where σ_w denotes the window spread parameter. The window function is real and even and has a normalized energy of $\int_{-\infty}^{\infty} h^2(t)dt = 1$. The short-time complex channel gain is given according to [15, Eq. (2.3.1)] by

$$x(t',t) = \mu(t')h(t'-t) \tag{C.10}$$

where the variables t' and t are the running time and the observation time, respectively. Continuing with *Step 2*, we calculate the short-time-Fourier-transform (STFT) by computing the Fourier-transform of the short-time signal $X(t',t)$ w.r.t. the running time t' as follows

$$X(f,t) = \int_{-\infty}^{\infty} x(t',t) e^{-j2\pi f t'} dt'. \tag{C.11}$$

For the sake of brevity, we do not provide the expression for the STFT. Finally, the last step is multiplying the STFT $X(f,t)$ in (C.11) by its complex conjugate to obtain the spectrogram $S_\mu(f,t)$ as

$$S_\mu(f,t) \;=\; |X(f,t)|^2 \;=\; S_\mu^{(a)}(f,t) + S_\mu^{(c)}(f,t) \tag{C.12}$$

where the functions $S_\mu^{(a)}(f,t)$ and $S_\mu^{(c)}(f,t)$ denote the auto-term and the cross-term, respectively. By using the approximate expression of the Doppler frequency $f_{n,m,l}(t)$ in (C.3), the approximate solution of the auto-term $S_\mu^{(a)}(f,t)$ is given by

$$\begin{aligned} S_\mu^{(a)}(f,t) = &\sum_{m=1}^{N_\mathrm{C}} \sum_{n=1}^{N_m} c_{n,m,\mathrm{M}}^2 \, G\left(f, f_{n,m,l}(t), \sigma_{n,m,l,\mathrm{M}}^2\right) \\ &+ \sum_{m=1}^{M} c_{m,\mathrm{F}}^2 \, G\left(f, 0, \sigma_{m,\mathrm{F}}^2\right) \end{aligned} \tag{C.13}$$

for $t_l < t \leq t_{l+1}$ $(l = 0, 1, \cdots, L-1)$, where

$$G(x,\mu,\sigma^2) \;=\; \frac{e^{\frac{-(x-\mu)^2}{2\sigma^2}}}{\sqrt{2\pi\sigma^2}} \tag{C.14}$$

$$\sigma_{n,m,l,\mathrm{M}}^2 \;=\; \frac{1 + \left(2\pi\sigma_w^2 k_{n,m,l}\right)^2}{2(2\pi\sigma_w)^2} \tag{C.15}$$

$$\sigma_{m,\mathrm{F}}^2 \;=\; \frac{1}{2(2\pi\sigma_w)^2}. \tag{C.16}$$

The auto-term $S_{\mu}^{(a)}(f,t)$ given by (C.13) consists of a sum of $\sum_{m=1}^{N_{\mathrm{C}}} N_m + M$ components. It is a real and positive function that represents an approximation of the desired TV Doppler power spectral density of the complex channel gain $\mu(t)$ discussed in Section C.3. The first term of the auto-term $S_{\mu}^{(a)}(f,t)$ in (C.13) is a double sum of weighted Gaussian functions, where each component of this term corresponds to the nth moving scatterer of the mth cluster. Note that the Gaussian functions of the first term of the auto-term $S_{\mu}^{(a)}(f,t)$ are weighted by the squared path gain $c_{n,m,\mathrm{M}}^2$ and centered on the approximated Doppler frequency $f_{n,m,l}(t)$ of the nth moving scatterer of the mth cluster. The second term of the auto-term $S_{\mu}^{(a)}(f,t)$ in (C.13) is also a sum of Gaussian functions factorized by the squared path gain $c_{m,\mathrm{F}}^2$ of each fixed scatterer and centered on the zero-frequency value as a fixed scatterer does not introduce a Doppler shift in F2F channels. The parameters in (C.15) and (C.16) denote the variances of the Gaussian functions presented in (C.13). It should be mentioned that the variance of the Gaussian function in the first term of the auto-term in (C.13) is dependent on the slope of the Doppler frequency $f_{n,m,l}(t)$ given by (C.4). It should also be noted that the auto-term in (C.13) does not depend on the random channel phases $\theta_{n,m,\mathrm{M}}$ and $\theta_{n,\mathrm{F}}$.

The cross-term $S_{\mu}^{(c)}(f,t)$ is presented in (C.19) at the top of the next page. It represents an undesired spectral interference term that reduces the resolution of the spectrogram. The cross-term $S_{\mu}^{(c)}(f,t)$ in (C.19) has $(\sum_{m=1}^{N_{\mathrm{C}}} N_m + M)(\sum_{m=1}^{N_{\mathrm{C}}} N_m + M - 1)/2$ components. It is a real function and can have positive or negative values. Unlike the auto-term $S_{\mu}^{(a)}(f,t)$, the cross-term $S_{\mu}^{(c)}(f,t)$ depends on the random channel phases $\theta_{n,m,\mathrm{M}}$ and $\theta_{n,\mathrm{F}}$. Thus, it can be removed by taking the average of the spectrogram $S_{\mu}(f,t)$ over the phases, i.e., $E\left\{S_{\mu}(f,t)\right\}|_{\theta_{n,m,\mathrm{M}},\theta_{m,\mathrm{F}}} = S_{\mu}^{(a)}(f,t)$. The parameter $\mu_{m,\mathrm{F}}$ (function $\mu_{n,k,\mathrm{M}}(t)$) in (C.19) denotes the complex channel gain of the mth fixed scatterer (nth moving scatterer of the kth cluster). The operators $\Re\{\cdot\}$ and $\{*\}$ in (C.19) compute the real part and the complex conjugate of a complex function, respectively. The parameters $\sigma_{x,n,m,l,\mathrm{M}}^2$ and $\sigma_{x,m,\mathrm{F}}^2$ in (C.19) are given by

$$\sigma_{x,n,m,l,\mathrm{M}}^2 = \frac{1 - j2\pi\sigma_w^2 k_{n,m,l}}{(2\pi\sigma_w)^2} \tag{C.17}$$

$$\sigma_{x,m,\mathrm{F}}^2 = \frac{1}{(2\pi\sigma_w)^2} \tag{C.18}$$

respectively. The TV mean Doppler shift $B_{\mu}^{(1)}(t)$ and the TV Doppler spread $B_{\mu}^{(2)}(t)$ can be obtained by using the spectrogram as follows [5]

$$B_{\mu}^{(1)}(t) = \frac{\int_{-\infty}^{\infty} f S_{\mu}(f,t) df}{\int_{-\infty}^{\infty} S_{\mu}(f,t) df} \tag{C.20}$$

$$S_{\mu}^{(c)}(f,t) = \frac{2}{\sigma_w\sqrt{\pi}}\Re\Bigg\{ \sum_{m=1}^{N_{\mathrm{C}}} \sum_{n=1}^{N_m-1} \sum_{k=n+1}^{N_m} G\left(f, f_{n,m,l}(t), \sigma^2_{x,n,m,l,\mathrm{M}}\right)$$
$$\times G^*\left(f, f_{k,m,l}(t), \sigma^2_{x,k,m,l,\mathrm{M}}\right)\, \mu_{n,m,\mathrm{M}}(t)\, \mu^*_{k,m,\mathrm{M}}(t)$$
$$+ \sum_{n=1}^{M-1} \sum_{m=n+1}^{M} G\big(f, 0, \sigma^2_{x,n,\mathrm{F}}\big) G^*\big(f, 0, \sigma^2_{x,m,\mathrm{F}}\big)\, \mu_{n,\mathrm{F}} \mu^*_{m,\mathrm{F}}$$
$$+ \sum_{m=1}^{N_{\mathrm{C}}} \sum_{n=1}^{N_m} \sum_{k=1}^{M} G\left(f, f_{n,m,l}(t), \sigma^2_{x,n,m,l,\mathrm{M}}\right) G^*\big(f, 0, \sigma^2_{x,k,\mathrm{F}}\big) \mu_{n,m,\mathrm{M}}(t) \mu^*_{k,\mathrm{F}}$$
$$+ \sum_{m=1}^{N_{\mathrm{C}}-1} \sum_{q=k+1}^{N_{\mathrm{C}}} \sum_{n=1}^{N_m} \sum_{k=1}^{N_q} G\left(f, f_{n,m,l}(t), \sigma^2_{x,n,m,l,\mathrm{M}}\right)\, G^*\left(f, f_{k,q,l}(t), \sigma^2_{x,k,q,l,\mathrm{M}}\right)\, \mu_{n,m,\mathrm{M}}(t)\, \mu^*_{k,q,\mathrm{M}}(t) \Bigg\} \tag{C.19}$$

---

and

$$B_{\mu}^{(2)}(t) = \sqrt{\frac{\int_{-\infty}^{\infty} f^2 S_{\mu}(f,t) df}{\int_{-\infty}^{\infty} S_{\mu}(f,t) df} - \left(B_{\mu}^{(1)}(t)\right)^2} \tag{C.21}$$

respectively.

C.5 Numerical Results

In this section, we discuss some numerical results regarding the spectrogram, the TV mean Doppler shift, and the TV Doppler spread.

First, we introduce the trajectory models for the ankles, wrists, trunk (waist), and head of a walking person. The velocities of the right ankle and left ankle along with the x-axis are defined as piecewise functions by

$$v_{x,\mathrm{RA}}(t) = \begin{cases} v_x \left(1 - \cos\left(\frac{2\pi t}{T_{\mathrm{step}}}\right)\right), & \text{if } 0 \leq t \leq T_{\mathrm{step}}, \\ 0, & \text{if } T_{\mathrm{step}} < t \leq 2T_{\mathrm{step}} \end{cases} \tag{C.22}$$

$$v_{x,\mathrm{LA}}(t) = \begin{cases} 0, & \text{if } 0 \leq t \leq T_{\mathrm{step}} \\ v_x \left(1 - \cos\left(\frac{2\pi t}{T_{\mathrm{step}}}\right)\right), & \text{if } T_{\mathrm{step}} \leq t \leq 2T_{\mathrm{step}} \end{cases} \tag{C.23}$$

respectively, where the parameter v_x (T_{step}) stands for the constant speed (step duration). The trajectories of the right ankle and left ankle in the vertical direction, i.e., in the direction

of the z-axis are computed by

$$z_{\mathrm{RA}}(t) = \begin{cases} H_{\mathrm{foot}} \left(1 - \cos(\frac{2\pi t}{T_{\mathrm{step}}}\right), & \text{if } 0 \leq t \leq T_{\mathrm{step}}, \\ 0, & \text{if } T_{\mathrm{step}} < t \leq 2T_{\mathrm{step}} \end{cases} \tag{C.24}$$

$$z_{\mathrm{LA}}(t) = \begin{cases} 0, & \text{if } 0 \leq t \leq T_{\mathrm{step}}, \\ H_{\mathrm{foot}} \left(1 - \cos(\frac{2\pi t}{T_{\mathrm{step}}}\right), & \text{if } T_{\mathrm{step}} < t \leq 2T_{\mathrm{step}} \end{cases} \tag{C.25}$$

respectively, where the parameter H_{foot} represents the maximum displacement of the foot while walking along the z-axis. The ankle models presented in (C.22)–(C.25) were inspired by the ankle model of humanoid robotics provided in [16]. Next, we define the displacements of the right and left wrist in the x-direction as follows

$$x_{\mathrm{RW}}(t) = \frac{v_x t}{2} + x_{\mathrm{w}} \cos\left(\frac{\pi t}{T_{\mathrm{step}}}\right) \tag{C.26}$$

$$x_{\mathrm{LW}}(t) = \frac{v_x t}{2} - x_{\mathrm{w}} \cos\left(\frac{\pi t}{T_{\mathrm{step}}}\right) \tag{C.27}$$

respectively, where the parameter x_{w} denotes the maximum displacement of the wrists. The main reason for using a positive sign in (C.26) and a negative sign in (C.27) is that the displacement in the x-direction of the right (left) wrist is synchronous with the displacement of the left (right) ankle. Note that the period of the cosine functions in (C.26)–(C.27) is twice as long as in (C.22)–(C.23). The displacements in the z-direction of the right and left wrist are the same and calculated by

$$z_{\mathrm{RW}}(t) = z_{\mathrm{LW}}(t) = z_{\mathrm{w}} \cos\left(\frac{2\pi t}{T_{\mathrm{step}}}\right) \tag{C.28}$$

where the parameter z_{w} denotes the maximum vertical displacement of the wrists. It should be mentioned that the displacements of the wrists are out of phase in the x-direction and in phase in the z-direction. The displacements in the x-direction and the z-direction of the head and waist have the same expression, which are given by [17, 18]

$$\begin{aligned} x_{\mathrm{Head}}(t) &= x_{\mathrm{Waist}}(t) = \frac{v_x t}{2} \\ z_{\mathrm{Head}}(t) &= z_{\mathrm{Waist}}(t) = H_{\mathrm{H,W}} \left(1 - \cos\left(\frac{2\pi t}{T_{\mathrm{step}}}\right)\right) \end{aligned} \tag{C.29}$$

respectively, where the parameter $H_{\mathrm{H,W}}$ in (C.29) designates the maximum vertical displacement in the z-direction. When generating the scenario for the walking person, we chose the values of T_{step}, v_x, H_{foot}, x_{w}, z_{w}, and $H_{\mathrm{H,W}}$ to be 1 s, 0.8 m/s, 0.1 m, 0.1 m, 0.025 m, and 0.025 m, respectively. The heights of ankles, wrists, head, and waist were set to 0.1 m, 1 m,

1.7 m, and 1.1 m, respectively. The number of walking steps were chosen to be 10 steps. Fig. C.2 depicts the displacements of the ankles, wrists, head, and waist in the x-direction. A good synchronization is shown in Fig. C.2 between the trajectories of the body parts, i.e., when the right ankle moves a step forward, the left wrist also swings forward, while the right wrist swings backward and the left leg stands on the ground. The forward displacements presented in Fig. C.2 in the x-direction of the ankles were computed by generating 5 piecewise functions of the forward velocities provided by (C.22) and (C.23) for the right ankle and left ankle, respectively. Then, the forward displacement is computed by integrating the forward velocities in (C.22) and (C.23) w.r.t. time t. Fig. C.3 shows a good synchronization between the displacements in the z-direction of the ankles, wrists, head, and waist, i.e., when the person takes a step forward with his right foot, the ankle moves upward in the z-direction until it crosses the left foot and then, it moves downward until it reaches the ground. The head and waist reach the maximum displacement at the time instant, in which the right or left foot reaches the maximum upward displacement. The wrists reach their maximum vertical displacements at the time instant, in which the heels are on the ground.

Fig C.4 depicts the walking scenario of the moving person in 3D. The number of clusters N_{C} was set to 1 and the number of moving scatterers in the cluster N_m was chosen to be 6. We used the same values of the motion parameters mentioned earlier in this section. The only difference is that the horizontal angle of motion $\alpha_{v_{n,m}}(t)$ was set to 15°, i.e., the direction of motion of the body was chosen to be 15°. The locations of the transmitter T_x and the receiver R_x were chosen to be (5.5 m, 2.5 m, 2.25 m) and (5 m, 2.5 m, 2.25 m), respectively. It is supposed that the LOS is blocked.

When computing the spectrogram, we chose the number of fixed scatterers M to be 6. Fig. C.5 depicts the result of the approximation of the spectrogram given by (C.12). The path gains of the moving scatterers and fixed scatterers are given by

$$c_{n,m,\mathrm{M}} = \sqrt{\frac{2\eta}{\sum_{m=1}^{N_{\mathrm{C}}} N_m}} \qquad \text{and} \qquad c_{m,\mathrm{F}} = \sqrt{\frac{2\,(1-\eta)}{M}} \tag{C.30}$$

respectively, where the parameter $\eta \leq 1$ is used for balancing the contribution of the fixed and moving scatterers on the mean power of the complex channel gain $\mu(t)$. Here, the parameter η was set to 0.6. We chose the value of 5.9 GHz for the carrier frequency f_0. The window spread parameter σ_w was set to 0.0335 s. Fig. C.5 shows the influence of the motion of major body parts on the spectrogram of $\mu(t)$. The spectrogram in Fig. C.5 is blurred due to the impact of the cross-term $S_{\mu}^{(c)}(f,t)$. The simulation results of the spectrogram are close to the analytical results, but they are not provided in the paper for brevity. In the simulation, we generated the values of the trajectories for the wrists, ankles, head, and waist in 3D using the mathematical models and their parameters provided earlier in this section. Then, we computed the HAOM $\alpha_{v_{n,m}}(t)$, VAOM $\beta_{v_{n,m}}(t)$, AAOA $\alpha^{R}_{n,m,\mathrm{M}}(t)$, EAOA $\beta^{R}_{n,m,\mathrm{M}}(t)$,

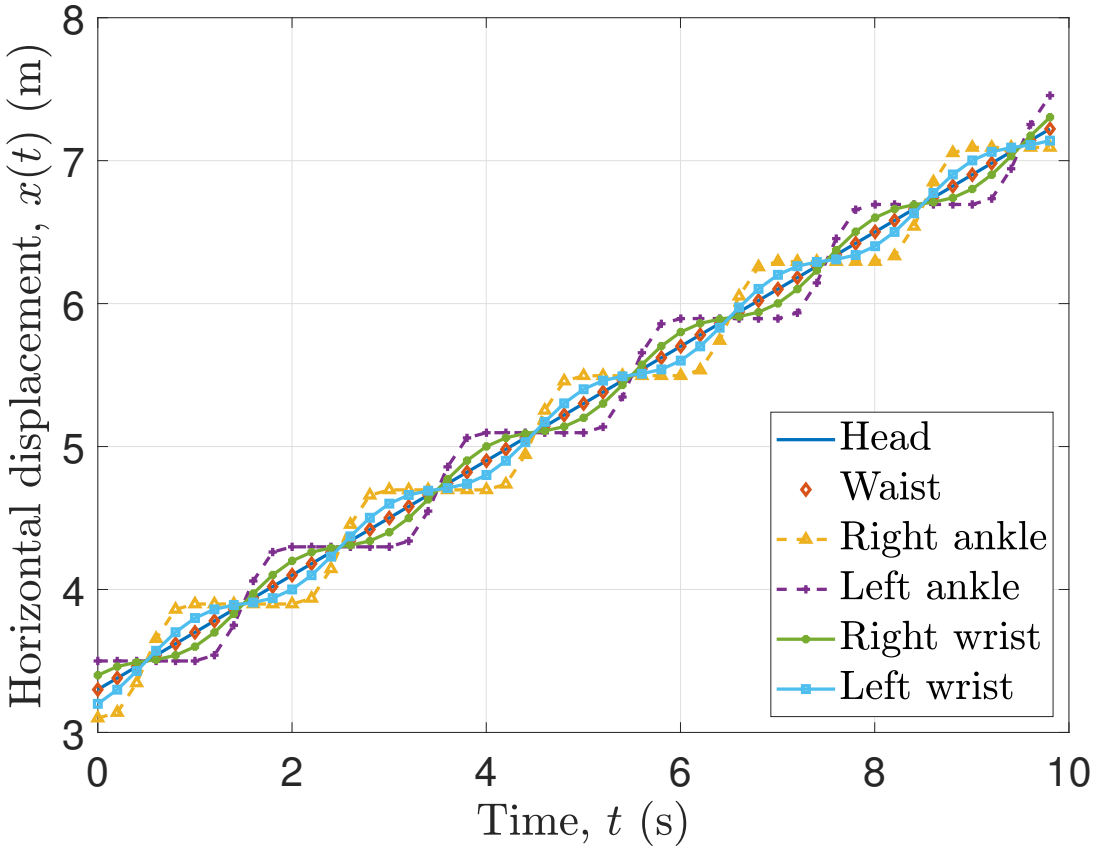

Figure C.2: TV forward displacements in the x-direction $x(t)$ of the 6-point scatterers representing the walking person.

AAOD $\alpha^T_{n,m,\mathrm{M}}(t)$, and EAOD $\beta^T_{n,m,\mathrm{M}}(t)$ from the displacement values and the values of the locations of the transmitter T_x and the receiver R_x. After that, the Doppler frequencies were computed using (C.1) and approximated using (C.3). Next, we integrated the Doppler frequencies of each moving scatterer w.r.t. time t. After that, each one of the integrated Doppler frequencies is added to an outcome of a random generator with a uniform distribution from $-\pi$ to π to obtain the instantaneous channel phase $\theta_{n,m,\mathrm{M}}(t)$ of each moving scatterer according to (C.5). For the fixed multipath components, which are not Doppler shifted, we obtained the associated phases $\theta_{m,\mathrm{F}}$ by generating the outcomes of a random generator with a uniform distribution from $-\pi$ to π for each scatterer. After performing the procedures described above, we obtained the complex channel gain $\mu(t)$ in (C.6). Fig. C.6 visualizes the approximated auto-term $S^{(a)}_{\mu}(f,t)$ of the spectrogram provided by (C.13). It can be shown that the resolution of the spectrogram improves after removing the cross-term by averaging the spectrogram $S_{\mu}(f,t)$ over the random channel phases $\theta_{n,m,\mathrm{M}}$ and $\theta_{m,\mathrm{F}}$. Fig. C.6 shows more clearly the influence of the fixed scatterers and the cluster of the moving scatterers on

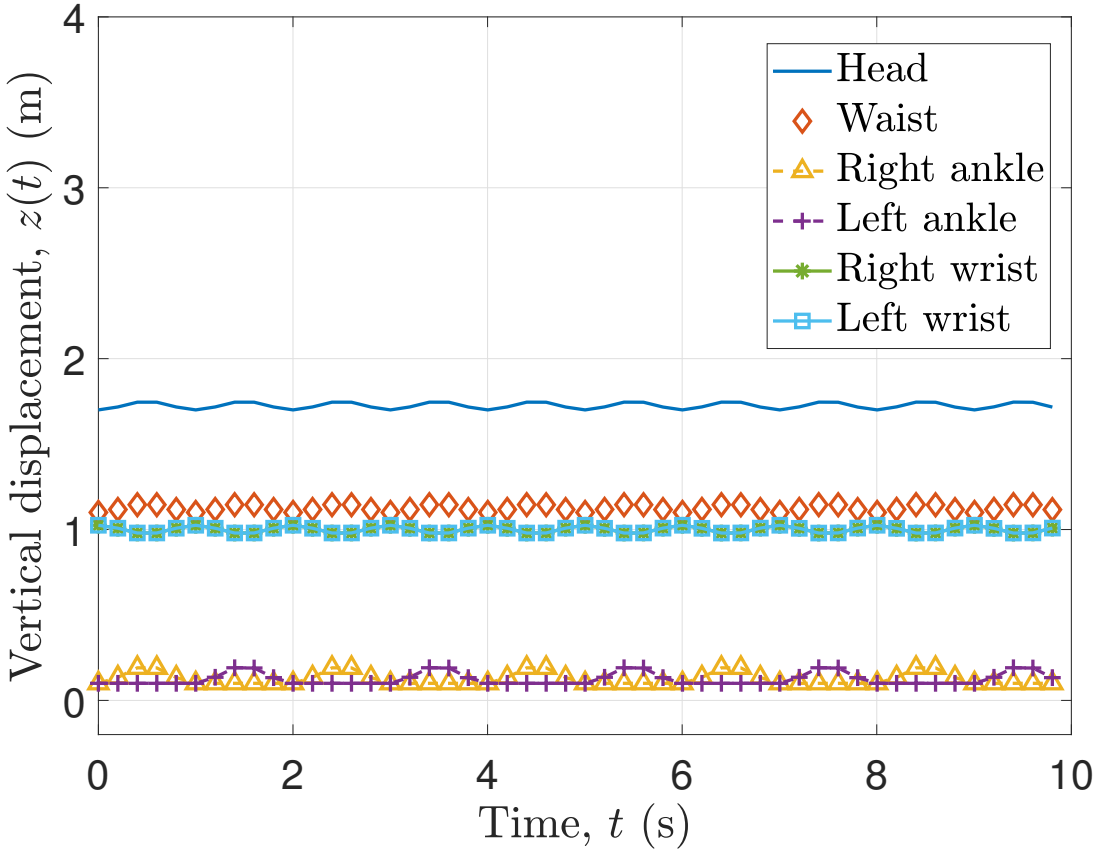

Figure C.3: TV vertical displacements $z(t)$ of the moving scatterers of the walking person.

the spectrogram. Note that the TV Doppler frequencies of the ankles in Fig. C.6 have the highest values that range from -40 Hz to 40 Hz.

Fig. C.7 depicts the TV mean Doppler shifts $B_f^{(1)}(t)$ and $B_\mu^{(1)}(t)$ computed according to (C.7) and (C.20), respectively. The spectrogram of $\mu(t)$ was simulated by using MATLAB. The TV mean Doppler shift $B_\mu^{(1)}(t)$ was computed numerically according to (C.20) using the approximate solution of the spectrogram $S_\mu(f,t)$ in (C.12), the simulated spectrogram, and the approximated auto-term $S_\mu^{(a)}(f,t)$ of the spectrogram in (C.13). It is shown in Fig. C.7 that the TV mean Doppler shifts obtained by using the spectrogram $S_\mu(f,t)$ are affected by the cross-term $S_\mu^{(c)}(f,t)$. There is a good match between the TV mean Doppler shift obtained by using the approximated solution of the spectrogram and the simulated spectrogram. Also, there is a good match between the TV mean Doppler shift $B_f^{(1)}(t)$ computed by (C.7) and the TV mean Doppler shift calculated by (C.20) using the auto-term $S_\mu^{(a)}(f,t)$.

Fig. C.8 depicts the TV Doppler spreads computed according to (C.8) and (C.21). The TV Doppler spread $B_\mu^{(2)}(t)$ was computed numerically according to (C.21) using the approximate solution of the spectrogram $S_\mu(f,t)$ in (C.12), the simulated spectrogram, and the approxi-

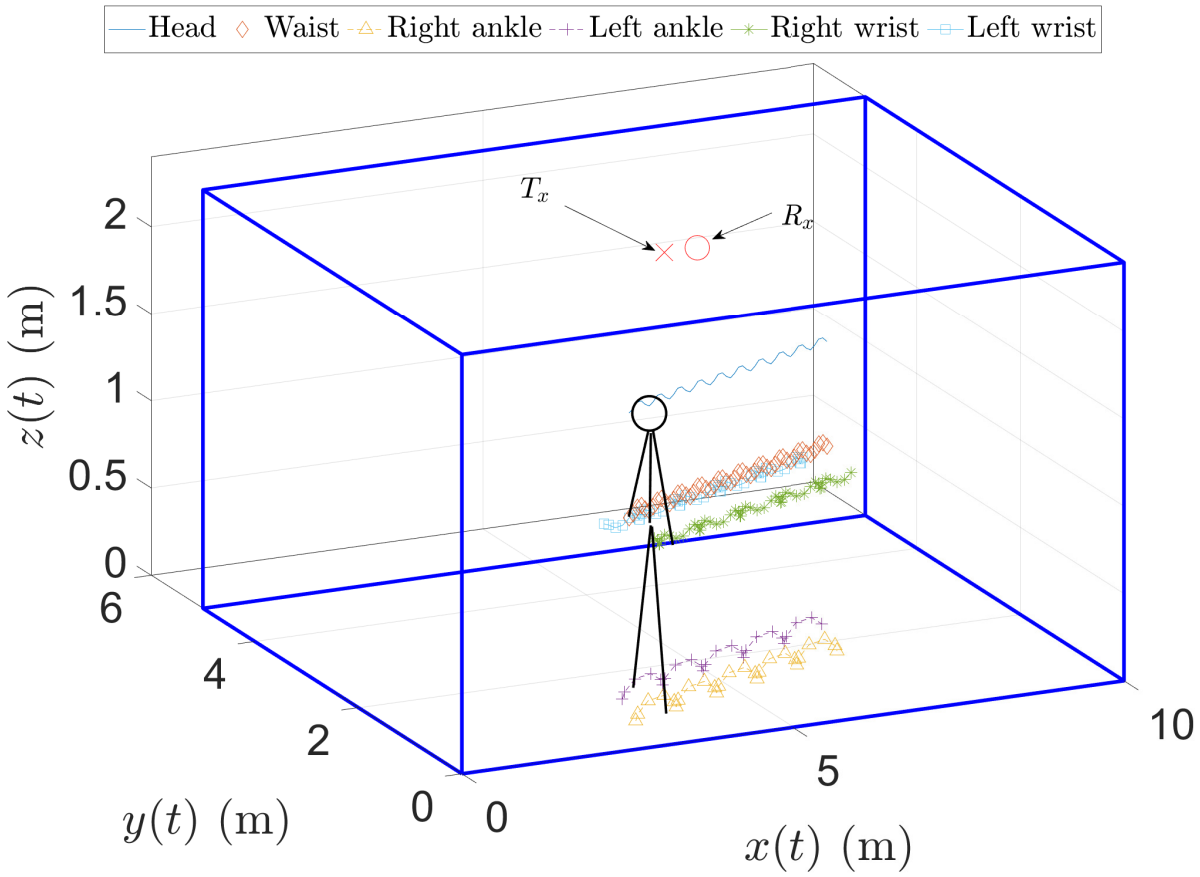

Figure C.4: Simulation scenario and 3D trajectories of the major body parts of a moving person.

mated auto-term $S_{\mu}^{(a)}(f,t)$ of the spectrogram in (C.13). It can be seen in Fig. C.8 that the TV Doppler spread $B_{\mu}^{(2)}(f,t)$ obtained by using the spectrogram $S_{\mu}(f,t)$ is affected by the cross-term $S_{\mu}^{(c)}(f,t)$. There is a good match between the TV Doppler spreads obtained by using the approximated solution of the spectrogram and the simulated spectrogram. The TV Doppler spread $B_{f}^{(2)}(f,t)$ computed by (C.8) and the TV Doppler spread $B_{\mu}^{(2)}(t)$ calculated by (C.21) using the auto-term $S_{\mu}^{(a)}(f,t)$ do not match. This is due to the influence of the variance $\sigma^2_{n,m,l,\mathrm{M}}$ and $\sigma^2_{m,\mathrm{F}}$ in (C.15) and (C.16) on the TV Doppler spread in (C.21), respectively, of the Gaussian functions of the auto-term $S_{\mu}^{(a)}(f,t)$.

C.6 Conclusion

In this paper, we introduced a 3D non-stationary channel model by modelling moving humans as clusters of synchronized moving scatterers to study the impact of major body parts of a walking person on the spectrogram of the complex channel gain of indoor F2F channels. We provided expressions for the TV Doppler frequencies and the TV phases of the

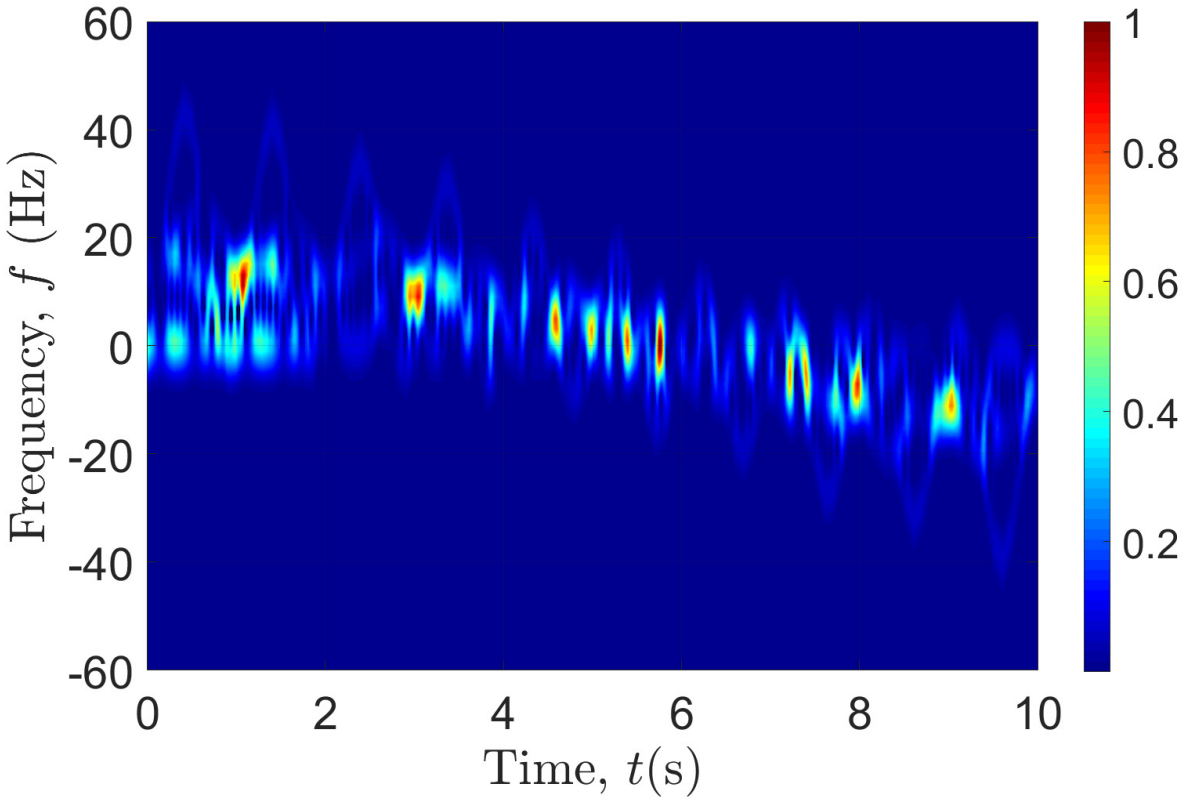

Figure C.5: Spectrogram $S_\mu(f,t)$ (analysis) of the complex channel gain $\mu(t)$.

moving scatterers representing the major body parts. Moreover, we presented mathematical expressions for the complex channel gain and showed the impact of a walking human on the spectrogram, for which an approximate solution has been presented. Furthermore, we presented trajectory models of different body parts of the walking human, such as ankles, wrists, head, and waist. Simulations validated the accuracy of the approximated-form of the spectrogram. For future work, we suggest validating the trajectory models and the channel model presented her in this paper with wearable IMU sensors and RF-measured data, respectively.

C

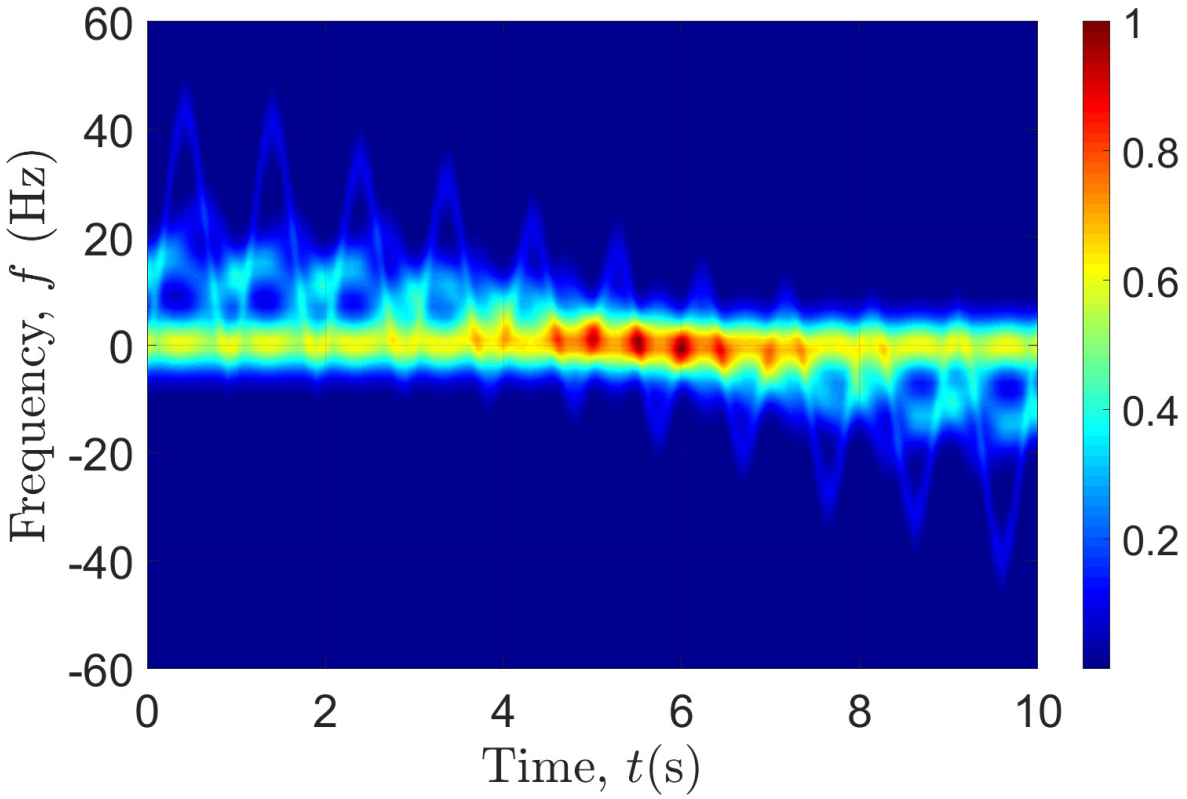

Figure C.6: The auto-term of the spectrogram $S_{\mu}^{(a)}(f,t)$ (analysis) of the complex channel gain $\mu(t)$.

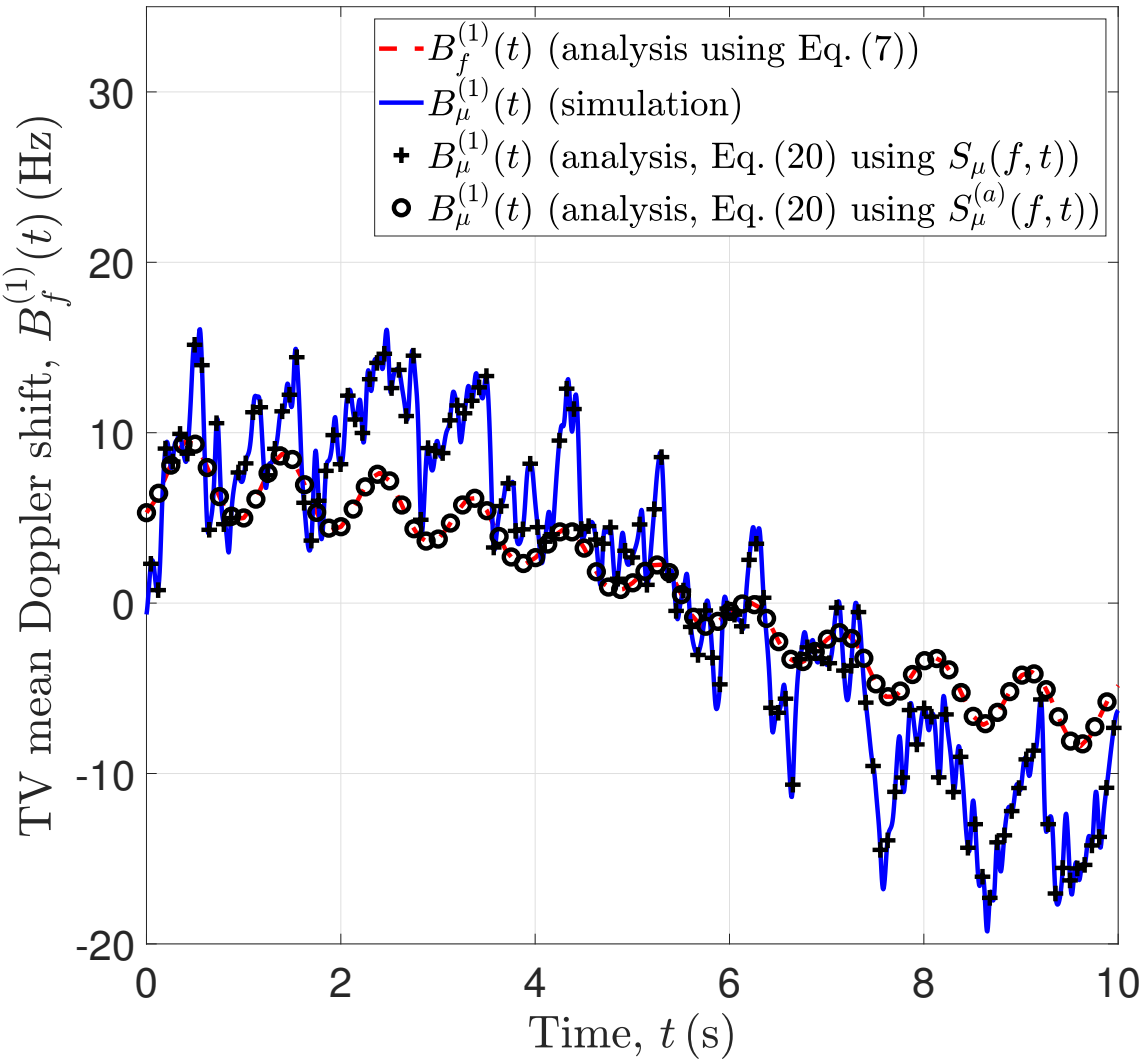

Figure C.7: TV mean Doppler shift according to (C.7) and (C.20).

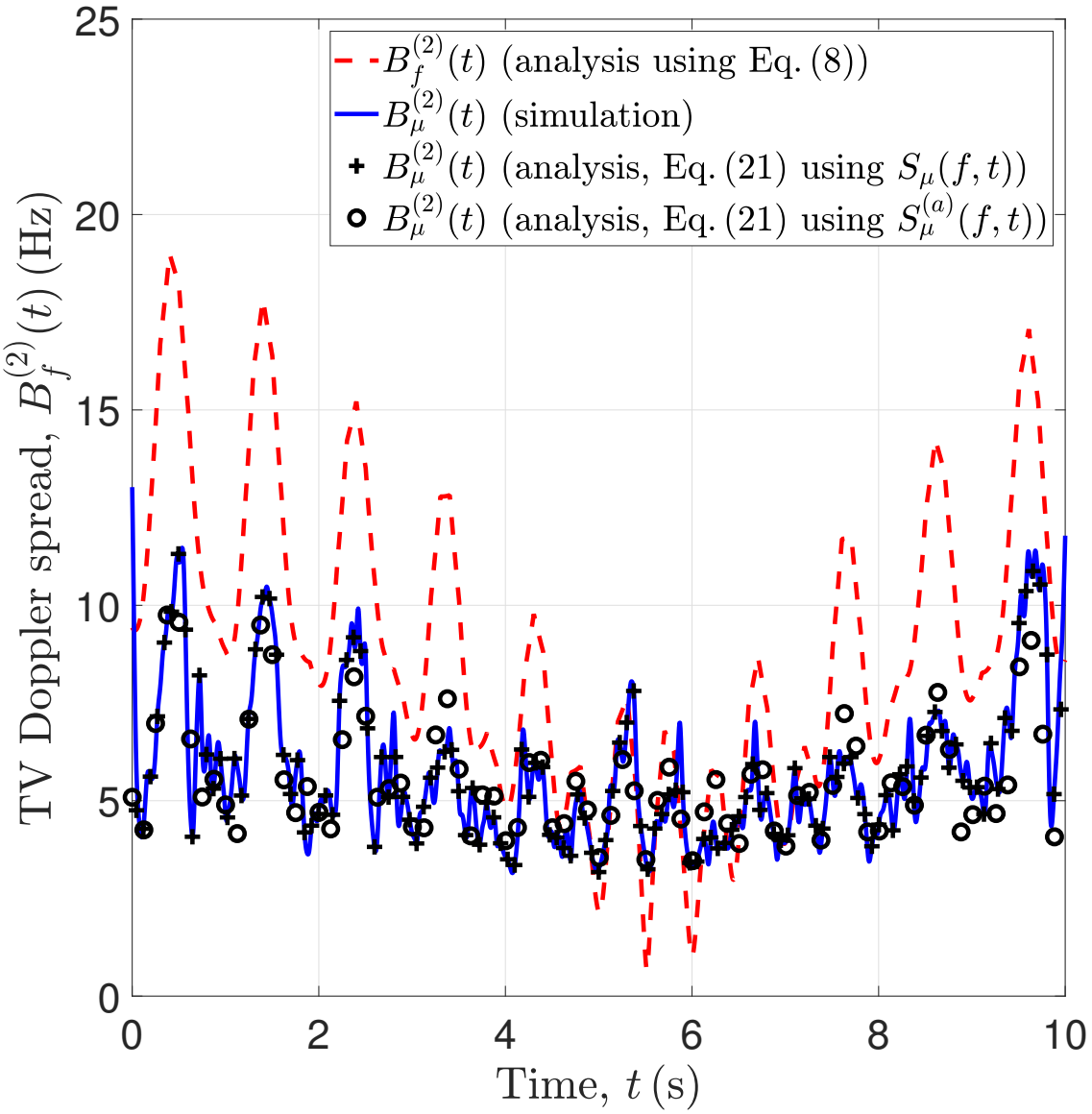

Figure C.8: TV Doppler spread according to (C.8) and (C.21).

Bibliography

[1] United Nations, Department of Economic and Social Affairs, Population Division , "World population ageing," 2017. Highlights (ST/ESA/SER.A/408).

[2] Y. Yan and Y. Ou, "Accurate fall detection by nine-axis IMU sensor," in *IEEE International Conference on Robotics and Biomimetics (ROBIO)*, pp. 854–859, Dec. 2017.

[3] V.-H. Pham, M.-H. Taieb, J.-Y. Chouinard, S. Roy, and H.-T. Huynh, "On the double Doppler effect generated by scatterer motion," *REV Journal on Electronics and Communications*, vol. 1, pp. 30–37, Mar. 2011.

[4] F. Adib, Z. Kabelac, D. Katabi, and R. C. Miller, "3D tracking via body radio reflections," in *Proc. of the 11th USENIX Conference on Networked Systems Design and Implementation NSDI'14*, (Berkeley, CA, USA), pp. 317–329, USENIX Association, 2014.

[5] A. Abdelgawwad and M. Pätzold, "On the influence of walking people on the Doppler spectral characteristics of indoor channels," in *Proc. 28th IEEE Int. Symp. on Personal, Indoor and Mobile Radio Communications, PIMRC 2017*, Montreal, Canada, Oct. 2017.

[6] A. Abdelgawwad and M. Pätzold, "A framework for activity monitoring and fall detection based on the characteristics of indoor channels," in *IEEE 87th Vehicular Technology Conference (VTC Spring)*, Porto, Portugal, Jun. 2018.

[7] J. Bian, C. Wang, M. Zhang, X. Ge, and X. Gao, "A 3-D non-stationary wideband MIMO channel model allowing for velocity variations of the mobile station," in *IEEE International Conference on Communications (ICC)*, pp. 1–6, May 2017.

[8] F. Hlawatsch and G. F. Boudreaux-Bartels, "Linear and quadratic time-frequency signal representations," *IEEE Signal Processing Magazine*, vol. 9, pp. 21–67, Apr. 1992.

[9] G. A. M, Y. D. Zhang, F. Ahmad, and K. C. D. Ho, "Radar signal processing for elderly fall detection: The future for in-home monitoring," *IEEE Signal Processing Magazine*, vol. 33, pp. 71–80, Mar. 2016.

[10] M. Wu, X. Dai, Y. D. Zhang, B. Davidson, M. G. Amin, and J. Zhang, "Fall detection based on sequential modeling of radar signal time-frequency features," in *IEEE International Conference on Healthcare Informatics*, pp. 169–174, Sep. 2013.

[11] Y. Kim and H. Ling, "Human activity classification based on micro-Doppler signatures using a support vector machine," *IEEE Transactions on Geoscience and Remote Sensing*, vol. 47, pp. 1328–1337, May 2009.

[12] F. Fioranelli, M. Ritchie, S.-Z. Gürbüz, and H. Griffiths, "Feature diversity for optimized human micro-Doppler classification using multistatic radar," *IEEE Transactions on Aerospace and Electronic Systems*, vol. 53, pp. 640–654, Apr. 2017.

[13] M. Pätzold and C. A. Gutiérrez, "Enhancing the resolution of the spectrogram of non-stationary channels by using massive MIMO techniques," in *Proc. IEEE 86th Vehicular Technology Conference, VTC2017-Fall*, Toronto, Canada, Sep. 2017.

[14] M. Pätzold, C. A. Gutiérrez, and N. Youssef, "On the consistency of non-stationary multipath fading channels with respect to the average Doppler shift and the Doppler spread," in *Proc. IEEE Wireless Communications and Networking Conference, WCNC 2017*, San Francisco, CA, USA, Mar. 2017.

[15] B. Boashash, *Time-Frequency Signal Analysis and Processing – A Comprehensive Reference*. Elsevier, Academic Press, 2nd ed., 2015.

[16] J. Liu and O. Urbann, "Walking pattern generation involving 3D waist motion for a biped humanoid robot," in *13th International Conference on Control Automation Robotics Vision (ICARCV)*, pp. 462–467, Singapore, Dec. 2014.

[17] J. Carpentier, M. Benallegue, and J.-P. Laumond, "On the centre of mass motion in human walking," *International Journal of Automation and Computing*, vol. 14, pp. 542–551, Oct. 2017.

[18] S.-U. Jung and M.-S. Nixon, "Estimation of 3D head region using gait motion for surveillance video," in *4th International Conference on Imaging for Crime Detection and Prevention 2011, ICDP 2011*, pp. 1–6, London, UK, Nov. 2011. DOI: 10.1049/ic.2011.0105.

Appendix D

Paper D

Title:	Doppler Power Characteristics Obtained from Calibrated Channel State Information for Human Activity Recognition
Authors:	Ahmed Abdelgawwad[1], Andreu Català[2], and Matthias Pätzold[1]
Affiliation:	[1]University of Agder, Faculty of Engineering and Science, P. O. Box 509, NO-4898 Grimstad, Norway [2]Universitat Politècnica de Catalunya (UPC), Rambla de l'Exposició, 59-69, 08800 Vilanova i la Geltrú, Barcelona, Spain
Conference:	*2020 IEEE 91th Vehicular Technology Conference (VTC Spring)*, Antwerp, Belgium, 2020.
DOI:	10.1109/VTC2020-Spring48590.2020.9129187.

Doppler Power Characteristics Obtained from Calibrated Channel State Information for Human Activity Recognition

Ahmed Abdelgawwad[1], Andreu Català[2] , and Matthias Pätzold[1]
[1]Faculty of Engineering and Science, University of Agder,P.O. Box 509, 4898 Grimstad, Norway
[2]Universitat Politècnica de Catalunya (UPC), Rambla de l'Exposició, 59-69, 08800 Vilanova i la Geltrú, Barcelona, Spain
E-mails: [1]{ahmed.abdel-gawwad, matthias.paetzold}@uia.no, [2]andreu.catala@upc.edu

Abstract **— This paper demonstrates the time-variant (TV) Doppler power characteristics of human activities using measured channel state information (CSI). We model the measured CSI as a complex channel transfer function corresponding to a 3D non-stationary multipath fading channel consisting of a fixed transmitter, a fixed receiver, fixed scatterers representing fixed objects, and a cluster of moving scatterers representing a moving person performing some human activities. We demonstrate the relationship between the TV Doppler frequency caused by each moving scatterer and the rate of change of its corresponding TV propagation delay. Furthermore, we express the TV mean Doppler shift in terms of the path gains of the fixed scatterers, the TV path gains, and the TV Doppler frequencies of the moving scatterers. To provide an insight into the TV Doppler power characteristics of the measured calibrated CSI, we employ the spectrogram from which we derive the TV mean Doppler shift. Finally, we present the spectrograms and the TV mean Doppler shifts of the measured calibrated CSI for different human activities. The results show the possibility of designing human activity recognition systems using commercial Wi-Fi devices by employing deep learning or machine learning algorithms.**

Index Terms **— Non-stationary, spectrogram, complex channel transfer function, TV Doppler power characteristics, CSI, human activity recognition.**

D.1 Introduction

According to the statistics in [1], 28.7 % of the adults above 65 years have fall incidents. An increase in mortality and healthcare costs is a consequence of these fall incidents, especially for people aged 75 years or older. According to the United Nations' World Ageing Report [2], the number of adults over 60 is increasing. The number of adults over 80 is expected to rise from 137 million to 425 million between 2017 and 2050. As a result, it is expected that the demand for indoor human activity recognition (HAR) systems will increase. The main role of HAR systems is to distinguish between normal activities and dangerous activities such as falls. One of the types of HAR systems are radio-frequency-based (RF-based) non-wearable systems [3]. Such systems track human activities by using frequency-modulated carrier waves scattered by the major body segments, such as wrists, head, torso, and legs. These scattered waves contain the micro-Doppler characteristics caused by the moving body segments.

The time-variant (TV) compound Doppler effect caused by moving body segments (modelled for simplicity as a cluster of moving scatterers) has been incorporated in 3D channel models by taking into account the TV azimuth angle of motion (AAOM), the elevation angle of motion (EAOM), the azimuth angle of departure (AAOD), the elevation angle of departure (EAOD), the azimuth angle of arrival (AAOA), and the elevation angle of arrival (EAOA) in fixed-to-fixed (F2F) channel models. Such a phenomenon opened up the opportunity for many applications such as HAR [3, 4], detection of gait asymmetry [5], fall detection [6, 7], distinguishing between armed and unarmed humans for security [8], and gesture recognition [9]. Most of these applications are based on applying different machine learning, deep learning, or detection algorithms to the spectrograms of the measured multi-component radar signals. By employing the concept of the spectrogram, which is a time-frequency distribution, an insight into the TV Doppler power characteristics influenced by the moving body segments is revealed.

The authors of [10] introduced a software tool that can capture the channel state information (CSI). Such a tool operates according to the IEEE 802.11n standard [11] and collects data over 30 subcarriers operating in orthogonal-frequency-division-multiplexing (OFDM) mode. When it comes to processing the complex CSI data collected by this tool, one of the main challenges is that the transmitter and the receiver are not clock synchronized [12–14]. Consequently, the phases of the complex CSI data are highly distorted, which makes it impossibile to explore the spectrograms of the complex CSI data. Attempts to overcome this issue have been proposed in [15, 16] by utilizing the principle component analysis or applying linear transformations on the distorted phases. However, these techniques do not contribute to the study of the true TV Doppler characteristics, since they partially or completely eliminate the true phases containing the Doppler shifts caused by the moving scatterers. The authors of [17] successfully eliminated the TV phase distortions by calibrating the transmitter and the receiver stations using a back-to-back (B2B) connection between them. They validated the

proposed method by measurements from a vector network analyzer. They tested the procedure by exploring the TV Doppler power characteristics of a simple hand gesture experiment and validated the results by simulation.

To the best of the authors' knowledge, no one has yet researched the TV Doppler power characteristics of measured calibrated CSI with B2B connection for human activities, such as walking, falling, etc. All the studies in the literature regarding the CSI were either on the amplitude or the distortion-eliminated phases through linear transformations. The main goal of this paper is to present some measurement results of calibrated CSI with B2B connection for some human activities. First, we model the channel transfer function (CTF) of a 3D non-stationary F2F channel and the TV Doppler frequencies caused by the moving scatterers. We elaborate on the relationship between the TV Doppler frequencies and the TV propagation delays. Then, we discuss the spectrogram of the presented channel model associated with each subcarrier and illustrate how the TV mean Doppler shift can be obtained from the spectrogram. Finally, we explore the spectrogram and the TV mean Doppler shift of the measured calibrated CSI for some human activities. The results of this paper are important for getting a better understanding of the influence of the channel parameters on the spectral characteristics of the channels in the presence of a moving person.

The rest of this paper is divided as follows. Section D.2 presents a model for the complex CTF and the TV Doppler shift caused by human activities. The spectrogram of the presented model and the computation of the TV mean Doppler shift from the spectrogram are discussed in Section D.3. Section D.4 demonstrates the measurement scenario, processing the CSI, the spectrogram of the measured CSI, and the analysis of the measured TV mean Doppler shift. Section D.5 gives concluding remarks and directions for future work.

D.2 Modelling the CTF

In this paper, we consider the scenario depicted in Fig. D.1. We have a fixed Wi-Fi transmitter T_x and a fixed Wi-Fi receiver R_x located at $(x^T,\, y^T,\, z^T)$ and $(x^R,\, y^R,\, z^R)$, respectively. The scenario shows a moving person whose major body segments are modelled for simplicity by a cluster of $\mathcal{N}$ moving point scatterers $S_{\mathrm{M},n}$ for $n = 1, 2, \ldots, \mathcal{N}$. The fixed point scatterers $S_{\mathrm{F},m}$ ($m = 1, 2, \ldots, \mathcal{M}$) in Fig. D.1 simply represent $\mathcal{M}$ fixed objects such as walls, furniture, etc. Each moving point scatterer is characterized by its TV displacement $(x_{\mathrm{M},n}(t),\, (y_{\mathrm{M},n}(t),\, (z_{\mathrm{M},n}(t))$. The TV Euclidean distance between T_x (R_x) and the nth moving scatterer is denoted by $d^T_{\mathrm{M},n}(t)$ ($d^R_{\mathrm{M},n}(t)$). Single-bounce scattering is assumed, i.e., each wave launched from the T_x is scattered only once by either a fixed scatterer $S_{\mathrm{F},m}$ or a moving scatterer $S_{\mathrm{M},n}$ before arriving at the R_x.

The TV Euclidean distance $d^T_{\mathrm{M},n}(t)$ between the transmitter T_x and the nth moving scatterer $S_{\mathrm{M},n}$ is expressed in terms of the TV position of $S_{\mathrm{M},n}$ and the fixed position of T_x by

$$d^T_{\mathrm{M},n}(t) \;=\; \sqrt{(x_{\mathrm{M},n}(t) - x^T)^2 + (y_{\mathrm{M},n}(t) - y^T)^2 + (z_{\mathrm{M},n}(t) - z^T)^2}. \tag{D.1}$$

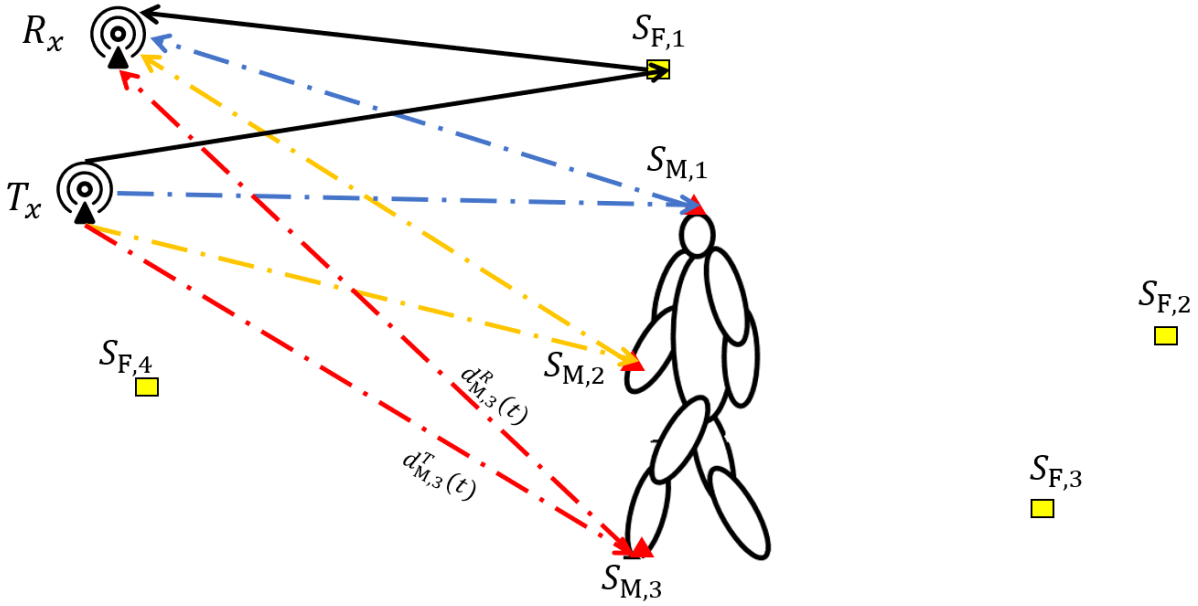

Figure D.1: Propagation scenario consisting of a fixed transmitter T_x, fixed receiver R_x, a moving person modelled by a cluster of $\mathcal{N}$ moving scatterers $S_{\mathrm{M},n}$, and $\mathcal{M}$ fixed scatterers $S_{\mathrm{F},m}$.

Similarly, the Euclidean distance $d^R_{\mathrm{M},n}(t)$ between the receiver R_x and the nth moving scatterer $S_{\mathrm{M},n}$ is given by

$$d^R_{\mathrm{M},n}(t) = \sqrt{(x_{\mathrm{M},n}(t) - x^R)^2 + (y_{\mathrm{M},n}(t) - y^R)^2 + (z_{\mathrm{M},n}(t) - z^R)^2}. \tag{D.2}$$

Using the expressions in (D.1) and (D.2), the total TV propagation delay $\tau_{\mathrm{M},n}(t)$ of the wave travelled from T_x via $S_{\mathrm{M},n}$ to R_x is determined by

$$\tau_{\mathrm{M},n}(t) = \frac{d^T_{\mathrm{M},n}(t) + d^R_{\mathrm{M},n}(t)}{c_0} \tag{D.3}$$

where the parameter c_0 indicates the speed of light.

The complex TV CTF of the 3D non-stationary F2F channel model can be expressed as

$$H\left(t, \Delta f^{(q)}\right) = \sum_{n=1}^{\mathcal{N}} c^{(q)}_{\mathrm{M},n}(t)\, e^{j\left[\theta_{\mathrm{M},n} - 2\pi\left(f_0 + \Delta f^{(q)}\right)\tau_{\mathrm{M},n}(t)\right]} + \sum_{m=1}^{\mathcal{M}} c_{\mathrm{F},m}\, e^{j\left[\theta_{\mathrm{F},m} - 2\pi\left(f_0 + \Delta f^{(q)}\right)\tau_{\mathrm{F},m}\right]}. \tag{D.4}$$

The parameter $\Delta f^{(q)}$ in (D.4) denotes the subcarrier frequency, which is associated with the qth subcarrier according to

$$\Delta f^{(q)} = q \cdot \Delta \tag{D.5}$$

for $q = -28, -26, \ldots, -2, -1, 1, 3, \ldots, 27, 28$. The parameter Δ in (D.5) designates the difference between the subcarrier frequencies, which has a constant value of 312.5 kHz [11]. The first term in (D.4) denotes the sum of multipath components corresponding to the $\mathcal{N}$ moving scatterers. Each component of the first term in (D.4) is characterized by a constant phase shift $\theta_{\mathrm{M},n}$, a TV propagation delay $\tau_{\mathrm{M},n}(t)$, and a TV path gain $c^{(q)}_{\mathrm{M},n}(t)$, which are associated with the nth moving scatterer $S_{\mathrm{M},n}$. The TV path gain $c^{(q)}_{\mathrm{M},n}(t)$ depends on the gains of T_x and R_x antennas, the propagation distances $d^{T}_{\mathrm{M},n}(t)$ and $d^{R}_{\mathrm{M},n}(t)$, the transmission power, the wavelength of the qth subcarrier $c_0/(f_0 + \Delta f^{(q)})$ [18], and the radar cross-section [19]. The second term in (D.4) denotes the sum of multipath components of the $\mathcal{M}$ fixed scatterers. Each component corresponding to the mth fixed scatterer is characterized by a path gain $c_{\mathrm{F},m}$ and a phase shift $\theta_{\mathrm{F},m}$ due to the interaction with the fixed scatterer. In the simulation, the phases $\theta_{\mathrm{M},n}$ and $\theta_{\mathrm{F},m}$ are the outcomes of identically and independently distributed random variables with a uniform distribution over $-\pi$ and π [20, P. 36].

The Doppler shift $f^{(q)}_n(t)$ associated with the qth subcarrier caused by the nth moving scatterers can be expressed using the relationship $f^{(q)}_n(t) = -(f_0 + \Delta f^{(q)})\dot{\tau}_{\mathrm{M},n}(t)$, which can be found in [21, Eq. (22)] as

$$f^{(q)}_n(t) \;\; = -f^{(q)}_{n,\max}(t)\gamma_n(t)\,. \tag{D.6}$$

The function $f^{(q)}_{n,\max}(t)$ denotes the maximum Doppler shift of the qth subcarrier.

$$f^{(q)}_{n,\max}(t) = \frac{\left(f_0 + \Delta f^{(q)}\right)\mathrm{v}_n(t)}{c_0} \tag{D.7}$$

and $\gamma_n(t)$ is given by

$$\begin{aligned}\gamma_n(t) = &\cos\left(\beta_{v_n}(t)\right)\Big[\cos\left(\beta^T_n(t)\right)\cos\left(\alpha^T_n(t) - \alpha_{v_n}(t)\right) + \cos\left(\beta^R_n(t)\right)\cos\left(\alpha_{v_n}(t) - \alpha^R_n(t)\right)\Big] \\ &+ \sin\left(\beta_{v_n}(t)\right)\Big[\sin\left(\beta^T_n(t)\right) + \sin\left(\beta^R_n(t)\right)\Big].\end{aligned} \tag{D.8}$$

The functions $\mathrm{v}_n(t)$, $\beta_{v_n}(t)$, $\alpha_{v_n}(t)$, $\alpha^T_n(t)$, $\beta^T_n(t)$, $\alpha^R_n(t)$, and $\beta^R_n(t)$ in (D.7) and (D.8) designate the TV speed of the nth moving scatterer, the TV elevation angle of motion (EAOM), the TV azimuth angle of motion (AAOM), the TV azimuth angle of departure (AAOD), the TV elevation angle of departure (EAOD), the TV azimuth angle of arrival (AAOA), and the TV elevation angle of arrival (EAOA), respectively. More details about these expressions can be found in [22]. The proof of the relationship between the Doppler frequency $f^{(q)}_n(t)$ and the propagation delay $\tau_{\mathrm{M},n}(t)$ can be found in [21]. Note that the function $\gamma_n(t)$ scales the maximum Doppler shift $f_{n,\max}(t)$. The function can be positive or negative depending on the movement of the moving scatterer $S_{\mathrm{M},n}$ relative to the T_x and R_x. If the moving scatterer $S_{\mathrm{M},n}$ moves away from T_x and R_x, its corresponding TV propagation delay $\tau_{\mathrm{M},n}(t)$ increases, i.e., its rate of change with respect to time $\dot{\tau}_{\mathrm{M},n}(t)$ and $\gamma_n(t)$ have positive values.

Hence, according to (D.6), the Doppler frequency $f_n^{(q)}(t)$ has negative values. If the moving scatterer $S_{\mathrm{M},n}$ moves towards T_x and R_x, its corresponding TV propagation delay $\tau_{\mathrm{M},n}(t)$ decreases, and thus, its rate of change with respect to time $\dot{\tau}_{\mathrm{M},n}(t)$ and $\gamma_n(t)$ have negative values. Hence, according to (D.6), the Doppler frequency $f_n^{(q)}(t)$ is larger than zero. The TV mean Doppler shift $B_{f^{(q)}}^{(1)}(t)$ of the presented model in (D.4), associated with the qth subcarrier, can be computed in terms of the path gains $c_{\mathrm{M},n}^{(q)}(t)$ and $c_{\mathrm{F},m}$, and the Doppler frequency $f_n^{(q)}(t)$ as [21]

$$B_{f^{(q)}}^{(1)}(t) = \frac{\sum\limits_{n=1}^{\mathcal{N}} \left(c_{\mathrm{M},n}^{(q)}(t)\right)^2 f_n^{(q)}(t)}{\sum\limits_{n=1}^{\mathcal{N}} \left(c_{\mathrm{M},n}^{(q)}(t)\right)^2 + \sum\limits_{m=1}^{\mathcal{M}} c_{\mathrm{F},m}^2}. \tag{D.9}$$

The expression in (D.9) is the first-order spectral moment which provides the average Doppler shift of the model presented in (D.4) as a sum of the Doppler shifts $f_n^{(q)}(t)$ caused by the moving scatterers $S_{\mathrm{M},n}$ multiplied by their corresponding path gains $c_{\mathrm{M},n}^{(q)}(t)$ and normalized by the sum of the squared path gains of the fixed and moving scatterers. Note that the mean Doppler shift $B_{f^{(q)}}^{(1)}(t)$ in (D.9) is influenced by the path gains of the moving scatterers $c_{\mathrm{M},n}^{(q)}(t)$ and those corresponding to the fixed scatterers $c_{\mathrm{F},m}$. If the path gains of the fixed scatterers $c_{\mathrm{F},m}$ have high values in comparison to those of the moving scatterers $c_{\mathrm{M},n}^{(q)}(t)$, the TV mean Doppler shift $B_{f^{(q)}}^{(1)}(t)$ in (D.9) has small values that approach zero. This can happen in practice if the person moves too far from T_x/R_x. For measured channels, the expression in (D.9) cannot be used, but there is an alternative to estimate it by utilizing the spectrogram, which will be discussed in the next section.

D.3 Spectrogram of the CTF

To compute the spectrogram, an even and positive window function is needed. In this paper, we used the Gaussian window function $w(t)$ given by

$$w(t) = \frac{1}{\sqrt{\sigma_w \sqrt{\pi}}} e^{-\frac{t^2}{2\sigma_w^2}} \tag{D.10}$$

where σ_w denotes the Gaussian window spread parameter. Choosing the value of such a parameter is a trade-off between the frequency resolution and the time localization. If the window spread σ_w is large, the frequency resolution is high, but the time localization is low, and vice versa. Note that the window function has normalized energy, i.e., $\int_{-\infty}^{\infty} w^2(t) = 1$.

After choosing the window function, the spectrogram can be computed in three steps. The first step is to compute the short-time CTF $x^{(q)}(t', t)$ which is obtained by multiplying

the sliding window $w(t'-t)$ with the CTF $H(t', \Delta f^{(q)})$, i.e.,

$$x^{(q)}(t', t) = H\left(t', \Delta f^{(q)}\right) w\left(t' - t\right) \tag{D.11}$$

where the parameters t' and t designate the running time and the local time, respectively. The second step is to compute the short-time Fourier-transform (STFT) $X^{(q)}(f, t)$ by transforming the running time t' to frequency f. The STFT of $H(t', \Delta f^{(q)})$ associated with the qth subcarrier is given by

$$X^{(q)}(f, t) \;=\; \int_{-\infty}^{\infty} x(t', t) e^{-j2\pi f t'} dt' = \sum_{n=1}^{\mathcal{N}} X_{\mathrm{M},n}^{(q)}(f, t) + \sum_{m=1}^{\mathcal{M}} X_{\mathrm{F},m}^{(q)}. \tag{D.12}$$

The first and second terms in (D.12) denote the sum of the STFTs corresponding to the $\mathcal{N}$ moving scatterers and the sum of the STFTs corresponding to the $\mathcal{M}$ fixed scatterers, respectively. The last step is to compute the spectrogram $S_{H^{(q)}}(f, t)$ associated with the qth subcarrier by multiplying the STFT in (D.12) with its complex conjugate, which results in

$$S_{H^{(q)}}(f, t) = |X^{(q)}(f, t)|^2 = S_{H^{(q)}}^{(a)}(f, t) + S_{H^{(q)}}^{(c)}(f, t) \tag{D.13}$$

where the functions $S_{H^{(q)}}^{(a)}(f, t)$ and $S_{H^{(q)}}^{(c)}(f, t)$ indicate the auto-term and the cross-term of the spectrogram, respectively. The auto-term $S_{H^{(q)}}^{(a)}(f, t)$ provides insight into the true TV Doppler power characteristics. It is determined by

$$S_{H^{(q)}}^{(a)}(f, t) = \sum_{n=1}^{\mathcal{N}} \left| X_{\mathrm{M},n}^{(q)}(f, t) \right|^2 + \sum_{m=1}^{\mathcal{M}} \left| X_{\mathrm{F},m}^{(q)} \right|^2. \tag{D.14}$$

The first term in (D.14) denotes the superposition of the auto-terms caused by the $\mathcal{N}$ moving scatterers, whereas the second term in (D.14) designates the sum of the auto-terms corresponding to the $\mathcal{M}$ fixed scatterers, i.e., the auto-term consists of $\mathcal{N} + \mathcal{M}$ components. Each component of the first (second) term in (D.14) has the Doppler power characteristics corresponding to the nth moving (mth fixed) scatterer $S_{\mathrm{M},n}$ ($S_{\mathrm{F},m}$). The cross-term $S_{H^{(q)}}^{(c)}(f, t)$ is expressed by (D.15), which can be found at the top of the next page. This term consists of $(\mathcal{N} + \mathcal{M})(\mathcal{N} + \mathcal{M} - 1)/2$ components. The operators $\{\cdot\}^*$ and $\Re\{\cdot\}$ represent the conjugate and the real value operators, respectively. This cross-term in (D.15) represents the undesired spectral interference components that reduce the resolution of the spectrogram. The first term of the cross-term $S_{H^{(q)}}^{(c)}(f, t)$ represents the sum of the spectral interference terms between two different moving scatterers, whereas the second term consists of the sum of the spectral interference terms between two different fixed scatterers. The last term in (D.15) denotes the sum of the spectral interference terms between moving and fixed scatterers. An approximate solution of the spectrogram $S_{H^{(q)}}(f, t)$ of the channel model when using a Gaussian window can be found in [22] by approximating the Doppler frequencies $f_n^{(q)}(t)$ into linear piecewise

$$S^{(c)}_{H^{(q)}}(f,t) = 2\Re\Bigg[\sum_{n=1}^{\mathcal{N}-1}\sum_{i=n+1}^{\mathcal{N}} X^{(q)}_{\mathrm{M},n}(f,t)X^{*(q)}_{\mathrm{M},i}(f,t) + \sum_{m=1}^{\mathcal{M}-1}\sum_{i=m+1}^{\mathcal{M}} X^{(q)}_{\mathrm{F},m}X^{*(q)}_{\mathrm{F},i} + \sum_{n=1}^{\mathcal{N}}\sum_{i=1}^{\mathcal{M}} X^{(q)}_{\mathrm{M},n}(f,t)X^{*(q)}_{\mathrm{F},i}\Bigg] \tag{D.15}$$

functions. In theory, the cross-term can be eliminated by averaging the spectrogram $S_{H^{(q)}}(f,t)$ over the random phases $\theta_{\mathrm{M},n}$ and $\theta_{\mathrm{F},m}$, i.e., $\mathbf{E}\{S_{H^{(q)}}(f,t)\}|_{\theta_{\mathrm{M},n},\theta_{\mathrm{F},m}} = S^{(a)}_{H^{(q)}}(f,t)$. In practice, however, the cross-term cannot be removed because of the limited number of available snapshot measurements.

From the spectrogram $S_{H^{(q)}}(f,t)$, the TV mean Doppler shift can be computed as

$$B^{(1)}_{H^{(q)}}(t) = \frac{\int_{-\infty}^{\infty} f S_{H^{(q)}}(f,t)df}{\int_{-\infty}^{\infty} S_{H^{(q)}}(f,t)df}. \tag{D.16}$$

The expression in (D.16) can be applied to both, simulation and measurements. Note that the expression in (D.16) is influenced by the cross-term $S_{H^{(q)}}(f,t)$. If the auto-term $S^{(a)}_{H^{(q)}}(f,t)$ is used in the simulation instead of the spectrogram $S_{H^{(q)}}(f,t)$, then the TV mean Doppler shifts $B^{(1)}_{H^{(q)}}(t)$ and $B^{(1)}_{f^{(q)}}(t)$ become equal [23] when computing the TV mean Doppler shift in (D.16).

D.4 Experimental Results

In this section, the spectrograms of the measured CSI for different human activities, and their corresponding TV mean Doppler shifts will be explored. The measurement scenario will be discussed first. Then, the steps for calibrating and processing the CSI data will be described. Finally, the measurement results will be discussed.

D.4.1 Measurement Scenario

A pair of horn antennas YE572113-30SMAM from Laird™ were used as T_x and R_x antenna. They had the same location and the same height, which was 0.8 m. A 22-year-old male candidate with a height of 1.8 m and a weight of 76 kg, was asked to perform some activities while collecting the CSI data. Fig. D.2 illustrates the measurement scenario and the locations corresponding to the activities done by the candidate. The candidate was asked to carry out the following activities:

- *Falling away*: The candidate stood 4 m away from the T_x and R_x and fell in their opposite direction onto a 15 cm high mattress.
- *Falling towards*: The candidate stood 4 m away from the T_x and R_x and fell in the direction towards them onto a 15 cm high mattress.
- *Walking away*: The candidate stood a few centimeters away from the T_x and R_x and walked 4 m away from them.
- *Walking towards*: The candidate stood 4 m away from the T_x and R_x and walked towards them until they were reached.
- *Sitting*: The candidate stood 4 m away from the T_x and R_x, facing them and then sat down on a chair.
- *Bending and straightening*: The candidate stood 4 m away from the T_x and R_x, facing them and then bent forward towards them picking an imaginary object from the floor and then straightening up again.

The candidate did not move after finishing each activity.

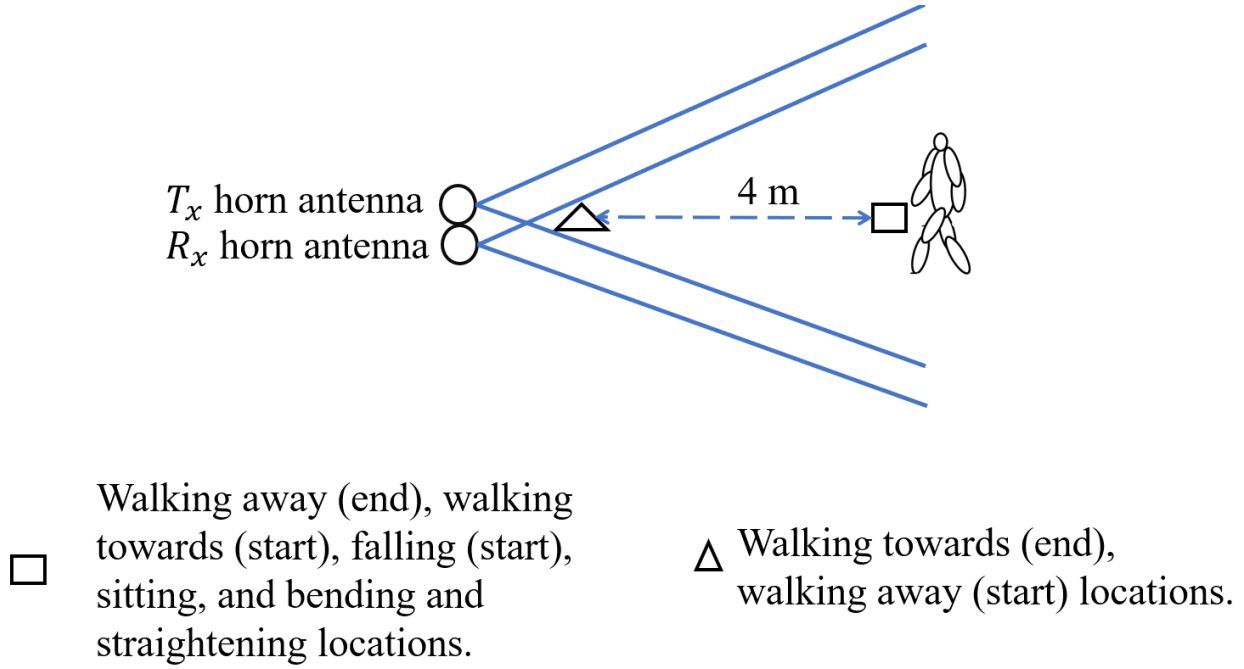

Figure D.2: CSI measurement scenario.

D.4.2 Processing CSI Data

In order to collect RF data, we used two HP Elitebook 6930p laptops equipped with Intel NIC5300. Both laptops had Ubuntu 14.04 LTS operating system, and CSI tool [10] installed. One of the laptops was connected to the T_x antenna, while the other was connected to the R_x antenna. The T_x laptop was working in injector mode, and the R_x laptop was working in monitor mode. Channel 149 was used for recording the CSI data, i.e., the carrier frequency f_0 was chosen to be 5.745 GHz. The bandwidth was set to 20 MHz. The sampling frequency f_s was set to 1 kHz. To overcome the TV phase distortions due to the clock-asynchronization between the T_x and the R_x stations, a B2B connection was employed as illustrated in [17]. To setup the B2B connection, an RF power splitter ZFSC-2-10G+ with one input and two output ports, 4 RF cables 141-1MSM+, and a 30 dB attenuator from Mini-Circuits® were utilized. The transmission port of the T_x laptop was connected to the input port of the splitter via an RF cable. For the two output ports of the splitter, one of them was connected to the T_x horn antenna and the other was connected to the attenuator, and then, to one of the RF ports of the R_x laptop using an RF cable. One of the remaining ports of the R_x laptop was used to connect to the R_x horn antenna through an RF cable.

The captured CSI data were stored on two matrices. One of them contained the CTF corresponding to the B2B connection. This matrix had the TV phase distortions. The other matrix contained the CTF corresponding to the R_x antenna and the TV phase distortions. This matrix had channel characteristics and the TV phase distortions. MATLAB 2019b was used for processing the CSI data. The matrix corresponding to the R_x antenna was divided by the matrix corresponding to the B2B connection in elementwise form and stored in a new matrix. This new matrix contained the true micro-Doppler (TV Doppler power) characteristics of the recorded CSI.

Before computing the spectrogram, the CSI matrix containing the true TV Doppler power characteristics was filtered by using a highpass equiripple filter to reduce the effect of the fixed scatterers. Then, we took the sum of the CTF over the subcarriers as follows:

$$\mu(t) = \sum_{q} H\left(t, \Delta f^{(q)}\right). \tag{D.16}$$

This was done for better visualization as it reduces the background noise of the spectrogram. Finally, we computed the spectrogram $S_\mu(f,t)$ of $\mu(t)$, using the same steps as in Section D.3. The window spread parameter σ_w was set to 0.05 s.

D.4.3 Demonstration of the Results

Figs. D.3(a)–D.3(f) exhibit the spectrograms $S_\mu(f,t)$ corresponding to the falling away, falling towards, walking away, walking towards, sitting, and bending and straightening activities of the candidate. For the spectrogram $S_\mu(f,t)$ of the falling away activity shown in Fig. D.3(a),

the Doppler frequency is negative as the candidate moves away from the T_x and R_x. Hence, the propagation delay $\tau_{\mathrm{M},n}(t)$ increases and its rate of change $\dot{\tau}_{\mathrm{M},n}(t)$ is positive (see (D.3) and (D.6)). The Doppler shift caused by the falling activity of the candidate keeps decreasing until it reaches a value around -120 Hz in Fig. D.3(a). Then, it returns to zero value. Fig. D.3(b) depicts the spectrogram $S_\mu(f,t)$ corresponding to the falling towards activity of the candidate. The Doppler frequency caused by the activity is positive since the candidate moves towards the T_x and R_x, thus the propagation delay $\tau_{\mathrm{M},n}(t)$ decreases and its rate of change $\dot{\tau}_{\mathrm{M},n}(t)$ is negative. The Doppler shift corresponding to the falling activity increases until it reaches a value around 100 Hz, then the value drops to zero as the candidate is not moving after the fall. Note that the fall activities depicted in Figs. D.3(a)–D.3(b) include short time intervals up to 2 s. Figs. D.3(c)–D.3(d) exhibit the spectrogram corresponding to the walking away and walking towards activities of the candidate. These activities consume almost 10 s time intervals. The Doppler shift corresponding to the walking away and walking towards activities reach -40 Hz and 40 Hz, respectively.

Fig. D.3(e) shows the spectrogram corresponding to the sitting activity of the candidate. It is shown that the sitting activity lasts for almost 3 s. The pattern of the spectrogram shown in Fig. D.3(e) is quite similar to that in Fig. D.3(a), but the Doppler shift reaches almost -40 Hz unlike the Doppler shift in Fig. D.3(a), which reaches almost -120 Hz. The spectrogram, which corresponds to bending and straightening, is shown in Fig. D.3(f). During the first interval from $t = 0$ s and $t = 2$ s, the Doppler shift reaches almost 20 Hz as when the candidate bends the back, the head gets closer to the T_x and R_x. Thus, the propagation delay $\tau_{\mathrm{M},n}(t)$ decreases and the Doppler shift is positive. In the second interval, from $t = 2$ s to $t \approx 3$ s, the Doppler shift has almost zero value as the person pauses. Thus, the corresponding propagation delay is time-invariant. During the interval from $t \approx 3$ s to $t = 5$ s, the candidate is straightens the back, the propagation delay increases and the Doppler shift is negative as shown in Fig. D.3(f).

Figs. D.4(a)-D.4(f) depict the TV mean Doppler shifts $B^{(1)}(t)$ corresponding to the falling away, falling towards, walking away, walking towards, sitting, and bending and straightening activities of the candidate. These TV mean Doppler shifts were computed by substituting $S_\mu(f,t)$ in (D.16) instead of $S_{H^{(q)}}(f,t)$. The TV mean Doppler shifts exhibited in Figs. D.4(a)-D.4(f) provide similar patterns to the Doppler frequencies shown in the spectrograms depicted in Figs. D.3(a)–D.3(f), but with different values. This is due to the effect of the fixed scatterers, which is not completely eliminated by the highpass filter, the background noise in the spectrogram, and having multiple moving scatterers (see the definition of the TV mean Doppler shift in Section D.2).

D.5 Conclusion

In this paper, we modelled of the CTF of 3D non-stationary F2F channels and the TV Doppler frequency caused by the moving scatterer in terms of the TV speed, the TV AAOM, the TV EAOM, the TV AAOA, the TV EAOA, the TV AAOD, and the TV AAOA. We demonstrated the relationship between the Doppler frequency and the TV propagation delay corresponding to the moving scatterer. We provided the expressions of the spectrogram of the CTF, which consists of the auto-term and the cross-term. We expressed the TV mean Doppler shift by means of the spectrogram. We presented the results of the spectrograms and the TV mean Doppler shifts of the calibrated measured CSI for six human activities. The measurement results showed the possibility of applying deep learning or machine learning algorithms for HAR to the spectrograms or the TV mean Doppler shift of the measured calibrated CSI, which can be collected by using commercial devices. For future work, we recommend the development of a channel simulator fed with realistic trajectories of human activities. Such a simulator will contribute to the development simulation-based HAR systems.

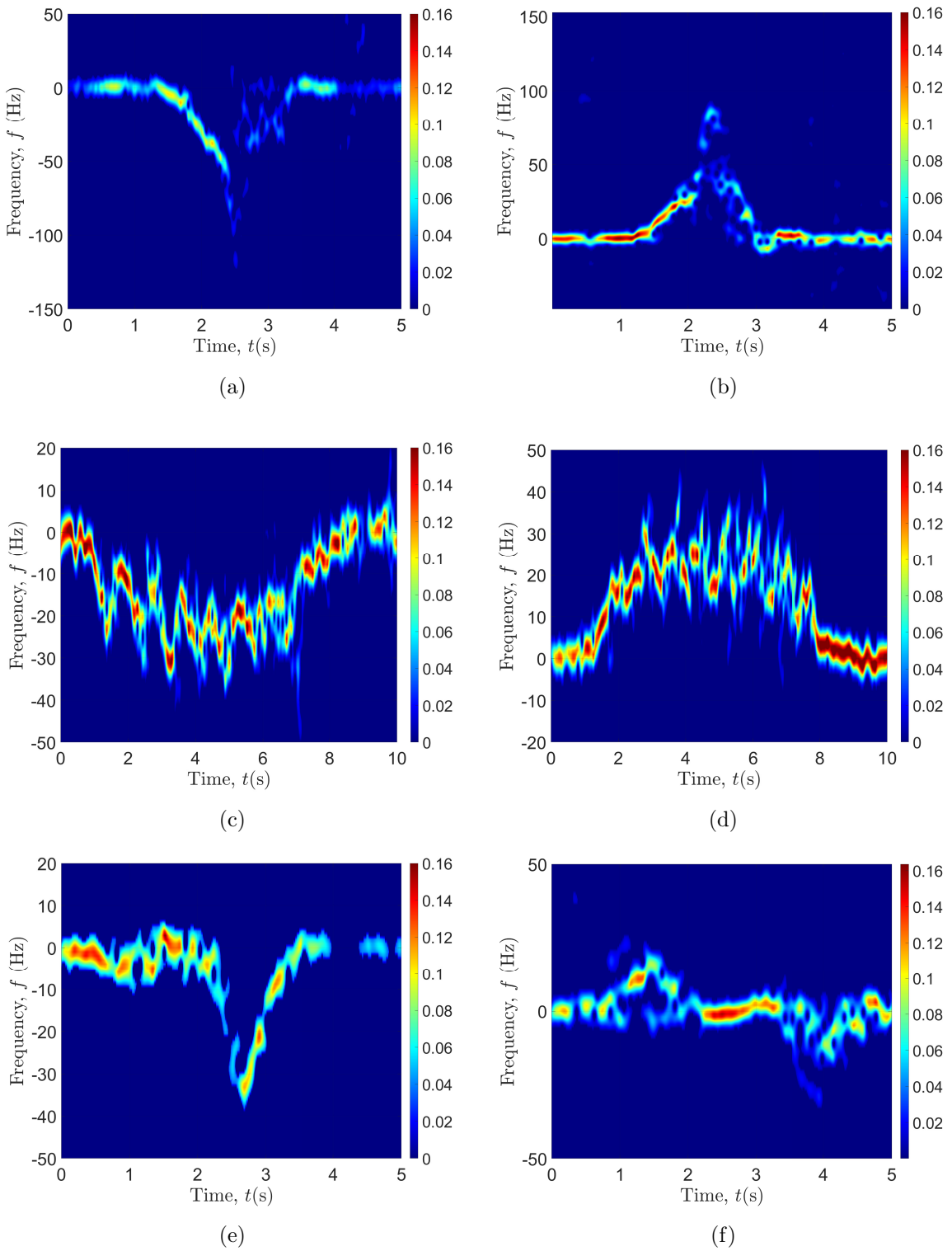

Figure D.3: Spectrograms $S_\mu(f,t)$ of calibrated measured CSI corresponding to the following 6 different human activities (a) falling away, (b) falling towards, (c) walking away, (d) walking towards, (e) sitting, and (f) bending and straightening.

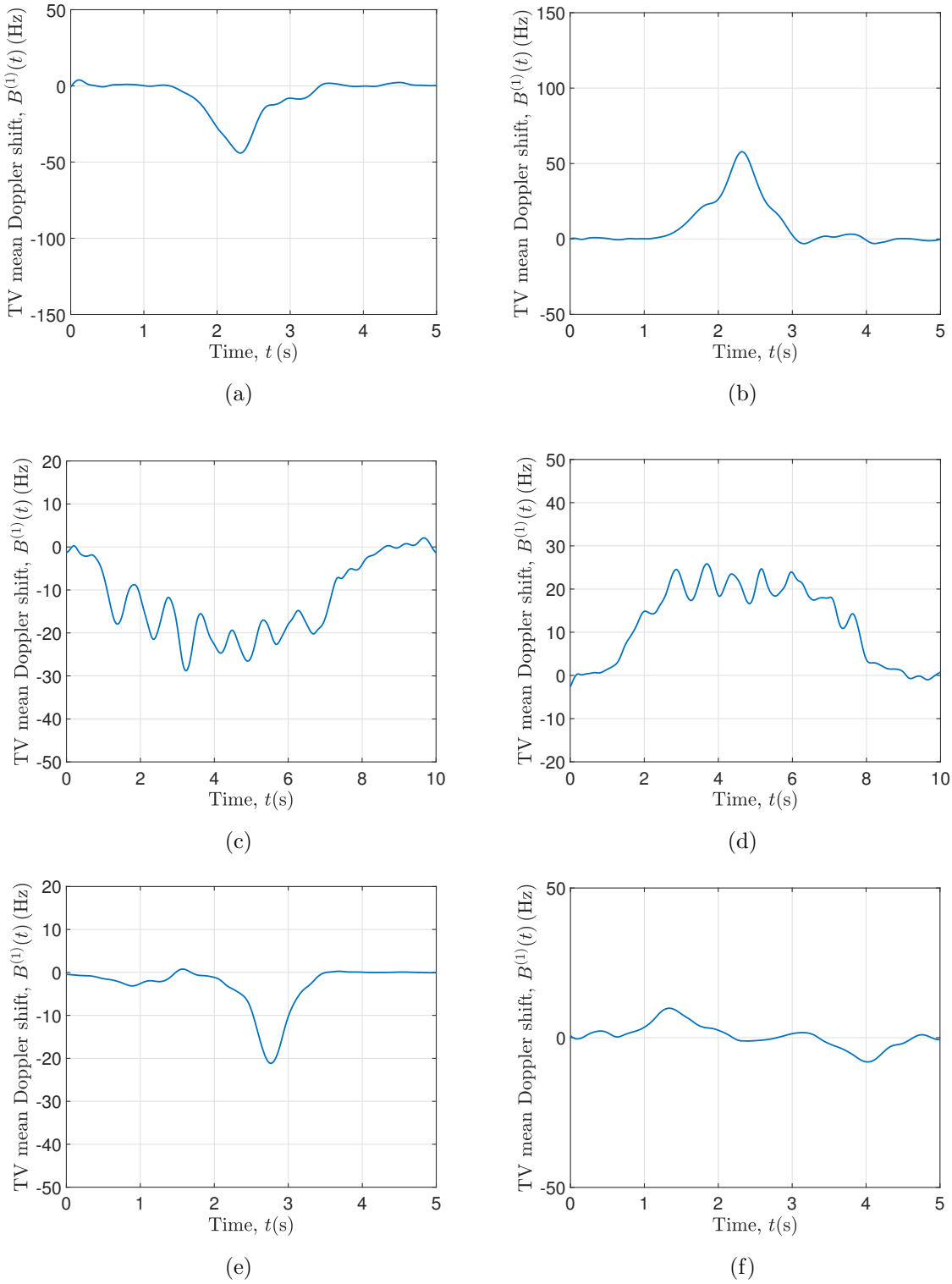

Figure D.4: TV mean Doppler shifts $B^{(1)}(t)$ of the measured calibrated CSI corresponding to (a) falling away, (b) falling towards, (c) walking away, (d) walking towards, (e) sitting, and (f) bending and straightening activities.

Bibliography

[1] K. A. Hartholt, R. Lee, E. R. Burns, and E. F. van Beeck, "Mortality from falls among US adults aged 75 years or older, 2000-2016," *JAMA*, vol. 321, pp. 2131–2133, 06 2019.

[2] United Nations, Department of Economic and Social Affairs, Population Division , "World population ageing," 2017. Highlights (ST/ESA/SER.A/408).

[3] F. Adib, Z. Kabelac, D. Katabi, and R. C. Miller, "3D tracking via body radio reflections," in *Proc. of the 11th USENIX Conference on Networked Systems Design and Implementation NSDI'14*, (Berkeley, CA, USA), pp. 317–329, USENIX Association, 2014.

[4] B. Erol and M. G. Amin, "Radar data cube processing for human activity recognition using multi subspace learning," *IEEE Transactions on Aerospace and Electronic Systems*, pp. 1–1, 2019.

[5] A. Seifert, A. M. Zoubir, and M. G. Amin, "Detection of gait asymmetry using indoor Doppler radar," in *2019 IEEE Radar Conference (RadarConf)*, pp. 1–6, April 2019.

[6] G. A. M, Y. D. Zhang, F. Ahmad, and K. C. D. Ho, "Radar signal processing for elderly fall detection: the future for in-home monitoring," *IEEE Signal Processing Magazine*, vol. 33, pp. 71–80, Mar. 2016.

[7] B. Jokanović and M. Amin, "Fall detection using deep learning in range-Doppler radars," *IEEE Transactions on Aerospace and Electronic Systems*, vol. 54, pp. 180–189, Feb 2018.

[8] F. Fioranelli, M. Ritchie, S.-Z. Gürbüz, and H. Griffiths, "Feature diversity for optimized human micro-Doppler classification using multistatic radar," *IEEE Transactions on Aerospace and Electronic Systems*, vol. 53, pp. 640–654, Apr. 2017.

[9] M. Ritchie and A. M. Jones, "Micro-Doppler gesture recognition using Doppler, time and range based features," in *2019 IEEE Radar Conference (RadarConf)*, pp. 1–6, April 2019.

[10] D. Halperin, W. Hu, A. Sheth, and D. Wetherall, "Tool release: gathering 802.11n traces with channel state information," *ACM SIGCOMM CCR*, vol. 41, p. 53, Jan. 2011.

[11] "IEEE standard for information technology– local and metropolitan area networks– Specific requirements– Part 11: Wireless LAN medium access control (MAC) and physical layer (PHY) specifications amendment 5: Enhancements for higher throughput," *IEEE Std 802.11n-2009 (Amendment to IEEE Std 802.11-2007 as amended by IEEE Std 802.11k-2008, IEEE Std 802.11r-2008, IEEE Std 802.11y-2008, and IEEE Std 802.11w-2009)*, pp. 1–565, Oct 2009.

[12] M. N. Mahfoudi *et al.*, "Orion: orientation estimation using commodity Wi-Fi," in *2017 IEEE International Conference on Communications Workshops (ICC Workshops)*, pp. 1233–1238, May 2017.

[13] M. Kotaru, K. Joshi, D. Bharadia, and S. Katti, "Spotfi: decimeter level localization using WiFi," *SIGCOMM Comput. Commun. Rev.*, vol. 45, pp. 269–282, August 2015.

[14] K. Qian *et al.*, "Tuning by turning: Enabling phased array signal processing for WiFi with inertial sensors," in *IEEE INFOCOM 2016 - The 35th Annual IEEE International Conference on Computer Communications*, pp. 1–9, April 2016.

[15] W. Wang, A. X. Liu, and M. Shahzad, "Gait recognition using WiFi signals," in *Proceedings of the 2016 ACM International Joint Conference on Pervasive and Ubiquitous Computing*, UbiComp '16, (New York, NY, USA), pp. 363–373, ACM, 2016.

[16] S. Sen, B. Radunovic, R. R. Choudhury, and T. Minka, "You are facing the Mona Lisa: spot localization using phy layer information," in *Proceedings of the 10th International Conference on Mobile Systems, Applications, and Services*, MobiSys '12, (New York, NY, USA), pp. 183–196, ACM, 2012.

[17] N. Keerativoranan, A. Haniz, K. Saito, and J.-i. Takada, "Mitigation of CSI temporal phase rotation with B2B calibration method for fine-grained motion detection analysis on commodity Wi-Fi devices," *Sensors*, vol. 18, no. 11, 2018.

[18] T. K. Sarkar, Zhong Ji, Kyungjung Kim, A. Medouri, and M. Salazar-Palma, "A survey of various propagation models for mobile communication," *IEEE Antennas and Propagation Magazine*, vol. 45, pp. 51–82, June 2003.

[19] V. Chen, *The Micro-Doppler Effect in Radar, Second Edition*. Artech House radar library, Artech House, 2019.

[20] G. L. Stüber, *Principles of Mobile Communications*. Springer Int. Publishing, 4th ed., 2017.

[21] M. Pätzold and C. A. Gutierrez, "Modelling of non-WSSUS channels with time-variant Doppler and delay characteristics," in *2018 IEEE Seventh International Conference on Communications and Electronics (ICCE)*, pp. 1–6, Hue, Vietnam, July 2018.

[22] A. Abdelgawwad and M. Pätzold, "A framework for activity monitoring and fall detection based on the characteristics of indoor channels," in *IEEE 87th Vehicular Technology Conference (VTC Spring)*, Porto, Portugal, Jun. 2018.

[23] A. Abdelgawwad and M. Pätzold, "On the influence of walking people on the Doppler spectral characteristics of indoor channels," in *Proc. 28th IEEE Int. Symp. on Personal, Indoor and Mobile Radio Communications, PIMRC 2017*, Montreal, Canada, Oct. 2017.

Appendix E

Paper E

Title:	Modelling, Analysis, and Simulation of the Micro-Doppler Effect in Wideband Indoor Channels with Confirmation Through Pendulum Experiments
Authors:	Ahmed Abdelgawwad, Alireza Borhani, and Matthias Pätzold
Affiliation:	University of Agder, Faculty of Engineering and Science, P. O. Box 509, NO-4898 Grimstad, Norway
Journal:	*Sensors 2020*, no. 4: 1049.
DOI:	10.3390/s20041049.

Modelling, Analysis, and Simulation of the Micro-Doppler Effect in Wideband Indoor Channels with Confirmation Through Pendulum Experiments

Ahmed Abdelgawwad*, Alireza Borhani, and Matthias Pätzold
Department of Information and Communication Technology
Faculty of Engineering and Science, University of Agder
P.O. Box 509, NO-4898 Grimstad, Norway
E-mails: {ahmed.abdel-gawwad, alireza.borhani, matthias.paetzold}@uia.no
Correspondence*: ahmed.abdel-gawwad@uia.no; Tel.: +47-37 23 32 63

Abstract **— This paper is about designing a 3D non-stationary wideband indoor channel model for radio-frequency sensing. The proposed channel model allows for simulating the time-variant (TV) characteristics of the received signal of indoor channel in the presence of a moving object. The moving object is modelled by a point scatterer which travels along a trajectory. The trajectory is described by the object's TV speed, TV horizontal angle of motion, and TV vertical angle of motion. An expression of the TV Doppler frequency caused by the moving scatterer is derived. Furthermore, an expression of the TV complex channel transfer function (CTF) of the received signal is provided, which accounts for the influence of a moving object and fixed objects, such as walls, ceiling, and furniture. An approximate analytical solution of the spectrogram of the CTF is derived. The proposed channel model is confirmed by measurements obtained from a pendulum experiment. In the pendulum experiment, the trajectory of the pendulum has been measured by using an inertial-measurement unit (IMU) and simultaneously collecting CSI data. For validation, we have compared the spectrogram of the proposed channel model fed with IMU data with the spectrogram characteristics of the measured CSI data. The proposed channel model paves the way towards designing simulation-based activity recognition systems.**

Index Terms **— spectrogram, 3D non-stationary channels, indoor channels, Doppler frequency, channel state information, Wi-Fi 802.11n, inertial measurement units, micro-Doppler effect, CSI.**

E.1 Introduction

In wireless communications, the compound Doppler effect caused by the moving objects or bodies opened up opportunities for many applications. These applications track the scattered wave components by the moving bodies for drone detection [1], gesture recognition [2], human gait assessment for diagnosis and rehabilitation [3], and tracking human activities using non-wearable radio-frequency-based (RF-based) elder-care [4]. Such waves contain the micro-Doppler effects corresponding to the moving bodies.

In channel modelling, the Doppler effect caused by moving scatterers has been modelled in two-dimensional (2D) stationary fixed-to-mobile radio in [5]. Then, this model has been extended for 2D non-stationary fixed-to-fixed (F2F) indoor channels by considering the time-variant (TV) speed of the moving scatterer, angle of motion, angle of arrival, and angle of departure [6]. Later on, the TV Doppler frequency caused by the moving scatterer has been incorporated in three-dimensional (3D) channels by taking into account the TV azimuth angles of motion (AAOM), elevation angle of motion (EAOM), azimuth angle of departure (AAOD), elevation angle of departure (EAOD), azimuth angle of arrival (AAOA), and elevation angle of arrival (EAOA) for fixed-to-fixed channel models [6, 7] and vehicle-to-vehicle channels [8]. To reveal the TV Doppler power characteristics of non-stationary multicomponent signals, a time-frequency distribution such as the spectrogram can be employed. The authors of [9] distinguished between aided and unaided gaits by means of the spectrogram. In [10] the angular velocities and lengths of rotating blades have been estimated by using the spectrogram. The spectrogram has been employed in gesture recognition [11] and human activity recognition (HAR) [12]. It has been used for the detection of gait asymmetry in [3, 13], distinguishing between armed and unarmed persons for security services [14], and fall detection [15–17], as well.

The authors of [18] developed a software tool that captures the complex channel state information (CSI) of 30 subcarriers corresponding to orthogonal-frequency-division-multiplexing (OFDM). This software tool is compatible with commercial devices equipped with Intel NIC 5300 network interface cards and operates on the Wi-Fi 802.11n protocol [19]. An overview of studies on signal recognition, action recognition, and activity recognition by utilizing the amplitude of the measured CSI can be found in [20]. One of the challenges faced while processing CSI data to extract the micro-Doppler signatures is that the phases of such data are distorted as the transmitter and receiver are not clock synchronized [21–28]. To overcome this issue, one of the attempts is to apply the principle component analysis (PCA) [29–32] on the magnitude of the complex CSI data to denoise it, then to apply a one-sided spectrogram on the denoised data to reveal the positive frequency components of the spectrogram. Another attempt has been applied by using a phase sanitization technique [32–34] by employing linear transformation operation on the distorted phases of the 30 subcarriers. Such an operation gives a better pattern of the transformed phases. These attempts do not help to reveal the

true Doppler power characteristics of the preprocessed CSI data. In [35] the phase distortions of CSI data have been eliminated by using a back-to-back (B2B) connection between the transmitter and receiver stations. This approach allows for revealing the true Doppler power characteristics of the measured CSI data.

The micro-Doppler effect of pendulum motion in bistatic and monostatic radar systems has been investigated in [36, 37]. In [36], the micro-Doppler effect was analyzed by means of the one-sided spectrogram of both simulated radar signal and verified with the experiment. According to the best of the authors' knowledge, there are no studies on the micro-Doppler effect of a swinging pendulum on measured calibrated CSI with B2B connection. There are no simultaneous conducted measurements by using the CSI tool and an IMU attached to the swinging pendulum, as well.

The Fresnel zone diffraction model has been described in [38–41]. Such a model has been used for CSI-based human activity recognition [42], human respiration sensing [43], and indoor human detection [44]. The Fresnel zone model is an envelope model that does not contain any phase information. The phase information is important for the analysis of the micro-Doppler signatures, which is our main focus in this paper. The motivation of this paper is to present a non-stationary wideband F2F channel model that has Doppler power characteristics similar to experimental data. According to the best of the authors' knowledge, RF-based HAR, gesture recognition, and fall detection systems are designed based on experimental data, i.e., the machine used for detection or classification is trained by using experimental data. Thus, proposing such a model will help for simulation-based activity recognition systems by using it for training instead of using experimental data. This approach is time efficient and cost-effective. Instead of wasting too much time for collecting RF data for training, one can generate data sets of different scenarios by using lab simulations. In order to design such a realistic channel model with Doppler power characteristics close to experimental data, the TV trajectory of a moving object plays an important role as the Doppler shift depends on the TV speed, AAOM, EAOM, EAOD, AAOD, EAOA, and AAOA. The trajectory of the moving object can be measured by using an IMU which captures linear accelerations, and Euler angles simultaneously. The Euler angles are used to rotate the measured linear accelerations from the frame of the IMU to the reference frame. Then the rotated linear accelerations can be integrated to obtain TV velocities and displacements (trajectories). The TV velocities and displacements suffer from linear and quadratic drifts, respectively. In [45, 46], these drift problems were addressed by employing zero update algorithms.

In this paper, we design a 3D non-stationary wideband channel model for activity recognition. We model a moving object as a moving scatterer. The expressions for the TV speed, AAOM, EAOM, EAOD, AAOD, EAOA, and AAOA corresponding to the moving scatterer are presented. Then, the expression for the TV Doppler frequency caused by the moving scatterer is provided. Furthermore, the instantaneous channel phase of the moving scatterer and the complex channel transfer function (CTF) of the non-stationary F2F channels are determined.

Next, an approximate solution of the spectrogram of the complex CTF is presented to provide insight into the TV Doppler power characteristics of this model. We perform measurements of the calibrated CSI and IMU, simultaneously during a moving object experiment. The CSI data is calibrated by using a B2B connection to eliminate the TV phase distortions. Then, we feed the proposed channel model with the measured trajectory using the IMU. Finally, we show that the spectrogram of the calibrated measured CSI data and the channel model are matching. The TV mean Doppler shifts computed from both spectrograms are matching as well. The proposed channel model paves the way towards the design of software-RF-based human activity recognition and fall detection systems.

The rest of the paper is structured as follows. Section E.2 exhibits the 3D multipath propagation scenario with moving and fixed objects. Section E.3 presents the expressions of the TV channel parameters and the complex channel transfer function. The approximate analytical solution of the spectrogram of the complex channel function is provided in Section E.4. Section E.5 discusses the numerical and measurement results. The conclusion and future work are discussed in Section E.6.

E.2 The 3D Geometrical Model

We consider the 3D geometrical model of a 3D multipath propagation channel shown in Figure E.1. This figure shows a fixed Wi-Fi transmitter T_x and a fixed Wi-Fi receiver R_x which operate according to the IEEE 802.11n standard [19] with carrier frequency $f_0 = 5.32$ GHz and bandwidth $B = 20$ MHz. The positions of T_x and R_x are denoted by $\left(x^T, y^T, z^T\right)$ and $\left(x^R, y^R, z^R\right)$, respectively. A moving object whose center of mass (CoM) is modelled for simplicity by a single moving (point) scatterer S^{M} initially located at $(x_{\mathrm{M}}, y_{\mathrm{M}}, z_{\mathrm{M}})$. The trajectory of the moving scatterer S^{M} is described by a TV velocity vector $\vec{v}_{\mathrm{M}}(t)$ which can be expressed by the TV speed $\mathrm{v}_{\mathrm{M}}(t)$, the TV AAOM $\alpha_{v_{\mathrm{M}}}(t)$, and the TV EAOM $\beta_{v_{\mathrm{M}}}(t)$. Each fixed object is modelled by a fixed scatterer S^{F}_m (▲) for $m = 1, 2, \ldots, \mathcal{M}$, where $\mathcal{M}$ denotes the number of fixed scatterers (objects). The TV parameters $\beta^T_{\mathrm{M}}(t)$, $\alpha^T_{\mathrm{M}}(t)$, $\beta^R_{\mathrm{M}}(t)$, and $\alpha^R_{\mathrm{M}}(t)$ designate the TV EAOD, TV AAOD, TV EAOA, and TV AAOA, respectively. We assume single-bounce scattering, i.e., each wave that is launched from T_x is bounced by either a fixed scatterer S^{F}_m or a moving scatterer S^{M} before arriving at R_x.

E.3 The Channel Transfer Function

The TV velocity vector $\vec{v}_{\mathrm{M}}(t)$ of the moving scatterer S^{M} is presented as

$$\vec{v}_{\mathrm{M}}(t) = \left[v_{\mathrm{M},x}(t) \ , \ v_{\mathrm{M},y}(t) \ , \ v_{\mathrm{M},z}(t)\right]^{\mathrm{T}} \tag{E.1}$$

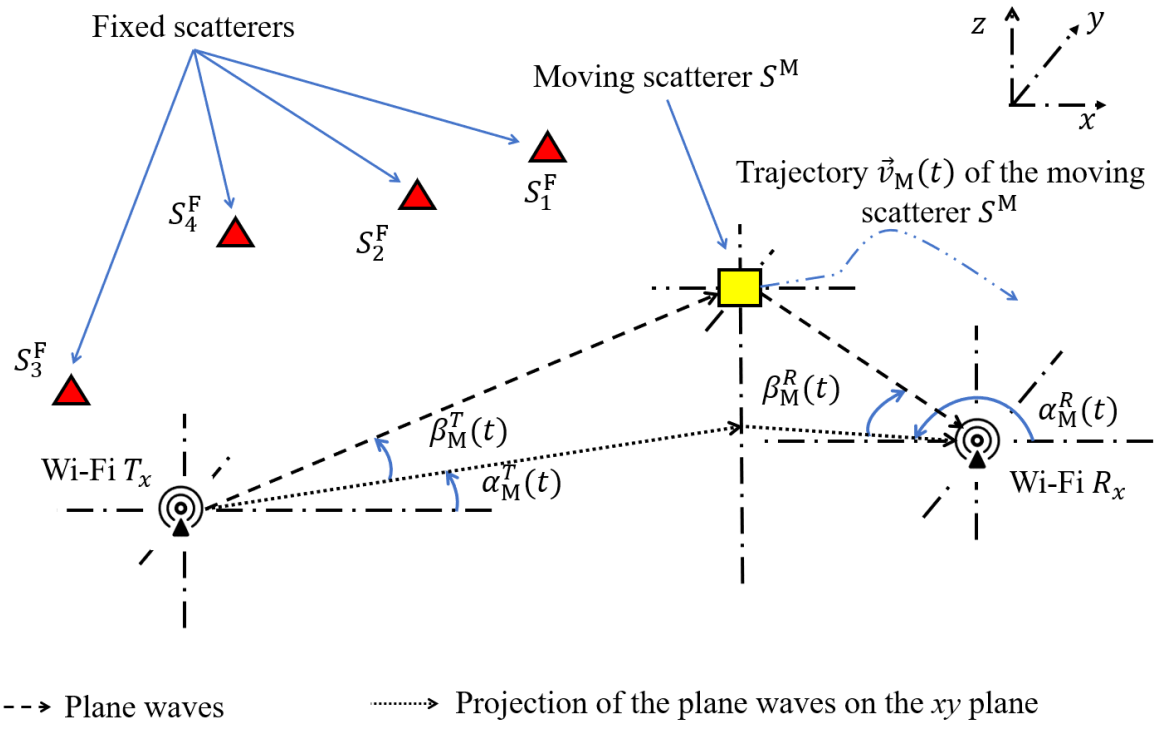

Figure E.1: Geometrical model of a 3D multipath propagation scenario with one moving scatterer S^{M} and $\mathcal{M}$ fixed scatterers S_m^{F}, $m = 1, 2, \ldots, \mathcal{M}$.

where $[\cdot]^{\mathrm{T}}$ denotes the vector transpose operation. The velocities $v_{\mathrm{M},x}(t)$, $v_{\mathrm{M},y}(t)$, and $v_{\mathrm{M},z}(t)$ can be expressed in terms of the TV speed $\mathrm{v}_{\mathrm{M}}(t)$, TV EAOM $\beta_{v_{\mathrm{M}}}(t)$, and TV AAOM $\alpha_{v_{\mathrm{M}}}(t)$ as

$$v_{\mathrm{M},x}(t) = \mathrm{v}_{\mathrm{M}}(t)\cos\left(\beta_{v_{\mathrm{M}}}(t)\right)\cos\left(\alpha_{v_{\mathrm{M}}}(t)\right) \tag{E.2}$$

$$v_{\mathrm{M},y}(t) = \mathrm{v}_{\mathrm{M}}(t)\cos\left(\beta_{v_{\mathrm{M}}}(t)\right)\sin\left(\alpha_{v_{\mathrm{M}}}(t)\right) \tag{E.3}$$

$$v_{\mathrm{M},z}(t) = \mathrm{v}_{\mathrm{M}}(t)\sin\left(\beta_{v_{\mathrm{M}}}(t)\right) \tag{E.4}$$

where

$$\alpha_{v_{\mathrm{M}}}(t) = \operatorname{atan2}\left(v_{\mathrm{M},y}(t), v_{\mathrm{M},x}(t)\right) \tag{E.5}$$

$$\beta_{v_{\mathrm{M}}}(t) = \arcsin\left(\frac{v_{\mathrm{M},z}(t)}{\sqrt{v_{\mathrm{M},x}^2(t) + v_{\mathrm{M},y}^2(t) + v_{\mathrm{M},z}^2(t)}}\right). \tag{E.6}$$

The function atan2$(\cdot)$ in (E.5) represents the four-quadrant inverse trigonometric tangent function that provides an azimuth angle $\alpha_{v_{\mathrm{M}}}(t)$ ranging from $-\pi$ to π, unlike the regular

arctan(·) function that provides an angle ranging from $-\pi/2$ to $\pi/2$. Note that the elevation angle $\beta_{v_{\mathrm{M}}}(t)$ is within the range from $-\pi/2$ to $\pi/2$. By using the components of the TV velocity vector $\vec{v}_{\mathrm{M}}(t)$ in (E.2)–(E.4), one can compute the displacements $x_{\mathrm{M}}(t)$, $y_{\mathrm{M}}(t)$, and $z_{\mathrm{M}}(t)$ of the moving scatterer S^{M} as

$$x_{\mathrm{M}}(t) = x_{\mathrm{M}} + \int_0^t v_{\mathrm{M},x}(t')dt' \tag{E.7}$$

$$y_{\mathrm{M}}(t) = y_{\mathrm{M}} + \int_0^t v_{\mathrm{M},y}(t')dt' \tag{E.8}$$

$$z_{\mathrm{M}}(t) = z_{\mathrm{M}} + \int_0^t v_{\mathrm{M},z}(t')dt'. \tag{E.9}$$

From the displacements in (E.7)–(E.9), the TV Euclidean distance $d_{\mathrm{M}}^T(t)$ between the transmitter T_x and the moving scatterer S^{M} can be computed by

$$d_{\mathrm{M}}^T(t) = \sqrt{(x_{\mathrm{M}}(t) - x^T)^2 + (y_{\mathrm{M}}(t) - y^T)^2 + (z_{\mathrm{M}}(t) - z^T)^2}. \tag{E.10}$$

Analogously, the Euclidean distance $d_{\mathrm{M}}^R(t)$ between the receiver R_x and the moving scatterer S^{M} is given by

$$d_{\mathrm{M}}^R(t) = \sqrt{(x_{\mathrm{M}}(t) - x^R)^2 + (y_{\mathrm{M}}(t) - y^R)^2 + (z_{\mathrm{M}}(t) - z^R)^2}. \tag{E.11}$$

By using the expressions of the displacements in (E.7)–(E.9) and the distances in (E.10)–(E.11), the TV EAOD $\beta_{\mathrm{M}}^T(t)$, TV AAOD $\alpha_{\mathrm{M}}^T(t)$, TV EAOA $\beta_{\mathrm{M}}^R(t)$, and TV AAOA $\alpha_{\mathrm{M}}^R(t)$ can be computed as follows:

$$\beta_{\mathrm{M}}^T(t) = \arcsin\left(\frac{z_{\mathrm{M}}(t) - z^T}{d_{\mathrm{M}}^T(t)}\right) \tag{E.12}$$

$$\alpha_{\mathrm{M}}^T(t) = \operatorname{atan2}\left(y_{\mathrm{M}}(t) - y^T,\, x_{\mathrm{M}}(t) - x^T\right) \tag{E.13}$$

$$\beta_{\mathrm{M}}^R(t) = \arcsin\left(\frac{z_{\mathrm{M}}(t) - z^R}{d_{\mathrm{M}}^R(t)}\right) \tag{E.14}$$

$$\alpha_{\mathrm{M}}^R(t) = \operatorname{atan2}\left(y_{\mathrm{M}}(t) - y^R,\, x_{\mathrm{M}}(t) - x^R\right) \tag{E.15}$$

where $\alpha_{\mathrm{M}}^T(t)$, $\alpha_{\mathrm{M}}^R(t) \in (-\pi, \pi]$ and $\beta_{\mathrm{M}}^T(t)$, $\beta_{\mathrm{M}}^R(t) \in [-\pi/2, \pi/2]$. The TV propagation delay $\tau_{\mathrm{M}}(t)$ of the propagation path from T_x via S^{M} to R_x is given by

$$\tau_{\mathrm{M}}(t) = \frac{d_{\mathrm{M}}^T(t) + d_{\mathrm{M}}^R(t)}{c_0}. \tag{E.16}$$

In (E.16), the parameter c_0 denotes the speed of light.

The CTF $H(t, \Delta f^{(q)})$ is given by

$$H\left(t, \Delta f^{(q)}\right) = H_{\mathrm{M}}\left(t, \Delta f^{(q)}\right) + \sum_{m=1}^{\mathcal{M}} H_{\mathrm{F},m} \tag{E.17}$$

where

$$H_{\mathrm{M}}\left(t, \Delta f^{(q)}\right) = c_{\mathrm{M}}\, e^{j\left[\theta_{\mathrm{M}} - 2\pi\left(f_0 + \Delta f^{(q)}\right)\tau_{\mathrm{M}}(t)\right]} \tag{E.18}$$

$$H_{\mathrm{F},m} = c_{\mathrm{F},m}\, e^{j\theta_{\mathrm{F},m}}. \tag{E.19}$$

The superscript q in (E.17) represents the subcarrier index of OFDM communication systems that follows the IEEE 802.11n standard [19]. The parameter $\Delta f^{(q)}$ in (E.17) designates the subcarrier frequency which is given by

$$\Delta f^{(q)} = q \cdot \Delta \tag{E.20}$$

for $q \in \{-28, -26, \ldots, -2, -1, 1, 3, \ldots, 27, 28\}$. In (E.20), the parameter Δ represents the subcarrier frequencies difference which has a value of 312.5 kHz [19]. The function $H_{\mathrm{M}}(t, \Delta f^{(q)})$ designates the complex CTF of the moving scatterer S^{M} and the parameter $H_{\mathrm{F},m}$ denotes the complex CTF corresponding the mth fixed scatterer S^{F}_m. The expression in (E.17) is similar to the one in [47, Eq.(21)]. The only difference is that the multipath effect associated with the fixed scatterers is taken into account by adding the second term in (E.17). The first term in (E.17) designates the TV part of the CTF corresponding to the moving scatterer S^{M} with a fixed path gain c_{M} and stochastic phase process $\theta_{\mathrm{M}} - 2\pi(f_0 + \Delta f^{(q)})\tau_{\mathrm{M}}(t)$ associated with the qth subcarrier [see (E.18)]. The second term in (E.17) is time-invariant and represents the sum of the $\mathcal{M}$ received multipath components corresponding to the $\mathcal{M}$ fixed scatterers. Each component of the second term in (E.17) is characterized by a fixed path gain $c_{m,\mathrm{F}}$ and a random phase variable $\theta_{m,\mathrm{F}}$ due to the interaction with the mth fixed scatterer S^{F}_m [see (E.19)]. It should be mentioned that the phases θ_{M} and $\theta_{m,\mathrm{F}}$ are identically and independently distributed (i.i.d), each follows a uniform distribution over $-\pi$ and π, i.e., $\theta_{\mathrm{M}},\, \theta_{m,\mathrm{F}} \sim \mathcal{U}\,(-\pi, \pi\,]$. The model presented in (E.17) is a stochastic model of the TV CTF $H(t, \Delta f^{(q)})$. The TV Doppler shift $f^{(q)}_{\mathrm{M}}(t)$ of the moving scatterer S^{M} and associated with the qth subcarrier index is expressed by using (E.16) in combination with the relationship $f^{(q)}_{\mathrm{M}}(t) = -(f_0 + \Delta f^{(q)})\dot{\tau}_{\mathrm{M}}(t)$, which can be found in [47, Eq.(22)] as [48]

$$\begin{aligned} f^{(q)}_{\mathrm{M}}(t) = -f^{(q)}_{\max}(t) \Big\{ & \cos\left(\beta_{v_{\mathrm{M}}}(t)\right) \Big[\cos\left(\beta^{T}_{\mathrm{M}}(t)\right) \cos\left(\alpha^{T}(t) - \alpha_{v_{\mathrm{M}}}(t)\right) \\ & + \cos\left(\beta^{R}_{\mathrm{M}}(t)\right) \cos\left(\alpha_{v_{\mathrm{M}}}(t) - \alpha^{R}_{\mathrm{M}}(t)\right) \Big] + \sin\left(\beta_{v_{\mathrm{M}}}(t)\right) \Big[\sin\left(\beta^{T}_{\mathrm{M}}(t)\right) + \sin\left(\beta^{R}_{\mathrm{M}}(t)\right) \Big] \Big\} \end{aligned} \tag{E.21}$$

where function $f_{\max}^{(q)}(t)$ designates the maximum Doppler shift caused by the moving scatterer S^{M} which is given by

$$f_{\max}^{(q)}(t) = \frac{\left(f_0 + \Delta f^{(q)}\right) \mathrm{v}_{\mathrm{M}}(t)}{c_0}. \tag{E.22}$$

From the expression in (E.21) and the relationship $f_{\mathrm{M}}^{(q)}(t) = -(f_0 + \Delta f^{(q)})\dot{\tau}_{\mathrm{M}}(t)$, one can conclude that if the moving scatterer S^{M} moves away from the T_x and R_x vicinity, the TV propagation delay $\tau_{\mathrm{M}}(t)$ and its slope $\dot{\tau}_{\mathrm{M}}(t)$ increase and the Doppler effect $f_{\mathrm{M}}(t)$ has negative values, and vice versa. To obtain an approximate solution for the spectrogram of the CTF $H(t, \Delta f^{(q)})$ that will be discussed in Section E.4, the Doppler frequency $f_{\mathrm{M}}^{(q)}(t)$ in (E.21) can be approximated by L linear piecewise functions according to

$$f_{\mathrm{M}}^{(q)}(t) \approx f_{\mathrm{M},l}^{(q)}(t) = f_{\mathrm{M}}^{(q)}(t_l) + k_{\mathrm{M},l}^{(q)}(t - t_l) \tag{E.23}$$

for $t_l < t \leq t_{l+1}$ and $l = 0, 1, \ldots, L-1$, where $k_{\mathrm{M},l}^{(q)}$ denotes the slope of the approximated Doppler frequency $f_{\mathrm{M}}^{(q)}(t)$ which is given by

$$k_{\mathrm{M},l}^{(q)} = \frac{f_{\mathrm{M}}^{(q)}(t_{l+1}) - f_{\mathrm{M}}^{(q)}(t_l)}{t_{l+1} - t_l}. \tag{E.24}$$

The difference between two consecutive time instances t_{l+1} and t_l, i.e., $\delta = t_{l+1} - t_l$ is the same for all values of $l = 0, 1, \ldots, L-1$.

The TV mean Doppler shift $B_{f^{(q)}}^{(1)}(t)$ of the proposed 3D channel model can be computed by using (E.21) as [49]

$$B_{f^{(q)}}^{(1)}(t) = \frac{c_{\mathrm{M}}^2 \, f_{\mathrm{M}}^{(q)}(t)}{c_{\mathrm{M}}^2 + \sum_{m=1}^{\mathcal{M}} c_{\mathrm{F},m}^2}. \tag{E.25}$$

The expression in (E.25) denotes the squared path gain c_{M}^2 multiplied by the Doppler frequency caused by the moving scatterer $f_{\mathrm{M}}^{(q)}(t)$ divided by the sum of the squared path gain of all of the scatterers. Note that, if the sum of the squared path gains $\sum_{m=1}^{\mathcal{M}} c_{\mathrm{F},m}^2$ is much less than the squared path gain of the moving scatterer c_{M}^2 of the moving scatterer S^{M}, i.e., $\sum_{m=1}^{\mathcal{M}} c_{\mathrm{F},m}^2 \ll c_{\mathrm{M}}^2$, then the TV mean Doppler shift $B_{f^{(q)}}^{(1)}(t)$ will have values closer to those of the Doppler frequency of the moving scatterer $f_{\mathrm{M}}^{(q)}(t)$, i.e., $B_{f^{(q)}}^{(1)}(t) \to f_{\mathrm{M}}^{(q)}(t)$.

E.4 Spectrogram Analysis

In this paper, we employ the spectrogram approach [50] to reveal the TV Doppler power spectrum of the proposed channel model. The spectrogram $S_{H^{(q)}}(f,t)$ of the CTF $H(t,\Delta f^{(q)})$ corresponding to the qth subcarrier index is computed in three steps. First, a sliding window $w(t)$ is multiplied by the CTF $H(t,\Delta f^{(q)})$. In this paper, we choose a Gaussian window function [50, Eq. (2.3.1)]

$$w(t) = \frac{1}{\sqrt{\sigma_w\sqrt{\pi}}} e^{-\frac{t^2}{2\sigma_w^2}} \tag{E.26}$$

where the parameter σ_w is called the Gaussian window spread. The window function $w(t)$ is real, positive, and even. It has a normalized energy, i.e., $\int_{-\infty}^{\infty} w^2(t) = 1$. By multiplying the window function $w(t)$ by the CTF $H(t,\Delta f^{(q)})$, the short-time CTF $x_{H^{(q)}}(t',t)$ is obtained as

$$x_{H^{(q)}}(t',t) = H\left(t',\Delta f^{(q)}\right) w(t'-t) \tag{E.27}$$

where the variables t and t' are the local time and the running time, respectively. The second step is to compute the short-time Fourier transform (STFT) $X_{H^{(q)}}(f,t)$ of $x_{H^{(q)}}(t',t)$. By using the approximation of the TV Doppler shift provided in (E.23), the STFT $X_{H^{(q)}}(f,t)$ associated with the qth subcarrier is obtained as

$$\begin{aligned} X_{H^{(q)}}(f,t) &= \int_{-\infty}^{\infty} x_{H^{(q)}}(t',t) e^{-j2\pi f t'} dt' \\ &\approx \frac{e^{-j2\pi f t}}{\sqrt{\sigma_w}\pi^{1/4}} \left\{ H_{\mathrm{M}}\left(t,\Delta f^{(q)}\right) G\left(f, f_{\mathrm{M},l}^{(q)}(t), \sigma_{x,\mathrm{M},l}^2\right) + \sum_{m=1}^{\mathcal{M}} H_{\mathrm{F},m}\, G\left(f,0,\sigma_{x,\mathrm{F},m}^2\right) \right\} \end{aligned} \tag{E.28}$$

for $t_l < t \leq t_{l+1}$ $(l = 0,1,\ldots,L-1)$, where

$$G\left(f, f_{\mathrm{M},l}^{(q)}(t), \sigma_{x,\mathrm{M},l}^2\right) = \frac{1}{\sqrt{2\pi}\sigma_{x,\mathrm{M},l}} e^{-\frac{(f-f_{\mathrm{M},l}^{(q)}(t))^2}{2\sigma_{x,\mathrm{M},l}^2}} \tag{E.29}$$

$$\sigma_{x,\mathrm{M},l}^2 = \frac{1 - j2\pi\sigma_w^2 k_{\mathrm{M},l}^{(q)}}{(2\pi\sigma_w)^2} \tag{E.30}$$

$$\sigma_{x,\mathrm{F},m}^2 = \frac{1}{(2\pi\sigma_w)^2}. \tag{E.31}$$

The expression in (E.29) is a complex Gaussian function with a TV mean $f_{\mathrm{M},l}^{(q)}(t)$ and a complex variance $\sigma_{x,\mathrm{M},l}^2$. Note that the complex variance $\sigma_{x,\mathrm{M},l}^2$ in (E.30) is dependent on

the slope $k_{\mathrm{M},l}^{(q)}$ of the Doppler frequency $f_{\mathrm{M},l}^{(q)}(t)$ [see (E.23)]. The last step is to obtain the spectrogram $S_{H^{(q)}}(f,t)$ associated with the qth subcarrier by squaring the magnitude of the STFT $X_{H^{(q)}}(f,t)$;, i.e.,

$$S_{H^{(q)}}(f,t) \;\approx\; |X_{H^{(q)}}(f,t)|^2 \;=\; S_{H^{(q)}}^{(a)}(f,t) + S_{H^{(q)}}^{(c)}(f,t) \tag{E.32}$$

where the functions $S_{H^{(q)}}^{(a)}(f,t)$ and $S_{H^{(q)}}^{(c)}(f,t)$ are called the auto-term and the cross-term of the spectrogram $S_{H^{(q)}}(f,t)$, respectively. The auto-term is given by

$$S_{H^{(q)}}^{(a)}(f,t) \approx c_{\mathrm{M}}^2\, G\left(f, f_{\mathrm{M},l}^{(q)}(t), \sigma_{\mathrm{M},l}^2\right) + \sum_{m=1}^{\mathcal{M}} c_{\mathrm{F},m}^2\, G\left(f, 0, \sigma_{\mathrm{F},m}^2\right) \tag{E.33}$$

for $t_l < t \leq t_{l+1}$, where

$$\sigma_{\mathrm{M},l}^2 \;=\; \frac{1 + \left(2\pi\sigma_w^2 k_{\mathrm{M},l}^{(q)}\right)^2}{2(2\pi\sigma_w)^2} \tag{E.34}$$

$$\sigma_{\mathrm{F},m}^2 \;=\; \frac{1}{2(2\pi\sigma_w)^2}. \tag{E.35}$$

The auto-term $S_{H^{(q)}}^{(a)}(f,t)$ in (E.33) is an approximation that provides insight into the Doppler power spectrum of the proposed 3D non-stationary channel model presented in Section E.2. This term is real, positive, and consists of a sum of $\mathcal{M}+1$ weighted Gaussian functions. The first Gaussian function, which is due to the moving scatterer S^{M} is weighted by the squared path gain c_{M}^2 and centered on the approximated TV Doppler frequency $f_{\mathrm{M},l}^{(q)}(t)$. The second term of the auto-term $S_{H^{(q)}}^{(a)}(f,t)$ in (E.33) is the sum of weighted Gaussian functions, which capture the effect of the $\mathcal{M}$ fixed scatterers S_m^{F}. The weighting factors are the squared path gains $c_{\mathrm{F},m}^2$ and each Gaussian function is centered on zero-frequency as the fixed scatterers do not cause Doppler shifts in F2F channels.

The cross-term $S_{H^{(q)}}^{(c)}(f,t)$ of the spectrogram corresponding to the qth subcarrier is given by

$$\begin{aligned} S_{H^{(q)}}^{(c)}(f,t) \;\approx\; & \frac{2}{\sigma_w\sqrt{\pi}}\,\Re\Bigg\{ \sum_{n=1}^{\mathcal{M}-1} \sum_{m=n+1}^{\mathcal{M}} G\left(f,0,\sigma_{x,\mathrm{F},n}^2\right)\, G^*\left(f,0,\sigma_{x,\mathrm{F},m}^2\right)\, H_{\mathrm{F},n}\, H_{\mathrm{F},m}^* \\ & + \sum_{m=1}^{\mathcal{M}} G\left(f, f_{\mathrm{M},l}^{(q)}(t), \sigma_{x,\mathrm{M},l}^2\right)\, G^*\left(f,0,\sigma_{x,\mathrm{F},m}^2\right)\, H_{\mathrm{M}}(t,\Delta f^{(q)})\, H_{\mathrm{F},m}^* \Bigg\}. \end{aligned} \tag{E.36}$$

The cross-term $S_{H^{(q)}}^{(c)}(f,t)$ in (E.36) represents the undesired spectral interference term consisting of $\mathcal{M}(\mathcal{M}+1)/2$ components which reduce the resolution of the spectrogram. This

term is real but not necessarily positive. The operators $\Re\{\cdot\}$ and $(\cdot)^*$ denote the real value operator and the complex conjugate operator, respectively. The cross-term in (E.36) consists of two terms. The first term of (E.36) designates the sum of the components corresponding to the spectral interference caused by the fixed scatterers. The mth component of the second term denotes the spectral interference between the moving scatterer S^{M} and the mth fixed scatterer S^{F}_m. The cross-term $S^{(c)}_{H^{(q)}}(f,t)$ in (E.36) is dependent on the random phases θ_{M} and $\theta_{\mathrm{F},m}$ unlike the auto-term $S^{(a)}_{H^{(q)}}(f,t)$. Hence, the cross-term $S^{(c)}_{H^{(q)}}(f,t)$ can be eliminated by taking the average over the random phases, i.e., $\mathbb{E}\{S^{(c)}_{H^{(q)}}(f,t)\}|_{\theta_{\mathrm{M}},\,\theta_{\mathrm{F},m}} = 0$, and thus, $\mathbb{E}\{S_{H^{(q)}}(f,t)\}|_{\theta_{\mathrm{M}},\,\theta_{\mathrm{F},m}} = S^{(a)}_{H^{(q)}}(f,t)$.

The TV mean Doppler shift can be obtained by using the spectrogram as follows

$$B^{(1)}_{H^{(q)}}(t) = \frac{\int\limits_{-\infty}^{\infty} f S_{H^{(q)}}(f,t)df}{\int\limits_{-\infty}^{\infty} S_{H^{(q)}}(f,t)df}. \tag{E.37}$$

If the spectrogram $S_{H^{(q)}}(f,t)$ in (E.37) is replaced by the auto-term $S^{(a)}_{H^{(q)}}(f,t)$, the TV mean Doppler shift $B^{(1)}_{H^{(q)}}(t)$ becomes equal to $B^{(1)}_{f^{(q)}}(t)$, i.e., $B^{(1)}_{H^{(q)}}(t)$=$B^{(1)}_{f^{(q)}}(t)$.

E.5 Measurements and Numerical Results

In this section, we discuss and compare the TV Doppler power characteristics of our proposed channel model with those of measured CSI data. We will describe the processing of the measured trajectory during the measurements.

E.5.1 Measurement Scenario

To complement the TV Doppler power characteristics of the proposed channel model, measurements have been performed. The CSI data and the trajectory of a pendulum (moving object) have been measured simultaneously. Two laptops have been used for measuring the CSI as Wi-Fi T_x and R_x. An IMU sensor fusion has been used to measure the trajectory of the pendulum. Figures E.2(a)–E.2(b) illustrate the measurement scenario in xy and xz planes, respectively. The pendulum was a 3 kg medicine ball, covered with aluminum foil and attached to the ceiling by a rope, and was swinging in a horizontal direction perpendicular to the line-of-sight (LoS). The distance between the ceiling and the center of mass (CoM) of the ball L was 1.17 m and the horizontal distance between Wi-Fi T_x antenna and the CoM of the ball was 1.5 m. The distance between Wi-Fi T_x and R_x antennas was 2 m and they had the same height value of 1.18 m. The initial location of the moving scatterer (ball) was the origin. The pendulum displacements $x_{\mathrm{M}}(t)$ and $z_{\mathrm{M}}(t)$ are computed as follows [36]:

$$x_{\mathrm{M}}(t) = L \sin\left(\arcsin\left(\frac{x_{\max}}{L}\right)\cos\left(\sqrt{\frac{g}{L}}t\right)\right) \tag{E.38}$$

$$y_{\mathrm{M}}(t) = 0 \tag{E.39}$$

$$z_{\mathrm{M}}(t) = L\left\{1 - \cos\left[\arcsin\left(\frac{x_{\mathrm{M}}(t)}{L}\right)\right]\right\} \tag{E.40}$$

where g denotes the acceleration of gravity. The parameters $x_{\max}$ and L in (E.38)-(E.40) were set to 0.55 m and 1.17 m according to Figure E.2(a)-E.2(b), respectively.

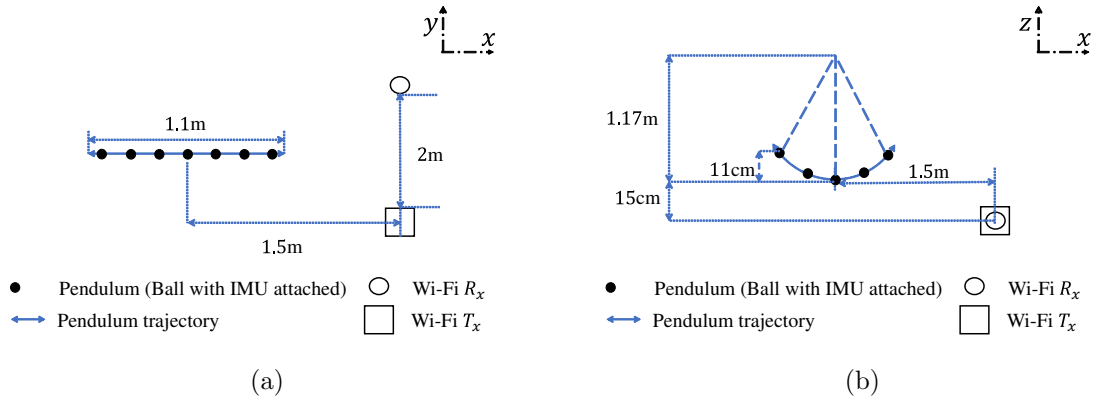

(a) (b)

Figure E.2: A presentation of the experiment scenario in the (a) xy plane and (b) xz plane.

E.5.2 Motion Capturing Using IMU

A MetaMotionR sensor fusion (IMU) [51] was attached to the swinging ball. A smartphone was connected via Bluetooth to control the IMU and log the data files. The IMU was used to record quaternions and linear accelerations during the experiment. Euler angles were computed by using the recorded quaternions to rotate the measured linear accelerations. Next, the raw rotated linear accelerations were smoothed by using quadratic regression provided by the signal analysis toolbox in MATLAB 2019a. After that, the rotated linear accelerations were integrated and double integrated to obtain the velocities and the displacements (trajectories), respectively. Due to measurement errors of the IMU, the velocities and the displacements suffer from linear and quadratic drifts, respectively. To overcome this drift issue, zero-update (ZUPT) algorithms [45] were employed. Since the pendulum motion is periodic, its horizontal and vertical velocities reach zero when the horizontal and vertical accelerations approach their maximum or minimum values. Similarly, the values of horizontal and vertical displacements approach zero values when the velocities tend to their maximum or minimum values. Hence, by searching for the indices corresponding to the local maximum or minimum values of the

accelerations, the velocity drift is removed between two consecutive indices. Also, by knowing the indices of the local maximum or minimum values of the drift-eliminated velocities, the drift of the displacement is removed. The source code of the ZUPT algorithm, where the sensors are placed on the toes of a walking person for position tracking, is available online [46]. This algorithm was repeated to also eliminate the drift of the displacement. Figure E.3(a) depicts the TV drift-free horizontal displacements $x_{\mathrm{M}}(t)$ of the captured data from the IMU and the mechanical model of the pendulum in (E.38) by using the pendulum parameters shown in Figure E.2. The TV drift-free vertical displacements $z_{\mathrm{M}}(t)$ of the captured data from the IMU and the mechanical model of the pendulum in (E.40) by using the pendulum parameters shown in Figure E.2, are depicted in Figure E.3(b). A minimal error is noticed between the IMU data and the model in the order of centimeters during the whole interval of 15 s.

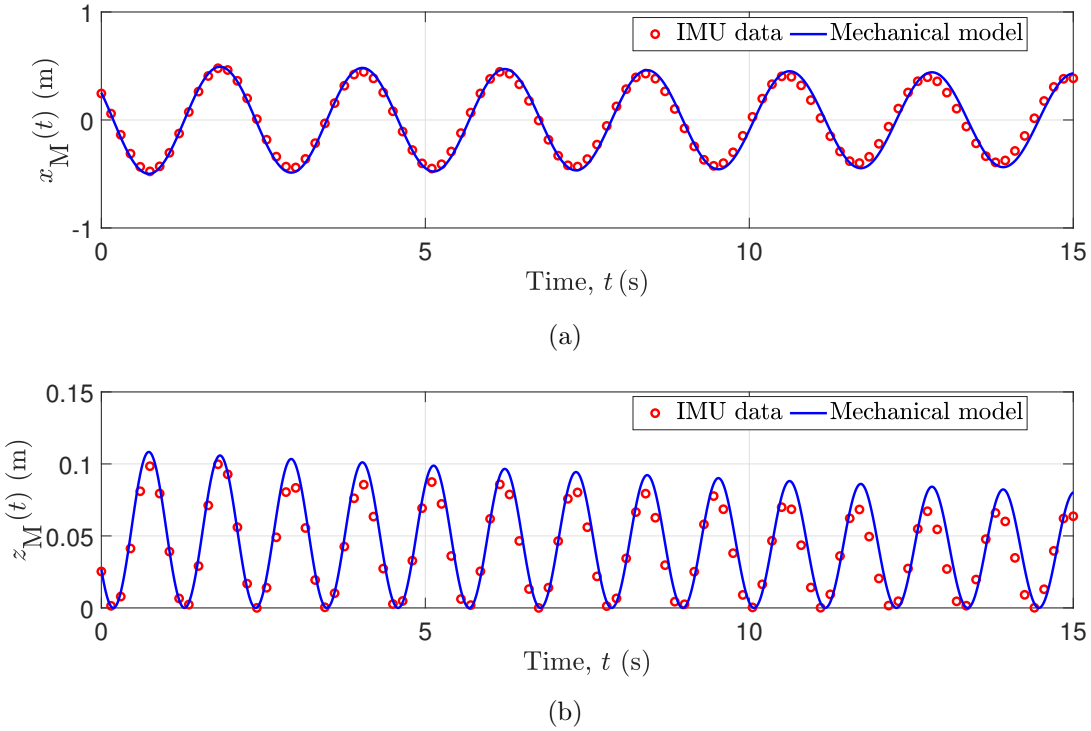

Figure E.3: Trajectories of the mechanical model and measured IMU data in (a) horizontal direction $x_{\mathrm{M}}(t)$ and (b) vertical direction $z_{\mathrm{M}}(t)$.

E.5.3 Capturing CSI Data

The CSI tool in [18] was installed to capture the CSI data (RF signals). Two HP Elitebook 6930p laptops equipped with Intel NIC5300 were used. An Ubuntu 14.04 LTS operating system was installed on both laptops. One laptop was the transmitter station in injector mode and the other laptop was the receiver operating in monitor mode. The carrier frequency f_0 was set to 5.32 GHz corresponding to channel 64 according to IEEE 802.11n standards [19]. The sampling frequency and the bandwidth were set to 1 KHz and 20 MHz, respectively. TV phase distortions exist due to carrier frequency offset [21–23], sampling frequency offset [24–26], and packet boundary delay [27, 28]. These TV phase distortions were eliminated by using a B2B connection between the transmitter station and the receiver station as described in [35]. Since there was only one RF transmission port in the Wi-Fi T_x, an RF power splitter ZFSC-2-10G+ from Mini-Circuits® with two output ports was used. One of the output ports was used for the B2B connection and the other one was connected to the transmitting antenna. At the Wi-Fi receiver laptop, one of the ports was used for the B2B connection, and another port was connected to the receiver antenna. The port used for the B2B connection was connected to a 30 dB attenuator. RF cables 141-1MSM+ from Mini-Circuits® were used as well. The processing of the captured CSI data was done by using MATLAB R2019a. Two matrices are stored in a file. One matrix contains the CSI data that corresponds to the captured signal with the fingerprint information associated with the motion of the pendulum and TV phase distortions. The other matrix corresponds to the B2B connection, i.e., it only contains the TV phase distortions. Then, the matrix that contains the fingerprint information and TV phase distortions is divided by the matrix corresponding to the B2B connection in elementwise form. The output matrix resulting from the elementwise division only contains the fingerprint information. After the elementwise division, a highpass filter has been used to reduce the power of zero-frequency components associated with the fixed scatterers and/or the line-of-sight.

Regarding the channel model and its spectrogram, Figure E.4(a) shows the block diagram of the proposed channel model discussed in Section E.3 fed with IMU data as inputs and the computation of the spectrogram. Figure E.4(b) shows the block diagram of the proposed channel model discussed in Section E.3 fed with the mechanical model as inputs and the computation of the spectrogram. Note that the difference between Figure E.4(a) and Figure E.4(b) is how the trajectories are obtained to feed the channel model. If they are measured using IMU, then the preprocessing mentioned Section E.5.2 should be considered before feeding them to the simulator. If they are computed using the expressions in (E.38)-(E.40), then they can be fed into the simulator directly. The channel model can be fed with the TV displacements from either the IMU (after applying ZUPT) or the mechanical model presented earlier in Section E.5.2, as inputs. The carrier frequency of the simulator f_0 was set to 5.32 GHz for consistency with CSI measurement scenario. The number of the fixed scatterers

$\mathcal{M}$ was chosen to be 6. The initial location of the moving scatterer S^{M} and the locations of the Wi-Fi T_x, Wi-Fi R_x were set according to the experiment scenario as presented in Figure E.2, i.e., they can be located anywhere, but the distances should be the same as those illustrated in Figure E.2. Then, the TV displacements as presented in Figure E.3 were added to the initial location of the moving scatterer S^{M}. After that, the TV Doppler frequency $f_{\mathrm{M}}^{(q)}(t)$ caused by the moving scatterer S^{M} was computed according to (E.21). The path gains of the moving scatterer S^{M} and each fixed scatterer S_m^{F} were computed by

$$c_{\mathrm{M}} = \sqrt{2\eta} \qquad \text{and} \qquad c_{\mathrm{F},m} = \sqrt{\frac{2\,(1-\eta)}{\mathcal{M}}} \tag{E.41}$$

respectively. The parameter η is used to balance the contribution of the fixed and moving scatterers and was set to 0.8. The phases θ_{M} and $\theta_{\mathrm{F},m}$ were generated as realizations of random variables with uniform distribution from $-\pi$ to π. Next, the STFT $X_{H^{(q)}}(f,t)$ for each subcarrier index q was computed according to (E.28). The window spread parameter σ_w was set 31.1 ms. Finally, the spectrogram $S(f,t)$ (or $\tilde{S}(f,t)$ in case of using IMU data as inputs) was computed as the squared magnitude of the sum of the STFT over the subcarriers by the following expression

$$S(f,t) \;=\; \left|\sum_{q} X_{H^{(q)}}(f,t)\right|^2 . \tag{E.42}$$

For computing the spectrogram of the recorded CSI as exhibited in Figure E.4(c), the CTF $\hat{H}^{(q)}(t,\Delta f^{(q)})$ is recorded. Then, the STFT $\hat{X}_{H^{(q)}}(f,t)$ was computed for each subcarrier q. After that the spectrogram $\hat{S}(f,t)$ is computed according to (E.42).

Figure E.5(a)–E.5(c) exhibit the spectrograms of $\tilde{S}(f,t)$, $S(f,t)$, and $\hat{S}(f,t)$ of the channel model with IMU data as inputs, the channel model fed with the mechanical model as inputs, and the recorded CSI data, respectively. It is shown that the TV Doppler power characteristics depicted by the spectrograms $\tilde{S}(f,t)$, $S(f,t)$, and $\hat{S}(f,t)$ in Figure E.5(a)–E.5(c) are fairly similar to each other, respectively. In Figure E.5(a)–E.5(c), the Doppler frequency associated with the moving scatterer (pendulum) S^{M} has negative values when the pendulum swings away from the Wi-Fi T_x and Wi-Fi R_x antennas and has positive values when it swings towards them. The Doppler frequency corresponding to the moving scatterer (pendulum) S^{M} approaches zero values at the time instants in which the moving scatterer reach its local maximum and minimum displacement values [see Figure E.3(a)–E.3(b)]. Therefore, the speed of the pendulum $\mathrm{v}_{\mathrm{M}}(t)$ approaches zero values. Thus, the Doppler shift at these instants is zero according to (E.22).

Figure E.6 depicts the TV mean Doppler shifts $\tilde{B}^{(1)}(t)$, $B^{(1)}(t)$, and $\hat{B}^{(1)}(t)$ computed from the spectrograms $\tilde{S}(f,t)$, $S(f,t)$, and $\hat{S}(f,t)$ using (E.37), respectively. There is a good match between $\tilde{B}^{(1)}(t)$, $B^{(1)}(t)$, and $\hat{B}^{(1)}(t)$. The mean Doppler shifts have negative values at

the time instants in which the pendulum (moving scatterer S^{M}) swings away from the Wi-Fi T_x and Wi-Fi R_x antennas. They have positive values when the pendulum swings towards the Wi-Fi T_x and Wi-Fi R_x antennas. The TV mean Doppler shifts $\tilde{B}^{(1)}(t)$, $B^{(1)}(t)$, and $\hat{B}^{(1)}(t)$ approach zero values at the moments when the pendulum reaches its local maximum and minimum displacement values. There exists a slight drift in the values of the mean Doppler shift $\hat{B}^{(1)}(t)$ in between the time instants $t \approx 11.5$ s and $t \approx 12.7$ s due to the noise of the measured CSI signal.

For quantitative evaluation, we collected CSI and IMU data for 20 experiments, i.e., $K = 20$. From the collected data measurement, we computed the normalized-mean-square-error (NMSE) γ_k between the TV mean Doppler shift $\tilde{B}_k^{(1)}(t)$ of the proposed channel model fed with the IMU data as inputs and the TV mean Doppler shift $\hat{B}_k^{(1)}(t)$ of the CSI data according to

$$\gamma_k = \frac{\int_0^{T_{\mathrm{obs}}} \left(\tilde{B}_k^{(1)}(t) - \hat{B}_k^{(1)}(t) \right)^2 dt}{\int_0^{T_{\mathrm{obs}}} \left(\hat{B}_k^{(1)}(t) \right)^2 dt} \tag{E.43}$$

for $k = 1, 2, \ldots, K$, where the parameter T_{obs} denotes the observation interval which was set to 15 seconds, i.e., $T_{\mathrm{obs}} = 15$ s. Figure E.7 depicts the NMSE γ_k for each experiment. The maximum NMSE belongs to the first experiment and has a value of 0.1829, whereas the minimum NMSE, with a value of 0.0477, belongs to fourteenth experiment. The average NMSE equals 0.0932, and the variance of the NMSE is 0.0013.

E.6 Conclusion

In this paper, we proposed a non-stationary wideband channel model and its TV Doppler power characteristics when there is a moving object in the 3D space. We derived the TV Doppler shift caused by the moving object in terms of the TV speed, AAOM, EAOM, AAOD, EAOD, AAOA, and EAOA. The TV Doppler characteristics of the proposed channel model were analyzed by using the spectrogram. Furthermore, we provided the approximate solution of the spectrogram of the channel model. We validated the proposed channel model by measuring the trajectory of the moving object using an IMU and calibrated CSI with B2B connection, simultaneously. Then, we fed the channel model with the trajectory data extracted form the IMU. The results showed a good agreement between the measured CSI and the channel model in terms of the spectrogram and the mean Doppler shift. We conclude that the proposed channel model can be used for designing simulation-based HAR systems. For the future, we aim to extend the proposed channel model for human activity recognition by modelling the moving human as multiple moving scatterers.

Acknowledgments

The authors would like to acknowledge Takada Lab in the Department of Transdisciplinary Science and Engineering, Tokyo Institute of Technology, Japan. In particular, the doctoral student, Nopphon Keerativoranan, and his supervisor, Prof. Jun-ichi Takada, consulted us with establishing the B2B connection in the measurement setup. Their contribution is highly appreciated.

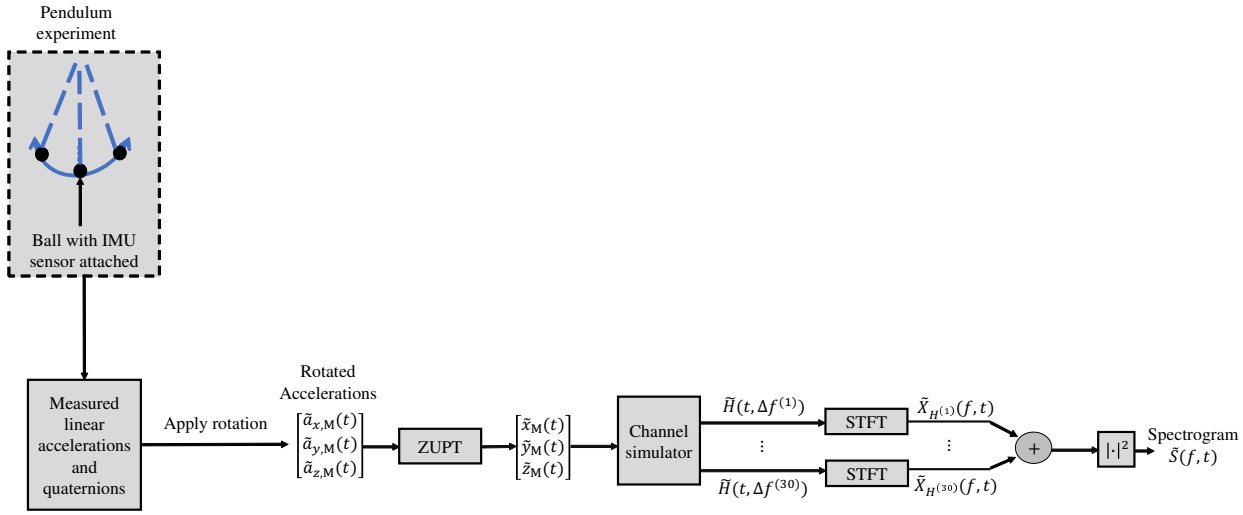

(a)

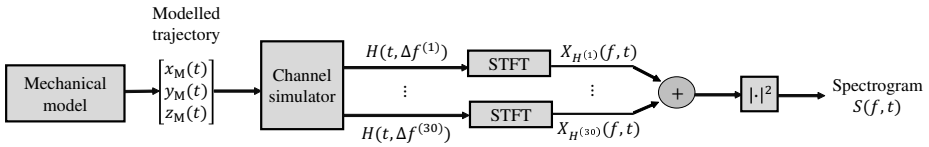

(b)

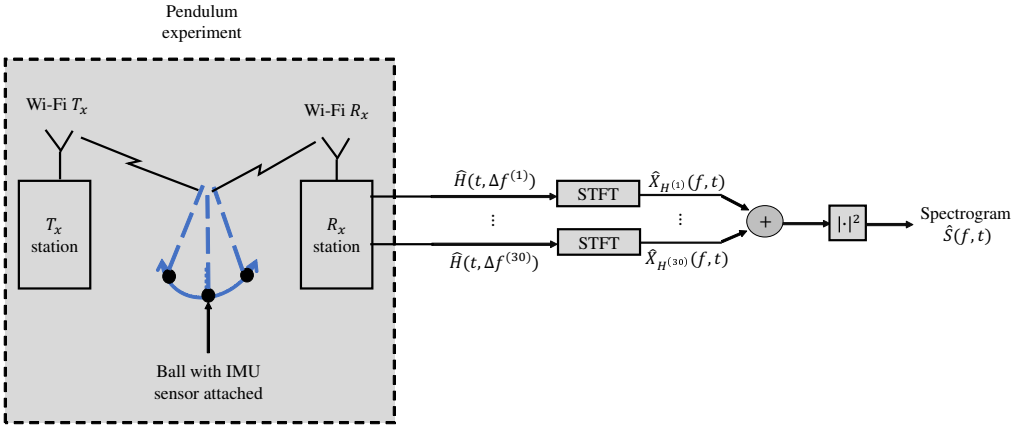

(c)

Figure E.4: Block diagrams illustrating steps to compute the spectrograms $\tilde{S}(f,t)$, $S(f,t)$, and $\hat{S}(f,t)$ of (a) the channel model with the IMU data as input, (b) the channel model with the trajectories of the mechanical model as inputs, and (c) measured CSI data, respectively.

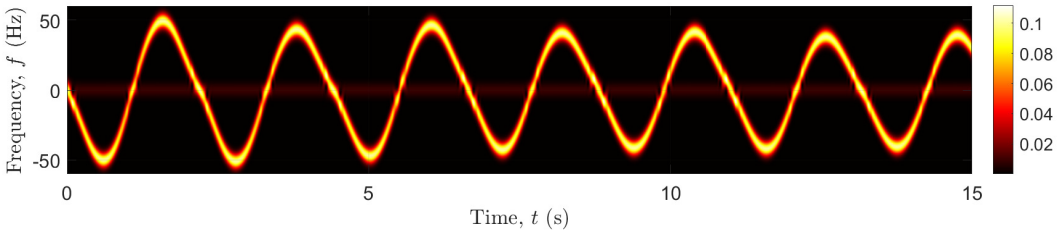

(a)

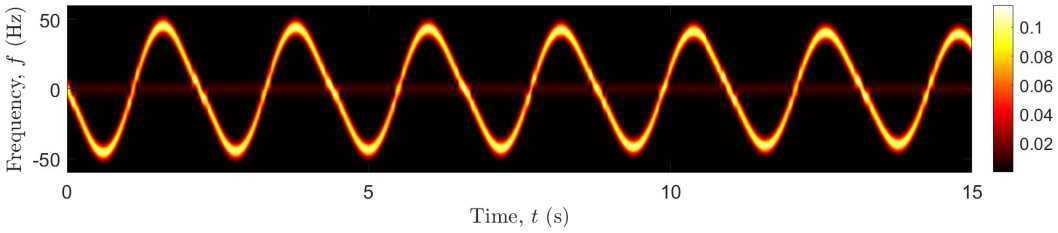

(b)

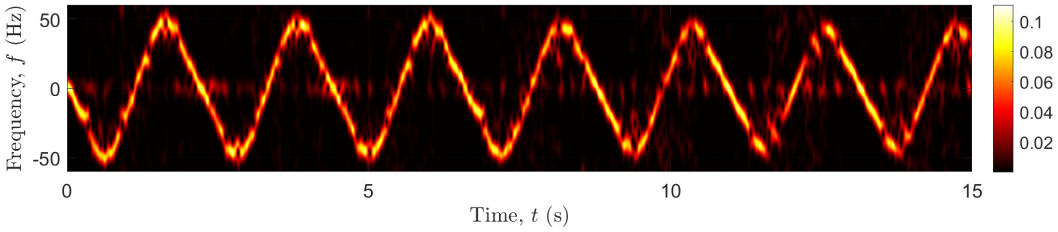

(c)

Figure E.5: Spectrograms $\tilde{S}(f,t)$, $S(f,t)$, and $\hat{S}(f,t)$ (a) the channel model with IMU data as inputs, (b) the channel model with the mechanical model of the pendulum as inputs, and (c) measured CSI, respectively.

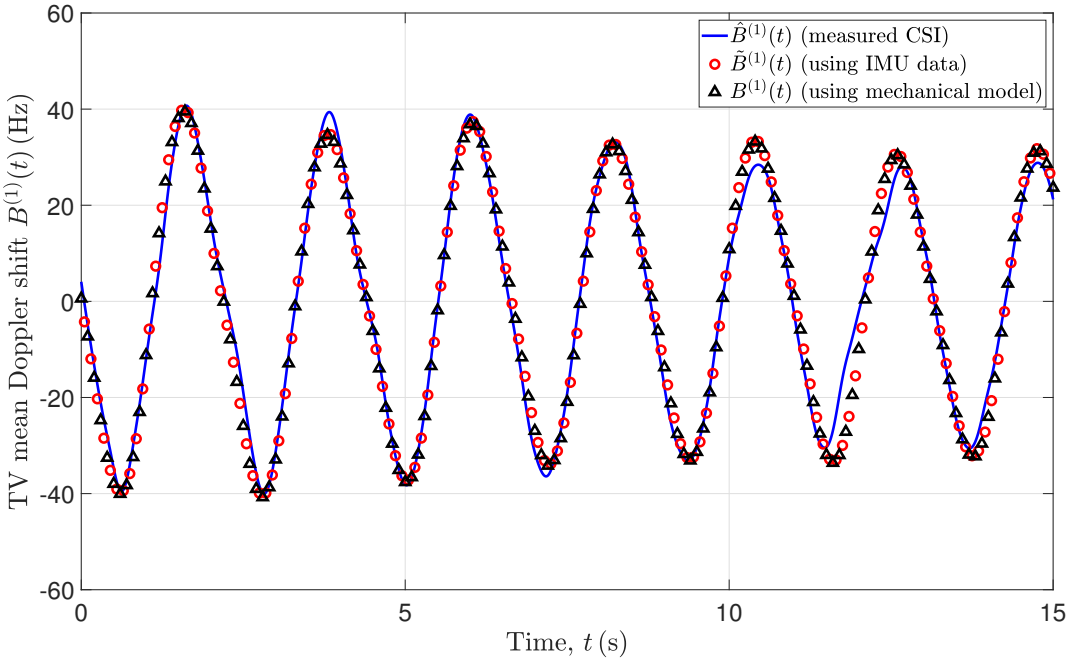

Figure E.6: TV mean Doppler shifts $\tilde{B}^{(1)}(t)$, $B^{(1)}(t)$, and $\hat{B}^{(1)}(t)$ computed from the spectrograms of the channel model with IMU data as inputs, mechanical model as inputs, and the measured CSI, respectively.

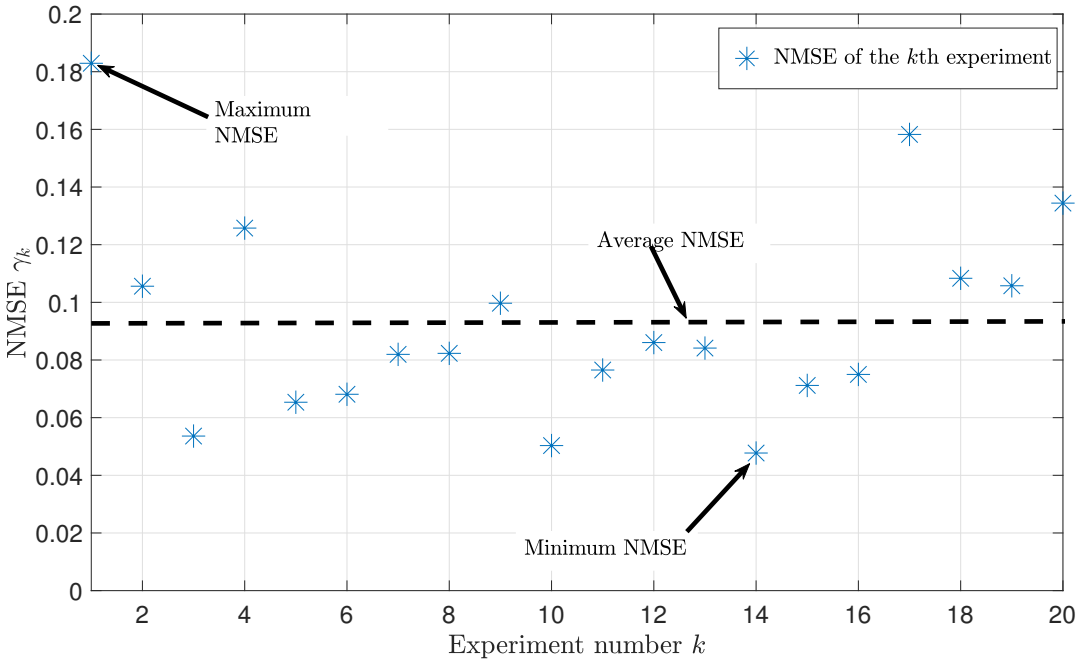

Figure E.7: NMSE γ_k of each experiment computed from the TV mean Doppler shift $\tilde{B}_k^{(1)}(t)$ of the channel model fed with IMU data as inputs and the measured TV mean Doppler shift $\hat{B}_k^{(1)}(t)$ for $k = 1, 2, \ldots, K$.

E

Bibliography

[1] M. Jian, Z. Lu, and V. C. Chen, "Drone detection and tracking based on phase-interferometric Doppler radar," in *2018 IEEE Radar Conference (RadarConf18)*, pp. 1146–1149, April 2018.

[2] M. G. Amin, Z. Zeng, and T. Shan, "Hand gesture recognition based on radar micro-Doppler signature envelopes," in *2019 IEEE Radar Conference (RadarConf)*, pp. 1–6, April 2019.

[3] A. Seifert, A. M. Zoubir, and M. G. Amin, "Detection of gait asymmetry using indoor Doppler radar," in *2019 IEEE Radar Conference (RadarConf)*, pp. 1–6, April 2019.

[4] F. Adib, Z. Kabelac, D. Katabi, and R. C. Miller, "3D tracking via body radio reflections," in *Proc. of the 11th USENIX Conference on Networked Systems Design and Implementation NSDI'14*, (Berkeley, CA, USA), pp. 317–329, USENIX Association, 2014.

[5] V.-H. Pham, M.-H. Taieb, J.-Y. Chouinard, S. Roy, and H.-T. Huynh, "On the double Doppler effect generated by scatterer motion," *REV Journal on Electronics and Communications*, vol. 1, pp. 30–37, Mar. 2011.

[6] A. Abdelgawwad and M. Pätzold, "On the influence of walking people on the Doppler spectral characteristics of indoor channels," in *Proc. 28th IEEE Int. Symp. on Personal, Indoor and Mobile Radio Communications, PIMRC 2017*, Montreal, Canada, Oct. 2017.

[7] A. Abdelgawwad and M. Paetzold, "A 3d non-stationary cluster channel model for human activity recognition," in *2019 IEEE 89th Vehicular Technology Conference (VTC2019-Spring)*, pp. 1–7, April 2019.

[8] J. Bian, C. Wang, M. Zhang, X. Ge, and X. Gao, "A 3-D non-stationary wideband MIMO channel model allowing for velocity variations of the mobile station," in *IEEE International Conference on Communications (ICC)*, pp. 1–6, May 2017.

[9] S. Z. Gurbuz, C. Clemente, A. Balleri, and J. J. Soraghan, "Micro-doppler-based in-home aided and unaided walking recognition with multiple radar and sonar systems," *IET Radar, Sonar Navigation*, vol. 11, no. 1, pp. 107–115, 2017.

[10] X. Wang, P. Wang, X. Cao, and V. C. Chen, "Interferometric angular velocity measurement of rotating blades: theoretical analysis, modeling and simulation study," *IET Radar, Sonar Navigation*, vol. 13, no. 3, pp. 438–444, 2019.

[11] M. Ritchie and A. M. Jones, "Micro-Doppler gesture recognition using doppler, time and range based features," in *2019 IEEE Radar Conference (RadarConf)*, pp. 1–6, April 2019.

[12] B. Erol and M. G. Amin, "Radar data cube processing for human activity recognition using multi subspace learning," *IEEE Transactions on Aerospace and Electronic Systems*, pp. 1–1, 2019.

[13] A. Seifert, M. G. Amin, and A. M. Zoubir, "Toward unobtrusive in-home gait analysis based on radar micro-Doppler signatures," *IEEE Transactions on Biomedical Engineering*, vol. 66, pp. 2629–2640, Sep. 2019.

[14] F. Fioranelli, M. Ritchie, S.-Z. Gürbüz, and H. Griffiths, "Feature diversity for optimized human micro-Doppler classification using multistatic radar," *IEEE Transactions on Aerospace and Electronic Systems*, vol. 53, pp. 640–654, Apr. 2017.

[15] M. Wu, X. Dai, Y. D. Zhang, B. Davidson, M. G. Amin, and J. Zhang, "Fall detection based on sequential modeling of radar signal time-frequency features," in *IEEE International Conference on Healthcare Informatics*, pp. 169–174, Sep. 2013.

[16] G. A. M, Y. D. Zhang, F. Ahmad, and K. C. D. Ho, "Radar signal processing for elderly fall detection: the future for in-home monitoring," *IEEE Signal Processing Magazine*, vol. 33, pp. 71–80, Mar. 2016.

[17] B. Jokanović and M. Amin, "Fall detection using deep learning in range-Doppler radars," *IEEE Transactions on Aerospace and Electronic Systems*, vol. 54, pp. 180–189, Feb 2018.

[18] D. Halperin, W. Hu, A. Sheth, and D. Wetherall, "Tool release: gathering 802.11n traces with channel state information," *ACM SIGCOMM CCR*, vol. 41, p. 53, Jan. 2011.

[19] "IEEE standard for information technology– local and metropolitan area networks– specific requirements– part 11: Wireless lan medium access control (mac) and physical layer (phy) specifications amendment 5: Enhancements for higher throughput," *IEEE Std 802.11n-2009 (Amendment to IEEE Std 802.11-2007 as amended by IEEE Std 802.11k-2008, IEEE Std 802.11r-2008, IEEE Std 802.11y-2008, and IEEE Std 802.11w-2009)*, pp. 1–565, Oct 2009.

[20] Z. Wang, B. Guo, Z. Yu, and X. Zhou, "Wi-Fi CSI-based behavior recognition: from signals and actions to activities," *IEEE Communications Magazine*, vol. 56, pp. 109–115, May 2018.

[21] X. Wang, C. Yang, and S. Mao, "Phasebeat: exploiting csi phase data for vital sign monitoring with commodity wifi devices," in *2017 IEEE 37th International Conference on Distributed Computing Systems (ICDCS)*, pp. 1230–1239, June 2017.

[22] Y. Xie, Z. Li, and M. Li, "Precise power delay profiling with commodity wifi," in *Proceedings of the 21st Annual International Conference on Mobile Computing and Networking*, MobiCom '15, (New York, NY, USA), pp. 53–64, ACM, 2015.

[23] D. Vasisht, S. Kumar, and D. Katabi, "Decimeter-level localization with a single wifi access point," in *Proceedings of the 13th Usenix Conference on Networked Systems Design and Implementation*, NSDI'16, (Berkeley, CA, USA), pp. 165–178, USENIX Association, 2016.

[24] L. Gong, W. Yang, D. Man, G. Dong, M. Yu, and J. Lv, "Wifi-based real-time calibration-free passive human motion detection," in *Sensors*, 2015.

[25] M. N. Mahfoudi, T. Turletti, T. Parmentelat, F. Ferrero, L. Lizzi, R. Staraj, and W. Dabbous, "Orion: orientation estimation using commodity wi-fi," in *2017 IEEE International Conference on Communications Workshops (ICC Workshops)*, pp. 1233–1238, May 2017.

[26] M. Kotaru, K. Joshi, D. Bharadia, and S. Katti, "Spotfi: decimeter level localization using wifi," *SIGCOMM Comput. Commun. Rev.*, vol. 45, pp. 269–282, August 2015.

[27] K. Qian, C. Wu, Z. Yang, Z. Zhou, X. Wang, and Y. Liu, "Tuning by turning: Enabling phased array signal processing for wifi with inertial sensors," in *IEEE INFOCOM 2016 - The 35th Annual IEEE International Conference on Computer Communications*, pp. 1–9, April 2016.

[28] Y. Zhuo, H. Zhu, and H. Xue, "Identifying a new non-ninear csi phase measurement error with commodity wifi devices," in *2016 IEEE 22nd International Conference on Parallel and Distributed Systems (ICPADS)*, pp. 72–79, Dec 2016.

[29] W. Wang, A. X. Liu, and M. Shahzad, "Gait recognition using wifi signals," in *Proceedings of the 2016 ACM International Joint Conference on Pervasive and Ubiquitous Computing*, UbiComp '16, (New York, NY, USA), pp. 363–373, ACM, 2016.

[30] X. Wu, Z. Chu, P. Yang, C. Xiang, X. Zheng, and W. Huang, "Tw-see: human activity recognition through the wall with commodity wi-fi devices," *IEEE Transactions on Vehicular Technology*, vol. 68, pp. 306–319, Jan 2019.

[31] C. Du, X. Yuan, W. Lou, and Y. T. Hou, "Context-free fine-grained motion sensing using wifi," in *2018 15th Annual IEEE International Conference on Sensing, Communication, and Networking (SECON)*, pp. 1–9, June 2018.

[32] J. Chen, F. Li, H. Chen, S. Yang, and Y. Wang, "Dynamic gesture recognition using wireless signals with less disturbance," *Personal and Ubiquitous Computing*, vol. 23, pp. 17–27, Feb 2019.

[33] S. Sen, B. Radunovic, R. R. Choudhury, and T. Minka, "You are facing the mona lisa: spot localization using phy layer information," in *Proceedings of the 10th International*

Conference on Mobile Systems, Applications, and Services, MobiSys '12, (New York, NY, USA), pp. 183–196, ACM, 2012.

[34] K. Qian, C. Wu, Z. Yang, Y. Liu, and Z. Zhou, "Pads: Passive detection of moving targets with dynamic speed using phy layer information," in *2014 20th IEEE International Conference on Parallel and Distributed Systems (ICPADS)*, pp. 1–8, Dec 2014.

[35] N. Keerativoranan, A. Haniz, K. Saito, and J.-i. Takada, "Mitigation of csi temporal phase rotation with b2b calibration method for fine-grained motion detection analysis on commodity wi-fi devices," *Sensors*, vol. 18, no. 11, 2018.

[36] R. S. A. R. Abdullah, A. Alnaeb, A. A. Salah, N. E. A. Rashid, A. Sali, and I. Pasya, "Micro-Doppler estimation and analysis of slow moving objects in forward scattering radar system," *Remote Sensing*, vol. 9, no. 7, 2017.

[37] V. Chen, *The Micro-Doppler Effect in Radar, Second Edition*. Artech House radar library, Artech House, 2019.

[38] D. E. Dauger, "Simulation and study of Fresnel diffraction for arbitrary two-dimensional apertures," *Computers in Physics*, vol. 10, no. 6, pp. 591–604, 1996.

[39] R. He, Z. Zhong, B. Ai, J. Ding, and K. Guan, "Analysis of the relation between Fresnel zone and path loss exponent based on two-ray model," *IEEE Antennas and Wireless Propagation Letters*, vol. 11, pp. 208–211, 2012.

[40] A. Goldsmith, *Wireless Communications*. U.K. Cambridge, Cambridge University. Press, 2004.

[41] T. Rappaport, *Wireless Communications: Principles and Practice*. USA: Prentice Hall PTR, 2nd ed., 2001.

[42] F. Zhang *et al.*, "Towards a diffraction-based sensing approach on human activity recognition," *Proc. ACM Interact. Mob. Wearable Ubiquitous Technol.*, vol. 3, Mar. 2019.

[43] F. Zhang, D. Zhang, J. Xiong, H. Wang, K. Niu, B. Jin, and Y. Wang, "From Fresnel diffraction model to fine-grained human respiration sensing with commodity Wi-Fi devices," *Proceedings of the ACM on Interactive, Mobile, Wearable and Ubiquitous Technologies*, vol. 2, no. 1, pp. 1–23, 2018.

[44] T. Xin, B. Guo, Z. Wang, P. Wang, J. C. K. Lam, V. O. K. Li, and Z. Yu, "Freesense: a robust approach for indoor human detection using Wi-Fi signals," *IMWUT*, vol. 2, pp. 143:1–143:23, 2018.

[45] X. Yun, E. R. Bachmann, H. Moore, and J. Calusdian, "Self-contained position tracking of human movement using small inertial/magnetic sensor modules," in *Proceedings 2007 IEEE International Conference on Robotics and Automation*, pp. 2526–2533, April 2007.

[46] "Matlab code for 3D tracking with IMU," Available online: `https://github.com/xioTechnologies/Gait-Tracking-With-x-IMU`.

[47] M. Pätzold and C. A. Gutierrez, "Modelling of non-WSSUS channels with time-variant Doppler and delay characteristics," in *2018 IEEE Seventh International Conference on Communications and Electronics (ICCE)*, pp. 1–6, Hue, Vietnam, July 2018.

[48] A. Abdelgawwad and M. Pätzold, "A framework for activity monitoring and fall detection based on the characteristics of indoor channels," in *IEEE 87th Vehicular Technology Conference (VTC Spring)*, Porto, Portugal, Jun. 2018.

[49] M. Pätzold, C. A. Gutiérrez, and N. Youssef, "On the consistency of non-stationary multipath fading channels with respect to the average Doppler shift and the Doppler spread," in *Proc. IEEE Wireless Communications and Networking Conference, WCNC 2017*, San Francisco, CA, USA, 2017.

[50] B. Boashash, *Time-Frequency Signal Analysis and Processing – A Comprehensive Reference*. Elsevier, Academic Press, 2nd ed., 2015.

[51] "Sensors for motion capture, biomechanics, industrial control, robotics, facility management, cold storage, research, and product development," `https://mbientlab.com/`.

Appendix F

Paper F

Title:	An IMU-Driven 3D Non-Stationary Channel Model for Human Activity Recognition
Authors:	Ahmed Abdelgawwad[1], Andreu Català[2], and Matthias Pätzold[1]
Affiliation:	[1]University of Agder, Faculty of Engineering and Science, P. O. Box 509, NO-4898 Grimstad, Norway
	[2]Universitat Politècnica de Catalunya (UPC), Rambla de l'Exposició, 59-69, 08800 Vilanova i la Geltrú, Barcelona, Spain
Journal:	Submitted to *IEEE Access*.

An IMU-Driven 3D Channel Model for Human Activity Recognition

Ahmed Abdelgawwad[1], Andreu Català[2], and Matthias Pätzold[1]
[1]Faculty of Engineering and Science, University of Agder, P.O. Box 509, 4898 Grimstad, Norway
[2]Universitat Politècnica de Catalunya (UPC), Rambla de l'Exposició, 59-69, 08800 Vilanova i la Geltrú, Barcelona, Spain
Emails: [1]{ahmed.abdel-gawwad, matthias.paetzold}@uia.no, [2]andreu.catala@upc.edu

Abstract **— This paper concerns the design, analysis, and simulation of a 3D non-stationary channel model fed with inertial measurement unit (IMU) data. The work in this paper provides a framework for simulating the micro-Doppler signatures of indoor channels for human activity recognition by using radio-frequency-based sensing technologies. The major human body segments, such as wrists, ankles, torso, and head, are modelled as a cluster of moving point scatterers. We provide expressions for the time variant (TV) speed and TV angles of motion based on 3D trajectories of the moving person. Moreover, we present mathematical expressions for the TV Doppler shifts and TV path gains associated with each moving point scatterer. Furthermore, a model of the non-stationary TV channel transfer function (TV-CTF) is provided, which takes into account the effects caused by a moving person as well as fixed objects, such as furniture, walls, and ceiling. The micro-Doppler signatures of the moving person is extracted from the TV-CTF by employing the concept of the spectrogram, whose expression is also provided in closed form. Our model is confirmed by channel-state-information (CSI) measurements taken during walking, falling, and sitting activities. The proposed channel model is fed with IMU data that has been collected. We evaluate the micro-Doppler signature of the model and CSI measurements. The results show a good agreement between the spectrograms and the TV mean Doppler shifts of our IMU-driven channel model and the measured CSI. The proposed model enables a paradigm shift from traditional experimental-based approaches to future simulation-based approaches for the design of human activity recognition systems.**

Index Terms **— Human activity recognition, non-stationary fading channels, channel state information, channel transfer function, spectrogram, time-variant Doppler power characteristics, micro-Doppler signature, channel measurements, inertial measurement units, Internet of things, wireless sensing.**

F

F.1 Introduction

The unsupervised monitoring of human mobility parameters during the activities of daily living is generating a high interest in the medical community, especially after the explicit recommendation of the US Food and Drug Administration [1] and the European Medicines Agency [2] that it is desirable to include information from portable or context-aware systems in clinical trials. Other reasons for the high interest are the increase of fall incidents among adults over 65 years according to the US fall report [3] and the high mortality rate caused by fall incidents according to the World Population Ageing Report of the United Nations [4]. Although there are still many problems to solve, mainly in the lack of gold standards, a good indication of the growth prospect of these context-aware systems is their adoption and development in the next five years by the main pharmaceutical companies of the diseases related to pathological human movement [5]. Monitoring systems can detect movement disorders, which can be signs of physical and mental illness and fragility. Small changes in the quality and complexity of movements can be indicators of an impending deterioration in health status, which in many cases can be reversed with appropriate rehabilitation measures.

The first challenge in the development of monitoring systems is to clearly identify the main types of movements used in clinical practice, such as cadence when walking, stride length, sit to stand, stand to sit, turns, and adverse events such as falls. The accurate and convenient measurement of the above parameters at the user's home over long periods of time is a milestone that may lead to significant advances in geriatrics.

This article is part of a recent line of research that tries to extract knowledge from human activities at home using conventional Wi-Fi systems. Such systems have the advantages over wearable systems as they are easy to use, comfortable, have low cost, no stigmatization, and universal availability. The enormous penetration of Wi-Fi systems in all households carries a high degree of acceptance. In addition, such systems do not violate the users' privacy like human activity recognition (HAR) systems based on camera surveillance [6–9]. Moreover, they do not require user involvement, which is mandatory when using smartphones or wearable sensors [10–13] that may be forgotten to wear. With Wi-Fi systems, it is possible to collect radio-frequency (RF) sensing data continuously while the users can carry out their daily living activities without disturbance.

The literature describes radar systems for classifying human activities [14–19], such as arm motion recognition for human-computer interaction in smart homes [20], gesture recognition [21–23], differentiation of unarmed and armed people for security services [24], and the detection of gait asymmetries [25,26]. In all these mentioned applications the spectrogram was employed. The spectrogram is a quadratic time-frequency power distribution that provides insight into the micro-Doppler signature of non-stationary multicomponent signals influenced by human activities.

A tool for capturing the complex channel-state-information (CSI) has been developed by

the authors of [27]. Such a tool enables the collection of RF data over 30 subcarriers and operates according to the IEEE 802.11n standard [28]. Laptops equipped with the NIC 5300 wireless network module are able to run this tool. The authors of [29] provided a survey on many contributions of different activity recognition systems by analyzing the amplitude of the CSI data acquired by the NIC 5300 module. The main drawback of the CSI tool is that the phases of the data collected are highly distorted. This is due to the clock asynchronization between the transmitter and receiver stations which makes it challenging to analyze the micro-Doppler signatures of the collected CSI data. If the spectrogram of the measured CSI is very noisy, it does not provide a clear insight into the time variant (TV) Doppler power characteristics. For noise supression, the principle component analysis [30] was applied to the amplitudes of measured CSI data, and then the one-sided spectrogram was computed. An alternative approach is to apply a linear transformation to the highly distorted phases to eliminate the phase distortions [31]. Although this approach succeeds in providing a good pattern of the transformed phases, it can partially eliminate the desired phases, which might limit the insight into the true micro-Doppler signature. A reliable solution to eliminate the phase distortions is to employ a physical back-to-back (B2B) connection. This approach was introduced, implemented, tested, and verified in [32].

The main disadvantage of the systems based on RF sensing in [14–22, 24–26] is that they require measurement data to train the classifier. This consumes a huge amount of time and effort to collect non-reproducible data. An alternative approach is to generate simulation-based reproducible data to train the classifier. In the literature, many attempts have been done to simulate radar micro-Doppler signatures of human activities such as walking in [33,34]. The authors of [35] have provided a framework to estimate the gait parameters from simulated radar micro-Doppler signatures of human walking activity, where the Thalmann human walking model described in [36] has been incorporated. Motion capture (MOCAP) databases have been employed in [37] to simulate the radar micro-Doppler signatures of different human activities such as crawling, creeping, and running. An alternative approach was to use the Microsoft Kinect sensor for collecting the trajectories to simulate the radar micro-Doppler signatures of human activities, such as walking, running, leaping, and boxing in [38].

To the best of our knowledge, inertial measurement units (IMUs) have not been used to simulate the micro-Doppler signatures of CSI channel models under the influence of human activities. The trajectories of the moving body segments can be measured by attaching the IMUs to the moving body segments. The IMUs collect the accelerations and the Euler angles. Then, we rotate the accelerations to get their projections on the reference frame. Finally, the trajectories computed from the rotated accelerations can be fed to the channel model. Such an IMU-driven channel model enables to simulate the micro-Doppler signatures.

In this paper, we present an IMU-driven non-stationary channel model that enables to simulate the multipath components associated with different body segments. Moreover, such a

model allows for in-depth understanding of the parameters that have influence on the Doppler shifts caused by the moving body segments. The contributions of this paper are listed as follows

- The moving body segments are modelled as a cluster of moving point scatterers.
- We present expressions of the TV speed, time-variant azimuth angle of motion (TV-AAOM), and time-variant elevation angle of motion (TV-EAOM) corresponding to each moving point scatterer.
- The expressions of the TV Doppler shift and the TV propagation delay associated with each moving point scatterer are provided.
- The TV path gains of the moving point scatterers are taken into account to make the proposed channel model more realistic.
- We present a model for the TV channel transfer function (TV-CTF).
- The micro-Doppler signature is extracted from the TV-CTF by means of the spectrogram, of which the closed-form expressions are provided.
- The proposed channel model is confirmed by performing the CSI and IMU measurements simultaneously for human activities.
- The spectrograms of both the CSI measurements and the IMU-driven channel model are evaluated. In addition, the results of the time variant mean Doppler shifts (TV-MDSs) computed from the spectrograms are matching.

The contributions of this paper pave the way towards design of the simulation-based HAR systems.

The rest of the paper is organized as follows. Section F.2 describes the 3D multipath propagation scenario and presents the expressions of the TV Doppler shifts, TV path gains, and the non-stationary TV-CTF corresponding to the IMU-driven channel model. Section F.3 presents the expressions of the spectrogram of the TV-CTF. Section F.4 shows how the CSI and IMU data were collected, addresses the challenges faced while processing the data, and exhibits the results of the proposed IMU-driven channel model and the measured CSI data. Section F.5 is left for the conclusion and provides an outlook to future research.

F.2 Modelling the TV-CTF

F.2.1 The Geometrical Model

In this paper, we consider an indoor propagation scenario described by the geometrical model in Fig. F.1. The geometrical model includes a Wi-Fi transmitter and a Wi-Fi receiver denoted

by T_x and R_x, respectively. Both T_x and R_x are stationary and located at $\left(x^T,\, y^T,\, z^T\right)$ and $\left(x^R,\, y^R,\, z^R\right)$, respectively, and operate according to the IEEE 802.11n standard [28]. We consider a person performing some activities during which the person's main body segments are modelled by a cluster of $\mathcal{N}$ moving point scatterers $S_{\mathrm{M},n}$ for $n = 1,\, 2,\, \ldots,\, \mathcal{N}$. Moreover, the fixed objects, such as walls, furniture, etc. are modelled as $\mathcal{M}$ fixed scatterers $S_{\mathrm{F},m}$ for $m = 1,\, 2,\, \ldots,\, \mathcal{M}$. Single-bounce scattering is assumed, i.e., any wave transmitted from the T_x reaches the R_x via either a moving point scatterer $S_{\mathrm{M},n}$ or a fixed scatterer $S_{\mathrm{F},m}$. The line-of-sight is assumed to be obstructed.

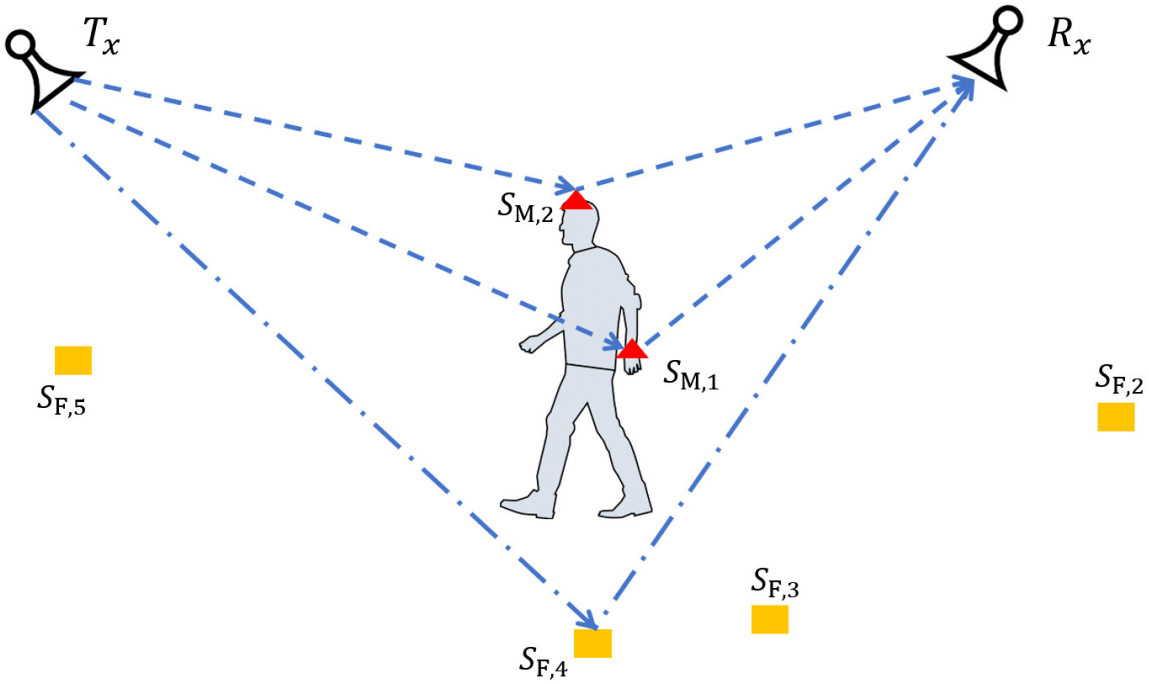

Figure F.1: Geometrical model of an indoor propagation scenario with a fixed transmitter T_x, a fixed receiver R_x, a moving person modelled by moving point scatterers (▲), and several fixed scatterers (■) representing stationary objects, such as walls, furniture, etc.

F.2.2 The TV Trajectories

The TV velocity $\vec{v}_{\mathrm{M},n}\,(t)$ associated with the nth moving point scatterer $S_{\mathrm{M},n}$ is presented as

$$\vec{v}_{\mathrm{M},n}\,(t) = \left[v_{\mathrm{M},n,x}\,(t)\ ,\ v_{\mathrm{M},n,y}\,(t)\ ,\ v_{\mathrm{M},n,z}\,(t)\right]^{\mathrm{T}} \tag{F.1}$$

where the vector transpose operation is denoted by $[\cdot]^{\mathrm{T}}$. The velocities $v_{\mathrm{M},n,x}\,(t)$, $v_{\mathrm{M},n,y}\,(t)$, and $v_{\mathrm{M},n,z}\,(t)$ in x, y, and z directions, respectively can be expressed in terms of the TV speed

$\mathrm{v}_{\mathrm{M},n}(t)$, TV-EAOM $\beta_{v_{\mathrm{M},n}}(t)$ and TV-AAOM $\alpha_{v_{\mathrm{M},n}}(t)$ as

$$v_{\mathrm{M},n,x}(t) = \mathrm{v}_{\mathrm{M},n}(t)\cos\left(\beta_{v_{\mathrm{M},n}}(t)\right)\cos\left(\alpha_{v_{\mathrm{M},n}}(t)\right) \quad \text{(F.2)}$$

$$v_{\mathrm{M},n,y}(t) = \mathrm{v}_{\mathrm{M},n}(t)\cos\left(\beta_{v_{\mathrm{M},n}}(t)\right)\sin\left(\alpha_{v_{\mathrm{M},n}}(t)\right) \quad \text{(F.3)}$$

$$v_{\mathrm{M},n,z}(t) = \mathrm{v}_{\mathrm{M},n}(t)\sin\left(\beta_{v_{\mathrm{M},n}}(t)\right) \quad \text{(F.4)}$$

respectively. The TV functions $\alpha_{v_{\mathrm{M},n}}(t)$ and $\beta_{v_{\mathrm{M},n}}(t)$ are computed by

$$\alpha_{v_{\mathrm{M},n}}(t) = \arctan2\left(v_{\mathrm{M},n,y}(t), v_{\mathrm{M},n,x}(t)\right) \quad \text{(F.5)}$$

$$\beta_{v_{\mathrm{M},n}}(t) = \arcsin\left(\frac{v_{\mathrm{M},n,z}(t)}{\sqrt{v^2_{\mathrm{M},n,x}(t) + v^2_{\mathrm{M},n,y}(t) + v^2_{\mathrm{M},n,z}(t)}}\right) \quad \text{(F.6)}$$

respectively. The elevation angle $\beta_{v_{\mathrm{M},n}}(t)$ described in (F.6) has a range from $-\pi/2$ to $\pi/2$, i.e., $\beta_{v_{\mathrm{M},n}}(t) \in [-\pi/2, \pi/2]$. The function $\arctan2(\cdot)$ returns an angle with a range from $-\pi$ to π, i.e., $\alpha_{v_{\mathrm{M},n}}(t) \in [-\pi, \pi)$. From (F.2)–(F.4), the TV displacements $x_{\mathrm{M},n}(t)$, $y_{\mathrm{M},n}(t)$, and $z_{\mathrm{M},n}(t)$ can be calculated as follows

$$x_{\mathrm{M},n}(t) = x_{\mathrm{M},n} + \int_0^t v_{\mathrm{M},x}(t')dt' \quad \text{(F.7)}$$

$$y_{\mathrm{M},n}(t) = y_{\mathrm{M},n} + \int_0^t v_{\mathrm{M},y}(t')dt' \quad \text{(F.8)}$$

$$z_{\mathrm{M},n}(t) = z_{\mathrm{M},n} + \int_0^t v_{\mathrm{M},z}(t')dt' \quad \text{(F.9)}$$

respectively. The parameters $x_{\mathrm{M},n}$, $y_{\mathrm{M},n}$, $z_{\mathrm{M},n}$ designate the initial positions of $S_{\mathrm{M},n}$ in the x, y, and z directions, respectively. By using the TV displacements in (F.7)–(F.9) and the location of T_x, the TV Euclidean distance $d^T_{\mathrm{M},n}(t)$ between the nth moving point scatterer $S_{\mathrm{M},n}$ and the transmitter T_x is given by

$$d^T_{\mathrm{M},n}(t) = \Big(\left(x_{\mathrm{M},n}(t) - x^T\right)^2 + \left(y_{\mathrm{M},n}(t) - y^T\right)^2 + \left(z_{\mathrm{M},n}(t) - z^T\right)^2 \Big)^{\frac{1}{2}}. \quad \text{(F.10)}$$

Similarly, the TV Euclidean distance $d^R_{\mathrm{M},n}(t)$ between the nth moving point scatterer $S_{\mathrm{M},n}$ and the receiver R_x can be expressed by

$$d^R_{\mathrm{M},n}(t) = \Big(\left(x_{\mathrm{M},n}(t) - x^R\right)^2 + \left(y_{\mathrm{M},n}(t) - y^R\right)^2 + \left(z_{\mathrm{M},n}(t) - z^R\right)^2 \Big)^{\frac{1}{2}}. \quad \text{(F.11)}$$

By using the expressions in (F.7)–(F.11), the time variant azimuth angle of departure (TV-AAOD) $\alpha^T_{\mathrm{M},n}(t)$, time variant azimuth angle of arrival (TV-AAOA) $\alpha^R_{\mathrm{M},n}(t)$, time variant elevation angle of departure (TV-EAOD) $\beta^T_{\mathrm{M},n}(t)$, and time variant elevation angle of arrival (TV-EAOA) $\beta^R_{\mathrm{M},n}(t)$ can be expressed by

$$\alpha^T_{\mathrm{M},n}(t) = \arctan2\left(y_{\mathrm{M},n}(t) - y^T,\, x_{\mathrm{M},n}(t) - x^T\right) \tag{F.12}$$

$$\alpha^R_{\mathrm{M},n}(t) = \arctan2\left(y_{\mathrm{M},n}(t) - y^R,\, x_{\mathrm{M},n}(t) - x^R\right) \tag{F.13}$$

$$\beta^T_{\mathrm{M},n}(t) = \arcsin\left(\frac{z_{\mathrm{M},n}(t) - z^T}{d^T_{\mathrm{M},n}(t)}\right) \tag{F.14}$$

$$\beta^R_{\mathrm{M},n}(t) = \arcsin\left(\frac{z_{\mathrm{M},n}(t) - z^R}{d^R_{\mathrm{M},n}(t)}\right) \tag{F.15}$$

respectively. The TV functions in (F.12)–(F.15) are playing an essential role in providing an expression for the Doppler frequency caused by the nth moving point scatterer, which will be discussed later in this section. The TV propagation delay $\tau_{\mathrm{M},n}(t)$ of the wave transmitted by T_x via the nth moving point scatterer $S_{\mathrm{M},n}$ and arriving at the receiver R_x can be computed by

$$\tau_{\mathrm{M},n}(t) = \frac{d^T_{\mathrm{M},n}(t) + d^R_{\mathrm{M},n}(t)}{c_0} \tag{F.16}$$

where the parameter c_0 denotes the speed of light.

F.2.3 The TV Model Parameters

Using the relationship $f_{n,q}(t) = -(f_0 + f_q)\dot{\tau}_{\mathrm{M},n}(t)$ in [39, 40], the TV Doppler shift $f_{n,q}(t)$ caused by the nth moving point scatterer $S_{\mathrm{M},n}$ and associated with the qth subcarrier index can be computed by

$$f_{n,q}(t) \;=\; -f_{n,q,\max}(t)\gamma_n(t) \tag{F.17}$$

where the function $f_{n,q,\max}(t)$ denotes the maximum Doppler shift caused by the speed of motion of the nth moving point scatterer $S_{\mathrm{M},n}$. It is given by

$$f_{n,q,\max}(t) = \frac{(f_0 + f_q)\,\mathrm{v}_{\mathrm{M},n}(t)}{c_0} \tag{F.18}$$

where the parameter f_0 denotes the carrier frequency. The parameter f_q is the qth subcarrier frequency, which is given by

$$f_q = q \cdot \Delta f. \tag{F.19}$$

The parameter $q \in \{-28, -26, \ldots, -2, -1, 1, 3, \ldots, 27, 28\}$ in the expression above designates the subcarrier frequency index in OFDM communication systems that follow the IEEE 802.11n standard [28]. The parameter Δf has a constant value of 312.5 kHz.

The function $\gamma_n(t)$ in (F.17) is calculated by

$$\begin{aligned}
&\gamma_n(t) = \\
&\cos\left(\beta_{v_{\mathrm{M},n}}(t)\right)\Big[\cos\left(\beta^T_{\mathrm{M},n}(t)\right)\cos\left(\alpha^T_{\mathrm{M},n}(t) - \alpha_{v_{\mathrm{M},n}}(t)\right) \\
&+\cos\left(\beta^R_{\mathrm{M},n}(t)\right)\cos\left(\alpha_{v_{\mathrm{M},n}}(t) - \alpha^R_{\mathrm{M},n}(t)\right)\Big] \\
&+\sin\left(\beta_{v_{\mathrm{M},n}}(t)\right)\Big[\sin\left(\beta^T_{\mathrm{M},n}(t)\right) + \sin\left(\beta^R_{\mathrm{M},n}(t)\right)\Big].
\end{aligned} \tag{F.20}$$

The TV function described by (F.20) is a combination of the trigonometric functions of the TV-AAOD $\alpha^T_{\mathrm{M},n}(t)$, TV-AAOA $\alpha^R_{\mathrm{M},n}(t)$, TV-EAOD $\beta^T_{\mathrm{M},n}(t)$, TV-EAOA $\beta^R_{\mathrm{M},n}(t)$, TV-EAOM $\beta_{v_{\mathrm{M},n}}(t)$, and TV-AAOM $\alpha_{v_{\mathrm{M},n}}(t)$. Thus, it depends on the direction of motion and location of the moving point scatterer $S_{\mathrm{M},n}$ and the fixed locations of the T_x and R_x. Note that the function $\gamma_n(t)$ can have either positive or negative values and scales the maximum Doppler shift $f_{n,q,\max}(t)$. If the moving point scatterer $S_{\mathrm{M},n}$ moves towards the T_x and R_x, the propagation delay $\tau_{\mathrm{M},n}(t)$ decreases, and its rate of change $\dot{\tau}_{\mathrm{M},n}(t)$ is negative. Thus, from (F.17) it follows that the function $\gamma_n(t)$ is negative and the Doppler frequency $f_{n,q}(t)$ has positive values according to (F.17). When $S_{\mathrm{M},n}$ moves away from the T_x and R_x, the propagation delay $\tau_{\mathrm{M},n}(t)$ increases, and the rate of change $\dot{\tau}_{\mathrm{M},n}(t)$ has positive values. Hence, the function $\gamma_n(t)$ is positive and the TV Doppler frequency $f_{n,q}(t)$ becomes negative. This shows how strongly the locations of the moving point scatterer $S_{\mathrm{M},n}$, T_x, and R_x influence the values of the TV Doppler frequency $f_{n,q}(t)$. Thus, by changing the locations of the T_x and R_x, we will have different values of the Doppler frequency $f_{n,q}(t)$. Note that the Doppler frequency $f_{n,q}(t)$ in (F.17) is assumed to be linear function of time over short time intervals. A special case occurs when the T_x and R_x are co-located, e.g., as in a mono-static radar configuration, then the TV functions $\alpha^T_{\mathrm{M},n}(t)$ and $\beta^T_{\mathrm{M},n}(t)$ become equivalent to $\alpha^R_{\mathrm{M},n}(t)$ and $\beta^R_{\mathrm{M},n}(t)$, respectively. Hence, the expression for $\gamma_n(t)$ reduces to

$$\begin{aligned}
&\gamma_n(t) = 2\times \\
&\Big[\cos\left(\beta_{v_{\mathrm{M},n}}(t)\right)\cos\left(\beta^T_{\mathrm{M},n}(t)\right)\cos\left(\alpha^T_{\mathrm{M},n}(t) - \alpha_{v_{\mathrm{M},n}}(t)\right) \\
&+\sin\left(\beta_{v_{\mathrm{M},n}}(t)\right)\sin\left(\beta^T_{\mathrm{M},n}(t)\right)\Big].
\end{aligned} \tag{F.21}$$

Note that if the subcarrier frequency f_q is much smaller than the values of the carrier frequency f_0, i.e., $f_q \ll f_0$, the influence of the subcarrier frequency f_q on the Doppler frequency is much smaller than that of the carrier frequency f_0. Thus, the Doppler frequency of the moving

point scatterer $S_{\mathrm{M},n}$ is the same for all the subcarrier frequencies, i.e., $f_{n,q}(t) \approx f_{n,p}(t)$ for $p \neq q$.

The TV path gain $c_{\mathrm{M},n}(t)$ associated with the nth moving point scatterer $S_{\mathrm{M},n}$ is expressed by [41, 42]

$$c_{\mathrm{M},n}(t) = \lambda\, a_{\mathrm{M},n}\, \left[d^R_{\mathrm{M},n}(t)\, d^T_{\mathrm{M},n}(t)\right]^{-\frac{\eta}{2}}. \tag{F.22}$$

The TV path gain $c_{\mathrm{M},n}(t)$ depends on the distances $d^R_{\mathrm{M},n}(t)$ and $d^T_{\mathrm{M},n}(t)$, the wavelength $\lambda = c_0/f_0$, the transmit and receive antenna gains and the contribution of the nth moving point scatterer $a_{\mathrm{M},n}$ [43], and the path loss exponent η. Note that the TV path gain $c_{\mathrm{M},n}(t)$ in (F.22) does not change quickly with respect to time. Hence, it can be assumed that the path gain $c_{\mathrm{M},n}(t)$ is constant over short-time intervals. The parameters $a_{\mathrm{M},n}$ in (F.22) is given by

$$a_{\mathrm{M},n} = \sqrt{P_{T_x} G_{T_x} P_{R_x} G_{R_x} A_{\mathrm{M},n}} \tag{F.23}$$

for $n = 1, 2, \ldots, \mathcal{N}$, where the symbols P_{T_x}, G_{T_x}, P_{R_x}, G_{R_x}, and $A_{\mathrm{M},n}$ designate the transmit power, gain of the T_x antenna, receive power, gain of the R_x antenna, and the radar cross-section of the nth moving point scatterer $S_{\mathrm{M},m}$, respectively. These parameters are unknown. A method for estimating the parameters $a_{\mathrm{M},n}$ by using the TV-MDS will be demonstrated in Section F.4.2.

F.2.4 The CTF

The TV-CTF $H(t, f_q)$ is given by

$$H(t, f_q) \;=\; \sum_{n=1}^{\mathcal{N}} H_{\mathrm{M},n}(t, f_q) + \sum_{m=1}^{\mathcal{M}} H_{\mathrm{F},m} \tag{F.24}$$

where the first term in (F.24) denotes the superposition of $\mathcal{N}$ components corresponding to the moving point scatterers. The second term designates the superposition of the $\mathcal{M}$ components corresponding to the fixed scatterers. The components of the first and the second term in (F.24) are given by

$$H_{\mathrm{M},n}(t, f_q) = c_{\mathrm{M},n}(t)\, e^{j\left[\theta_{\mathrm{M},n} - 2\pi(f_0+f_q)\tau_{\mathrm{M},n}(t)\right]} \tag{F.25}$$

$$H_{\mathrm{F},m} = c_{\mathrm{F},m}\, e^{j\theta_{\mathrm{F},m}} \tag{F.26}$$

respectively. The TV-CTF $H_{\mathrm{M},n}(t, f_q)$ in (F.25) is characterized by a TV path gain $c_{\mathrm{M},n}(t)$, TV propagation delay $\tau_{\mathrm{M},n}(t)$, and phase shift $\theta_{\mathrm{M},n}$ corresponding to the nth moving point scatterer $S_{\mathrm{M},n}$.

The expression in (F.26) is the TV-CTF associated with the mth fixed point scatterer $S_{\mathrm{F},m}$ characterized by a constant path gain $c_{\mathrm{F},m}$ and phase shift $\theta_{\mathrm{F},m}$. The phases $\theta_{\mathrm{M},n}$ and

$\theta_{\mathrm{F},m}$ are assumed to be identically and independently distributed (i.i.d.), random variables that follow a uniform distribution between $-\pi$ and π, i.e., $\theta_{\mathrm{M},n}$, $\theta_{\mathrm{F},m}\ \mathcal{U}(-\pi,\,\pi]$ [44, p. 36]. The model presented in (F.24) corresponds to the class of 3D non-stationary fixed-to-fixed (F2F) wideband channels.

The TV-MDS $B_{f_q}(t)$ of the proposed trajectory-driven channel can be expressed in terms of $c_{\mathrm{M},n}(t)$, $c_{\mathrm{F},m}$, and $f_{n,q}(t)$ as

$$B_{f_q}(t) = \frac{\sum\limits_{n=1}^{\mathcal{N}} c_{\mathrm{M},n}^2(t) f_{n,q}(t)}{\sum\limits_{n=1}^{\mathcal{N}} c_{\mathrm{M},n}^2(t) + \sum\limits_{m=1}^{\mathcal{M}} c_{\mathrm{F},m}^2}. \tag{F.27}$$

The expression above represents the first-order spectral moment, which provides insight into the average Doppler shift caused by the moving point scatterers in the model. This quantity is the sum of the Doppler shifts $f_{n,q}(t)$ weighted by their squared TV path gains $c_{\mathrm{M},n}^2(t)$ and divided by the total sum of the squared path gains of the fixed and moving point scatterers $c_{\mathrm{F},m}^2$ and $c_{\mathrm{M},n}^2(t)$, respectively. The fixed scatterers $S_{\mathrm{F},m}$ do not have any influence on the numerator in (F.27), as the Doppler shifts caused by the fixed scatterers in F2F channels are zero. On the other hand, their squared path gains $c_{\mathrm{F},m}^2$ influence the denominator in (F.27). Hence, high values of the path gains $c_{\mathrm{F},m}$ result in small values of the TV-MDS $B_{f_q}(t)$. The expression in (F.27) can be evaluated by simulations, but not by measurements. That is due to the fact that the values of $f_{n,q}(t)$, $c_{\mathrm{F},m}$, and $c_{\mathrm{M},n}(t)$ are not accessible in the measurement data. An alternative approach for estimating the TV-MDS of CSI measurements by using the spectrogram is presented in the next section.

F.3 Micro-Doppler Signature of the TV-CTF

To study the micro-Doppler signature of the non-stationary TV-CTF presented in Section F.2.4, a time-frequency-power distribution (TFPD) is employed. There are different TFPDs according to the literature [45–47]. In this section we use the spectrogram that requires an even, real, and positive window $w(t)$ with normalized energy for computation. In this paper, we utilize a Gaussian window function defined as

$$w(t) = \frac{1}{\sqrt{\sigma_w \sqrt{\pi}}} e^{-\frac{t^2}{2\sigma_w^2}} \tag{F.28}$$

where the parameter σ_w denotes the Gaussian window spread.
There are three steps to calculate the spectrogram of the TV-CTF $H(t, f_q)$. First, the TV-CTF $H(t', f_q)$ is multiplied with the sliding window function $w(t' - t)$ to obtain the short-time CTF (ST-CTF) $x_q(t', t)$ according to [47, Eq. (2.3.1)] as

$$x_q(t', t) = H(t', f_q)\, w(t' - t). \tag{F.29}$$

Here, the parameters t and t' denote the local time at which we investigate the micro-Doppler signature and the running time, respectively. The next step is to compute the short-time Fourier transform (STFT) $X_q(f,t)$ associated with the qth subcarrier by computing the Fourier transform of the ST-CTF $x_q(t',t)$ in (F.29) as follows

$$\begin{aligned} X_q(f,t) &= \int_{-\infty}^{\infty} x_q(t',t) e^{-j2\pi f t'} dt' \\ &\approx \frac{e^{-j2\pi f t}}{\sqrt{\sigma_w \sqrt{\pi}}} \left\{ \sum_{n=1}^{\mathcal{N}} X_{\mathrm{M},n,q}(f,t) + \sum_{m=1}^{\mathcal{M}} X_{\mathrm{F},m} \right\} \end{aligned} \tag{F.30}$$

where

$$X_{\mathrm{M},n,q}(f,t) \approx H_{\mathrm{M},n}(t, f_q)\; G\left(f, f_{n,q}(t), \sigma^2_{x,n,q,\mathrm{M}}\right) \tag{F.31}$$

$$X_{\mathrm{F},m} = H_{\mathrm{F},m}\, G\left(f, 0, \sigma^2_{x,\mathrm{F}}\right) \tag{F.32}$$

$$G\left(f, \mu, \sigma^2\right) = \frac{1}{\sqrt{2\pi}\sigma} e^{-\frac{(f-\mu)^2}{2\sigma^2}} \tag{F.33}$$

$$\sigma^2_{x,n,q,\mathrm{M}} = \frac{1 - j2\pi\sigma_w^2 k_{n,q}}{(2\pi\sigma_w)^2} \tag{F.34}$$

$$\sigma^2_{x,\mathrm{F}} = \frac{1}{(2\pi\sigma_w)^2} \tag{F.35}$$

$$k_{n,q} = \frac{df_{n,q}(t)}{dt}. \tag{F.36}$$

The expression in (F.30) consists of two terms. The first term designates the superposition of STFTs of $\mathcal{N}$ components corresponding to the moving point scatterers. Each component of the first term in (F.30) is associated with the nth moving point scatterer $S_{\mathrm{M},n}$. An approximate solution of each component of the first term is provided in (F.31), which has been obtained by assuming that the path gains $c_{\mathrm{M},n}(t)$ are constant and the Doppler frequencies $f_{n,q}(t)$ are linear functions of time t, over the window function for each moving point scatterer $S_{\mathrm{M},n}$ as mentioned in Section F.2.4. The function $G(\cdot)$ denotes a Gaussian distribution whose expression is provided in (F.33). The second term in (F.30) denotes the superposition of $\mathcal{M}$ components corresponding to the fixed scatterers. Each component of the second term in (F.32) corresponds to the mth fixed scatterer $S_{\mathrm{F},m}$. Note that the STFT in (F.30) is complex valued. The third step is to compute the spectrogram $S_q(f,t)$ associated with the qth subcarrier index by taking the magnitude squared of the STFT in (F.30) as

$$S_q(f,t) = |X_q(f,t)|^2 = S_q^{(a)}(f,t) + S_q^{(c)}(f,t). \tag{F.37}$$

The first term in (F.37) denotes the auto-term $S_q^{(a)}(f,t)$, whereas the second term is the cross-term $S_q^{(c)}(f,t)$. Note that the spectrogram in (F.37) is real and positive. The auto-term

$S_q^{(a)}(f,t)$ in (F.37) is real and positive, and its approximation is given by

$$S_q^{(a)}(f,t) \approx \sum_{n=1}^{\mathcal{N}} |X_{\mathrm{M},n,q}(f,t)|^2 + \sum_{m=1}^{\mathcal{M}} c_{\mathrm{F},m}^2\, G\left(f, 0, \sigma_{\mathrm{F}}^2\right) \tag{F.38}$$

where [40]

$$|X_{\mathrm{M},n,q}(f,t)|^2 \approx c_{\mathrm{M},n}^2(t) G\left(f, f_{n,q}(t), \sigma_{n,q,\mathrm{M}}^2\right) \tag{F.39}$$

$$\sigma_{n,q,\mathrm{M}}^2 = \frac{1 + \left(2\pi\sigma_w^2 k_{n,q}\right)^2}{2(2\pi\sigma_w)^2} \tag{F.40}$$

$$\sigma_{\mathrm{F}}^2 = \frac{1}{2(2\pi\sigma_w)^2}. \tag{F.41}$$

The auto-term in (F.38) is the superposition of $\mathcal{N}+\mathcal{M}$ components. The first term in (F.38) denotes the superposition of the auto-terms associated with the $\mathcal{N}$ moving point scatterers. Each component of the first term in (F.38) contains the desired TV Doppler power characteristics of the nth moving point scatterer $S_{\mathrm{M},n}$ associated with the qth subcarrier. The expression in (F.39) represents the approximation of auto-term corresponding to the nth moving point scatterer $S_{\mathrm{M},n}$. It is a Gaussian function, which is centered on the Doppler shift $f_{n,q}(t)$, has a variance denoted by $\sigma_{n,q,\mathrm{M}}^2$, and is weighted by the squared path gain $c_{\mathrm{M},n}^2(t)$. The second term in (F.38) denotes the sum of the auto-terms of $\mathcal{M}$ fixed scatterers. Each component of the second term in (F.38) corresponds to the mth fixed scatterer $S_{\mathrm{F},m}$. Moreover, each component of the second term in (F.38) is a Gaussian function centered on a zero-frequency value as the Doppler frequencies of the fixed scatterers in F2F channels are zero. The Gaussian functions in the second term of (F.38) are weighted by the squared path gain $c_{\mathrm{F},m}^2$ of the mth fixed scatterer $S_{\mathrm{F},m}$. The expression in (F.38) provides an approximate solution of the power distribution over time and frequency, jointly.

The cross-term $S_q^{(c)}(f,t)$ associated with the qth subcarrier is expressed in (F.41), at the top of the next page. It consists of $(\mathcal{N}+\mathcal{M})(\mathcal{N}+\mathcal{M}-1)/2$ components. It represents the undesired spectral interference term that reduces the resolution of the spectrogram. This term is real, but not necessarily positive. The operators $\Re\{\cdot\}$ and $\{\cdot\}^*$ in (F.41) denote the real and complex conjugate operators, respectively. The first term in (F.41) denotes the sum of the spectral interference components between two moving point scatterers $S_{\mathrm{M},n}$ and $S_{\mathrm{M},i}$ for $n \neq i$. The second term in (F.41) designates the sum of the spectral interference components between two fixed scatterers $S_{\mathrm{F},m}$ and $S_{\mathrm{F},i}$ for $m \neq i$. Finally, the last term in (F.41) represents the sum of the spectral interference components between the fixed scatterers $S_{\mathrm{F},m}$ and the moving point scatterers $S_{\mathrm{M},n}$. Averaging the spectrogram $S_q(f,t)$ over the random phases $\theta_{\mathrm{M},n}$ and $\theta_{\mathrm{F},m}$ by simulations removes the cross-term $S_q^{(c)}(f,t)$, i.e., $\mathbf{E}\{S_q(f,t)\}|_{\theta_{\mathrm{M},n},\,\theta_{\mathrm{F},m}} = S_q^{(a)}(f,t)$ [48, 49]. In the case of measurements, eliminating the cross-term is still unknown; however, it has been

$$S_q^{(c)}(f,t) \approx \frac{2}{\sigma_w\sqrt{\pi}}\Re\left\{\sum_{n=1}^{\mathcal{N}-1}\sum_{i=n+1}^{\mathcal{N}} X_{\mathrm{M},n,q}(f,t)X_{\mathrm{M},i,q}^*(f,t) + \sum_{m=1}^{\mathcal{M}-1}\sum_{i=m+1}^{\mathcal{M}} X_{\mathrm{F},m}X_{\mathrm{F},i}^* + \sum_{n=1}^{\mathcal{N}}\sum_{i=1}^{\mathcal{M}} X_{\mathrm{M},n,q}(f,t)X_{\mathrm{F},i}^*\right\} \tag{F.41}$$

theoretically proven that massive MIMO techniques can help [50].
The TV-MDS $B_{H_q}(t)$ can be computed by means of the spectrogram $S_q(f,t)$ as follows

$$B_{H_q}(t) = \frac{\int_{-\infty}^{\infty} fS_q(f,t)df}{\int_{-\infty}^{\infty} S_q(f,t)df}. \tag{F.42}$$

The expression in (F.42) can be used in conjunction with simulations and measurements. The numerator of (F.42) represents the average frequency computed from the spectrogram at each time instant. The numerator in (F.42) is divided by the total power at each time instant. The TV-MDS $B_{H_q}(t)$ is influenced by the auto-term $S_q^{(a)}(f,t)$ and the cross-term $S_q^{(c)}(f,t)$ in case of measurements; however, it still provides insight into the mean Doppler shifts in the presence of human activities, i.e., $B_{H_q}(t) \approx B_{f_q}(t)$. In the case of simulations, the auto-term $S_q^{(a)}(f,t)$ can be used instead of the spectrogram $S_q(f,t)$ when computing $B_{H_q}(t)$ in (F.42). Hence, the TV-MDSs $B_{H_q}(t)$ and $B_{f_q}(t)$ become equal [48], i.e., $B_{H_q}(t) \triangleq B_{f_q}(t)$. It is worth mentioning that in the case of measurement data, a notch filter must be used before computing the spectrogram. This is due to the fact that the power spectral density of the signal components associated with the fixed scatterers is much higher than that of moving point scatterers.

F.4 Measurements and Numerical Results

In this section, the TV Doppler power characteristics, the TV-MDSs of the measured RF data and the IMU-driven channel model are presented for some human activities. Moreover, the measurement scenario and the processing of the RF and IMU data are discussed.

F.4.1 Measurement Scenario

Fig. F.2 shows the measurement scenario setup in the xy-plane. For RF recording, we used a CSI software tool described in [27, 51] and installed it on two HP Elitebooks 6930p laptops. Both laptops had Intel NIC 5300 network adapters and Ubuntu 14.04 LTS operating systems.

One laptop was operating in injector mode as T_x while the other was operating in monitor mode as R_x. The laptops were connected to a pair of Laird™ YE572113-30SMAM horn antennas. One was a T_x antenna connected to the transmitter station and the other one was an R_x antenna connected to the receiver station. We employed channel number 149 to record the CSI data, i.e., $f_0 = 5.745$ GHz [28]. The bandwidth B was 40 MHz. A B2B connection was used to remove the TV phase distortions, which occur due to the clock asynchronization between the T_x and R_x stations, as shown in Fig. F.2 and described in [32]. For realizing the B2B connection, the RF cables 141-MSM+, and RF power splitter ZFSC-2-10G+ with two output and one input ports have been deployed. The input port of the splitter was connected to the T_x station. One of the output ports was connected to a port of the R_x station as a B2B connection, whereas the other port was connected to the T_x antenna. Both of T_x and R_x antennas were collocated at a height of 0.8 m. The source MATLAB code for reading the measured CSI data can be found in [52].

Six IMUs were used to capture motion data simultaneously while collecting the CSI data. Four of the IMUs were from MetaMotionR [53] and the other two were from the Polytechnic School of Engineering of Vilanova i la Geltrú at the Technical University of Catalonia (UPC). A 22-year-old male candidate weighing 76 kg and 1.8 m tall was asked to perform the following activities (see Fig. F.2):

- Walking: The candidate stood in front of the T_x and R_x antennas. He wore six IMUs, two on his wrists, two on his ankles, one on his torso, and one on his head. He walked 4 m away from T_x and R_x antennas, and then he stopped.

- Falling: The candidate stood still facing the T_x and R_x antennas at a distance of 4 m. Then, he fell forward on a 15 cm thick mattress. He was wearing two IMUs. One attached to the torso, and the other one was placed on his head.

- Sitting: He stood still facing the T_x and R_x antennas at a distance of 4 m. Then, he sat down on a chair. He was wearing two IMUs at the same locations as those in the falling activity.

The candidate stopped moving for a while after finishing each activity. In the simulation, the location $\left(x^T,\, y^T,\, z^T\right)$ of T_x and the location $\left(x^R,\, y^R,\, z^R\right)$ of R_x and were chosen to be $(0,\, -0.05,\, 0.8)$ and $(0,\, 0.05,\, 0.8)$, respectively. The initial positions $(x_{\mathrm{M},n},\, y_{\mathrm{M},n},\, z_{\mathrm{M},n})$ of the moving point scatterers are exhibited in Table F.1 for each activity.

F.4.2 Processing of the Collected Data

Fig. F.3(a) illustrates the steps for processing the recorded CSI data. The collected CSI data were stored in two matrices at the R_x station. The first matrix stored the CSI data of the B2B connection, which includes only the TV phase distortions caused the clock asynchronization

Table F.1: Initial positions ($x_{\mathrm{M},n}$, $y_{\mathrm{M},n}$, $z_{\mathrm{M},n}$) of each moving point scatterer $S_{\mathrm{M},n}$ associated with each activity.

	Walking	Falling	Sitting
Left ankle	(0.2, 0.15, 0.1)	–	–
Right ankle	(0.2, −0.15, 0.1)	–	–
Left wrist	(0.2, 0.25, 0.85)	–	–
Right wrist	(0.2, −0.25, 0.85)	–	–
Waist	(0.2, 0, 1.1)	(4, 0, 1.1)	(4, 0, 1.1)
Head	(0.2, 0, 1.75)	(4, 0, 1.75)	(4, 0, 1.75)

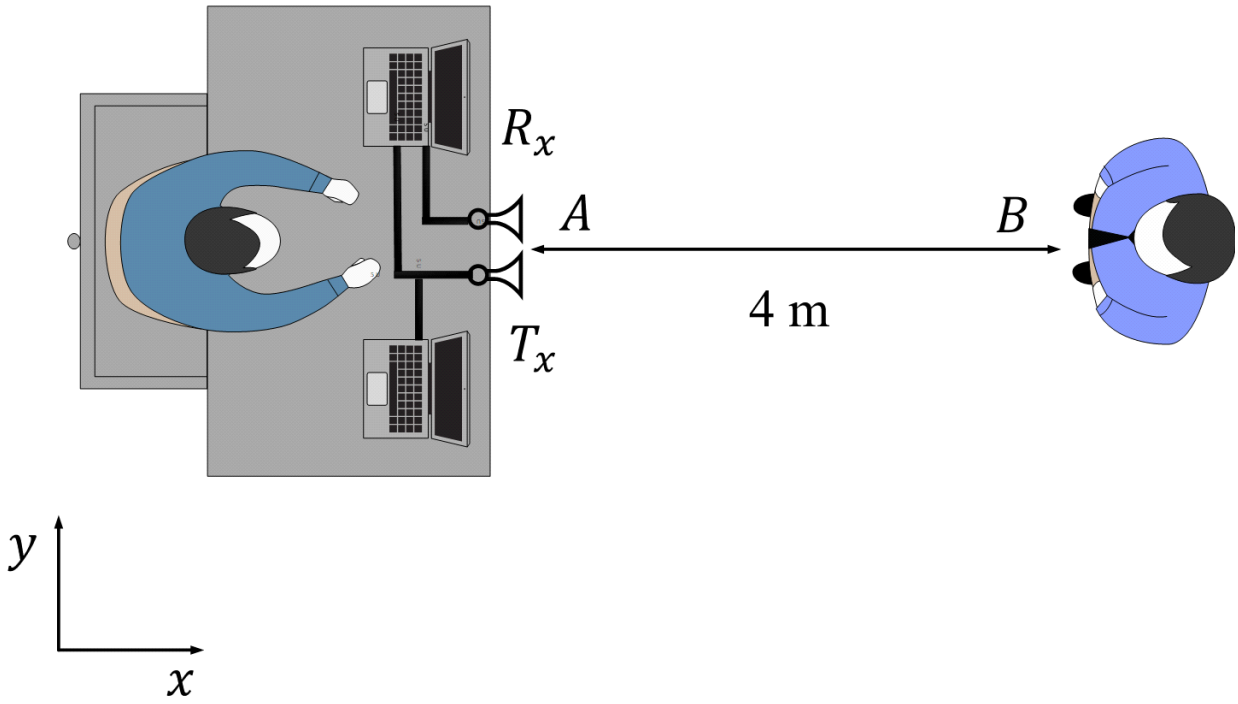

Figure F.2: Measurement scenario in xy-plane.

between the T_x station and the R_x station. The second matrix stored the data representing the desired fading behaviour of the measured channels and the TV phase distortions between the T_x and the R_x stations caused by the clock asynchronization. The second matrix was divided element-wise by the first matrix to get a new third matrix containing the channel transfer function (CTF) $\hat{H}\,(t, f_q)$, with the desired channel behaviour [54, 55]. Then, the CTF

$\hat{H}(t, f_q)$ was summed over the subcarriers to obtain the complex channel gain $\hat{\mu}(t)$

$$\hat{\mu}(t) = \sum_{q} \hat{H}(t, f_q). \tag{F.43}$$

This procedure reduces the background noise of the spectrogram that arises due to measurement imperfections. Because, as mentioned in Section F.2.3, the bandwidth B is much smaller than the carrier frequency f_0, the Doppler frequencies are almost the same for all subcarriers. Hence, the sum in (F.43) does not have an impact on the micro-Doppler signatures. The zero-value Doppler shifts due to static objects (fixed scatterers) were eliminated by utilizing a notch filter. The parameters of the filter designed in MATLAB can be found in Table F.2. Finally, the spectrogram $\hat{S}_q(f, t)$ was computed to reveal the micro-Doppler signature of the candidate's activity.

Fig. F.3(b) depicts the block diagram for developing the IMU-driven channel model. The IMU data was recorded simultaneously with the CSI data. The sensors were configured to record accelerations and quaternions simultaneously. Also, the timestamps were recorded and used to synchronize the data. The acceleration data was measured on the local axes of the IMUs. By using the quaternions, the Euler angles and the rotation matrix were constructed to rotate the measured accelerations to the reference frame. The rotated accelerations were numerically integrated first to obtain the TV velocities. The drifts in the obtained TV velocities were removed by using the zero-update (ZUPT) algorithm [56]. The source code of the ZUPT algorithm is available on GitHub [57]. After that, the displacements were determined by integrating the drift-removed velocities.

The spectrogram $\hat{S}_q(f, t)$ and TV-MDS $\hat{B}_{H_q}(t)$ of the measured CSI data were computed first. Then, the TV-MDS $\hat{B}_{H_q}(t)$ was used to compute the contribution of the nth moving scatterer $S_{\mathrm{M},n}$ by solving the following mean-square-error (MSE) optimization problem as follows

$$E_{B_{f_q}(t)} = \underset{\substack{a_{\mathrm{M},n} \\ n\in\{1,2,\ldots,\mathcal{N}\}}}{\operatorname{argmin}} \int_{0}^{T_{\mathrm{obs}}} \left(B_{f_q}(t) - \hat{B}_{H_q}(t) \right)^2 dt \tag{F.44}$$

where $B_{f_q}(t)$ and $\hat{B}_{H_q}(t)$ were computed by (F.27) and (F.42), respectively. After obtaining the contributions of the moving scatterers $a_{\mathrm{M},n}$, TV-CTF $H(t, f_q)$ was generated according to (F.24). The parameter η was set to 2. Finally, the spectrogram $S_q(f, t)$ and the TV-MDS $B_{f_q}(t)$ of $\mu(t)$ were computed. Table F.3 shows the estimated values of $a_{\mathrm{M},n}$ associated with each moving point scatterer corresponding to each activity.

F.4.3 Discussion of the Results

Figs. F.4(a) and F.4(b) exhibit the spectrograms $\hat{S}_q(f, t)$ and $S_q(f, t)$ corresponding to the walking activity of the measured CSI and the IMU-driven channel model, respectively. There

Table F.2: The parameters of the used notch filter.

Name	Value
Filter type	Highpass FIR
Stopband frequency	0.1 Hz
Passband frequency	1 Hz
Stopband attenuation	25 dB
Passband ripple	0.01
Design method	Equiripple

Table F.3: The values of the estimated parameter $a_{\mathrm{M},n}$ of each moving point scatterer $S_{\mathrm{M},n}$ corresponding to each activity.

	Walking	Falling	Sitting
Left ankle	0.150	–	–
Right ankle	0.138	–	–
Left wrist	0.086	–	–
Right wrist	0.105	–	–
Waist	0.347	0.825	0.652
Head	0.174	0.175	0.348

is a good match between the two spectrograms in Figs. F.4(a) and F.4(b). The spectrogram of the IMU-driven channel model was computed after the estimation of a_n for $n = 1, 2, \ldots, \mathcal{N}$ as in (F.44). The walking duration took almost 5.5 s, i.e., $T_{\mathrm{obs}} \approx 5.5$ s. The Doppler frequencies have negative values as the candidate was moving away from the T_x and R_x antennas. Thus, the propagation delays $\tau_{\mathrm{M},n}(t)$ and their rate of change $\dot{\tau}_{\mathrm{M},n}(t)$ were increasing. Hence, the Doppler frequencies have negative values according to (F.17) in Section F.2.3. The Doppler frequencies corresponding to the head and the torso have the highest power values, unlike the rest of the body segments, as they have the highest body areas. The Doppler shifts caused by the head and torso have ranges from 40 to 50 Hz. The values of the parameter $a_{\mathrm{M},n}$ corresponding to the walking activity are exhibited in Table F.3. These values are associated with the moving scatterers corresponding the left ankle, right ankle, left wrist, right wrist, waist, and head. According to this table, the waist and the head have the highest values, whereas the wrists have the lowest values.

Figs. F.5(a) and F.5(b) exhibit the analytical solutions of the spectrogram $S_q(f,t)$ and the auto-term $S_q^{(a)}(f,t)$ of the IMU-driven channel model corresponding to the walking activity,

respectively. Both of $S_q(f,t)$ and $S_q^{(a)}(f,t)$ were computed by approximating the Doppler frequencies as mentioned in Section F.3. Although the linear approximations of the Doppler frequencies are obvious in Fig. F.5(b), they do not have a huge impact on the spectrograms as shown in the figures. Furthermore, the Doppler frequency patterns depicted in the figures still provides useful insights in Figs. F.5(a) and F.5(b) of the walking activity. Note that in Fig. F.5(b), the Doppler frequencies corresponding to the moving scatterers are more obvious as there is no cross-term.

The spectrograms $\hat{S}_q(f,t)$ and $S_q(f,t)$ of the measured CSI and the IMU-driven channel model are depicted in Figs. F.6(a) and F.6(b), respectively. These spectrograms correspond to the falling activity. Surprisingly, there is a good match between $\hat{S}_q(f,t)$ and $S_q(f,t)$, although the candidate wore two IMUs in this scenario. The falling duration consumed around 1.5 s. The value of the observation interval T_{obs} was set to 3.5 s when evaluating the parameter computation in (F.44). The Doppler frequencies had positive values as the candidate was moving towards the T_x and R_x antennas. Thus, the propagation delays $\tau_{\text{M},n}(t)$ were decreasing and their rates of change $\dot{\tau}_{\text{M},n}(t)$ were negative. Hence, the Doppler frequencies had positive values according to (F.17) in Section F.2.3. The Doppler frequencies $f_n(t)$ had zero values before time $t \approx 1.5$ s. Then, they increased when the falling started, until they reached a value of 120 Hz approximately at time $t \approx 2.5$ s. At this time $t \approx 2.5$ s, the candidate almost approached the floor. Then, the Doppler frequencies $f_n(t)$ decreased rapidly until they reached zero values in less than 0.5 s. The values of the parameter $a_{\text{M},n}$ corresponding to the falling activity are exhibited in Table F.3. These values are associated with the moving scatterers corresponding the waist and head. According to the table, the waist has a higher value than the head.

Figs. F.7(a) and F.7(b) demonstrate the analytical solutions of the spectrogram $S_q(f,t)$ and the auto-term $S_q^{(a)}(f,t)$ of the IMU-driven channel model corresponding to the falling activity, respectively. The cross-term in Fig. F.7(a) does not have a high impact as the number of the moving scatterers $\mathcal{N}$ is 2 in the falling scenario. By comparing Figs. F.7(a) and F.7(b) with Fig. F.6(b), there are slight degradation of the linear Doppler frequencies at time $t \approx 3$ s. However, the falling patterns are still obvious in Figs. F.7(a) and F.7(b).

Figs. F.8(a) and F.8(b) illustrate the spectrograms $\hat{S}_q(f,t)$ and $S_q(f,t)$ corresponding to the sitting activity of the measured CSI data and the IMU-driven channel model, respectively. There is also a good match between $\hat{S}_q(f,t)$ and $S_q(f,t)$. The values of the Doppler frequencies were negative since the candidate was moving away down from the T_x and R_x. The value of T_{obs} was chosen to be 3 s. The sitting duration was 1.5 s; however, the Doppler frequencies $f_n(t)$ reached values of about -50 Hz, unlike those of the falling activity in Figs. F.8(a) and F.6(b). That is because the candidate's speed during the sitting activity was slower than that of the falling activity. The values of the Doppler frequencies started to decrease at $t \approx 0.5$ s until they reached values of about -50 Hz at $t \approx 1.5$ s. Then, they increased slowly until they reached zero values. The values of the parameter $a_{\text{M},n}$ corresponding to the sitting activity

and associated with the waist and the head are depicted in Table F.3. Again, the waist has a higher value than the head. Figs. F.9(a) and F.9(b) show the spectrograms $S_q(f,t)$ and $S_q^{(a)}(f,t)$ corresponding to the sitting activity of the measured CSI data and the IMU-driven channel model, respectively. A slight difference is depicted in Figs. F.9(a) and F.9(b) due to the linear approximation of the Doppler frequencies; however, the spectrograms still provide insightful results.

Fig. F.10(a) depicts the TV-MDSs $\hat{B}_{H_q}(t)$ and $B_{f_q}(t)$ corresponding to the walking activity of the collected CSI data and the IMU-driven channel model, respectively. The TV-MDSs $\hat{B}_{H_q}(t)$ and $B_{f_q}(t)$ in Fig. F.10(a) are matching. The TV-MDSs in Fig. F.10(a) provide the same trends as those in Figs. F.4(a) and F.4(b), but with different values. This happens due to the impact of the cross-terms. The TV-MDSs $\hat{B}_{H_q}(t)$ and $B_{f_q}(t)$ corresponding to the falling activity of the measured CSI data and the IMU-driven channel model are exhibited in Fig. F.10(b), respectively. There is a good match between $\hat{B}_{H_q}(t)$ and $B_{f_q}(t)$ in Fig. F.10(b). The TV-MDSs in Fig. F.10(b) show the same trends as those in Figs. F.6(a) and F.6(b), but with different values due to the influence of the cross-terms on the TV-MDSs. The TV-MDSs $\hat{B}_{H_q}(t)$ and $B_{f_q}(t)$ of the CSI data and the IMU-driven channel model corresponding to the sitting activity are shown in Fig. F.10(c), respectively. A good match is shown between the TV-MDSs $\hat{B}_{H_q}(t)$ and $B_{f_q}(t)$ in Fig. F.10(c). The trends of $\hat{B}_{H_q}(t)$ and $B_{f_q}(t)$ in Fig. F.10(c) are matching the TV frequency patterns shown in Figs. F.8(a) and F.8(b); however, they have different values as the cross-terms have influences on $\hat{B}_{H_q}(t)$ and $B_{f_q}(t)$. Note that in Figs. F.10(a) and F.10(c) the TV-MDSs $B_{f_q}(t)$ computed from the analytical solutions of the spectrogram and the auto-term are still insightful although the Doppler frequencies are linearly approximated.

F.5 Conclusion

In this paper, we demonstrated the possibility of designing an IMU-driven non-stationary channel model for human activity recognition. Such a model enables the reproducibility of micro-Doppler signatures. We modelled the non-stationary CTF fed with IMU data, TV path gains, and TV Doppler shifts. Furthermore, we explored the micro-Doppler signature of the proposed TV CTF by means of the spectrogram. We confirmed our proposed model by comparing the micro-Doppler signatures of measured CSI data with a channel model fed with IMU data. Both of the CSI and IMU data were measured simultaneously. The results showed a good match between the micro-Doppler signatures of the IMU-driven channel model and the CSI. For future work, we recommend to train fall classifiers with micro-Doppler signatures or the TV-MDSs of the proposed model and test them with measured RF data.

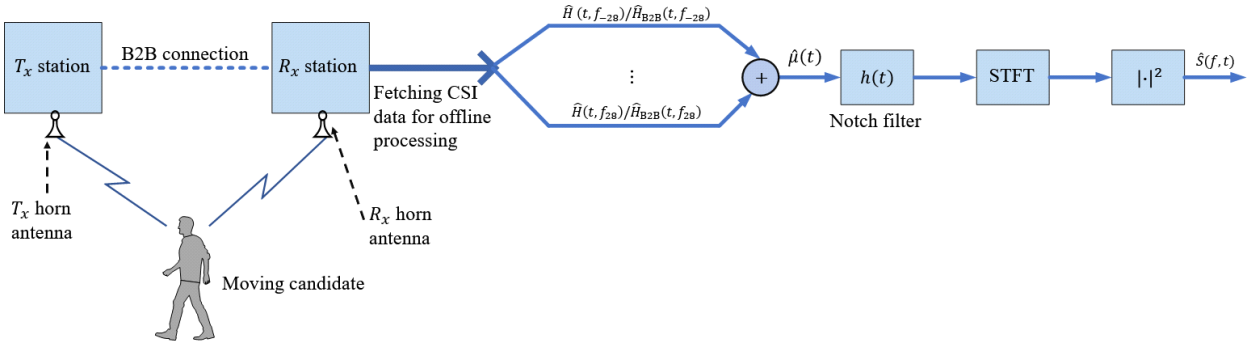

(a)

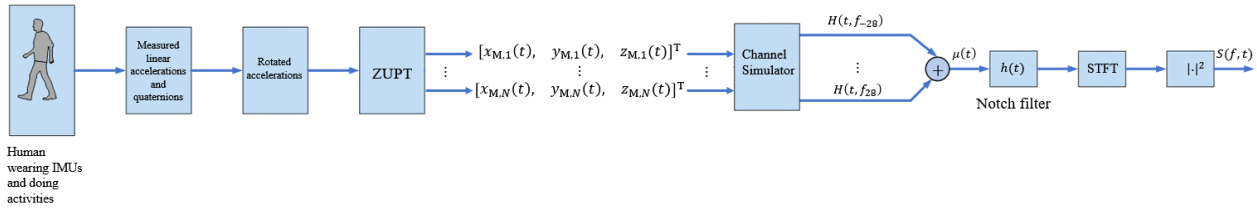

(b)

Figure F.3: Block diagrams for the (a) CSI data acquisition and processing and (b) IMU-driven channel model.

Acknowledgment

This article is a part of the WiCare project with grant number 261895/F20 and is funded by the Research Council of Norway (RCN).

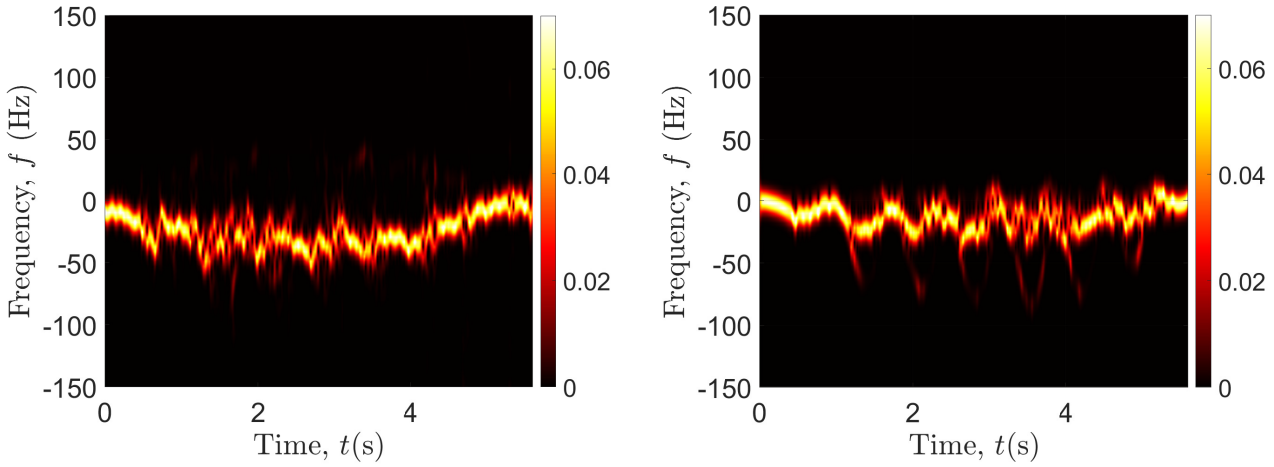

Figure F.4: Walking activity spectrograms $\hat{S}_q(f,t)$ and $S_q(f,t)$ of the (a) measured CSI data and (b) IMU-driven channel model, respectively.

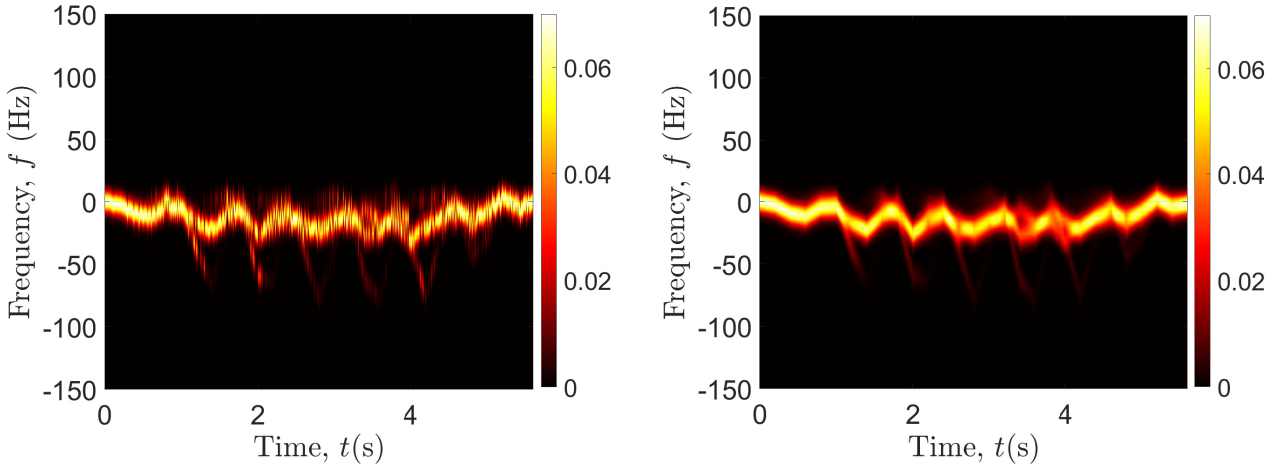

Figure F.5: Approximate analytical solutions of (a) the spectrogram $S_q(f,t)$ and (b) the auto-term $S_q^{(a)}(f,t)$ of the IMU-driven channel model corresponding to the walking scenario.

F

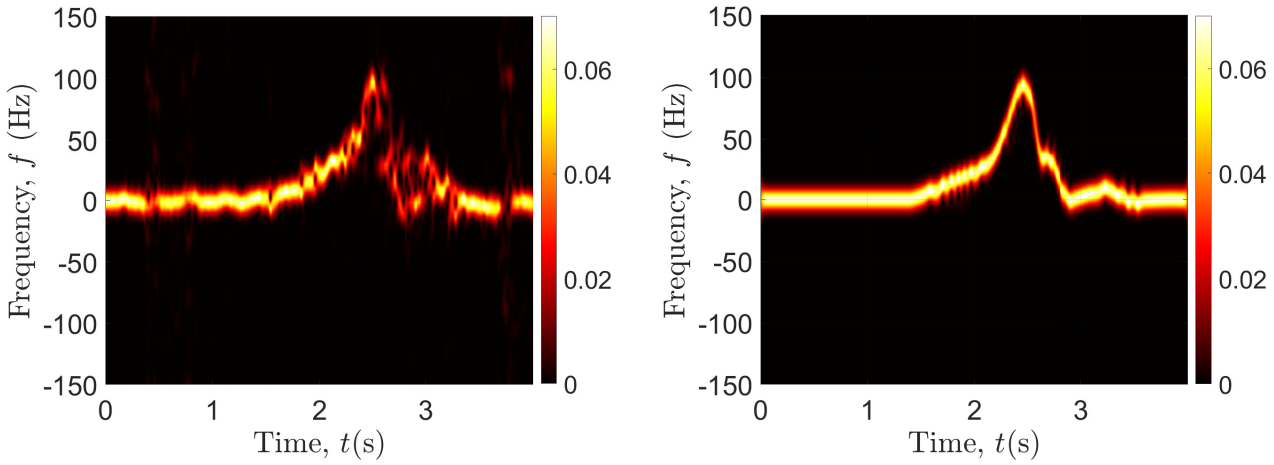

Figure F.6: Falling activity spectrograms $\hat{S}_q(f,t)$ and $S_q(f,t)$ of the (a) measured CSI data and (b) IMU-driven channel model, respectively.

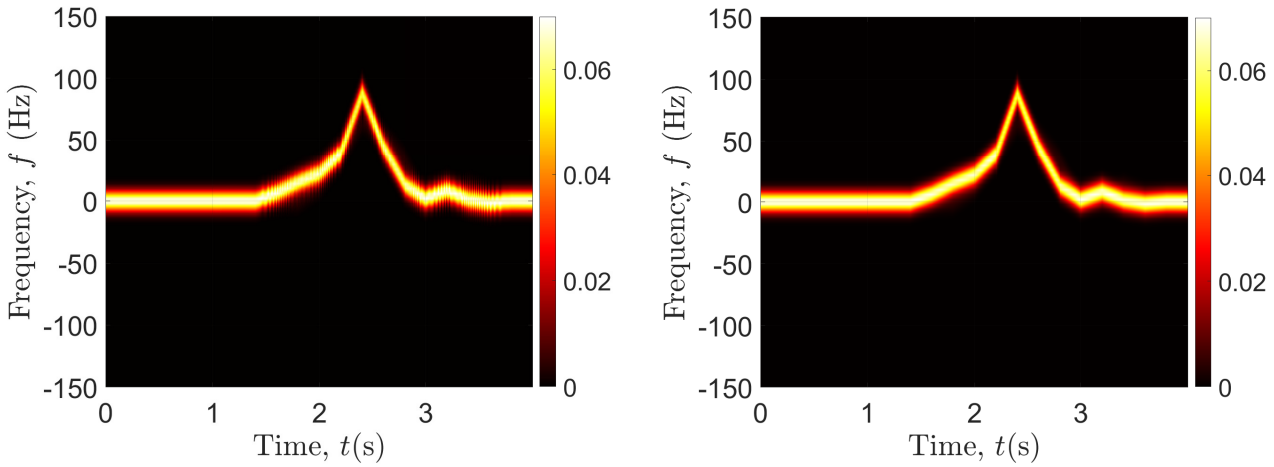

Figure F.7: Approximate analytical solutions of (a) the spectrogram $S_q(f,t)$ and (b) the auto-term $S_q^{(a)}(f,t)$ of the IMU-driven channel model corresponding to the falling scenario.

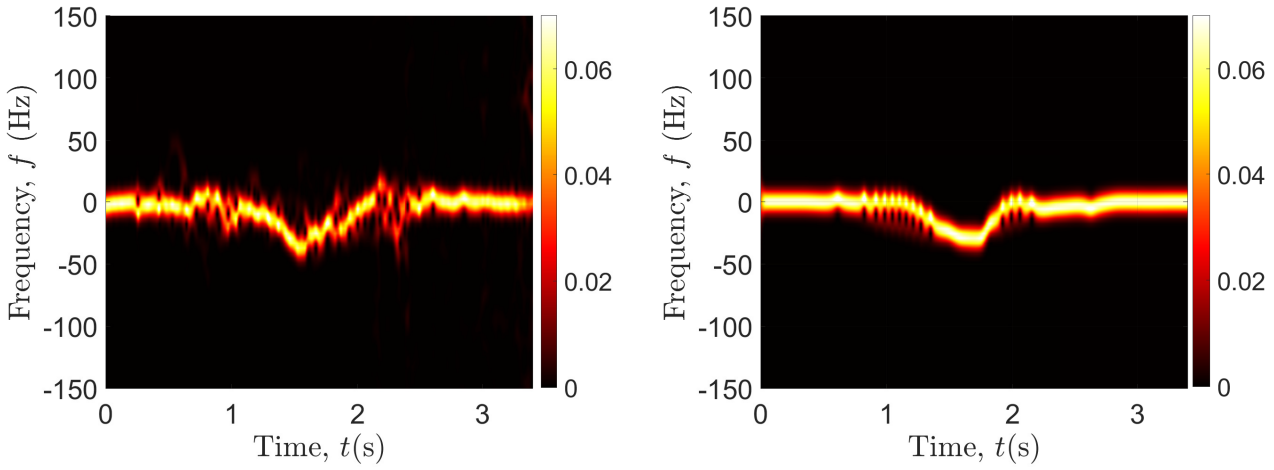

(a) (b)

Figure F.8: Sitting activity spectrograms $\hat{S}_q(f,t)$ and $S_q(f,t)$ of the (a) measured CSI data and (b) IMU-driven channel model, respectively.

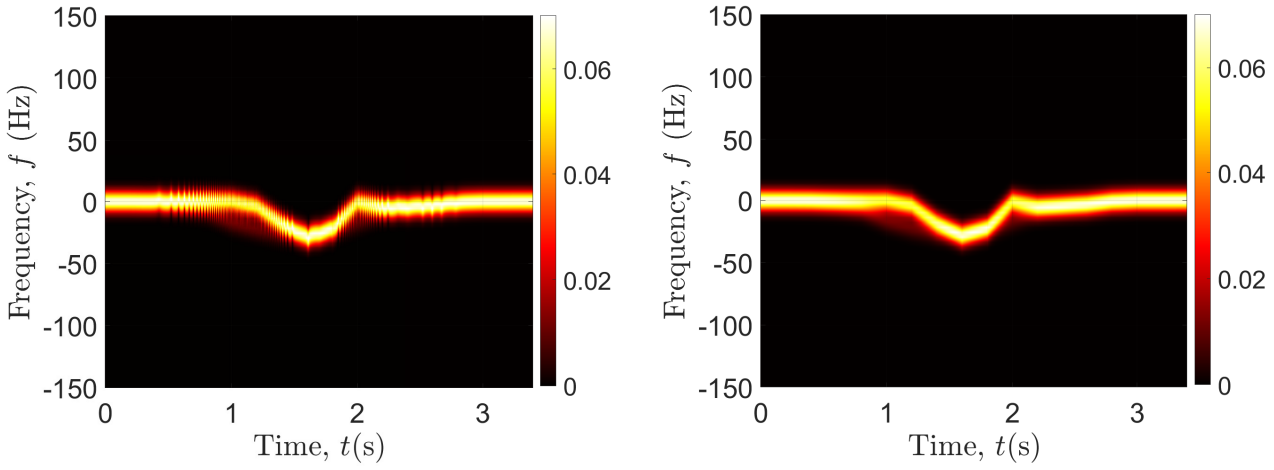

(a) (b)

Figure F.9: Approximate analytical solutions of the spectrogram $S_q(f,t)$ and (b) the auto-term $S_q^{(a)}(f,t)$ of the IMU-driven channel model corresponding to the sitting scenario.

F

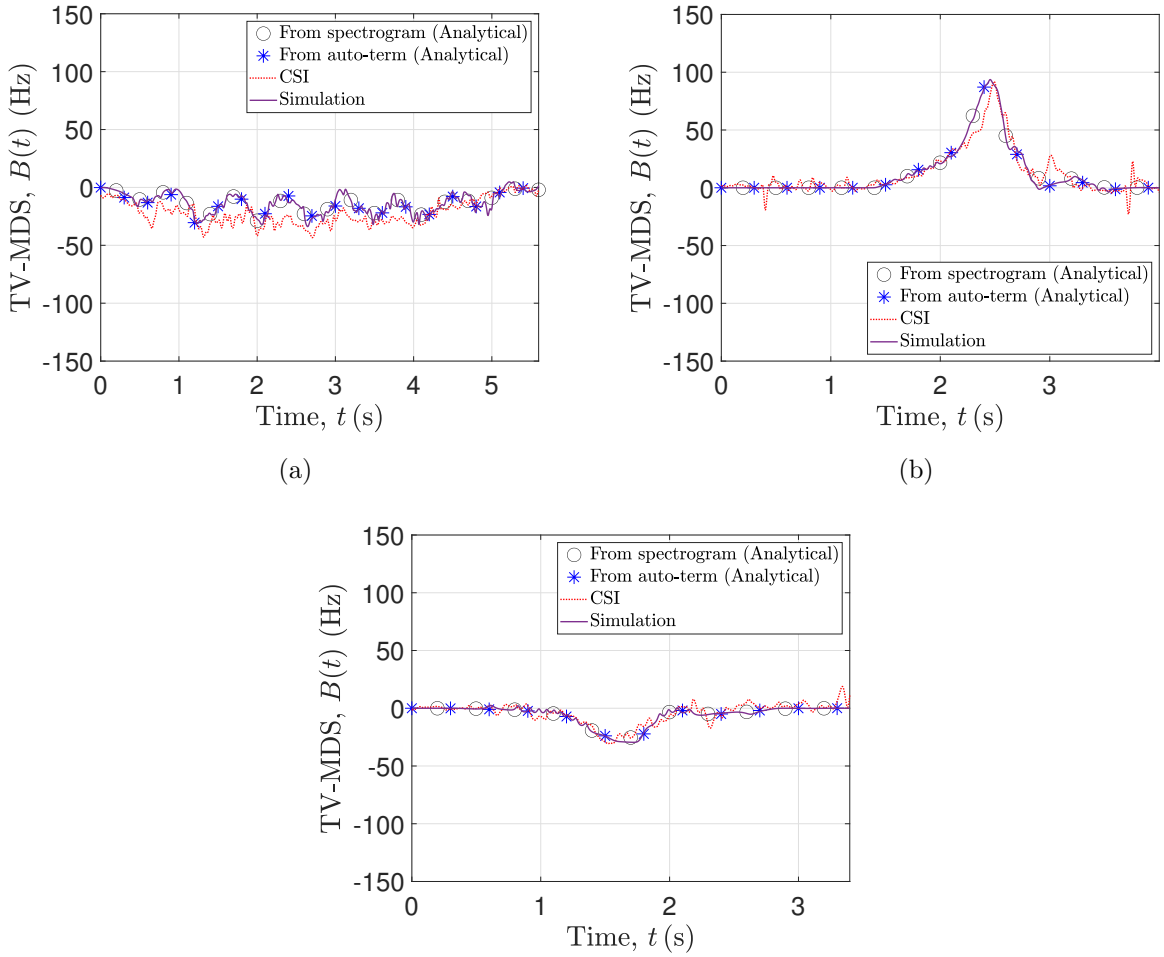

Figure F.10: The TV-MDSs $\hat{B}_{H_q}(t)$ and $B_{f_q}(t)$ of the measured CSI and the IMU-driven channel model, respectively, corresponding to the (a) walking, (b) falling, and (c) sitting activities.

Bibliography

[1] "Clinical trial transformation initiative. CTTI recommendations: Developing novel endpoints generated by mobile technology for use in clinical trials," June 2018.

[2] F. Cerreta, "EMA experience on mHealth technology," *PCWP and HCPWP joint meeting*, April 2018.

[3] K. A. Hartholt, R. Lee, E. R. Burns, and E. F. van Beeck, "Mortality from falls among US adults aged 75 years or older, 2000-2016," *JAMA*, vol. 321, pp. 2131–2133, 06 2019.

[4] United Nations, Department of Economic and Social Affairs, Population Division, "World population ageing," 2020. Highlights (ST/ESA/SER.A/408).

[5] E. Warmerdam *et al.*, "Long-term unsupervised mobility assessment in movement disorders," *The Lancet Neurology*, vol. 19, no. 5, pp. 462 – 470, 2020.

[6] M. Babiker, O. O. Khalifa, K. K. Htike, A. Hassan, and M. Zaharadeen, "Automated daily human activity recognition for video surveillance using neural network," in *2017 IEEE 4th International Conference on Smart Instrumentation, Measurement and Application (ICSIMA)*, pp. 1–5, 2017.

[7] K. K. Htike, O. O. Khalifa, H. A. Mohd Ramli, and M. A. M. Abushariah, "Human activity recognition for video surveillance using sequences of postures," in *The Third International Conference on e-Technologies and Networks for Development (ICeND2014)*, pp. 79–82, 2014.

[8] W. Lin, M.-T. Sun, R. Poovandran, and Z. Zhang, "Human activity recognition for video surveillance," in *2008 IEEE International Symposium on Circuits and Systems*, pp. 2737–2740, 2008.

[9] S. Park, J. Park, M. Al-masni, M. Al-antari, M. Uddin, and T.-S. Kim, "A depth camera-based human activity recognition via deep learning recurrent neural network for health and social care services," *Procedia Computer Science*, vol. 100, pp. 78 – 84, 2016. International Conference on ENTERprise Information Systems.

[10] F. Attal *et al.*, "Physical human activity recognition using wearable sensors," *Sensors*, vol. 15, p. 31314–31338, Dec 2015.

[11] A. Nandy, J. Saha, C. Chowdhury, and K. P. D. Singh, "Detailed human activity recognition using wearable sensor and smartphones," in *2019 International Conference on Opto-Electronics and Applied Optics (Optronix)*, pp. 1–6, 2019.

F

[12] J. Aggarwal and M. Ryoo, "Human activity analysis: A review," *ACM Comput. Surv.*, vol. 43, Apr. 2011.

[13] M. Ermes, J. Parkka, and L. Cluitmans, "Advancing from offline to online activity recognition with wearable sensors," in *2008 30th Annual International Conference of the IEEE Engineering in Medicine and Biology Society*, pp. 4451–4454, 2008.

[14] Y. He, F. Le Chevalier, and A. G. Yarovoy, "Range-Doppler processing for indoor human tracking by multistatic ultra-wideband radar," in *2012 13th International Radar Symposium*, pp. 250–253, 2012.

[15] J. Kwon, S. Lee, and N. Kwak, "Human detection by deep neural networks recognizing micro-Doppler signals of radar," in *2018 15th European Radar Conference (EuRAD)*, pp. 198–201, 2018.

[16] Y. Kim, S. Ha, and J. Kwon, "Human detection using Doppler radar based on physical characteristics of targets," *IEEE Geoscience and Remote Sensing Letters*, vol. 12, no. 2, pp. 289–293, 2015.

[17] B. Erol and M. G. Amin, "Radar data cube processing for human activity recognition using multisubspace learning," *IEEE Transactions on Aerospace and Electronic Systems*, pp. 1–1, 2019.

[18] B. Jokanović and M. Amin, "Fall detection using deep learning in range-Doppler radars," *IEEE Transactions on Aerospace and Electronic Systems*, vol. 54, pp. 180–189, Feb 2018.

[19] F. Fioranelli, J. Le Kernec, and S. A. Shah, "Radar for health care: Recognizing human activities and monitoring vital signs," *IEEE Potentials*, vol. 38, no. 4, pp. 16–23, 2019.

[20] Z. Zeng, M. Amin, and T. Shan, "Automatic arm motion recognition based on radar micro-Doppler signature envelopes," *IEEE Sensors Journal*, pp. 1–1, 2020.

[21] M. Ritchie and A. M. Jones, "Micro-Doppler gesture recognition using Doppler, time and range based features," in *2019 IEEE Radar Conference (RadarConf)*, pp. 1–6, April 2019.

[22] S. Skaria, A. Al-Hourani, M. Lech, and R. J. Evans, "Hand-gesture recognition using two-antenna Doppler radar with deep convolutional neural networks," *IEEE Sensors Journal*, vol. 19, no. 8, pp. 3041–3048, 2019.

[23] J. Lien *et al.*, "Soli: Ubiquitous gesture sensing with millimeter wave radar," *ACM Trans. Graph.*, vol. 35, July 2016.

[24] F. Fioranelli, M. Ritchie, S.-Z. Gürbüz, and H. Griffiths, "Feature diversity for optimized human micro-Doppler classification using multistatic radar," *IEEE Transactions on Aerospace and Electronic Systems*, vol. 53, pp. 640–654, Apr. 2017.

[25] A. Seifert, A. M. Zoubir, and M. G. Amin, "Detection of gait asymmetry using indoor Doppler radar," in *2019 IEEE Radar Conference (RadarConf)*, pp. 1–6, April 2019.

[26] A. Seifert, M. G. Amin, and A. M. Zoubir, "Toward unobtrusive in-home gait analysis based on radar micro-Doppler signatures," *IEEE Transactions on Biomedical Engineering*, vol. 66, pp. 2629–2640, Sep. 2019.

[27] D. Halperin, W. Hu, A. Sheth, and D. Wetherall, "Tool release: gathering 802.11n traces with channel state information," *ACM SIGCOMM CCR*, vol. 41, p. 53, Jan. 2011.

[28] "IEEE standard for information technology– local and metropolitan area networks– Specific requirements– Part 11: Wireless LAN medium access control (MAC) and physical layer (PHY) specifications amendment 5: Enhancements for higher throughput," *IEEE Std 802.11n-2009 (Amendment to IEEE Std 802.11-2007 as amended by IEEE Std 802.11k-2008, IEEE Std 802.11r-2008, IEEE Std 802.11y-2008, and IEEE Std 802.11w-2009)*, pp. 1–565, Oct 2009.

[29] Z. Wang, B. Guo, Z. Yu, and X. Zhou, "Wi-Fi CSI-based behavior recognition: from signals and actions to activities," *IEEE Communications Magazine*, vol. 56, pp. 109–115, May 2018.

[30] W. Wang, A. X. Liu, and M. Shahzad, "Gait recognition using WiFi signals," in *Proceedings of the 2016 ACM International Joint Conference on Pervasive and Ubiquitous Computing*, UbiComp '16, (New York, NY, USA), pp. 363–373, ACM, 2016.

[31] S. Sen, B. Radunovic, R. R. Choudhury, and T. Minka, "You are facing the Mona Lisa: spot localization using PHY layer information," in *Proceedings of the 10th International Conference on Mobile Systems, Applications, and Services*, MobiSys '12, (New York, NY, USA), pp. 183–196, ACM, 2012.

[32] N. Keerativoranan, A. Haniz, K. Saito, and J.-i. Takada, "Mitigation of CSI temporal phase rotation with B2B calibration method for fine-grained motion detection analysis on commodity Wi-Fi devices," *Sensors*, vol. 18, no. 11, 2018.

[33] S. S. Ram, R. Bhalla, and H. Ling, "Simulation of human radar signatures in the presence of ground," in *2009 IEEE Antennas and Propagation Society International Symposium*, pp. 1–4, 2009.

[34] J. Park and J. T. Johnson, "Measurements and simulations of multi-frequency human radar signatures," in *Proceedings of the 2012 IEEE International Symposium on Antennas and Propagation*, pp. 1–2, 2012.

[35] P. van Dorp and F. C. A. Groen, "Human walking estimation with radar," *IEE Proceedings - Radar, Sonar and Navigation*, vol. 150, no. 5, pp. 356–365, 2003.

[36] R. Boulic, N. Magnenat-Thalmann, and D. Thalmann, "A global human walking model with real-time kinematic personification," *Vis. Comput.*, vol. 6, p. 344–358, Nov. 1990.

[37] C. Karabacak *et al.*, "Knowledge exploitation for human micro-Doppler classification," *IEEE Geoscience and Remote Sensing Letters*, vol. 12, no. 10, pp. 2125–2129, 2015.

[38] B. Erol, C. Karabacak, S. Z. Gürbüz, and A. C. Gürbüz, "Simulation of human micro-doppler signatures with kinect sensor," in *2014 IEEE Radar Conference*, pp. 0863–0868, 2014.

[39] M. Pätzold and C. A. Gutierrez, "Modelling of non-WSSUS channels with time-variant Doppler and delay characteristics," in *2018 IEEE Seventh International Conference on Communications and Electronics (ICCE)*, pp. 1–6, Hue, Vietnam, July 2018.

[40] A. Abdelgawwad and M. Pätzold, "A framework for activity monitoring and fall detection based on the characteristics of indoor channels," in *IEEE 87th Vehicular Technology Conference (VTC Spring)*, Porto, Portugal, Jun. 2018.

[41] H. T. Friis, "A note on a simple transmission formula," *IEEE Proceedings of the IRE*, vol. 34, no. 5, pp. 254–256, May 1946.

[42] C. Phillips, D. Sicker, and D. Grunwald, "A survey of wireless path loss prediction and coverage mapping methods," *IEEE Commun. Surveys Tuts.*, vol. 15, no. 1, pp. 255–270, 1st Quart., 2013.

[43] V. Chen, *The Micro-Doppler Effect in Radar, 2nd ed.* Artech House radar library, Artech House, 2019.

[44] G. L. Stüber, *Principles of Mobile Communications*. Springer Int. Publishing, 4th ed., 2017.

[45] F. Hlawatsch and G. F. Boudreaux-Bartels, "Linear and quadratic time-frequency signal representations," *IEEE Signal Processing Magazine*, vol. 9, pp. 21–67, Apr. 1992.

[46] B. A. J and R. R. L, "A unified approach to short-time Fourier analysis and synthesis," *Proceedings of the IEEE*, vol. 65, pp. 1558–1564, Nov. 1977.

[47] B. Boashash, *Time-Frequency Signal Analysis and Processing – A Comprehensive Reference*. Elsevier, Academic Press, 2nd ed., 2015.

[48] A. Abdelgawwad and M. Pätzold, "On the influence of walking people on the Doppler spectral characteristics of indoor channels," in *Proc. 28th IEEE Int. Symp. on Personal, Indoor and Mobile Radio Communications, PIMRC 2017*, Montreal, Canada, Oct. 2017.

[49] M. Pätzold and C. A. Gutiérrez, "Spectrogram analysis of multipath fading channels under variations of the mobile speed," in *Proc. 84rd IEEE Vehicular Technology Conference, IEEE VTC2016-Fall*, Montreal, Canada, Sept. 2016.

[50] M. Pätzold and C. A. Gutiérrez, "Enhancing the resolution of the spectrogram of non-stationary channels by using massive MIMO techniques," in *Proc. IEEE 86th Vehicular Technology Conference, VTC2017-Fall*, pp. 1–7, Toronto, Canada, Sep. 2017.

[51] "Source code for the CSI tool," Available online: `https://github.com/dhalperi/linux-80211n-csitool/`.

[52] "Source code for processing CSI data," Available online: `https://github.com/dhalperi/linux-80211n-csitool-supplementary`.

[53] "Sensors for motion capture, biomechanics, industrial control, robotics, facility management, cold storage, research, and product development," Available online: `https://mbientlab.com/`.

[54] A. Abdelgawwad, A. Borhani, and M. Pätzold, "Modelling, analysis, and simulation of the micro-Doppler effect in wideband indoor channels with confirmation through pendulum experiments," *Sensors*, vol. 20, p. 1049, Feb 2020.

[55] A. Abdelgawwad, A. Català, and M. Pätzold, "Doppler power characteristics obtained from calibrated channel state information for human activity recognition," in *2020 IEEE 91st Vehicular Technology Conference (VTC2020-Spring)*, pp. 1–7, 2020.

[56] X. Yun, E. R. Bachmann, H. Moore, and J. Calusdian, "Self-contained position tracking of human movement using small inertial/magnetic sensor modules," in *Proceedings 2007 IEEE International Conference on Robotics and Automation*, pp. 2526–2533, April 2007.

[57] "MATLAB code for 3D tracking with IMU," Available online: `https://github.com/xioTechnologies/Gait-Tracking-With-x-IMU`.

F